UNIVERSITY OF CALIFORNIA,
IRVINE

Advances and Applications of Finite-Time Lyapunov Analysis

DISSERTATION

submitted in partial satisfaction of the requirements
for the degree of

DOCTOR OF PHILOSOPHY

in Mechanical and Aerospace Engineering

by

Marco Maggia

Dissertation Committee:
Professor Kenneth D. Mease, Chair
Associate Professor Anton Gorodetski
Assistant Professor Haithem E. Taha

2017

DEDICATION

To my sister Sabrina.

TABLE OF CONTENTS

LIST OF FIGURES

LIST OF TABLES

ACKNOWLEDGMENTS

I would like to express my deepest gratitude to my committee chair and advisor Professor Kenneth D. Mease for his excellent knowledge, caring and patience. I learned a lot from him, both academically, but also from a human perspective. Without his guidance and persistent help this dissertation would not have been possible.

I would like to thank my committee members, Professor Anton Gorodetski and Professor Haithem E. Taha for their feedback and their time during my studies at UCI.

In addition, a warm thank you to Professor Tryphon Georgiou, who has been a great source of motivation. Working with you has been a real pleasure.

Last but not least, I want to thank all my family, my girlfriend and all my friends. You have been extremely supportive during this long adventure of mine, and I will always be grateful to you for your patience and understanding, I love you all.

Some text of this dissertation is a reprint of the material as it appears in *Characterizing Two-Timescale Non-linear Dynamics Using Finite-Time Lyapunov Exponents and Vectors*, published in "Communications in Nonlinear Science and Numerical Simulation", Elsevier, Vol. 36, 2016. The first author listed in this publication directed and supervised research which forms the basis for the dissertation.

Permission to incorporate parts of previously published work into this dissertation has been granted by Prof. Kenneth D. Mease, Dr. Erkut Aykutluğ, and Prof. Ufuk Topcu.

This material is based upon work supported by the National Science Foundation under Grants CMMI-0010085 and CMMI-1069331.

CURRICULUM VITAE

Marco Maggia

EDUCATION

Doctor of Philosophy in Mechanical and Aerospace Engineering — **June, 2017**
University of California, Irvine — *Irvine, California*

Master of Science in Aerospace Engineering — **October, 2010**
University of Padua — *Padua, Italy*

Bachelor of Science in Aerospace Engineering — **December, 2007**
University of Padua — *Padua, Italy*

RESEARCH EXPERIENCE

Graduate Research Assistant — **2010–2017**
University of California, Irvine — *Irvine, California*

TEACHING EXPERIENCE

Teaching Assistant — **2014-2016**

Astronautics (ENGRMAE 146) — **Winter 2014,2015,2016**
University of California, Irvine — *Irvine, California*

Introduction to Control Systems (ENGRMAE 170) — **Fall 2015**
University of California, Irvine — *Irvine, California*

Engineering Analysis I (ENGRMAE 200A) — **Fall 2016**
University of California, Irvine — *Irvine, California*

PUBLICATIONS

- Maggia, M., Mease, K.D., *"Stationkeeping for Collinear Libration Point Orbits Via Finite-Time Lyapunov Analysis."*, submitted to Celestial Mechanics and Dynamical Astronomy, Springer, 2017.
- Mease, K.D., Topcu, U., Aykutulug, E., Maggia, M. *"Characterizing Two-Timescale Nonlinear Dynamics Using Finite-Time Lyapunov Exponents and Vectors."* Communications in Nonlinear Science and Numerical Simulation, Volume 36 , July 2016, Pages 148-174.
- Maggia, M., Mease, K.D., *"Flow Structure Identification for Nonlinear Dynamical Systems via Finite-Time Lyapunov Analysis"*, Math. Model. Nat. Phenom. Vol. 10, No. 3, 2015, pp. 91-104.
- Maggia, M., Mease, K.D., Villac F.B.,*"Finite-Time Lyapunov Analysis of Orbits Near L1"*, Conference Paper, AIAA SPACE 2014, San Diego, 4-7 August 2014.
- Aykutulug, E., Maggia, M., Mease, K.D., *"Solving Partially Hyper-Sensitive Optimal Control Problems Using Manifold Structure"*. Conference Paper, International Federation of Automatic Controls, Toulouse, 4-6 September 2013.
- Maggia, M., *"Aerodynamics and Development of a Simulator for an Airship for Planetary Exploration in Matlab-SimulinkÂ® Environment"*. M.S. Thesis. University of Padova, 2010.
- Maggia, M., *"Fluid Dynamic Simulations of Airfoil Cascades for Gas Turbines"*. B.S. Thesis. University of Padova, 2007.

HONORS AND AWARDS

National Science Foundation Fellowship **2011-2014**
University of California, Irvine *Irvine, California*

Holmes Graduate Fellowship **2010-2011**
University of California, Irvine *Irvine, California*

Educational Abroad Program Scholarship **2009-2010**
University of California, Irvine *Irvine, California*

ESU Scholarship **2004-2008**
University of Padova *Padova, Italy*

Literary Award "Pasquale Lo Re" **2003**
Liceo Scientifico "E. Curiel" *Padova, Italy*

ABSTRACT OF THE DISSERTATION

Advances and Applications of Finite-Time Lyapunov Analysis

By

Marco Maggia

Doctor of Philosophy in Mechanical and Aerospace Engineering

University of California, Irvine, 2017

Professor Kenneth D. Mease, Chair

Many physical systems can be modeled through nonlinear time-invariant differential equations. When the dynamics of such systems are hyper-sensitive to the initial conditions, such equations are often challenging to solve. However, if the flow of such dynamical systems is also characterized by multiple timescales (e.g., fast-slow behavior), there may be a manifold structure associated with it. Focusing on this manifold structure, that is, adopting a geometric perspective, holds potential for a simpler solution process and a better understanding of the system behavior.

We adopt finite-time Lyapunov analysis (FTLA) as the methodology to diagnose the timescale behavior and to characterize the manifold structure. FTLA is based on finite-time Lyapunov exponents (FTLEs) and vectors (FTLVs) and its main advantage is that it is more widely applicable with respect to other methodologies. In fact, for nonlinear dynamical systems, FTLA is not restricted to equilibria nor periodic solutions, nor does it require require the equations to be in a special form. We will show that the accuracy of FTLA depends solely on how fast certain linear subspaces computed using FTLVs converge to their invariant counterparts.

This work is dedicated to continuing the advancement of the methodology and to its applications to two-timescale partially hyperbolic dynamical systems. In the first part of this dissertation, we

provide a detailed presentation of the methodology, with particular attention to the diagnosis of a uniform hyperbolic finite-time two-timescale set and to the computation of points on finite-time approximations of the invariant manifolds.

The second and third parts of the dissertation focus entirely on the application of FTLA to two major problems. Firstly, we use FTLA as a means of computing the approximation of the local stable, center and unstable directions at points on orbits around libration points in the circular restricted three-body problem (CR3BP). After assessing the accuracy of the FTLA results for points on periodic orbits, where Floquet theory gives exact results, we move to aperiodic orbits, demonstrating that FTLA results maintain a degree of accuracy that is otherwise lost when applying Floquet theory in an approximate manner. Secondly, we propose a new stationkeeping strategy for spacecraft orbiting about libration points in the Earth-Moon CR3BP. The strategy is based on performing instantaneous velocity corrections that place the spacecraft on the stable manifold of some orbit in the neighborhood of a prescribed reference orbit. We demonstrate via several test cases that the proposed strategy is reliable and therefore can be considered as a good alternative or addition to existent stationkeeping strategies.

In the last part, we focus our attention on developing a solution strategy for partially hyper-sensitive optimal control problems. The strategy exploits the existence of the invariant center-stable and center-unstable manifolds to construct an approximation to the optimal solution by matching trajectories on such invariant manifolds. The approach is specifically applied to the optimal control of a nonlinear spring-mass-damper system. The approximate solution is shown to be accurate by comparison with a solution obtained by a collocation method.

In conclusion, we have contributed in advancing finite-time Lyapunov analysis and applied it to models of physical problems demonstrating its effectiveness.

Chapter 1

Introduction

The purpose of this dissertation is to describe the latest developments and advances in finite-time Lyapunov analysis and to present two original applications for the methodology. The first application concerns orbital dynamics and in particular, we will study the stationkeeping of spacecraft orbiting around libration points in the circular restricted three-body problem. The second application deals with approximating solutions of partially hyper-sensitive optimal control problems. This work has been inspired by and is the natural continuation of (51; 4). For both the applications, the motivation for using finite-time Lyapunov analysis stems from the fact that viewing and analyzing problems from a geometric perspective, often gives useful insight to the nature of the solution that would be otherwise very difficult to grasp. Moreover, the methodologies that are currently utilized to solve these problems may not be accurate enough or may have limited applicability.

The dissertation is structured as follows. After the introduction, Chapter 2 is dedicated to the meticulous description of the methodology. The theory is followed by practical examples to understand the potential of finite-time Lyapunov analysis. Chapter 3 and Chapter 4 are dedicated to the aforementioned applications. Finally, in Chapter 5 we draw some final conclusions.

1.1 Advances to Finite-Time Lyapunov Analysis

Finite-time Lyapunov analysis is a methodology that utilizes exponents and subspaces to define and diagnose boundary-layer type, two-timescale behavior in the tangent linear dynamics and to determine the associated manifold structure in the flow of finite-dimensional nonlinear autonomous dynamical systems. Two-timescale behavior is characterized by a slow-fast splitting of the tangent bundle for a phase space region. Such slow-fast splitting is defined using finite-time Lyapunov exponents and vectors, which are determined from the asymptotic theory of partially hyperbolic sets, with important modifications for the finite-time case. The splitting is used to characterize and locate points approximately on normally hyperbolic center manifolds and other invariant manifolds, via tangency conditions for the vector field.

The flow of a finite-dimensional autonomous nonlinear dynamical system with multiple timescales may have manifold structure. Characterizing this structure can facilitate simplified analysis and computation, and lead to greater understanding of the system behavior. The relevant timescales are most generally in the linear variational dynamics, i.e., tangent linear dynamics. Our objective is to diagnose two-timescale behavior in tangent linear dynamics with slow dynamics and both stable and unstable fast dynamics, and to compute the associated manifold structure in the flow of the nonlinear system. Because the intent is to analyze finite-time behavior, we first define two-timescale behavior in this context. Although in this chapter we only directly consider two timescales and the associated normally hyperbolic center manifolds, the discussion and results are relevant also to additional manifold structure, such as the center-stable and center-unstable manifolds relevant to the solution of certain boundary-value problems (3; 29; 57; 67).

Many of the methods available for computing invariant manifolds (i) operate off the linear structure at an equilibrium point or a periodic orbit (14), or (ii) require *a priori* knowledge of system coordinates adapted to the manifold structure, e.g. (61), or (iii) require *a priori* knowledge of a

manifold that can be analytically or numerically continued to the manifold of interest, e.g. (8; 59), or (iv) require that the manifold is transversally stable (20; 49).

The situation of interest is when two-timescale behavior is suspected in a region of state space, perhaps based on simulation experience, and one wants a means of diagnosing whether or not there are two (or more) disparate timescales and, if there are, a means of characterizing the associated flow structure. In addition to requiring methodology that works away from equilibria and periodic orbits and does not require the singularly perturbed normal form, there is the challenge that, for many applications, the methodology must be effective when only finite-time behavior is considered. The approach addressed in this work, which we refer to as finite-time Lyapunov analysis (FTLA), uses finite-time Lyapunov exponents (FTLEs) and the associated vectors (FTLVs), to diagnose two-timescale behavior and characterize the associated tangent bundle structure, and then uses invariance-based orthogonality conditions to locate and compute the associated manifold structure. Orthogonality conditions are used in the intrinsic low-dimensional manifold (ILDM) method (48) in the chemical kinetics context to compute a slow manifold, but the tangent bundle structure is determined by a means other than FTLA. Orthogonality conditions are also used for the computation of invariant manifolds in (59), but the tangent bundle structure is derived from a known neighboring manifold in a numerical continuation scheme.

FTLA is used in different ways in several application contexts. In particular the maximum FTLE field is used to determine Lagrangian coherent structures in fluid flows with time-dependent velocity fields (13; 30; 63; 69) and to assess the stability of orbits in celestial mechanics (19; 70). FTLA is used to identify the fastest growing direction(s) of initialization errors in weather predictability theory (9; 44; 71; 72).

FTLA is applied to systems with slow-fast behavior in (2; 52; 53; 60). In (52), Lyapunov analysis is proposed as a means of diagnosing timescales and suggesting adapted coordinates as an alternative

to the singular perturbation approach. In (53), the ILDM and computational singular perturbation (CSP) (42; 43) methods for slow-fast behavior are interpreted geometrically using Fenichel theory and the idea of using FTLE/Vs to improve the ILDM method is proposed. In (2) Lyapunov analysis is applied to periodic and chaotic attractors, as well as slow manifolds, and an approach for computing FTLVs is developed. Lorenz (46) seems to have been the first to use FTLA in analyzing a chaotic attractor. In (60), FTLA is used to identify the dimension of the attracting slow manifold along a trajectory. The application of FTLA to the solution of two-timescale boundary value problems related to optimal control is discussed in (3).

The main contributions of this work are to extend FTLA to the diagnosis and computation of normally hyperbolic center manifolds and to clarify more generally the definitions and procedures for meaningful finite-time tangent bundle splittings. Because the finite time is limited, it is crucial to define the tangent bundle splitting of interest in the fastest converging way and to clarify the finite time required to accurately approximate the invariant tangent bundle splitting. Guided by the theory of partially hyperbolic sets (32), a finite-time two-timescale set is defined, requiring spatial and temporal uniformity of the spectral gap between the slow and fast FTLEs. A *fast stable / slow / fast unstable* tangent bundle splitting is specified in terms of the FTLVs. The size of the spectral gap dictates the rate of exponential convergence of the tangent bundle splitting toward the desired invariant splitting, providing a guideline for how large the finite time needs to be. We account for both fast stable and fast unstable behavior and provide orthogonality conditions for approximately computing points on normally hyperbolic center manifolds.

1.2 Stationkeeping of Spacecraft in the Circular Restricted Three-Body Problem

In recent years, interest about space missions targeting libration points of the circular restricted three-body problem has substantially grown. The libration points are equilibrium points in space where the combined gravitational forces of two large celestial bodies, such as Earth and the sun or Earth and the moon, equal the centrifugal force felt by a much smaller third body which in our case we identify as a spacecraft. Due to their fixed position with respect to the two large celestial bodies, libration points are particularly suitable for space missions whose goal is for instance the direct and continuous observation of one or both of the celestial bodies.

Examples of space missions to libration points are: the Solar and Heliospheric Observatory (SOHO) launched in 1995 (75), ARTEMIS launched in 2007 (76), and the upcoming James Webb Space Telescope, scheduled to be launched in 2018 (74). During its operational phase, the spacecraft is usually put in a periodic or quasiperiodic orbit about a libration point. Many of these orbits are unstable, causing the spacecraft to drift away from its ideal trajectory. To correct the unstable dynamical behavior, stationkeeping operations are necessary to maintain the spacecraft on a desired or acceptable course.

The stationkeeping strategies that are found in literature can essentially be divided in two main categories: the first kind of approach computes the magnitude and direction of the correction maneuvers using an optimal-constrained multiple shooting strategy (Target Point)(17; 33; 38; 26; 55). The other methodology is, instead, based on dynamical system theory; the main idea behind the approach is to design stationkeeping maneuvers that cancel the unstable component of the phase space error between the spacecraft and a desired point on a periodic orbit of reference (38). The local unstable directions and the local approximations to the manifold structure near the reference

orbit are computed using Floquet modes (24; 65). This methodology has also been extended to quasiperiodic orbits (65; 25). Because such extension is theoretically non justifiable, in this chapter we propose finite-time Lyapunov analysis, as an alternative means of determining the manifold structure. FTLA is also based on dynamical system theory, but its applicability is independent of orbit periodicity. Our goal is to use FTLA to exploit the partially hyperbolicity of the phase space region around the collinear libration points and use finite-time Lyapunov vectors and exponents to identify the tangent subspaces that can serve as local approximations to the associated manifolds (50; 51). We then propose a new stationkeeping strategy based on FTLA: once the information about the manifold structure is obtained, the stationkeeping maneuvers are designed so that the spacecraft is placed on some apposite manifold. The natural dynamics will guide the spacecraft towards a reference orbit keeping it in the phase space region of interest until the next maneuver is performed.

1.3 Approximating Solutions of Partially Hyper-Sensitive Optimal Control Problems

Hyper-sensitivity to unknown boundary conditions plagues indirect methods of solving optimal control problems as a Hamiltonian boundary-value problem for both state and costate. Yet, the hyper-sensitivity may imply manifold structure in the Hamiltonian flow, knowledge of which would yield insight regarding the optimal solutions and suggest a solution approximation strategy that circumvents the hyper-sensitivity. We propose the use of finite-time Lyapunov analysis to provide a means of diagnosing hyper-sensitivity to determine the associated manifold structure.

The first-order necessary conditions for the solution to an optimal control problem comprise a Hamiltonian boundary-value problem (HBVP). An optimal control problem is called hyper-sensitive

if the final time is large relative to some of the contraction and expansion rates of the associated Hamiltonian system. The solution to a hyper-sensitive problem can be qualitatively described in three segment as “take-off”, “cruise” and “landing” analogous to optimal flight of an aircraft between distant locations (41). The “cruise” segment is primarily determined by the cost function and the state dynamics, whereas the “take-off” and “landing” segments are determined by the boundary conditions and the goal of connecting these to the “cruise” segment.

As the final time increases so does the duration of the cruise segment which shadows a trajectory on a reduced-order slow invariant manifold. When the final time is large with respect to , the sensitivity of the final state to the unknown initial conditions makes the HBVP ill-conditioned. The ill-conditioning can be removed by approximating the solution by a composite solution: a trajectory on a center-stable manifold that satisfies the initial boundary conditions is matched with a trajectory on a center-unstable manifold that satisfies the final boundary conditions.

The key to implementing this approach is a means of determining the unknown boundary conditions such that the solution end points lie on the appropriate invariant manifolds to sufficient accuracy. If the differential equations are in singularly perturbed normal form, then appropriate equilibrium-based manifold structure can be used. However, since the singularly perturbed normal form is often not available and a general approach to converting a system to this form does not exist, a method that does not require this normal form is desired. We describe how finite-time Lyapunov exponents and vectors can be used for this purpose and the issues involved.

Relevant previous research concerning optimal control is discussed and cited in (57; 68; 3). And, though the focus in (29) is not optimal control, the proposed solution approach keys off the same geometric structure as our method, yet it is different in that it relies on the singularly perturbed form. The manifold structure of two-timescale (“slow-fast”) systems is addressed in (16; 35).

Chapter 2

Finite-Time Lyapunov Analysis

The chapter is organized as follows. In Section 2.1, we specify the dynamical system to be considered and recall some definitions from geometry and section 2.2 provides a perspective of the approach. Section 2.3 covers Lyapunov analysis: first we briefly describe the asymptotic theory of partially hyperbolic sets; second we define finite-time Lyapunov exponents and vectors (FTLE/Vs) and describe their use for the identification of tangent space structure; third we address the convergence of the tangent space structure; and fourth we contrast the properties of the FTLE/Vs and their asymptotic counterparts. In Section 2.4 we define a finite-time two-timescale set and a finite-time center manifold. The procedure for applying the approach is given in Section 2.5. Section 2.6 contains detailed examples that serve to illustrate and clarify the approach, and to demonstrate its feasibility and effectiveness in locating and approximating invariant center manifolds.

This chapter is an adaptation of work that was published as ref.(51) and co-authored with Prof. Kenneth D. Mease, Dr. Ufuk Topcu, and Dr. Erkut Aykutluğ. My specific contributions are in sections 2.3.3, 2.4, 2.4.3, 2.5, 2.5.1, 2.5.2, and 2.6.

2.1 Dynamical System Description and Relevant Geometry

The methodology we develop will be applied to a given coordinate representation of a dynamical system. Denoting the vector of coordinates by $\mathbf{x} \in \mathbb{R}^n$, in the standard basis with $2 \leq n < \infty$, the $\mathbf{x}$-representation of the dynamical system is

$$\dot{\mathbf{x}} = \mathbf{f}(\mathbf{x}), \tag{2.1}$$

where the vector field $\mathbf{f} : \mathbb{R}^n \to \mathbb{R}^n$ is a smooth function. The solution of (2.1) for the initial condition $\mathbf{x}$ is denoted by $\mathbf{x}(t) = \phi(t, \mathbf{x})$, where $\phi(t, \cdot) : \mathbb{R}^n \to \mathbb{R}^n$ is the t-dependent flow associated with the vector field $\mathbf{f}$ and $\phi(0, \mathbf{x}) = \mathbf{x}$. We assume that ϕ is complete on $\mathbb{R}^n$ for simplicity, but the methodology developed will only be applied on a subset of the state space and the properties of the flow outside this subset are irrelevant.

The linearized dynamics associated with (2.1) are

$$\dot{\mathbf{v}} = D\mathbf{f}(\mathbf{x})\mathbf{v} \tag{2.2}$$

where $D\mathbf{f} := \partial \mathbf{f}/\partial \mathbf{x}$ and will be analyzed to characterize the timescales. An initial point $(\mathbf{x}, \mathbf{v})$ is mapped in time t to the point $(\mathbf{x}(t), \mathbf{v}(t)) = (\phi(t, \mathbf{x}), \Phi(t, \mathbf{x})\mathbf{v})$ where Φ is the fundamental matrix for the linearized dynamics, defined such that $\Phi(0, \mathbf{x}) = I$, the $n \times n$ identity matrix. With this initial condition, we refer to Φ as the transition matrix and note that $\Phi = \partial \phi/\partial \mathbf{x}$. Geometrically, for a pair $(\mathbf{x}, \mathbf{v})$, we view $\mathbf{v}$ as taking values in the tangent space at $\mathbf{x}$ denoted by $T_{\mathbf{x}}\mathbb{R}^n$. The tangent bundle $T\mathbb{R}^n$ is the union of the tangent spaces over the state space $\mathbb{R}^n$ and $(\mathbf{x}, \mathbf{v})$ is a point in the tangent bundle, with $\mathbf{v}$ the tangent vector and $\mathbf{x}$ the base point. We need the interpretation $(\mathbf{x}, \mathbf{v}) \in T\mathbb{R}^n$, because the analysis of the linearized dynamics will define a subspace decomposition of the tangent space and the orientation of the subspaces will vary with the base point $\mathbf{x}$. Henceforth (2.2)

is called the *tangent linear dynamics*.

We adopt the Euclidean metric for $\mathbb{R}^n$ and the Euclidean norm to define the length of a tangent vector, i.e., for $\mathbf{v} \in T_{\mathbf{x}}\mathbb{R}^n$, its length is $\|\mathbf{v}\| = \langle \mathbf{v}, \mathbf{v} \rangle^{1/2}$ and $\langle \cdot, \cdot \rangle$ is the standard inner product.

Let $\mathbf{w}_1, \mathbf{w}_2, \ldots, \mathbf{w}_k$, $k \leq n$, denote vector fields, defined on $\mathbb{R}^n$, that vary continuously with $\mathbf{x}$ and have the property that at each $\mathbf{x} \in \mathbb{R}^n$, the vectors $\mathbf{w}_1(\mathbf{x}), \ldots, \mathbf{w}_k(\mathbf{x})$ are linearly independent in $T_{\mathbf{x}}\mathbb{R}^n$. Then at each $\mathbf{x}$, $\Delta(\mathbf{x}) = \text{span}\{\mathbf{w}_1(\mathbf{x}), \ldots, \mathbf{w}_k(\mathbf{x})\}$ is a k-dimensional subspace. If $k = n$, then $\Delta(\mathbf{x}) = T_{\mathbf{x}}\mathbb{R}^n$ and for each $\mathbf{x}$ the set of vectors provides a basis for $T_{\mathbf{x}}\mathbb{R}^n$. If $k < n$, then $\Delta(\mathbf{x})$ is a linear subspace of $T_{\mathbf{x}}\mathbb{R}^n$; let $\Delta := \bigcup_{\mathbf{x} \in R^n} \Delta(\mathbf{x})$ denote the subbundle (or distribution) on $\mathbb{R}^n$. A subbundle is Φ-invariant, if for any $\mathbf{x} \in \mathbb{R}^n$ and $\mathbf{v} \in \Delta(\mathbf{x})$, the property $\Phi(t, \mathbf{x})\mathbf{v} \in \Delta(\phi(t, \mathbf{x}))$ holds for all t. Subbundles $\Delta_1, \ldots, \Delta_m$ allow a splitting of the tangent bundle if $T\mathbb{R}^n = \Delta_1 \oplus \cdots \oplus \Delta_m$. If each subbundle in the splitting is Φ-invariant, then the splitting is a Φ-invariant splitting.

Let $\mathcal{X}$ be a domain in $\mathbb{R}^n$. A smooth submanifold $\mathcal{M} \subset \mathcal{X} \subset \mathbb{R}^n$ of dimension $m < n$ is $\mathcal{X}$-relatively ϕ-invariant, if for each $\mathbf{x} \in \mathcal{M}$, $\phi(t, \mathbf{x}) \in \mathcal{M}$ for all t for which $\phi(t, \mathbf{x})$ has not left $\mathcal{X}$. An equivalent requirement for invariance is that $\mathbf{f}(\mathbf{x}) \in T_{\mathbf{x}}\mathcal{M}$ for all $\mathbf{x} \in \mathcal{M}$.

2.2 Perspective on the Strategy

Using the terminology from the previous section, we now provide a perspective on the strategy to be implemented using FTLA in the remainder of this work. Consider a domain $\mathcal{X} \subset \mathbb{R}^n$ on which the behavior of (2.1) on a time interval $[0, t_f]$ is of interest, with t_f a specified final time. The tangent linear dynamics (2.2) are analyzed to determine if there is a splitting of the tangent bundle into stable, center, and unstable subbundles $T\mathcal{X} = \mathcal{E}^s \oplus \mathcal{E}^c \oplus \mathcal{E}^u$ of dimensions n^s, n^c, and n^u, respectively, where the associated exponential rates indicate that, relative to the time interval

$[0, t_f]$, vectors in the stable subbundle $\mathcal{E}^s$ decay quickly in forward time, vectors in the unstable subbundle $\mathcal{E}^u$ decay quickly in backward time, and vectors in the center subbundle evolve slowly.[1] Then postulate that there are corresponding invariant manifolds that organize the flow in the state space on the time interval of interest. For example, an n^c-dimensional invariant center manifold $\mathcal{W}^c \subset \mathcal{X}$ can be postulated. At each $\mathbf{x} \in \mathcal{W}^c$, $T_{\mathbf{x}}\mathcal{W}^c = \mathcal{E}^c(\mathbf{x})$ and the tangency condition $\mathbf{f}(\mathbf{x}) \in \mathcal{E}^c(\mathbf{x})$ holds. If $\{\mathbf{w}_1(\mathbf{x}), \ldots, \mathbf{w}_{n-n^c}(\mathbf{x})\}$ is a basis for $[\mathcal{E}^c(\mathbf{x})]^\perp$, the orthogonal complement of $\mathcal{E}^c(\mathbf{x})$, then a necessary condition for a point $\mathbf{x}$ to belong to $\mathcal{W}^c$ is that at $\mathbf{x}$ the orthogonality condition

$$\langle \mathbf{f}(\mathbf{x}), \mathbf{w}_i(\mathbf{x}) \rangle = 0, \quad i = 1, ..., n - n^c \tag{2.3}$$

is satisfied. The orthogonality condition expresses that $\mathbf{f}(\mathbf{x})$ lies in $T_{\mathbf{x}}\mathcal{W}^c$ at each $\mathbf{x} \in \mathcal{W}^c$, i.e., the invariance of $\mathcal{W}^c$. The orthogonality conditions for $\mathbf{f}$ in (2.3) can be viewed as partial-equilibrium conditions, partial in the sense that the vector field $\mathbf{f}$ need only be zero when projected into a certain subspace. Similarly, orthogonality conditions can characterize points on the center-stable $\mathcal{W}^{cs}$ and center-unstable $\mathcal{W}^{cu}$ manifolds.

Figures 2.1 and 2.2 show examples of center manifolds in a three-dimensional state space, the relevant geometric objects, and the spectra of characteristic exponents indicating the exponential rates in the tangent linear dynamics, consistent with the geometry. Diagnosing timescale separation and computing such geometric structure, encompassing both the normally attracting center manifold (Fig. 2.1) and normally hyperbolic center manifold (Fig. 2.2) cases, is our goal. Computationally, only determining low-dimensional manifolds may be feasible, but computing selected points on higher-dimensional manifolds is also possible and useful (e.g. (3)).

[1] As mentioned earlier, we use a broader notion of 'center'. It is not necessary that vectors in the center subspace stay constant.

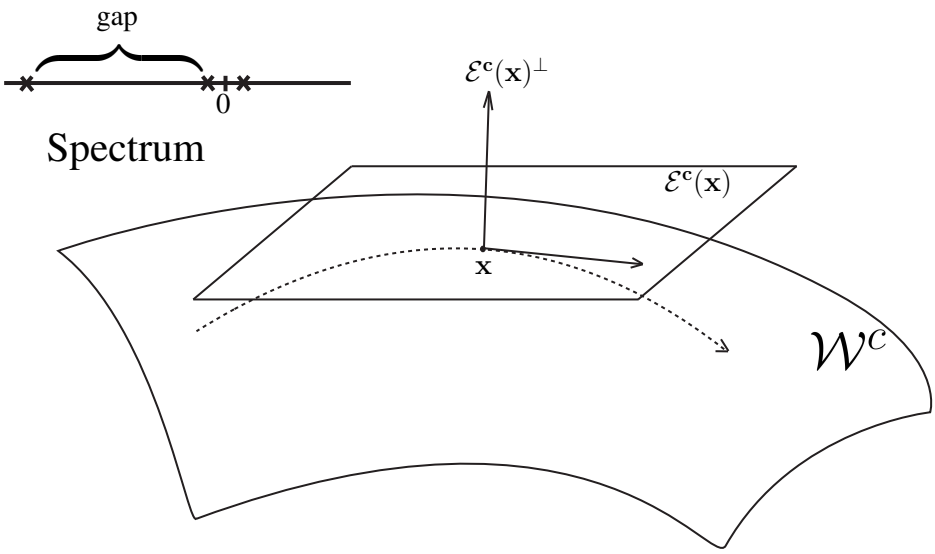

Figure 2.1: Geometry of a two-timescale 3D system with a 2D normally attracting center manifold.

2.3 Lyapunov Analysis and Partially Hyperbolic Sets - Finite-Time versus Asymptotic

In this section we present the methodology for characterizing the tangent linear dynamics (2.2), along trajectories of the nonlinear system (2.1), that will be used to define and diagnose two-timescale behavior. We refer to this methodology as *Lyapunov analysis*. Because we need to determine, in a limited finite-time, a good approximation of an invariant splitting that in principle requires asymptotic Lyapunov analysis, we need to define the finite-time splitting in a way that will converge as fast as possible towards the desired invariant splitting. We clarify how defining the splitting in terms of FTLVs accomplishes this.

In the first subsection, we describe how asymptotic Lyapunov exponents or vectors can be used to define the ideal invariant splittings. In the second subsection we present a finite-time version of Lyapunov analysis, modeled after the asymptotic version described in Barreira and Pesin (6) and Katok and Hasselblatt (37). See (44; 71; 72) for other presentations of finite-time Lyapunov

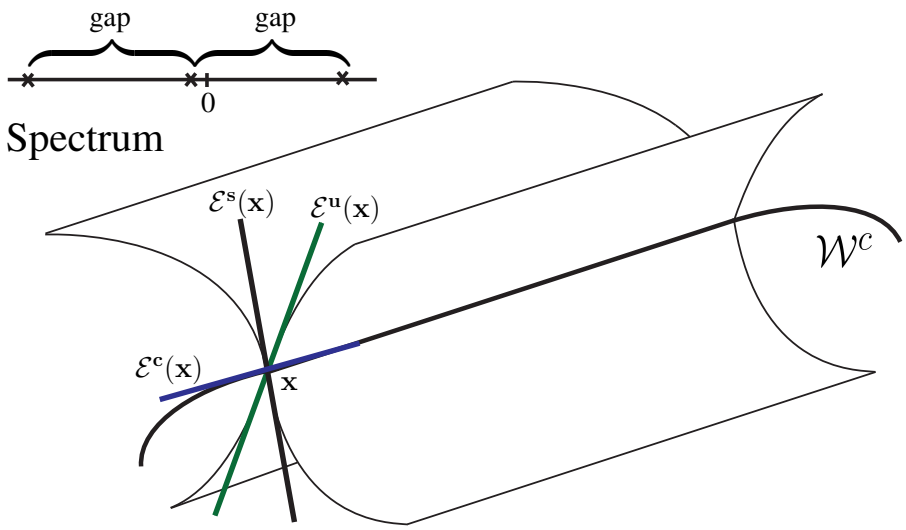

Figure 2.2: Geometry of a two-timescale 3D system with a 1D normally hyperbolic center manifold.

analysis. In the third subsection, the convergence rate of a Lyapunov subspace is characterized; and in the final subsection, the results of asymptotic and finite-time Lyapunov analysis are contrasted in preparation for the finite-time approach presented in the remaining sections.

2.3.1 Asymptotic Lyapunov Analysis and Partially Hyperbolic Set

We draw from (6; 32) to present the asymptotic theory, covering only those definitions and results that serve to motivate and support our definitions and results for the finite-time case. Asymptotic Lyapunov analysis was introduced in (47) and related to tangent space geometry in (54). The theory of partially hyperbolic sets is described in (32) where references to the original work are given. The definition of a uniform partially hyperbolic set given next requires exponential bounds uniformly, i.e., on all time intervals for a given trajectory as well as for all trajectories in the set.

Definition 2.3.1. *(32) A compact ϕ-invariant set $\mathcal{Y} \subset \mathbb{R}^n$ is a* **uniform partially hyperbolic set***, if there exists a Φ-invariant splitting*

$$T_{\mathbf{x}}\mathbb{R}^n = \mathcal{E}^s(\mathbf{x}) \oplus \mathcal{E}^c(\mathbf{x}) \oplus \mathcal{E}^u(\mathbf{x}) \tag{2.4}$$

on $\mathcal{Y}$ and numbers σ, ν, and C, with $0 < \sigma < \nu$ and $1 \leq C < \infty$, such that $\forall t > 0$

$$\begin{aligned} \mathbf{v} \in \mathcal{E}^s(\mathbf{x}) &\Rightarrow \|\Phi(t,\mathbf{x})\mathbf{v}\| \leq Ce^{-\nu t}\|\mathbf{v}\|, \\ \mathbf{v} \in \mathcal{E}^c(\mathbf{x}) &\Rightarrow C^{-1}e^{-\sigma t}\|\mathbf{v}\| \leq \|\Phi(t,\mathbf{x})\mathbf{v}\| \leq Ce^{\sigma t}\|\mathbf{v}\|, \\ \mathbf{v} \in \mathcal{E}^u(\mathbf{x}) &\Rightarrow \|\Phi(-t,\mathbf{x})\mathbf{v}\| \leq Ce^{-\nu t}\|\mathbf{v}\|. \end{aligned} \tag{2.5}$$

Consistent with the definition, consider for the moment a compact, invariant set $\mathcal{Y} \subset \mathbb{R}^n$. Assuming the system (2.1) is *forward regular* and *backward regular* at $\mathbf{x}$ (6), the forward and backward Lyapunov exponents for a vector $\mathbf{v} \in T_{\mathbf{x}}\mathbb{R}^n$ are given by

$$\mu^{\pm}(\mathbf{x},\mathbf{v}) = \lim_{T\to\infty} \frac{1}{T} \ln \|\Phi(\pm T,\mathbf{x})\mathbf{v}\|. \tag{2.6}$$

with 'ln' denoting natural log and where T is the propagation time, also referred to as the averaging time, which is always taken to be positive whether the propagation is forward or backward. Variables computed by forward and backward propagation are labeled with superscripts $^+$ and $^-$ respectively. There are at most n distinct exponents for the vectors in $T_{\mathbf{x}}\mathbb{R}^n \backslash \{0\}$. Assume that there are n distinct exponents, denoted $\mu_i^+(\mathbf{x})$, $i = 1,\ldots,n$ for forward time and $\mu_i^-(\mathbf{x})$, $i = 1,\ldots,n$ for backward time, with the forward exponents in ascending order and the backward exponents in descending order. Lyapunov subspaces are defined by $\mathcal{L}_i^+(\mathbf{x}) := \{\mathbf{v} \in T_{\mathbf{x}}\mathbb{R}^n : \mu^+(\mathbf{x},\mathbf{v}) \leq \mu_i^+(\mathbf{x})\}$ and $\mathcal{L}_i^-(\mathbf{x}) := \{\mathbf{v} \in T_{\mathbf{x}}\mathbb{R}^n : \mu^-(\mathbf{x},\mathbf{v}) \leq \mu_i^-(\mathbf{x})\}$. If a collection of $r \leq n$ linear subspaces of $T_{\mathbf{x}}\mathbb{R}^n$ can be ordered such that $\Delta_1(\mathbf{x}) \subset \Delta_2(\mathbf{x}) \subset \cdots \subset \Delta_r(\mathbf{x}) = T_{\mathbf{x}}\mathbb{R}^n$ with all inclusions strict, then this collection of nested subspaces defines a *filtration* of $T_{\mathbf{x}}\mathbb{R}^n$. The nested sequences of subspaces

$$\{\mathbf{0}\} =: \mathcal{L}_0 \subset \mathcal{L}_1^+(\mathbf{x}) \subset \mathcal{L}_2^+(\mathbf{x}) \subset \cdots \subset \mathcal{L}_n^+(\mathbf{x}) = T_{\mathbf{x}}\mathbb{R}^n, \tag{2.7}$$

$$T_{\mathbf{x}}\mathbb{R}^n = \mathcal{L}_1^-(\mathbf{x}) \supset \mathcal{L}_2^-(\mathbf{x}) \supset \cdots \supset \mathcal{L}_n^-(\mathbf{x}) \supset \mathcal{L}_{n+1}^- := \{\mathbf{0}\}, \tag{2.8}$$

are forward and backward filtrations of $T_{\mathbf{x}}\mathbb{R}^n$. The system is *Lyapunov regular* (6) at $\mathbf{x}$ if

(i) It is forward and backward regular at $\mathbf{x}$.

(ii) $\mu_i^+(\mathbf{x}) = -\mu_i^-(\mathbf{x})$, $i = 1, \ldots, n$.

(iii) The forward and backward filtrations have the same dimensions.

(iv) There exists a splitting $T_{\mathbf{x}}\mathcal{Y} = \mathcal{E}^1(\mathbf{x}) \oplus \cdots \oplus \mathcal{E}^n(\mathbf{x})$ into invariant subspaces such that $\mathcal{L}_i^+(\mathbf{x}) = \mathcal{E}^1(\mathbf{x}) \oplus \cdots \oplus \mathcal{E}^i(\mathbf{x})$ and $\mathcal{L}_i^-(\mathbf{x}) = \mathcal{E}^i(\mathbf{x}) \oplus \cdots \oplus \mathcal{E}^n(\mathbf{x})$, $i = 1, \ldots, n$.

(v) For any $\mathbf{v} \in \mathcal{E}^i(\mathbf{x}) \setminus \{0\}$, $\lim_{t \to \pm\infty} \frac{1}{|t|} \ln \|\Phi(t, \mathbf{x})\mathbf{v}\| = \mu_i^{\pm}(\mathbf{x})$.

The invariant splitting described in (iv) and (v) is referred to as Oseledec's decomposition.

Next we describe how the Lyapunov exponents and vectors can be used to diagnose and specify a uniform partially hyperbolic set. For the purpose of motivating the finite-time theory presented in the next section, assume the system (2.1) is Lyapunov regular at all the points of a compact, invariant set $\mathcal{Y}$. Suppose we find that at each $\mathbf{x} \in \mathcal{Y}$, there are, n^s large negative exponents, n^c smaller in absolute value exponents, and n^u large positive exponents, with $n^s + n^c + n^u = n$. That is, uniformly in $\mathbf{x}$, there is a splitting of the forward Lyapunov spectrum $sp^+(\mathbf{x})$ of the form $sp^+(\mathbf{x}) := sp^s(\mathbf{x}) \cup sp^c(\mathbf{x}) \cup sp^u(\mathbf{x})$ where $sp^s(\mathbf{x}) := \{\mu_1^+(\mathbf{x}), \ldots, \mu_{n^s}^+(\mathbf{x})\}$, $sp^c(\mathbf{x}) :=$

$\{\mu^+_{n^s+1}(\mathbf{x}), \ldots, \mu^+_{n^s+n^c}(\mathbf{x})\}$, and $sp^u(\mathbf{x}) := \{\mu^+_{n^s+n^c+1}(\mathbf{x}), \ldots, \mu^+_n(\mathbf{x})\}$. We can construct a Φ-invariant splitting with

$$\begin{aligned} \mathcal{E}^s(\mathbf{x}) &= \mathcal{L}^+_{n^s}(\mathbf{x}), \\ \mathcal{E}^c(\mathbf{x}) &= \mathcal{L}^+_{n^s+n^c}(\mathbf{x}) \cap \mathcal{L}^-_{n^s+1}(\mathbf{x}), \\ \mathcal{E}^u(\mathbf{x}) &= \mathcal{L}^-_{n^s+n^c+1}(\mathbf{x}). \end{aligned} \tag{2.9}$$

Although vectors are not normally used to define the subspaces in the asymptotic theory, they can be as follows. Let $\{\mathbf{l}^+_i(\mathbf{x}), i = 1, \ldots, n\}$ denote an orthonormal basis for $T_{\mathbf{x}}\mathbb{R}^n$ such that $\{\mathbf{l}^+_j(\mathbf{x}), j = 1, \ldots, i\}$ is a basis for $\mathcal{L}^+_i(\mathbf{x})$ for $i = 1, \ldots, n$. Let $\{\mathbf{l}^-_i(\mathbf{x}), i = 1, \ldots, n\}$ denote an orthonormal basis for $T_{\mathbf{x}}\mathbb{R}^n$ such that $\{\mathbf{l}^-_j(\mathbf{x}), j = i, \ldots, n\}$ is a basis for $\mathcal{L}^-_i(\mathbf{x})$ for $i = 1, \ldots, n$. When there are n distinct Lyapunov exponents as we are assuming, it follows that these bases are unique up to multiplication of individual vectors by ± 1.

The final step in specifying the uniform partially hyperbolic set is to define the constants $\sigma = \sigma_0 + \varepsilon$ and $\nu = \nu_0 - \varepsilon$ where $\varepsilon > 0$ is an arbitrarily small constant,

$$\sigma_0 := \max\{|\overline{\mu}^c|, |\underline{\mu}^c|\}, \nu_0 := \min\{-\overline{\mu}^s, \underline{\mu}^u\}, \tag{2.10}$$

and

$$\begin{aligned} \overline{\mu}^s &= \sup_{\mathbf{x}\in\mathcal{Y}} \mu^+_{n^s}(\mathbf{x}), & \overline{\mu}^c &= \sup_{\mathbf{x}\in\mathcal{Y}} \mu^+_{n^s+n^c}(\mathbf{x}), \\ \underline{\mu}^u &= \inf_{\mathbf{x}\in\mathcal{Y}} \mu^+_{n^s+n^c+1}(\mathbf{x}), & \underline{\mu}^c &= \inf_{\mathbf{x}\in\mathcal{Y}} \mu^+_{n^s+1}(\mathbf{x}). \end{aligned} \tag{2.11}$$

The bounds are specified in terms of the forward-time exponents μ^+ as defined in (2.6), but given the property (ii) of Lyapunov regularity, the backward-time exponents could have been used. For a partially hyperbolic set we must have $0 < \sigma_0 < \nu_0$. Then for sufficiently small ε, there exists a

positive, finite constant C such that the bounds (2.5) hold.

2.3.2 Finite-Time Lyapunov Exponents/Vectors and Tangent Space Structure

The forward and backward FTLEs for a nonzero vector $\mathbf{v} \in T_{\mathbf{x}}\mathbb{R}^n$ are given by

$$\mu^{\pm}(T, \mathbf{x}, \mathbf{v}) := \frac{1}{T} \ln \frac{\|\Phi(\pm T, \mathbf{x})\mathbf{v}\|}{\|\mathbf{v}\|}. \tag{2.12}$$

For $\mathbf{v} = \mathbf{0}$, define $\mu^{+}(T, \mathbf{x}, \mathbf{0}) = \mu^{-}(T, \mathbf{x}, \mathbf{0}) = -\infty$. The FTLE is the average exponential rate of growth/decay over the time interval $[0, T]$.

Discrete forward and backward Lyapunov spectra, for each $(T, \mathbf{x})$, can be defined as follows. Define $\mathbf{l}_i^{+}(T, \mathbf{x})$, $i = 1, \ldots, n$, to be an orthonormal basis of $T_{\mathbf{x}}\mathbb{R}^n$ with the minimum sum of exponents, i.e., the minimum value of $\Sigma_{i=1}^{n} \mu_i^{+}(T, \mathbf{x}, \mathbf{l}_i^{+}(T, \mathbf{x}))$ over all orthonormal bases (10). The forward Lyapunov spectrum is the set of exponents corresponding to the minimizing solution, namely, $\{\mu_i^{+}(T, \mathbf{x}), i = 1, \ldots, n\}$. The FTLEs are assumed to be in ascending order. The Lyapunov spectrum is unique, though the minimizing basis is not in general.

Geometrically, the unit n-sphere centered at the origin in $T_{\mathbf{x}}\mathbb{R}^n$ propagates under the tangent linear dynamics to an n-dimensional ellipsoid in $T_{\phi(T,\mathbf{x})}\mathbb{R}^n$; the principal semi-axes of the ellipsoid are $\exp[\mu_i^{+}(T, \mathbf{x})T]\mathbf{n}_i^{+}(T, \mathbf{x})$, $i = 1, \ldots, n$ and the unit vectors in $T_{\mathbf{x}}\mathbb{R}^n$ that evolve to these vectors are respectively $\mathbf{l}_i^{+}(T, \mathbf{x}), i = 1, \ldots, n$.

The backward Lyapunov spectrum $\{\mu_i^{-}, i = 1, \ldots, n\}$ consists of the exponents for the unit vectors $\mathbf{l}_i^{-}(T, \mathbf{x}), i = 1, \ldots, n$ in $T_{\mathbf{x}}\mathbb{R}^n$ that map to principal axes of an n-ellipsoid in $T_{\phi(-T,\mathbf{x})}\mathbb{R}^n$. Descending order is assumed for the backward FTLEs.

The $\mathbf{l}_i^+(T,\mathbf{x})$ and the $\mathbf{l}_i^-(T,\mathbf{x})$ vectors, for $i = 1,\ldots,n$, referred to as forward and backward FTLVs, respectively, will be used to define subspaces in $T_{\mathbf{x}}\mathbb{R}^n$ associated with different exponential rates.See Fig. 2.3 for the case of $n = 2$.

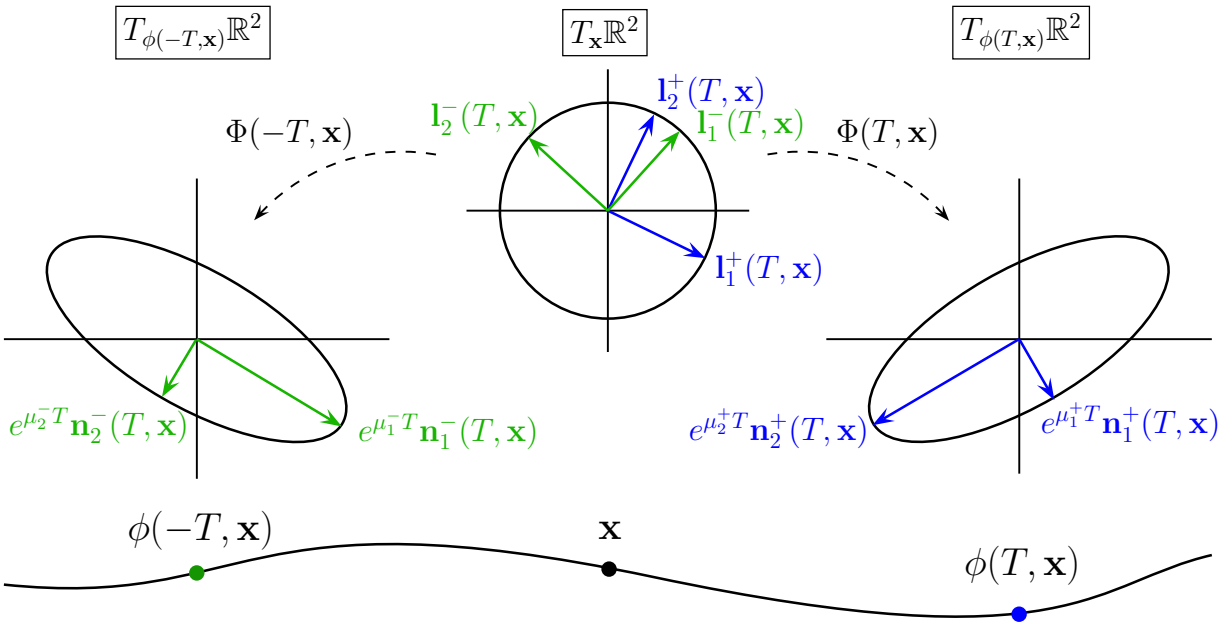

Figure 2.3: Trajectory of nonlinear system and associated tangent spaces, illustrating the role of the Lyapunov exponents and vectors in the forward and backward propagation of a sphere of tangent vectors. Blue objects correspond to forward propagation, and green objects correspond to backward propagation. The arguments $(T,\mathbf{x})$ of the FTLE/Vs have been suppressed.

We assume that the FTLEs are always distinct, i.e., non-degenerate. This assumption simplifies the presentation and is needed in slightly stronger form for the subspace convergence proof presented in Appendix A. We note that distinctness is also related to integral separation and the stability of the Lyapunov exponents with respect to perturbations in the linearized system matrix, $D\mathbf{f}(\mathbf{x})$ (10). Later we accommodate degeneracies in an initial "transient" phase that is short relative to the time interval under consideration by modifying the assumption to hold for $T \geq t_s$, for an appropriate value of the time t_s.

The following subspaces, for $i = 1, \ldots, n$, can be defined by the orthonormal FTLVs

$$\begin{aligned} \mathcal{L}_i^+(T, \mathbf{x}) &:= span\{\mathbf{l}_1^+(T, \mathbf{x}), \ldots, \mathbf{l}_i^+(T, \mathbf{x})\}, \\ \mathcal{L}_i^-(T, \mathbf{x}) &:= span\{\mathbf{l}_i^-(T, \mathbf{x}), \ldots, \mathbf{l}_n^-(T, \mathbf{x})\}, \end{aligned} \tag{2.13}$$

and will be referred to as finite-time Lyapunov subspaces. For any $i \in \{1, 2, \ldots, n\}$, $\mu^+(T, \mathbf{x}, \mathbf{v}) \leq \mu_i^+(T, \mathbf{x})$ for any $\mathbf{v} \in \mathcal{L}_i^+(T, \mathbf{x})$. However, for finite T, there also exist vectors $\mathbf{v} \in T_{\mathbf{x}}\mathbb{R}^n \backslash \mathcal{L}_i^+(T, \mathbf{x})$ for which $\mu^+(T, \mathbf{x}, \mathbf{v}) \leq \mu_i^+(T, \mathbf{x})$. Analogous properties hold for the backward-time exponents and subspaces.

Forward and backward filtrations are defined similarly to (2.7) and (2.8) using the finite-time Lyapunov subspaces. We need both forward and backward filtrations, because their intersections are of particular interest, as seen in (2.9) and motivated by the following. Consider a two-dimensional nonlinear system with an equilibrium point $\mathbf{x}_e$. Assume the linearized dynamics at $\mathbf{x}_e$ are characterized by distinct eigenvalues λ_1 and λ_2, with $\lambda_1 < \lambda_2 < 0$, and corresponding unit eigenvectors $\mathbf{e}_1$ and $\mathbf{e}_2$. As $T \to \infty$, the FTLEs at $\mathbf{x}_e$ approach the eigenvalues, i.e., $\mu_1^+(T, \mathbf{x}_e) \to \lambda_1$ and $\mu_2^+(T, \mathbf{x}_e) \to \lambda_2$, and the first Lyapunov vector approaches the corresponding eigenvector $\mathbf{l}_1^+(T, \mathbf{x}_e) \to \mathbf{e}_1$. The second Lyapunov vector $\mathbf{l}_2^+(T, \mathbf{x}_e)$ approaches $\mathbf{e}_1^\perp$, the vector perpendicular to $\mathbf{e}_1$. The subspace $\mathcal{L}_1^+(T, \mathbf{x}_e)$ thus approaches $\mathcal{E}^1(\mathbf{x}_e) = span\{\mathbf{e}_1\}$, the eigenspace for λ_1 as $T \to \infty$, whereas $\mathcal{L}_2^+(T, \mathbf{x}_e) = T_{\mathbf{x}_e}\mathbb{R}^2$ for any T. It is desired instead to obtain the invariant splitting $T_{\mathbf{x}_e}\mathbb{R}^2 = \mathcal{E}^1(\mathbf{x}_e) \oplus \mathcal{E}^2(\mathbf{x}_e)$ where $\mathcal{E}^2(\mathbf{x}_e) = span\{\mathbf{e}_2\}$. However, asymptotically all the vectors not in $\mathcal{L}_1^+$ have the Lyapunov exponent $\mu_2^+ = \lambda_2$; thus the Lyapunov exponents for forward-time propagation do not distinguish $\mathcal{E}^2$. The way to obtain $\mathcal{E}^2$ is by repeating the same analysis for backward-time propagation; in this case, the situation is reversed: asymptotically $\mathbf{l}_2^-(T, \mathbf{x}_e) \to \mathbf{e}_2$ and $\mathcal{E}^2$ can be distinguished, whereas $\mathcal{E}^1$ cannot (37; 73).

2.3.3 Exponential Lyapunov Subspace Convergence

In this subsection, we relate the finite-time tangent space structure introduced in Section 2.3.2 to the asymptotic tangent space structure described in Section 2.3.1. Basically the important subspaces converge exponentially fast to their asymptotic counterparts, and it is this property that makes FTLA viable.

We need to consider the distance between the subspaces $\mathcal{L}_j^+(T_1, \mathbf{x})$ and $\mathcal{L}_j^+(T_2, \mathbf{x})$ in $T_{\mathbf{x}}\mathbb{R}^n$. For any value of j in the index set $\{1, 2, \ldots, n\}$, let $L_j^+(T, \mathbf{x})$ denote the matrix whose columns are the Lyapunov vectors $\mathbf{l}_i^+(T, \mathbf{x})$, $i = 1, \ldots, j$, and $L_{j'}^+(T, \mathbf{x})$ denote the matrix whose columns are the Lyapunov vectors $\mathbf{l}_i^+(T, \mathbf{x})$, $i = j+1, \ldots, n$. Then the distance between the subspaces $\mathcal{L}_j^+(T_1, \mathbf{x})$ and $\mathcal{L}_j^+(T_2, \mathbf{x})$ is

$$\begin{aligned} \text{dist}(\mathcal{L}_j^+(T_1, \mathbf{x}), \mathcal{L}_j^+(T_2, \mathbf{x})) &= \|L_j^+(T_1, \mathbf{x})^T L_{j'}^+(T_2, \mathbf{x})\|_2 \\ &= \|L_j^+(T_2, \mathbf{x})^T L_{j'}^+(T_1, \mathbf{x})\|_2. \end{aligned} \tag{2.14}$$

This result is a special case of Theorem 2.6.1 in (23), page 76, and the facts that the columns of $L_j^+(T, \mathbf{x})$ provide an orthogonal basis for $\mathcal{L}_j^+(T, \mathbf{x})$ and the columns of $L_{j'}^+(T, \mathbf{x})$ are mutually orthogonal to the columns of $L_j^+(T, \mathbf{x})$.

At a forward regular point $\mathbf{x}$ for which there exists $t_s > 0$ such that for $T > t_s$ there is a nonzero lower bound $\Delta\mu_j^+(\mathbf{x})$ on the spectral gap $\mu_{j+1}^+(T, \mathbf{x}) - \mu_j^+(T, \mathbf{x})$, for a specific value of j, the subspace $\mathcal{L}_j^+(T, \mathbf{x})$ approaches the fixed subspace $\mathcal{L}_j^+(\mathbf{x})$, defined in Section 2.3.1 in terms of the asymptotic Lyapunov exponent $\mu_j^+(\mathbf{x})$. It approaches it at an exponential rate characterized, for every sufficiently small $\Delta T > 0$, by

$$\text{dist}(\mathcal{L}_j^+(T, \mathbf{x}), \mathcal{L}_j^+(T + \Delta T, \mathbf{x})) \leq K e^{-\Delta\mu_j^+(\mathbf{x}) \cdot T}, \tag{2.15}$$

for all $T > t_s$, where $K > 0$ is ΔT dependent but T independent. Similarly, as T increases, the subspace $\mathcal{L}_k^-(T, \mathbf{x})$ approaches the fixed subspace $\mathcal{L}_k^-(\mathbf{x})$ at a rate proportional to $exp(-\Delta\mu_k^-(\mathbf{x}) \cdot T)$ where $\Delta\mu_k^-(\mathbf{x})$ is the spectral gap lower bound for backward propagation and $T > t_s$. For the technical details see Appendix A.

2.3.4 Differences Between Finite-Time and Asymptotic Lyapunov Analysis

As discussed in Section 2.3.1, in the asymptotic setting either Lyapunov exponents or vectors can serve to define the Lyapunov subspaces and tangent space splitting, and the results are equivalent. In contrast, the FTLEs and FTLVs define different tangent space objects. Because the FTLV-defined Lyapunov subspace convergence is exponential in T, while the Lyapunov exponent convergence is much slower, perhaps proportional to $1/T$ (22), in the finite-time setting we define the Lyapunov subspaces in terms of the FTLVs.

The asymptotic Lyapunov exponents for Lyapunov regular points exist as limits, are metric independent, are constant on a trajectory, and include a zero exponent associated with the vector field direction. These properties are not shared in general by the FTLEs. The FTLEs depend on $\mathbf{x}$ and T; there need not be a zero exponent associated with the vector field direction. FTLEs can indicate local behavior which, if not uniformly present, would not be indicated by the asymptotic Lyapunov exponents. Another potential feature in the FTLEs is "nonmodal behavior" (62) which has required the introduction of the delayed start time $t_s \geq 0$ to avoid a brief initial transient, relative to the time interval of interest, during which the FTLEs can be quite different than they will be for even moderate finite times. FTLEs are in general metric dependent. In this work, we use the Euclidean metric exclusively, though any Riemmanian metric could be used (27; 45; 52). If finite-time two-timescale behavior is not present in the original metric under consideration, there may be another metric for which there is two-timescale behavior, as noted by Greene and Kim

(27).

2.4 Finite-Time Two-Timescale Set and Center Manifold - Theory

We identify the potential for manifold structure in a state-space region by determining if a representative set $\mathcal{X} \subset \mathbb{R}^n$ is a uniform finite-time two-timescale set. A two-timescale set has a special tangent space structure and allows us to formulate invariance-based orthogonality conditions that would be satisfied at points of center $\mathcal{W}^c$, center-stable $\mathcal{W}^{cs}$, and center-unstable $\mathcal{W}^{cu}$ manifolds, if such manifolds are present. For the purpose of defining and diagnosing two-timescale behavior, and determining tangent space structure, $\mathcal{X}$ could be a point or a segment of a trajectory, as examples, but in the search for manifold structure, $\mathcal{X}$ is typically a domain of the state space. The domain is typically not ϕ-invariant, so it is crucial to clarify what information is required and how much time it takes to resolve it. And because only limited integration time is available, the definition of a finite-time two-timescale set must account for finite-time features that are of no consequence in asymptotic Lyapunov theory.

2.4.1 Finite-Time Two-Timescale Set

Definition 2.4.1 of a uniform finite-time two-timescale set is modeled after Def. 2.3.1 of a uniform partially hyperbolic set with modifications for the finite-time setting. Several time constants[2] play key roles. The convergence time constant $\Delta\mu^{-1}$, where $\Delta\mu$ is the spectral gap, along with the common available maximum averaging time $\overline{T}$, determines the accuracy with which the tangent

[2]For an exponential function of time, $e^{\kappa t}$, the time constant $|\kappa|^{-1}$ is the time t at which the function equals e^{+1} or e^{-1} as appropriate for the sign of κ.

space splitting can be resolved. The fast and slow time constants (i.e., timescales), ν^{-1} and σ^{-1}, appear in the bounds that characterize the disparate exponential rates in the tangent linear dynamics, as further interpreted in Section 2.4.3. The basic ingredients of this definition are the same as those in the definition of a uniform finite-time hyperbolic solution given in (30), but the details are different.

Definition 2.4.1. *A set $\mathcal{X} \subset \mathbb{R}^n$, $n \geq 2$, is a **uniform finite-time two-timescale set** for* (2.1) *with respect to the Euclidean metric, characterized by fast time constant ν^{-1}, slow time constant σ^{-1}, and convergence time constant $\Delta\mu^{-1}$, and resolvable over $\Delta\mu(\overline{T} - t_s)$ convergence time constants, if there exist non-negative integers n^s, n^c and n^u, with $n^s + n^c + n^u = n$, $n^c \geq 1$, and $n^s + n^u \geq 1$, a delayed start time t_s, a cut-off time t_c, and an available averaging time $\overline{T}$ with $0 \leq t_s < t_c \leq \overline{T}$ such that the following three properties are satisfied. We use the notation $\mathcal{T} = (t_s, \overline{T}]$ and $\mathcal{T}_c = (t_s, t_c]$.*

1. *Uniform Spectral Gaps – There exist positive constants α and β with $\beta - \alpha > 0$ such that, uniformly on $\mathcal{T} \times \mathcal{X}$, the forward and backward Lyapunov spectra are separated by gaps of size $\Delta\mu = \beta - \alpha$ into n^s, n^c and n^u dimensional subsets as illustrated in Fig. 2.4 and specified by*

$$\begin{aligned} \mu^+_{n^s} \leq -\beta \leq -\alpha \leq \mu^+_{n^s+1}, \qquad \mu^+_{n^s+n^c} \leq \alpha \leq \beta \leq \mu^+_{n^s+n^c+1}, \\ -\mu^-_{n^s} \leq -\beta \leq -\alpha \leq -\mu^-_{n^s+1}, \quad -\mu^-_{n^s+n^c} \leq \alpha \leq \beta \leq -\mu^-_{n^s+n^c+1}. \end{aligned} \tag{2.16}$$

2. *Tangent Bundle Splitting – On $\mathcal{X}$, there is a continuous splitting*

$$T_{\mathbf{x}}\mathbb{R}^n = \mathcal{E}^s(\overline{T}, \mathbf{x}) \oplus \mathcal{E}^c(\overline{T}, \mathbf{x}) \oplus \mathcal{E}^u(\overline{T}, \mathbf{x}), \tag{2.17}$$

where

$$\begin{aligned}\mathcal{E}^s(\overline{T},\mathbf{x}) &= \mathcal{L}^+_{n^s}(\overline{T},\mathbf{x}),\\ \mathcal{E}^c(\overline{T},\mathbf{x}) &= \mathcal{L}^+_{n^s+n^c}(\overline{T},\mathbf{x})\cap\mathcal{L}^-_{n^s+1}(\overline{T},\mathbf{x}),\\ \mathcal{E}^u(\overline{T},\mathbf{x}) &= \mathcal{L}^-_{n^s+n^c+1}(\overline{T},\mathbf{x}).\end{aligned} \tag{2.18}$$

3. *Two Timescales – There exist positive numbers ν and σ with $\nu > \sigma$ such that at each $\mathbf{x}\in\mathcal{X}$ for all $t\in\mathcal{T}_c$*

$$\begin{aligned}\mathbf{v}\in\mathcal{E}^s(\overline{T},\mathbf{x}) &\Rightarrow \begin{cases}\|\Phi(-t,\mathbf{x})\mathbf{v}\|\geq e^{\nu t}\|\mathbf{v}\|\\ \|\Phi(t,\mathbf{x})\mathbf{v}\|\leq e^{-\nu t}\|\mathbf{v}\|\end{cases},\\ \mathbf{v}\in\mathcal{E}^c(\overline{T},\mathbf{x}) &\Rightarrow \begin{cases}e^{-\sigma t}\|\mathbf{v}\|\leq\|\Phi(t,\mathbf{x})\mathbf{v}\|\leq e^{\sigma t}\|\mathbf{v}\|\\ e^{-\sigma t}\|\mathbf{v}\|\leq\|\Phi(-t,\mathbf{x})\mathbf{v}\|\leq e^{\sigma t}\|\mathbf{v}\|\end{cases},\\ \mathbf{v}\in\mathcal{E}^u(\overline{T},\mathbf{x}) &\Rightarrow \begin{cases}\|\Phi(-t,\mathbf{x})\mathbf{v}\|\leq e^{-\nu t}\|\mathbf{v}\|\\ \|\Phi(t,\mathbf{x})\mathbf{v}\|\geq e^{\nu t}\|\mathbf{v}\|\end{cases}.\end{aligned} \tag{2.19}$$

The properties are stated for the general case where n^s and n^u are both nonzero. Either n^s or n^u can be zero, but not both. For $n^s = 0$, $\mathcal{E}^s$ is not relevant; similarly, for $n^u = 0$, $\mathcal{E}^u$ is not relevant.

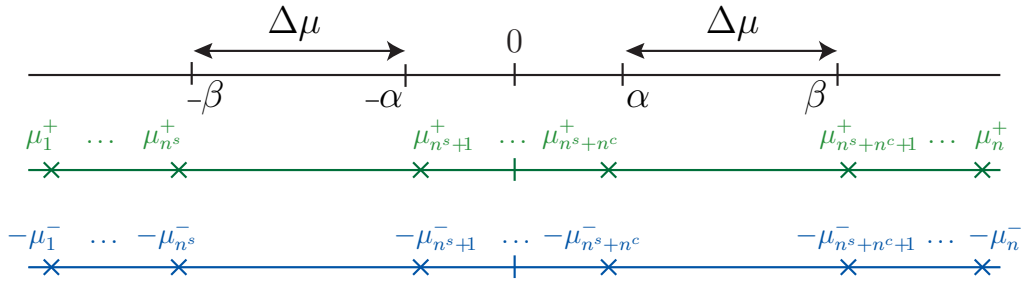

Figure 2.4: Spectra of forward and backward FTLEs illustrating the gaps.

In Def. 2.4.1, Property 1 ensures that common gaps in the forward and backward Lyapunov spectra

not only exist, but also separate the spectra in a dimensionally consistent manner, a relaxed version of Lyapunov regularity (6). The consistency between the forward and backward spectra is illustrated in Fig. 2.4 where the bounds and forward and backward exponents are plotted on aligned different copies of the real line for clarity. The exponents for particular values of T and $\mathbf{x}$ are pictured, but note that Property 1 requires this structure for all $(T, \mathbf{x}) \in \mathcal{T} \times \mathcal{X}$. The symmetry of the gaps with respect to zero is not necessary but is assumed here to simplify the presentation. The use of times up to $\overline{T}$ means that the computation of the Lyapunov exponents and vectors involves trajectories which, though they begin in $\mathcal{X}$, extend (unless $\mathcal{X}$ is $\phi-$invariant) into the larger set

$$\begin{aligned} \mathcal{X}_{ext} := \{\mathbf{y} \in \mathbb{R}^n : &\mathbf{y} = \phi(t, \mathbf{x}) \quad \text{or} \quad \mathbf{y} = \phi(-t, \mathbf{x}) \\ &\text{for some} \quad (t, \mathbf{x}) \in \mathcal{T} \times \mathcal{X}\}. \end{aligned} \tag{2.20}$$

The delayed start time t_s provides a grace period over which the FTLE bounds do not have to be satisfied, in order to accommodate "non-modal" behavior (62); see Section 7.1 for a clarifying example. $\overline{T}$ is the largest common time over which the uniformity in the exponents holds. We note that because $\overline{T}$ must apply at each $\mathbf{x}$, for a particular $\mathbf{x}$ larger forward and backward averaging times may be possible; this property is exploited for the example in Section 2.6.2. Given viable $\Delta\mu$, t_s, and $\overline{T}$, it can be stated that the Lyapunov subspaces are resolvable over at least $\Delta\mu(\overline{T} - t_s)$ convergence time constants.

In Property 2, the subspaces $\mathcal{E}^s(\overline{T}, \mathbf{x})$, $\mathcal{E}^c(\overline{T}, \mathbf{x})$ and $\mathcal{E}^u(\overline{T}, \mathbf{x})$ must uniformly define a splitting of the tangent space – a finite-time version of Oseledec's decomposition (6; 54). This condition is a transversality requirement. The continuity of the splitting follows from the continuous dependence of $\Phi(\overline{T}, \mathbf{x})$ on $\mathbf{x}$. We focus on the subspaces for $\overline{T}$ for the following reason. If the $T \to \infty$ limits could be computed, then we could compute the forward and backward Lyapunov subspaces at each point of $\mathcal{X}$ for arbitrarily large averaging times T and these subspaces would converge to form Φ-invariant subbundles (6). Limited to $T \leq \overline{T}$ we should use $T = \overline{T}$ to obtain subspaces that ap-

proximate the *ideal* invariant subspaces as closely as possible within the available averaging times. An argument similar to that in the proof of Proposition A.0.3 can be used to show that $\mathcal{L}^+_{n^s}(T,\mathbf{x})$, $\mathcal{L}^-_{n^s+1}(T,\mathbf{x})$, $\mathcal{L}^+_{n^s+n^c}(T,\mathbf{x})$, and $\mathcal{L}^-_{n^s+n^c+1}(T,\mathbf{x})$ approach, with increasing T, fixed subspaces at least at a rate proportional to $e^{-\Delta\mu T}$, and consequently so do the subspaces $\mathcal{E}^s(T,\mathbf{x})$, $\mathcal{E}^c(T,\mathbf{x})$ and $\mathcal{E}^u(T,\mathbf{x})$, where these latter subspaces are defined in terms of the Lyapunov subspaces as in (3.10) except for averaging time T.

Although the bounds α and β give some indication of the timescales, in Property 3 the action of the transition matrix on vectors in the particular subspaces of the splitting in Property 2 is characterized by exponential bounds. A procedure for determining ν and σ is given in Section 2.5.1. The time interval $\mathcal{T}_c$ over which the bounds apply is truncated at both ends. The delayed start time avoids the non-modal behavior and the cut-off time t_c avoids a potential final transient from t_c to $\overline{T}$ where a subspace rotates away from the ideal asymptotic subspace it is intended to approximate. For a two-timescale set, $\nu - \sigma$ is only required to be positive, but see the interpretation in Subsection 2.4.3.

Definition 2.4.1 identifies a uniform two-timescale set of points, where the uniform behavior is sought both spatially (i.e., on $\mathcal{X}$) and temporally (i.e., on $\mathcal{T}$). In many applications, however, it is sufficient to apply the definition point-wise only. In other words, when we apply the definition to single points $\mathbf{x} \in \mathbb{R}^n$, $\mathcal{X}$ is not properly defined and the uniformity is required on $\mathcal{T}$ only. Thus, the only properties that need to be checked are Property 1 and 2, while Property 3 and the cut-off time t_c become irrelevant. In particular, for Property 1 we have that $\Delta\mu = \Delta\mu(\mathbf{x})$ and the splitting in Property 2 has to hold at $\mathbf{x}$ only. For other applications, the definition can be loosened further by requiring a uniform spectral gap in one direction only. If we consider for instance the forward integration, we have $\Delta\mu = \Delta\mu(\mathbf{x})^+$ and the tangent space splitting can be written as $T_{\mathbf{x}}\mathbb{R}^n = \mathcal{E}^{cs}(\overline{T},\mathbf{x}) \oplus [\mathcal{E}^{cs}(\overline{T},\mathbf{x})]^\perp$ with $\mathcal{E}^{cs}(\overline{T},\mathbf{x}) = \mathcal{E}^s(\overline{T},\mathbf{x}) \oplus \mathcal{E}^c(\overline{T},\mathbf{x})$ and '$\mathcal{E}^\perp$' indicating the orthogonal complement to $\mathcal{E}$. For more details on the matter see the applications in chapter 2 and

3.

2.4.2 Invariant Manifold Approximation

If $\mathcal{X}$, now assumed to be a domain of $\mathbb{R}^n$, is a uniform finite-time two-timescale set, we postulate a corresponding manifold structure for the flow of the nonlinear system (2.1). The characteristics of the two-timescale set provide the dimensions and orientations of the manifolds. In particular, in the general case where neither n^s nor n^u is zero, center $\mathcal{W}^c$, center-stable $\mathcal{W}^{cs}$, and center-unstable $\mathcal{W}^{cu}$ invariant manifolds can be postulated along with a corresponding invariant splitting $T_x\mathcal{X} = \mathcal{E}^s(\mathbf{x}) \oplus \mathcal{E}^c(\mathbf{x}) \oplus \mathcal{E}^u(\mathbf{x})$. Points on the postulated invariant manifolds satisfy the tangency conditions

$$\begin{aligned} \mathbf{x} \in \mathcal{W}^c &\Rightarrow \mathbf{f}(\mathbf{x}) \in \mathcal{E}^c(\mathbf{x}) \\ \mathbf{x} \in \mathcal{W}^{cs} &\Rightarrow \mathbf{f}(\mathbf{x}) \in \mathcal{E}^s(\mathbf{x}) \oplus \mathcal{E}^c(\mathbf{x}) \\ \mathbf{x} \in \mathcal{W}^{cu} &\Rightarrow \mathbf{f}(\mathbf{x}) \in \mathcal{E}^c(\mathbf{x}) \oplus \mathcal{E}^u(\mathbf{x}) \end{aligned} \tag{2.21}$$

Approximating the postulated invariant splitting with our finite-time non-invariant splitting, we can search for points that satisfy the tangency conditions (which will be posed as orthogonality conditions in the next section). This leads to the definition of a finite-time center manifold.

Definition 2.4.2. *Given a uniform finite-time two-timescale set $\mathcal{X}$, a finite-time center manifold is an n^c-dimensional submanifold of $\mathcal{X}$ denoted $\mathcal{W}^c(\overline{T})$ such that $\mathbf{f}(\mathbf{x}) \in \mathcal{E}^c(\overline{T}, \mathbf{x})$ for all $\mathbf{x} \in \mathcal{W}^c(\overline{T})$.*

Analogous definitions can be given for the finite-time manifolds $\mathcal{W}^{cs}(\overline{T})$ and $\mathcal{W}^{cu}(\overline{T})$.

2.4.3 Interpretation and Significance

Consider the scenario in which the behavior of a system $\dot{\mathbf{x}} = \mathbf{f}(\mathbf{x})$ over the time interval $[0, t_f]$ is of interest. Assume the set $\mathcal{X}$ covers the region of state space in which this behavior takes place and has been diagnosed a uniform finite-time two-timescale set with time constants ν^{-1} and σ^{-1} and assume that t_s is a small fraction of $\overline{T}$ and t_f. If t_f is much larger than ν^{-1} and smaller than or similar to σ^{-1}, then there is slow-fast behavior in the tangent linear dynamics relative to the time interval of interest. If there is more than one way to separate the FTLE spectra to satisfy Def. 2.4.1, then the value of t_f of interest can suggest which way to consider.

For the general normally hyperbolic case, in order to compute points on finite-time center manifolds, it is required to obtain $\mathcal{E}^c$ by intersecting the tangent subspaces obtained from forward and backward integration of the tangent linear dynamics. As mentioned, center manifolds need not be slow manifolds. At a point $\mathbf{x} \in \mathcal{W}^c(\overline{T})$, the exponential bounds for $\mathcal{E}^c(\overline{T}, \mathbf{x})$ constrain the rate of change in the length of $\mathbf{f}(\mathbf{x})$ but the FTLA characterization does not constrain the length of $\mathbf{f}(\mathbf{x})$ and leaves rotational freedom, even fast rotation. Points on $\mathcal{W}^{cu}$ and $\mathcal{W}^{cs}$ can also be determined using tangency conditions and can benefit the solution of certain boundary-value problems (3; 29; 57; 58; 67).

2.5 Finite-Time Two-Timescale Set and Center Manifold - Procedure

If the goal is only to diagnose two-timescale behavior and determine the tangent space structure, then $\mathcal{X}$ can be any subset of $\mathbb{R}^n$. If one also wants to search for a center manifold, then $\mathcal{X}$ is typically a domain, or a set of grid points on a domain, because it will be necessary to iteratively

search for points that satisfy center manifold conditions in a state space region of full dimension. As mentioned, simulation experience with a set of boundary conditions of interest could suggest the domain $\mathcal{X}$ to explore. Establishing *a priori* that the domain $\mathcal{X}$ is a two-timescale set ensures that a uniform splitting exists and indicates the degree to which it can be resolved; however it is also possible to proceed directly to the search and assess the uniformity of the timescales and splitting in the process.

2.5.1 Diagnosing a Finite-Time Two-Timescale Set

The three properties in Def. 2.4.1 are checked on $\mathcal{X}$. To check Property 1, FTLEs are computed to determine if there exist a t_s and $\overline{T}$ for which there is a pattern as illustrated in Fig. 2.4 uniformly in $\mathbf{x}$ and for all $T \in \mathcal{T}$. Regarding uniformity, the individual exponents can vary with T and $\mathbf{x}$ as long as there is a sufficiently large uniform gap. However, unless $\mathcal{X}$ is $\phi-$invariant, the set $\mathcal{X}_{ext}$ (see (2.20)) grows with T; an upper limit on T may be required to avoid non-uniform behavior. If a uniform spectral gap is present, then the appropriate values of the constants n^s, n^c, n^u, t_s, t_c, $\overline{T}$ and $\Delta\mu$ are determined. Based on the initial survey, $\mathcal{X}$ could be adjusted.

If the tangent space structure is resolvable over a sufficient number[3] of convergence time constants for the required accuracy, then the subspaces $\mathcal{E}^s(\overline{T}, \mathbf{x})$, $\mathcal{E}^c(\overline{T}, \mathbf{x})$ and $\mathcal{E}^u(\overline{T}, \mathbf{x})$ are constructed and Property 2 is checked. The dimensions of these subspaces sum to n, but each pair of subspaces must intersect transversely to provide the splitting. We note that the convergence of the subspaces can be checked directly by monitoring the distance between the subspaces with increasing averaging time (illustrated in Section 2.6).

For each $\mathbf{x} \in \mathcal{X}$, the subspaces (2.18) that define the splitting of the tangent space $T_{\mathbf{x}}\mathbb{R}^n$ at $\overline{T}$ can

[3] A specific number is not specified because the required accuracy is application dependent. The examples in Section 2.6 provide some insight.

be expressed as the column spans (i.e., range spaces) of the following matrices

$$\begin{aligned} E^s(\overline{T},\mathbf{x}) &= [l_1^+(\overline{T},\mathbf{x}),...,l_{n^s}^+(\overline{T},\mathbf{x})], \\ E^c(\overline{T},\mathbf{x}) &= null\left[([E^c(\overline{T},\mathbf{x})]^\perp)^T\right], \\ E^u(\overline{T},\mathbf{x}) &= [l_{n^s+n^c+1}^-(\overline{T},\mathbf{x}),...,l_n^-(\overline{T},\mathbf{x})], \end{aligned} \tag{2.22}$$

$[E^c(\overline{T},\mathbf{x})]^\perp$ is given in terms of the FTLVs in the next subsection. We have used '$null(M)$' to denote the mapping from matrix M to an orthonormal matrix whose column span is the null space of the matrix M.

To check Property 3, we check if $\nu > \sigma$ after computing the constants ν and σ as

$$\nu = \min\{-\overline{\mu}^s, \underline{\mu}^u, \underline{\mu}^s, -\overline{\mu}^u\}, \quad \sigma = \max\{|\underline{\mu}^{c+}|, |\overline{\mu}^{c+}|, |\overline{\mu}^{c-}|, |\underline{\mu}^{c-}|\}$$

where

$$\begin{aligned} \overline{\mu}^s &= \sup_{(T,\mathbf{x})\in\mathcal{T}_c\times\mathcal{X}} \mu_{n^s}^{s+}(T,\mathbf{x}), \quad \underline{\mu}^{c+} = \inf_{(T,\mathbf{x})\in\mathcal{T}_c\times\mathcal{X}} \mu_1^{c+}(T,\mathbf{x}), \\ \underline{\mu}^u &= \inf_{(T,\mathbf{x})\in\mathcal{T}_c\times\mathcal{X}} \mu_1^{u+}(T,\mathbf{x}), \quad \overline{\mu}^{c+} = \sup_{(T,\mathbf{x})\in\mathcal{T}_c\times\mathcal{X}} \mu_{n^c}^{c+}(T,\mathbf{x}), \\ \underline{\mu}^s &= \inf_{(T,\mathbf{x})\in\mathcal{T}_c\times\mathcal{X}} \mu_{n^s}^{s-}(T,\mathbf{x}), \quad \overline{\mu}^{c-} = \sup_{(T,\mathbf{x})\in\mathcal{T}_c\times\mathcal{X}} \mu_1^{c-}(T,\mathbf{x}), \\ \overline{\mu}^u &= \sup_{(T,\mathbf{x})\in\mathcal{T}_c\times\mathcal{X}} \mu_1^{u-}(T,\mathbf{x}), \quad \underline{\mu}^{c-} = \inf_{(T,\mathbf{x})\in\mathcal{T}_c\times\mathcal{X}} \mu_{n^c}^{c-}(T,\mathbf{x}). \end{aligned} \tag{2.23}$$

The FTLEs for each subspace as needed in (2.23) are computed as

$$\mu_i^{j\pm}(T) = \frac{1}{T}\ln\left(\Sigma_{ii}^{j\pm}\right) \quad i = 1,...,n^j, j = s,c,u,$$

where the diagonal matrices $\Sigma^{j\pm}$ are obtained from the singular value decompositions

$$N^{j\pm}(\pm T, \phi(\pm T, \mathbf{x})) \cdot \Sigma^{j\pm}(\pm T, \mathbf{x}) \cdot L^{j\pm}(\pm T, \mathbf{x}) = \Phi(\pm T, \mathbf{x}) E^{j}(\overline{T}, \mathbf{x}) \tag{2.24}$$

and the subscript 'ii' on Σ denotes the i^{th} diagonal element of that matrix.

2.5.2 Computing Points on a Finite-Time Center Manifold

Provided that $\mathcal{X}$ satisfies Def. 2.4.1, where $\mathcal{X}$ is now assumed to be a domain of $\mathbb{R}^n$, we can look for a normally hyperbolic center manifold in $\mathcal{X}$. Within $\mathcal{X}$, the points in the set

$$\{\mathbf{x} \in \mathcal{X} : \langle \mathbf{f}(\mathbf{x}), \mathbf{w} \rangle = 0, \forall \mathbf{w} \in [\mathcal{E}^c(\overline{T}, \mathbf{x})]^{\perp}\} \tag{2.25}$$

satisfy a necessary condition for being on a finite-time center manifold. Whether or not this set, or a subset of it, is a submanifold of $\mathcal{X}$ has to be determined to the extent it can from numerical results, which is also the case with the ILDM method (48). We proceed under the assumption that the set is a manifold that can locally be parametrized by n^c of the n system coordinates and represented as a graph.

Rather than use eigenvectors of $D\mathbf{f}(\mathbf{x})$ to form an approximate basis for the orthogonal complement to $\mathcal{E}^c$ as in the ILDM method (48), we use the appropriate Lyapunov vectors to form the approximate basis as prescribed in the following proposition.

Proposition 2.5.1. *On a uniform finite-time two-timescale set $\mathcal{X}$, at each $\mathbf{x}$, the vectors*

$$\mathbf{l}_1^-(\overline{T}, \mathbf{x}), \ldots, \mathbf{l}_{n^s}^-(\overline{T}, \mathbf{x}), \mathbf{l}_{n^s+n^c+1}^+(\overline{T}, \mathbf{x}), \ldots, \mathbf{l}_n^+(\overline{T}, \mathbf{x}) \tag{2.26}$$

form a basis for $[\mathcal{E}^c(\overline{T}, \mathbf{x})]^{\perp}$.

Proof: In Def. 2.4.1, Property 2, the n^c-dimensional center subspace is given by $\mathcal{E}^c(\overline{T},\mathbf{x}) = \mathcal{L}^+_{n^s+n^c}(\overline{T},\mathbf{x}) \cap \mathcal{L}^-_{n^s+1}(\overline{T},\mathbf{x})$. Using an identity from (34), we have $[\mathcal{E}^c(\overline{T},\mathbf{x})]^\perp = [\mathcal{L}^-_{n^s+1}(\overline{T},\mathbf{x})]^\perp \oplus [\mathcal{L}^+_{n^s+n^c}(\overline{T},\mathbf{x})]^\perp$. The proposition then follows from the facts

$$\begin{aligned} \left[\mathcal{L}^-_{n^s+1}(\overline{T},\mathbf{x})\right]^\perp &= span\{\mathbf{l}^-_1(\overline{T},\mathbf{x}),\ldots,\mathbf{l}^-_{n^s}(\overline{T},\mathbf{x})\}, \\ \left[\mathcal{L}^+_{n^s+n^c}(\overline{T},\mathbf{x})\right]^\perp &= span\{\mathbf{l}^+_{n^s+n^c+1}(\overline{T},\mathbf{x}),\ldots,\mathbf{l}^+_{n}(\overline{T},\mathbf{x})\}. \end{aligned} \tag{2.27}$$

■

The set (2.25) is thus the solution set for the system of orthogonality conditions

$$\begin{aligned} \langle \mathbf{f}(\mathbf{x}), \mathbf{l}^-_i(\overline{T},\mathbf{x})\rangle &= 0, i = 1,\ldots,n^s \\ \langle \mathbf{f}(\mathbf{x}), \mathbf{l}^+_j(\overline{T},\mathbf{x})\rangle &= 0, j = n^s+n^c+1,\ldots,n \end{aligned} \tag{2.28}$$

In order to obtain the solution set, we designate n^c components of $\mathbf{x}$ as independent variables to parameterize the manifold and determine the values of the remaining $n-n^c$ components, the dependent variables, that satisfy the orthogonality conditions in (2.25). The directions of the Lyapunov vectors indicate how to separate the coordinates of $\mathbf{x}$ into independent and dependent variables, i.e., how to locally parametrize the postulated $\mathcal{W}^c(\overline{T})$. The independent variables must be chosen such that their coordinate axes are not parallel to any directions in $[\mathcal{E}^c]^\perp$. Different independent variables might be required for different sections of the center manifold. Because the FTLVs are in numerical form, we use a successive approximation approach described in Section 2.6.2. This is repeated for a grid on the space of independent variables. Additional numerical algorithms are provided in 3.2.2 and 4.3.4.

2.5.3 Numerical Methods for FTLA

Numerical methods for FTLA are addressed in (1; 2; 10; 21; 71) and the references therein. For completeness, the methods used for the computations presented in the rest of this work are described in this subsection. All the computations are done in the Matlab® environment. The numerical integration of the nonlinear state equations and the corresponding linear variational equations is performed with the 'ode45' integrator.

The FTLEs and FTLVs associated with an initial state $\mathbf{x}$ are computed for an averaging time T by SVD factorization. Only the computation of the forward-time FTLE/Vs is described, since the computation of the backward-time FTLE/Vs is analogous. The first step of both methods is to integrate the nonlinear state equations from $t = 0$ to $t = T$ and save the values of $\phi(t, \mathbf{x})$ at the N equally spaced times $\Delta t, 2\Delta t, \ldots, N\Delta t$, where $N\Delta t = T$.

In the SVD method, the transition matrix is computed and then the SVD is applied. The transition matrix is computed by integrating, simultaneously, the nonlinear equations and the associated linear variational equations over each segment of the base space trajectory, with the state initialized with the saved value at the beginning of the segment and the transition matrix initialized with the identity matrix. Using the notation $\Phi_k^{\Delta t} = \Phi(\Delta t, \phi[(k-1)\cdot\Delta t, \mathbf{x}])$ for $k = 1, 2, ..., N$, the transition matrix is constructed from the transition matrices for the segments as $\Phi(T, x) = \Phi_N^{\Delta t} \cdots \Phi_2^{\Delta t}\Phi_1^{\Delta t}$. The resulting transition matrix is then factored as $\Phi(T, \mathbf{x}) = N^+\Sigma^+(L^+)^T$ using the 'svd' command in Matlab®. Each FTLE is obtained by $\mu_i^+(T, \mathbf{x}) = \frac{1}{T}\ln\sigma_i^+$, where σ_i is the i^{th} singular value of Φ, the i^{th} diagonal element of Σ^+. If this procedure does not produce FTLEs in the ascending order we have assumed in our notation, the FTLEs and associated FTLVs are rearranged to conform. The FTLVs $\mathbf{l}_i^+(T, \mathbf{x}), i = 1, \ldots, n$ are the column vectors of L^+. Further details can be found in (51).

2.6 Application Examples

Two application examples are presented to demonstrate and further clarify the use of the FTLA methodology. The first example provides insight into the start and cut-off times used in Definition 2.4.1. The angles between the relevant vectors and subspaces are intentionally small to illustrate how the FTLA method handles the consequences. The other example illustrates the FTLA methodology for a 4D system involving a normally hyperbolic center manifold which happens to be a slow manifold. Given that our initial motivation for developing the FTLA method for determining a slow manifold was to improve the accuracy of the ILDM method in situations where the ILDM method is known to be inaccurate (36), the FTLA method results are compared to the results obtained with the ILDM method.

2.6.1 Example for Understanding Start and Cut-Off Times

Properties 1 and 3 in Def. 2.4.1 involve truncating the time interval at the beginning and end, using the start time t_s and the cut-off time t_c. The initial transient behavior that is excluded is associated with coordinate-dependent angles between certain vectors within the ideal asymptotic stable, center and unstable subspaces toward which the finite-time subspaces are converging. The final transient behavior that is excluded is produced by the lack of Φ-invariance of the finite-time subbundles $\mathcal{E}^s$, $\mathcal{E}^c$ and $\mathcal{E}^u$. To illustrate the behaviors and the roles of the constants t_s and t_c, we

consider a hypothetical 7D system, $\dot{\mathbf{x}} = \mathbf{f}(\mathbf{x})$, at an equilibrium point $\mathbf{x}_e$, i.e., for $\mathcal{X} = \{\mathbf{x}_e\}$, with

$$D\mathbf{f}(\mathbf{x}_e) = \begin{bmatrix} -5.4 & 1 & 0 & 0 & 0 & 0 & 0 \\ 0 & -5.2 & 0 & 0 & 30 & 0 & 0 \\ 0 & 0 & -0.3 & 0 & 0 & 0 & 10 \\ 0 & 0 & 0 & -0.1 & 0 & 0 & 0 \\ 0 & 0 & 0 & 0 & 0.2 & 0 & 0 \\ 0 & 0 & 0 & 0 & 0 & 4.0 & 8 \\ 0 & 0 & 0 & 0 & 0 & 0 & 4.6 \end{bmatrix}. \tag{2.29}$$

The triangular form of $D\mathbf{f}(\mathbf{x}_e)$ allows simple control of the timescales, the important angles, and the degree of dynamic coupling via specification of the diagonal and off-diagonal elements.

Barring numerical errors, in the limit $\overline{T} \to \infty$, the FTLEs will converge to the eigenvalues of $D\mathbf{f}(\mathbf{x}_e)$, i.e., the diagonal elements, and the subspaces $\mathcal{E}^s$, $\mathcal{E}^c$ and $\mathcal{E}^u$ will converge to the stable, center and unstable eigenspaces, i.e., the subspaces spanned by the appropriate subset of the eigenvectors of $D\mathbf{f}(\mathbf{x}_e)$ – the stable eigenspace spanned by the eigenvectors for the eigenvalues $\lambda_1 = -5.4$ and $\lambda_2 = -5.2$, the center eigenspace spanned by the eigenvectors for $\lambda_3 = -0.3$, $\lambda_4 = -0.1$ and $\lambda_5 = 0.2$ and the unstable eigenspace spanned by the eigenvectors for $\lambda_6 = 4.0$ and $\lambda_7 = 4.6$.

In order to determine the cut-off time t_c, the FTLEs for the subspaces $\mathcal{E}^s$, $\mathcal{E}^c$ and $\mathcal{E}^u$ are computed for a finite $\overline{T}$ ($\mu_i^{j\pm}, i = 1, ..., n^j, j = s, c, u$) to determine the exponential bounds as described in Section 2.5.1. For sufficiently large finite $\overline{T}$, the subspaces $\mathcal{E}^s$, $\mathcal{E}^c$ and $\mathcal{E}^u$ will closely approximate the corresponding eigenspaces, but when propagated to $\overline{T}$, there will be a final boundary-layer in which the subspaces rotate away from the eigenspaces, and this will affect the behavior of the FTLEs. For example, the stable eigenspace is asymptotically stable in backward time and unstable in forward time with respect to neighboring equi-dimensional subspaces. Thus, when propagated

forward in time, the finite-time approximation $\mathcal{E}^s$ will rotate away from the stable eigenspace. This is a non-uniform rotation taking place primarily near the time $\overline{T}$ for which $\mathcal{E}^s$ was computed. In general $\mathcal{E}^s$ and $\mathcal{E}^c$ will rotate toward $\mathcal{E}^u$ in forward time, and $\mathcal{E}^c$ and $\mathcal{E}^u$ will rotate toward $\mathcal{E}^s$ in backward time. The FTLEs for $\mathcal{E}^s$, $\mathcal{E}^c$ and $\mathcal{E}^u$ will be similar to those for their eigenspace counterparts except in cases involving propagation in the unstable direction when the averaging time is near $\overline{T}$. Thus we exclude a final period long enough to avoid the transient deviations in the FTLEs. Figure 2.5 shows the backward and forward FTLEs for each of the three subspaces for $\overline{T} = 6.0$. The final transients are short and the deviations are not large; the final transients that dictate $t_c = 5.5$ are the ones for the forward and backward propagations of the center subspace.

The start time t_s is dictated by the requirement of satisfying properties 1 and 3 of Definition 2.4.1. Therefore, we consider both the FTLEs that define the exponential bounds (2.18) and the FTLEs that define the spectral gap $\Delta\mu$. For convenience, we will refer to these two sets of FTLEs as $\mu^{\pm}_{EB}$ and $\mu^{\pm}$ respectively. The $\mu^{\pm}_{EB}$'s associated with a particular subspace, as functions of T, will have an initial transient period, if the subspace has dimension greater than one and there is one or more pair of eigenvectors within the eigenspace being approximated that are separated by an angle less than 90° in the coordinates being used. In this example, the angles referred to are those between the eigenvectors that span the stable, center, and unstable eigenspaces. Angles less than 90° are responsible for the funnel-shaped initial transient behavior of the $\mu^{\pm}_{EB}$. For instance, the angle between the two eigenvectors associated with the two largest eigenvalues is 9.7° and the backward μ^{-}_{EB} for $\mathcal{E}^u$ in the $T \to 0$ limit (i.e. the opposites of the eigenvalues of the symmetric part of $D\mathbf{f}(\mathbf{x}_e)$, which are -2.5 and -6.1) are not consistent with the μ^- for most averaging times up to $\overline{T}$; this initial transient is referred to as non-modal behavior (62). By excluding a period $[0, t_s]$ the initial transient behavior is eliminated. A similar argument can be made when considering the FTLEs $\mu^{\pm}$.

Figure 2.5 shows the FTLEs $\mu^{\pm}_{EB}$ used to determine the constants ν, σ as described in Section

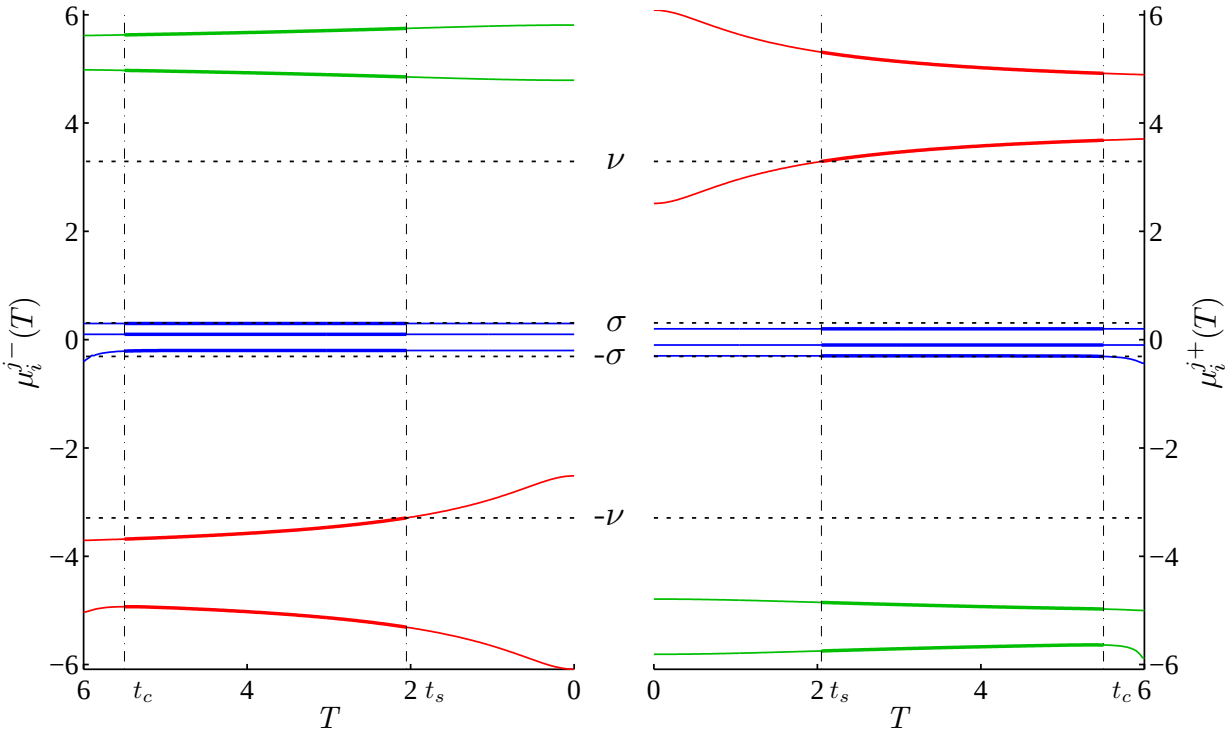

Figure 2.5: Backward and forward FTLEs ($\mu_i^{j\pm}$ with $i = 1, ..., n^j$ and $j = s, c, u$) for the subspaces $\mathcal{E}^s$ (green), $\mathcal{E}^u$ (red) and $\mathcal{E}^c$ (blue). The exponential bound constants σ and ν and the start and cutoff times t_s and t_c are shown.

2.5.1. With $t_s = 2.05$, for $T \in (t_s, t_c]$ we can define uniform exponential bounds with $\sigma = 0.31$ and $\nu = 3.29$. Figure 2.6 shows the FTLEs $\mu^{\pm}$, the start time t_s, and the bounds α and β that define the spectral gap $\Delta\mu$.

In the general case with tangent linear-time-varying (LTV) dynamics, there is similar behavior requiring the truncation of the time interval. The specification of the constants t_s and t_c can be exclusively based on behavior of the $\mu^{\pm}$ and $\mu_{EB}^{\pm}$; it is not necessary to determine angles within subspaces as was done in this example to provide insight into the root cause.

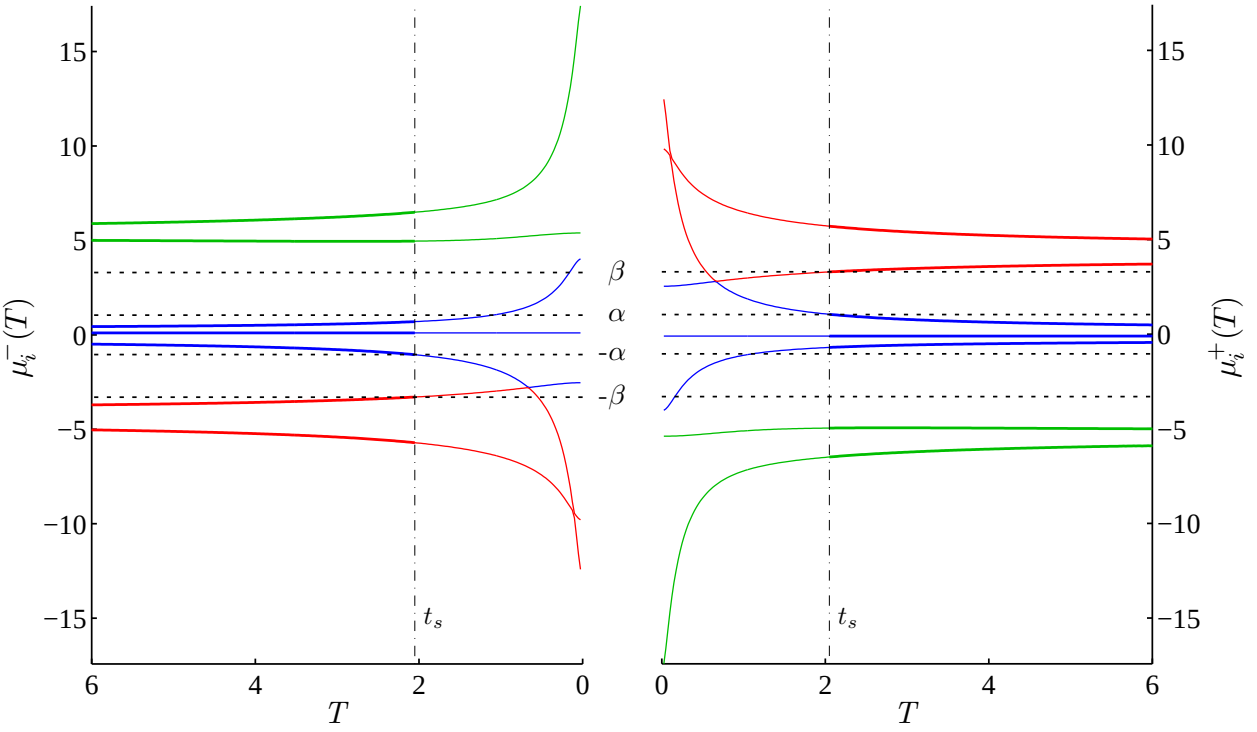

Figure 2.6: Backward and forward FTLEs ($\mu_i^{\pm}$ with $i = 1, ..., n$). The constants α and β and the start time t_s are shown.

2.6.2 4D Hamiltonian System: Mass-Spring-Damper System

To demonstrate the use of FTLA to locate points on a two-dimensional normally hyperbolic center manifold, we consider the optimal control of a mass-(nonlinear) spring-damper system modeled as

$$\begin{aligned} \dot{x}_1 &= x_2, \\ \dot{x}_2 &= -\tfrac{1}{m}\left(cx_2 + k_1 x_1 + k_2 x_1^3\right) + \tfrac{u}{m}, \end{aligned} \tag{2.30}$$

where x_1 is the displacement of the mass m measured from the rest position of the spring, u is the applied scalar control, k_1 and k_2 are the coefficients of the linear and cubic contributions to the

spring force, and c is the damping coefficient. For the problem of minimizing

$$J = \int_0^{t_f} \tfrac{1}{2} u^2 \, \mathrm{d}t \,, \tag{2.31}$$

subject to the dynamic constraint (2.30) and specified initial and final conditions on x_1 at a specified final time t_f, Pontryagin's minimum principle leads to first-order necessary conditions in the form of a boundary value problem for the Hamiltonian system

$$\begin{aligned} \dot{x}_1 &= x_2, \\ \dot{x}_2 &= -\tfrac{1}{m}\left(c x_2 + k_1 x_1 + k_2 x_1^3 + \tfrac{\lambda_2}{m}\right), \\ \dot{\lambda}_1 &= \tfrac{\lambda_2}{m}\left(k_1 + 3 k_2 x_1^2\right), \\ \dot{\lambda}_2 &= -\lambda_1 + c\tfrac{\lambda_2}{m}, \end{aligned} \tag{2.32}$$

where λ_1 and λ_2 are adjoint variables and the minimizing control is $u^* = -\lambda_2/m$. We consider (2.32) in the form $\dot{\mathbf{x}} = \mathbf{f}(\mathbf{x})$ with $\mathbf{x} = [x_1 \,,\, x_2 \,,\, \lambda_1 \,,\, \lambda_2]^T \in \mathbb{R}^4$ and $\mathbf{f}$ defined appropriately.

For small values of m, the Hamiltonian system is in singularly perturbed standard form (41), and the system can be expected to evolve on disparate timescales. Here we focus on applying FTLA to the Hamiltonian system (2.32) to diagnose two-timescale behavior and locate points on the center manifold, which is in this case a slow manifold. The linearized dynamics (2.2) have the Jacobian matrix

$$D\mathbf{f} = \begin{bmatrix} 0 & 1 & 0 & 0 \\ \frac{1}{m}\left(-k_1 - 3k_2 x_1^2\right) & -\frac{c}{m} & 0 & -\left(\frac{1}{m}\right)^2 \\ \frac{\lambda_2}{m}\left(6 k_2 x_1\right) & 0 & 0 & \frac{1}{m}\left(k_1 + 3 k_2 x_1^2\right) \\ 0 & 0 & -1 & \frac{c}{m} \end{bmatrix}. \tag{2.33}$$

For the numerical results we use $m = 0.5$, $k_1 = 1$, $k_2 = 0.01$, and $c = 4\sqrt{k_1 m}$.

Finite-Time Lyapunov Analysis

FTLA is applied in a region $\mathcal{X} = (-1.0, 6.0) \times (-5.0, -1.9) \times (7.0, 15.0) \times (0.8, 5.0)$, chosen such that the ILDM method is applicable (i.e., the eigenvalues of $D\mathbf{f}$ are real), yet the center manifold curvature is large enough that the ILDM method produces noticeable errors. We present results for the five points: $\mathbf{x}_1 = [3.00\ ,\ -2.0\ ,\ 7.5\ ,\ 2.0]^T$, $\mathbf{x}_2 = [2.85\ ,\ -2.0\ ,\ 9.3\ ,\ 2.0]^T$, $\mathbf{x}_3 = [2.70, -2.0, 11.0, 2.0]^T$, $\mathbf{x}_4 = [2.55, -2.0, 12.8, 2.0]^T$, and $\mathbf{x}_5 = [2.40, -2.0, 14.5, 2.0]^T$, with timescale structure representative of all the points in $\mathcal{X}$. Figure 2.7 shows the forward and backward Lyapunov exponents for the five points as functions of the averaging time T. Because the system is Hamiltonian, the FTLEs should be symmetric about the origin. With $n^s = n^u = 1$, $n^c = 2$, $\alpha = 0.52$, $\beta = 5.64$, $\Delta\mu = 5.12$, $\sigma = 0.66$, $\nu = 5.19$, $t_s = 0$ and $t_c = \overline{T} = 0.50$, the conditions given in Def. 2.4.1 for a uniform two-timescale set resolvable over 2.6 convergence time constants are satisfied. Figure 2.8 shows the FTLEs and exponential bounds that were computed as described in Section 2.5.1.

Computing Center Manifold Points Using FTLA

The center subspace $\mathcal{E}^c(\overline{T}, \mathbf{x})$ has dimension $n^c = 2$ and can be written as (2.18)

$$\mathcal{E}^c(\overline{T}, \mathbf{x}) \quad = \quad \mathcal{L}_3^+(\overline{T}, \mathbf{x}) \cap \mathcal{L}_2^-(\overline{T}, \mathbf{x}) \tag{2.34}$$

with its orthogonal complement (2.26) given by

$$[\mathcal{E}^c(\overline{T}, \mathbf{x})]^\perp = span\{\mathbf{l}_1^-(\overline{T}, \mathbf{x}), \mathbf{l}_4^+(\overline{T}, \mathbf{x})\}. \tag{2.35}$$

The existence of a 2D center manifold is postulated. As described in Section 2.4, n^c coordinates are chosen to parametrize $\mathcal{W}^c$ such that their coordinates axes are not parallel to any of the directions

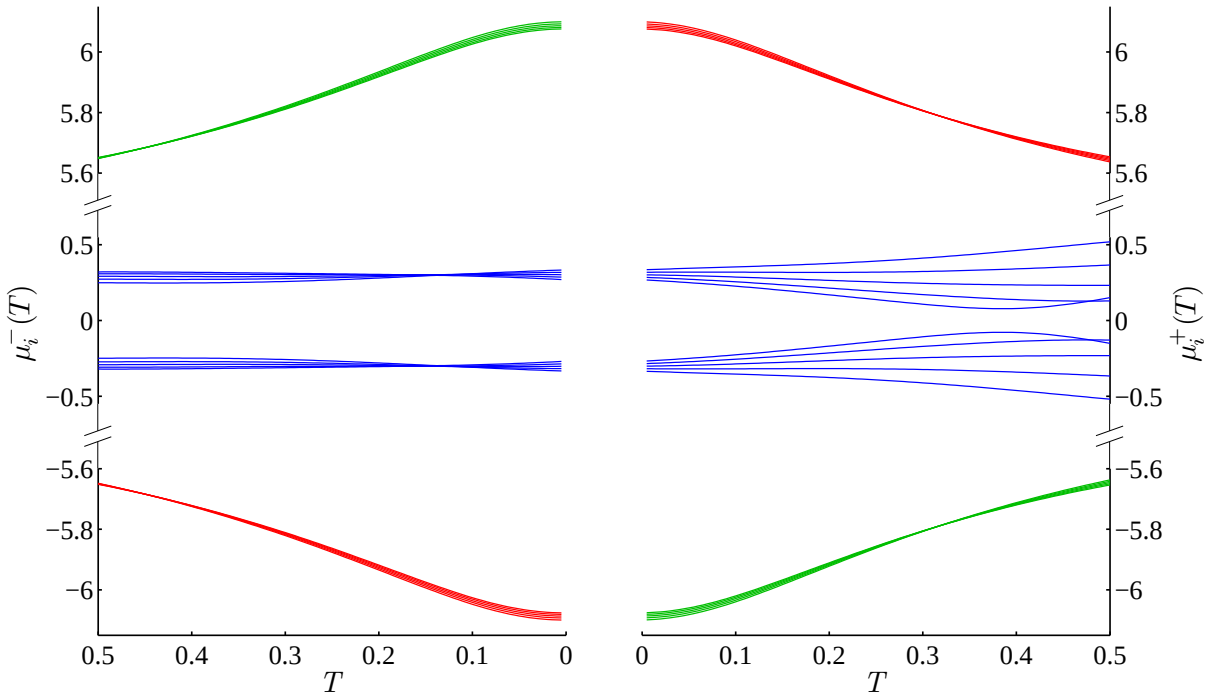

Figure 2.7: Superposition of backward and forward FTLEs for points $\mathbf{x}_1, \mathbf{x}_2, \mathbf{x}_3, \mathbf{x}_4$, and $\mathbf{x}_5$. Note that only segments of the y-axis are shown to highlight the center FTLEs.

in $[\mathcal{E}^c(\overline{T}, \mathbf{x})]^\perp$, namely in the $\mathbf{l}_1^-(\overline{T}, \mathbf{x})$ and $\mathbf{l}_4^+(\overline{T}, \mathbf{x})$ directions. For example

$$\begin{aligned} \mathbf{l}_1^-(0.5, \mathbf{x}_1) = &\quad [0.33\ ,\ 0.89\ ,\ 0.05\ ,\ 0.31]^T, \\ \mathbf{l}_4^+(0.5, \mathbf{x}_1) = &\quad [-0.01\ ,\ 0.00\ ,\ -0.16\ ,\ 0.99]^T. \end{aligned} \tag{2.36}$$

The directions of x_2 and λ_2 are almost parallel respectively to $\mathbf{l}_1^-$ and $\mathbf{l}_4^+$, so we choose the independent variables to be x_1 and λ_1. We use the (x_1, λ_1) coordinates of the five points $\mathbf{x}_j, j = 1, \ldots, 5$ as the grid in the independent coordinate plane and compute the (x_2, λ_2) coordinates for the graph of $\mathcal{W}^c(T)$ by solving the orthogonality conditions.

For Def. 2.4.1, the value of $\overline{T}$ must apply at each point in $\mathcal{X}$; to do so, it must be the minimum over all the maximum forward and backward averaging times on $\mathcal{X}$. It can be beneficial in computing center manifold points to use averaging times greater than $\overline{T}$ when possible. The following is an iterative procedure for determining the averaging time during convergence toward the center

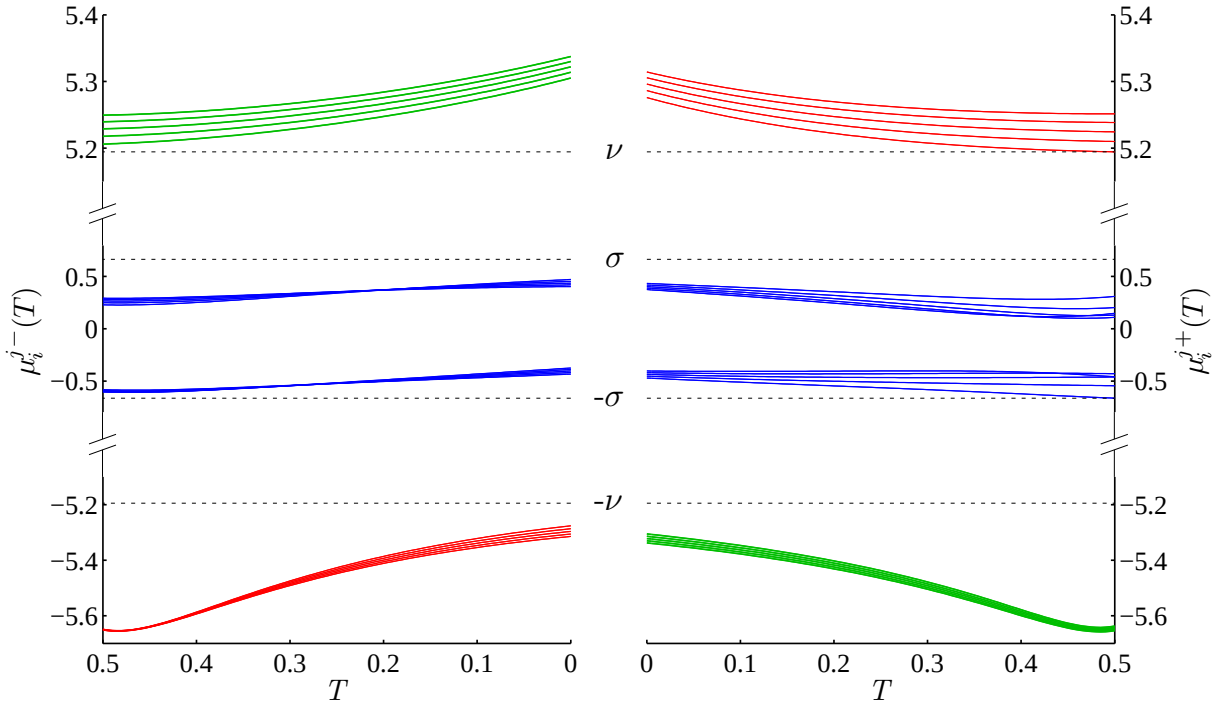

Figure 2.8: FTLEs $\mu_i^{j\pm}$ with $i = 1, ..., n^j$ and $j = s, c, u$ for the subspaces $\mathcal{E}^s(0.5, \mathbf{x})$, $\mathcal{E}^c(0.5, \mathbf{x})$, $\mathcal{E}^u(0.5, \mathbf{x})$ and determination of the constants ν and σ for $\mathbf{x}_1$, $\mathbf{x}_2$, $\mathbf{x}_3$, $\mathbf{x}_4$, and $\mathbf{x}_5$ as functions of time. The distance between ν and σ is actually larger than it appears since only segments of the vertical axis are shown.

manifold is described in. For the converged points, the forward and backward averaging times were increased to 5.0 and 2.0 respectively.

Averaging Time Determination

In order to automate determining the averaging time for $\mathbf{x}_j$ for the calculation of the FTLVs, the averaging time is iteratively increased, without restricting the forward and backward averaging times to be the same. For each pair (x_1, λ_1), the value of (x_2, λ_2) approximating a point on the invariant center manifold is computed using an algorithm consisting of two nested iteration loops with i indicating the inner-loop iteration and k the outer-loop iteration, with $i, k = 0, 1, 2, \ldots$. The variables and iteration indices follow the format: $T_{fwd}^{(k)}$, $T_{bwd}^{(k)}$, $\mathbf{x}_j^{(i,k)}$, $x_2^{(i,k)}$, and $\lambda_2^{(i,k)}$.

1. Initialization: Set $\mathbf{x}_j^{(0,0)} = \mathbf{x}_j$ and $(x_2^{(0,0)}, \lambda_2^{(0,0)})$ to the values of those coordinates in $\mathbf{x}_j^{(0,0)}$. Set $T_{fwd}^{(0)} = \overline{T} = 0.5$ and $T_{bwd}^{(0)} = \overline{T} = 0.5$.

2. Inner-loop iteration $i+1$ at outer iteration k: Calculate $\mathbf{l}_1^-(T_{bwd}^{(k)}, \mathbf{x}_j^{(i,k)})$ and $\mathbf{l}_4^+(T_{fwd}^{(k)}, \mathbf{x}^{(i,k)})$ and determine the values of $x_2^{(i+1,k)}$ and $\lambda_2^{(i+1,k)}$ that satisfy

$$\begin{aligned} \left\langle \mathbf{l}_1^-(T_{bwd}^{(k)}, \mathbf{x}_j^{(i,k)}), \mathbf{f}(\mathbf{x}_j^{(i+1,k)}) \right\rangle &= 0 \\ \left\langle \mathbf{l}_4^+(T_{fwd}^{(k)}, \mathbf{x}_j^{(i,k)}), \mathbf{f}(\mathbf{x}_j^{(i+1,k)}) \right\rangle &= 0. \end{aligned} \tag{2.37}$$

   For this example the unknowns appear linearly; thus analytical solutions for $x_2^{(i+1,k)}$ and $\lambda_2^{(i+1,k)}$ can be obtained. Iterate until the inner-loop stopping criteria are met. The stopping criteria consider the relative change in the dependent variables from the previous iteration and $\theta^{(i+1,k)}$ is the angle between $\mathbf{f}(\mathbf{x}_j^{(i+1,k)})$ and its orthogonal projection in $\mathcal{E}^c(T_{fwd}^{(k)}, T_{bwd}^{(k)}, \mathbf{x}_j^{(i,k)})$ according to

$$\begin{aligned} |x_2^{(i+1,k)} - x_2^{(i,k)}|/|x_2^{(i,k)}| &< tol_{x_2}, \\ |\lambda_2^{(i+1,k)} - \lambda_2^{(i,k)}|/|\lambda_2^{(i,k)}| &< tol_{\lambda_2}, \\ \theta^{(i+1,k)} &< tol_\theta. \end{aligned} \tag{2.38}$$

   For this example, we used $tol_{x_2} = tol_{\lambda_2} = tol_\theta = 10^{-5}$. The approximation at the end of the inner-loop is denoted by $\hat{\mathbf{x}}_j^{(k)}$.

3. Outer-loop iteration: Check the outer-loop stopping criterion

$$\|\hat{\mathbf{x}}_j^{(k)} - \hat{\mathbf{x}}_j^{(k-1)}\|_2 < tol \tag{2.39}$$

   We used $tol = 10^{-6}$. When $k = 0$, we use $\mathbf{x}_j$ in place of $\hat{\mathbf{x}}_j^{(k-1)}$. If the criterion is satisfied, stop and yield the final approximation $\hat{\mathbf{x}}_j$ to the center manifold point for the pair (x_1, λ_1) under consideration. Otherwise perform the $(k+1)^{th}$ outer-loop iteration with the averaging

times

$$T_{fwd}^{(k+1)} = T_{fwd}^{(k)} + dT_{fwd}, \quad T_{bwd}^{(k+1)} = T_{bwd}^{(k)} + dT_{bwd}. \tag{2.40}$$

We used $dT_{fwd} = 0.3$ and $dT_{bwd} = 0.1$. With the new averaging times, repeat the inner-loop iterations starting with $\hat{\mathbf{x}}_j^{(k)}$.

The computations for the five points required about 5 inner iterations for each outer iteration and the forward and backward averaging times were increased to about 5.0 and 2.0 respectively. Experiments with initializing the iterative process with different dependent variable estimates consistently led to the same invariant center manifold point approximations.

Accuracy Assessment

Because the exact location of the invariant center manifold is not known, we use the following means to assess accuracy. The estimated invariant center manifold points $\hat{\mathbf{x}}_j, j = 1, \ldots, 5$ are propagated backward and forward in time to $\phi(t^{\pm}, \hat{\mathbf{x}}_j)$. Then for each of the end points, we fix the independent variables, x_1 and λ_1, and use FTLA to recompute the dependent variables, x_2 and λ_2 for the center manifold point estimate. If the FTLA method computed points on the invariant center manifold without error, then the propagated estimates and re-estimated points would be the same; the degree of inconsistency is thus an indication of accuracy and invariance. The same procedure is used to assess the ILDM estimates.

Figure 2.9, showing points and trajectories projected onto the λ_1-x_2 plane, shows that FTLA is much more consistent than the ILDM method. The trajectories departing from initial points calculated with FTLA (black circles) propagate to points (black squares forward and black diamonds backward) close to those re-estimated, the interpretation being that by starting closer to the in-

variant center manifold the trajectories follow the center manifold for a longer time. Although the initial ILDM points (red circles) appear close to the initial FTLA points, the high degree of inconsistency at the end points indicates greater inaccuracy.

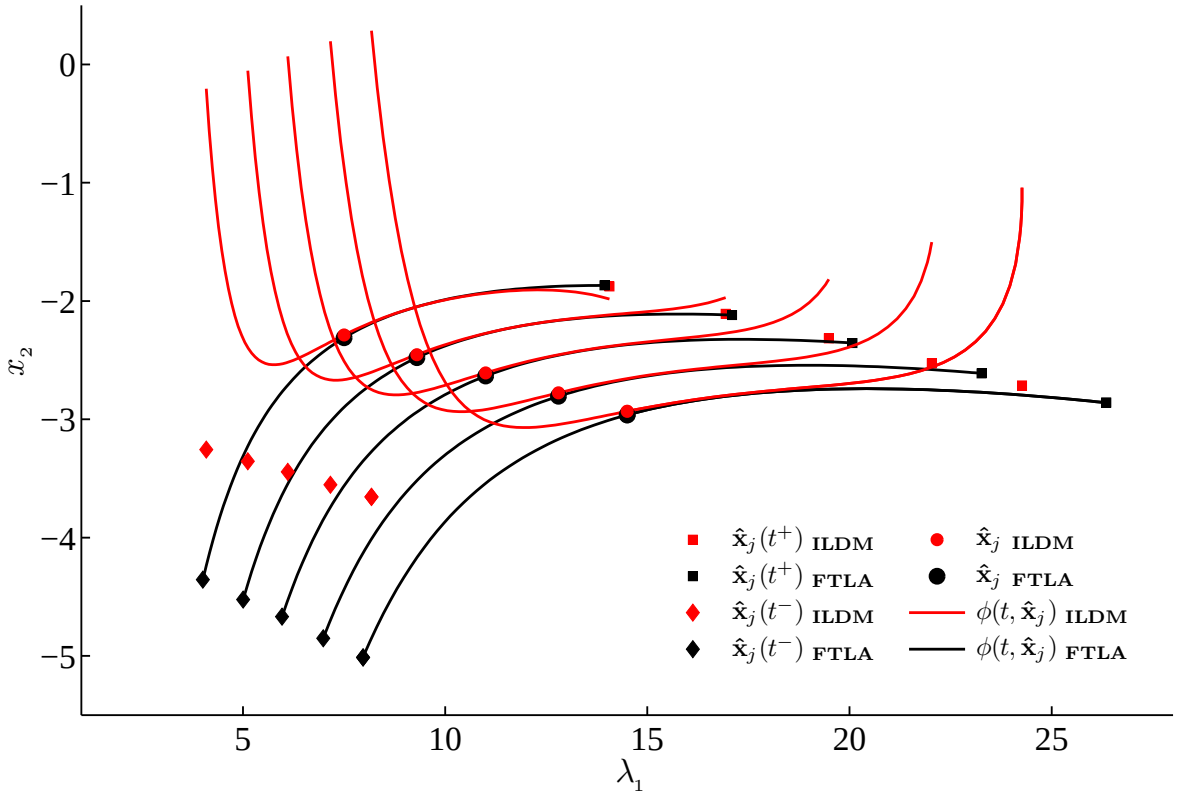

Figure 2.9: Projection onto the λ_1-x_2 plane of the forward and backward propagations from initial points on the center manifold (circles). The independent coordinates of the points at the end of the trajectories are used to compute new estimates on the center manifold (diamonds-backward, squares-forward). Points in black refer to estimates calculated via FTLA while the lighter ones are computed with ILDM.

Table 2.1 shows quantitatively the center manifold estimation error for the FTLA and ILDM methods. An invariance error percent (IP) is defined by

$$IP^{\pm}_{x_2} = \frac{\|x_2(\hat{\mathbf{x}}_j(t^{\pm})) - x_2(\phi(t^{\pm}, \hat{\mathbf{x}}_j))\|}{\|x_2(\hat{\mathbf{x}}_j(t^{\pm}))\|} * 100 \tag{2.41}$$

where $\hat{\mathbf{x}}_j(t^+)$ (squares) and $\hat{\mathbf{x}}_j(t^-)$ (diamonds) are estimates of points on the center manifold cal-

Table 2.1: Invariance error percent for x_2 and λ_2 for FTLA and ILDM methods.

	$IP^+_{x_2}$		$IP^-_{x_2}$		$IP^+_{\lambda_2}$		$IP^-_{\lambda_2}$	
	$FTLA$	$ILDM$	$FTLA$	$ILDM$	$FTLA$	$ILDM$	$FTLA$	$ILDM$
$\hat{\mathbf{x}}_1$	$1 \cdot 10^{-4}$	$5.7 \cdot 10^{0}$	$5.1 \cdot 10^{-2}$	$9.4 \cdot 10^{1}$	$3.0 \cdot 10^{-4}$	$1.1 \cdot 10^{1}$	$6.0 \cdot 10^{-4}$	$5.0 \cdot 10^{-1}$
$\hat{\mathbf{x}}_2$	$3.0 \cdot 10^{-4}$	$6.5 \cdot 10^{0}$	$2.5 \cdot 10^{-2}$	$9.8 \cdot 10^{1}$	$5.0 \cdot 10^{-4}$	$1.2 \cdot 10^{1}$	$3.0 \cdot 10^{-4}$	$5.6 \cdot 10^{-1}$
$\hat{\mathbf{x}}_3$	$1.0 \cdot 10^{-4}$	$2.2 \cdot 10^{1}$	$2.0 \cdot 10^{-3}$	$1.0 \cdot 10^{2}$	$2 \cdot 10^{-4}$	$3.8 \cdot 10^{1}$	$< 1 \cdot 10^{-5}$	$6.0 \cdot 10^{-1}$
$\hat{\mathbf{x}}_4$	$2.8 \cdot 10^{-3}$	$4.1 \cdot 10^{1}$	$3.5 \cdot 10^{-2}$	$1.1 \cdot 10^{2}$	$4.6 \cdot 10^{-3}$	$6.9 \cdot 10^{1}$	$4.0 \cdot 10^{-4}$	$6.5 \cdot 10^{-1}$
$\hat{\mathbf{x}}_5$	$1.4 \cdot 10^{-2}$	$6.2 \cdot 10^{1}$	$8.0 \cdot 10^{-2}$	$1.1 \cdot 10^{2}$	$2.2 \cdot 10^{-2}$	$1.0 \cdot 10^{2}$	$1.0 \cdot 10^{-4}$	$6.9 \cdot 10^{-1}$

culated respectively from $\phi(t^+, \hat{\mathbf{x}}_j)$ and $\phi(t^-, \hat{\mathbf{x}}_j)$ via FTLA or ILDM. The trajectory end points $\phi(t^\pm, \hat{\mathbf{x}}_j)$ in Fig. 2.9 are for $t^+ = 1.5$ and $t^- = -1.0$. Finally $x_2(\cdot)$ denotes the x_2 coordinate of argument. The explanation for $IP^\pm_{\lambda_2}$ is analogous. The IP values indicate that FTLA produces accurate approximations to points on the invariant center manifold and is significantly more accurate than the ILDM method.

Chapter 3

Spacecraft Stationkeeping in the Circular Restricted Three-Body Problem via Finite-Time Lyapunov Analysis

The chapter is structured like so: we first present a brief review of the circular restricted three-body problem. We then formulate the stationkeeping problem focusing on the geometric perspective, and describe the proposed stationkeeping strategy. An overview of FTLA applied specifically to the Earth-Moon CR3BP follows. The next sections focus on comparing FTLA results with the ones obtained with traditional methods. Finally, several examples are illustrated and analyzed.

3.1 Stationkeeping around Libration Points

3.1.1 Spacecraft Dynamics in the Circular Restricted Three-Body Problem

The three-body problem describes the dynamics of three bodies with masses m_1, m_2, and m_3, subject to mutual gravitational attraction. If we assume that one of the bodies (e.g. m_3) has negligible gravitational influence on the other two (i.e., $m_3 << m_1$ and $m_3 << m_2$), the problem is known as the restricted three-body problem. The bodies with mass m_1 and m_2 are called primaries and m_3 is the mass of the secondary body. Moreover, if the primaries are assumed to move on circular orbits around their barycenter, the problem further simplifies and is referred to as the circular restricted three-body problem (CR3BP). More details on the CR3BP can be found in (66).

We consider in particular the Earth-Moon-spacecraft CR3BP and we indicate with m_1 the Earth mass, with m_2 the Moon mass, and with m_3 the spacecraft mass. We work in the non-inertial, co-rotating (synodic) frame of reference, with origin at the center of mass of the Earth-Moon system, in which the Earth and Moon are stationary. The x-axis is directed towards the Moon, the z-axis is in the direction of the inertial angular velocities of the primaries, and the y-axis completes the right-handed $x - y - z$ orthogonal frame as shown in Fig. 3.1.

When writing the equations that describe the dynamics of the CR3BP, it is useful to represent the phase coordinates as non-dimensionalized quantities. In this representation, the mass, time, and length units are respectively the sum of the masses of the primaries, the mean orbital period of the primaries around the center of mass of the system, and the distance between the Earth and the Moon. The mass parameter, defined as $\mu_G := m_2/(m_1 + m_2)$, is thus the only parameter on which the CR3BP dynamical system depends. For the Earth-Moon system, the mass parameter is $\mu_G = 0.01215$ and the units of time, length, and velocity are $u_t = 4.34262$ days, $u_l = 384400$ km, and $u_v = 1.02452 \times 10^5$ cm/s, respectively. The lengths of the position vectors from the

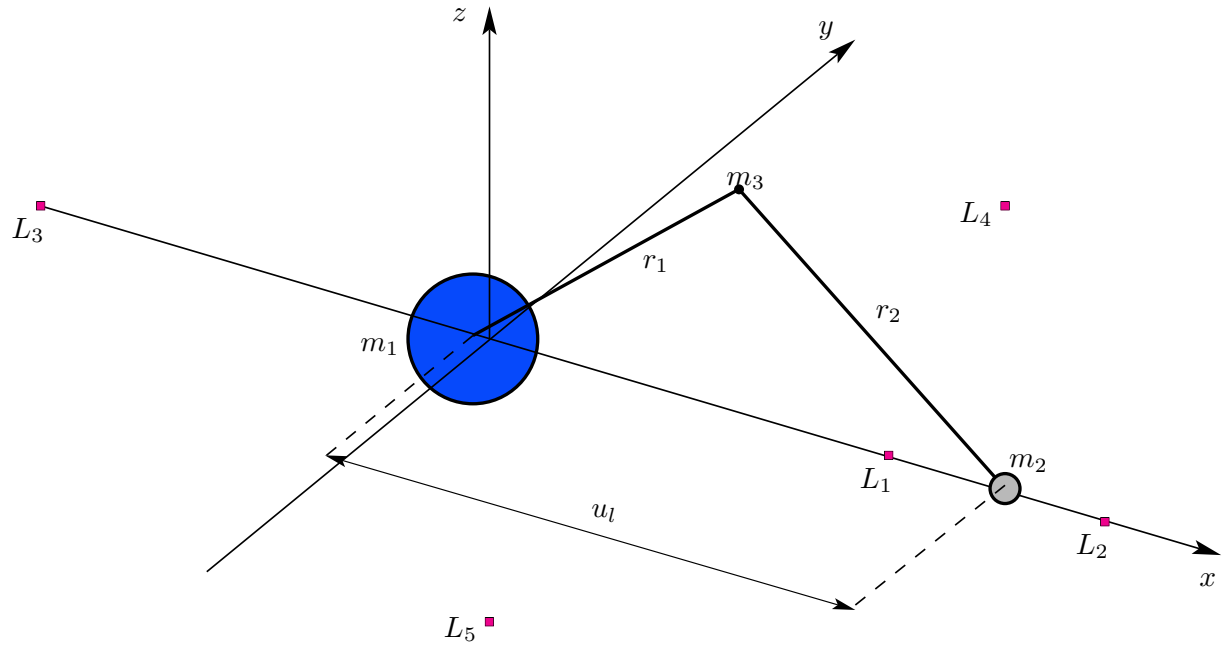

Figure 3.1: Frame of reference in the Earth-Moon Circular Restricted Three-Body Problem with libration points.

primary masses to the secondary mass (spacecraft) are $r_1 = \sqrt{(x+\mu_G)^2 + y^2 + z^2}$ and $r_2 = \sqrt{(x+\mu_G-1)^2 + y^2 + z^2}$.

The positions and velocities of the secondary mass are expressed as the coordinates of the phase point $\mathbf{x} = (\mathbf{p}^T, \mathbf{v}^T)^T$ with $\mathbf{p} = (x, y, z)^T$ and $\mathbf{v} = (v_x, v_y, v_z)^T$. The spacecraft dynamics, written

as a system of six first-order ordinary differential equations, are

$$
\begin{aligned}
\dot{x} &= v_x, \\
\dot{y} &= v_y, \\
\dot{z} &= v_z, \\
\dot{v}_x &= x + 2v_y - \frac{1-\mu_G}{r_1^3}(x+\mu_G) - \frac{\mu_G}{r_2^3}(x-1+\mu_G), \\
\dot{v}_y &= y - 2v_x - \frac{1-\mu_G}{r_1^3}y - \frac{\mu_G}{r_2^3}y, \\
\dot{v}_z &= -\frac{1-\mu_G}{r_1^3}z - \frac{\mu_G}{r_2^3}z.
\end{aligned}
\tag{3.1}
$$

The system (3.1) has five equilibria which lie in the x-y plane and are called Lagrangian or libration points. The libration points are indicated with L_1 through L_5 and can be seen in Fig. 3.1. L_1, L_2, and L_3 are collinear and lie on the x-axis, while L_4 and L_5 are symmetric with respect to the x-axis and each is a vertex of an equilateral triangle with the primaries m_1 and m_2 at the other vertices.

In this work, we focus on neighborhoods of the Earth-Moon collinear libration points, whose position coordinates are: $(x, y, z)_{L_1} = (0.8369180073, 0, 0)$, $(x, y, z)_{L_2} = (1.1556799131, 0, 0)$, and $(x, y, z)_{L_3} = (-1.0050624018, 0, 0)$ and all possess null velocity coordinates. Analyzing the linearized dynamics, we find that the collinear equilibria have a 'saddle $\times$ center $\times$ center' structure with two real eigenvalues equal in magnitude and opposite in sign and two pairs of purely imaginary conjugate eigenvalues. Thus, L_1, L_2, and L_3 are unstable equilibria. [1]

Around the collinear points, there exist families of periodic orbits, such as horizontal and vertical Lyapunov orbits, and Halo orbits as described in (11). Each periodic orbit is associated with a level

[1]Terms such as L_1 through L_5, as well as the word "spacecraft", may refer to their positions in the physical 3-D space or to phase points with position and velocity coordinates in the synodic frame; the proper interpretation should be clear from the context.

of specific energy, which is an integral of motion for the system (3.1) and is defined as

$$E = \frac{1-\mu_G}{r_1} + \frac{\mu_G}{r_2} - \frac{1}{2}(v_x^2 + v_y^2 + v_z^2 - x^2 - y^2). \tag{3.2}$$

For each energy level, and thus associated with each periodic orbit, there are families of quasiperiodic orbits which lie on invariant tori about the corresponding periodic orbit, in particular the Lissajous orbits are in correspondence to the Vertical Lyapunov and the quasihalo orbits are found around the Halo orbits (see for example (39)).

3.1.2 Stationkeeping Strategy

Let us first consider a periodic or quasiperiodic reference orbit $\mathcal{O}_{ref}$ about a collinear libration point L. Ideally, we would like to place our spacecraft exactly on $\mathcal{O}_{ref}$, and in the absence of perturbations, the spacecraft would continue to orbit indefinitely on $\mathcal{O}_{ref}$. Unfortunately, it is unrealistic to think that a spacecraft could be put in $\mathcal{O}_{ref}$ without any error, and even if that was possible, during its mission, the spacecraft would deviate from the reference trajectory because of external perturbations. In the real world, these perturbations are generated by many factors, among others, the gravitational influence of other celestial bodies, solar pressure, or imperfections in the modeling of the system. In the simulation environment, where the model can indeed be considered correct, *ad hoc* perturbations are introduced. Due to the unstable nature of the orbits about the collinear points, even an infinitesimal perturbation will grow exponentially over time, leading the spacecraft to eventually depart $\mathcal{O}_{ref}$. To prevent the spacecraft from getting too far from the reference orbit, stationkeeping maneuvers (SKM) are required. We assume that a stationkeeping maneuver consists of an impulsive thrust, during which the velocity of the spacecraft changes in-

stantaneously, while its position remains constant. For this reason, SKM will be synonym with instantaneous spacecraft velocity change $\Delta\mathbf{v}$.

A typical stationkeeping strategy calls for repeated maneuvers that need to be performed so that the total fuel requirement is equal or less than the available fuel allowed for stationkeeping. The fuel consumption of a single SKM is proportional to $e^{||\Delta\mathbf{v}||}$. A proper design should take into consideration several factors. For instance, the direction of the $\Delta\mathbf{v}$ vectors may be limited by the spacecraft attitude, the minimum and maximum bounds on $||\Delta\mathbf{v}||$ are dictated by the capabilities of the thrusters assigned for stationkeeping. Furthermore, the times and locations at which the maneuvers are performed are generally affected by other mission/hardware constraints. We assume that there are no constraints on either the direction or the magnitude of the computed $\Delta\mathbf{v}$ vectors, and we impose beforehand the locations or the timing for the stationkeeping maneuvers. When it comes to stationkeeping, mission requirements fall into two categories:

(i) *Strict*: the spacecraft is required to track a reference orbit $\mathcal{O}_{ref}$, trying to minimize the distance from it in terms of position and velocity at any given moment in time.

(ii) *Loose*: it is sufficient that the spacecraft is put in some orbit that neighbors the reference orbit $\mathcal{O}_{ref}$. In case a reference orbit is not provided, the spacecraft trajectory must lie within some prescribed spatial bounds.

Geometric Perspective

We recall that periodic and quasiperiodic orbits about a collinear libration point L are part of a four-dimensional invariant center manifold $\mathcal{W}^c$ associated with L. Each orbit $\mathcal{O} \in \mathcal{W}^c$ has an associated stable manifold $\mathcal{W}^s(\mathcal{O})$ which is the union of the local stable fibers at each point of the orbit (28). If a spacecraft is on $\mathcal{W}^s(\mathcal{O})$, it will approach $\mathcal{O}$ asymptotically forward in time. Periodic

and quasiperiodic orbits, along with their stable manifolds, lie on a five-dimensional manifold, the invariant center-stable manifold $\mathcal{W}^{cs}$. Analogously, $\mathcal{W}^{u}(\mathcal{O})$ indicates the unstable manifold of $\mathcal{O}$ and $\mathcal{W}^{cu}$ represents the invariant center-unstable manifold of L. Being on $\mathcal{W}^{cs}$ guarantees that the forward-time unstable component of the vector field is canceled; being on $\mathcal{W}^{cu}$ guarantees that the backward-time unstable component of the vector field is canceled. The superscripts 's', 'c', 'u', 'cs', and 'cu' stand for *stable, center, unstable, center-stable*, and *center-unstable*, respectively.

Let us now consider a spacecraft whose trajectory has been perturbed away from a reference orbit $\mathcal{O}_{ref} \in \mathcal{W}^{c}$. When the stationkeeping maneuver is scheduled to be performed, the spacecraft is likely to be off the invariant center manifold $\mathcal{W}^{c}$. From a geometric point of view, the SKM consists of a state correction $\Delta\mathbf{x} = (\mathbf{0}^T, \Delta\mathbf{v}^T)^T$ that aims to place the spacecraft as close as possible to either the stable manifold of the reference orbit $\mathcal{W}^{s}(\mathcal{O}_{ref})$ (*Strict* requirements) or to the stable manifold of a neighboring orbit $\mathcal{W}^{s}(\mathcal{O})$ (*Loose* requirements), with $\mathcal{O} \in \mathcal{W}^{c}$. Figure 3.2 offers a conceptual sketch of the stationkeeping procedure, showing the $\Delta\mathbf{x}$-corrections and trajectories before and after the SKM, for the two scenarios that have been described. Once the spacecraft is on either $\mathcal{W}^{s}(\mathcal{O}_{ref})$ or $\mathcal{W}^{s}(\mathcal{O})$, its trajectory will approach the corresponding orbit on the invariant center manifold $\mathcal{W}^{c}$. Since it is impossible to place a point exactly on $\mathcal{W}^{cs}$, after a certain amount of time, the spacecraft trajectory will start to deviate again from it, requiring a new stationkeeping maneuver to be performed.

In this work, we will focus on the "*Loose*" case, namely, we propose a stationkeeping procedure that recurrently places the spacecraft as close as possible to the invariant center-stable manifold $\mathcal{W}^{cs}$ of L in order to converge to some orbit $\mathcal{O}$ in the neighborhood of a reference orbit $\mathcal{O}_{ref}$. We will demonstrate that, if the spacecraft is initially close to $\mathcal{O}_{ref}$, and if the perturbations that cause it to deviate from it are small enough, the proposed stationkeeping strategy is capable of maintaining the spacecraft reasonably close to $\mathcal{O}_{ref}$.

We established that, in order to perform stationkeeping, it is beneficial to know the nonlinear

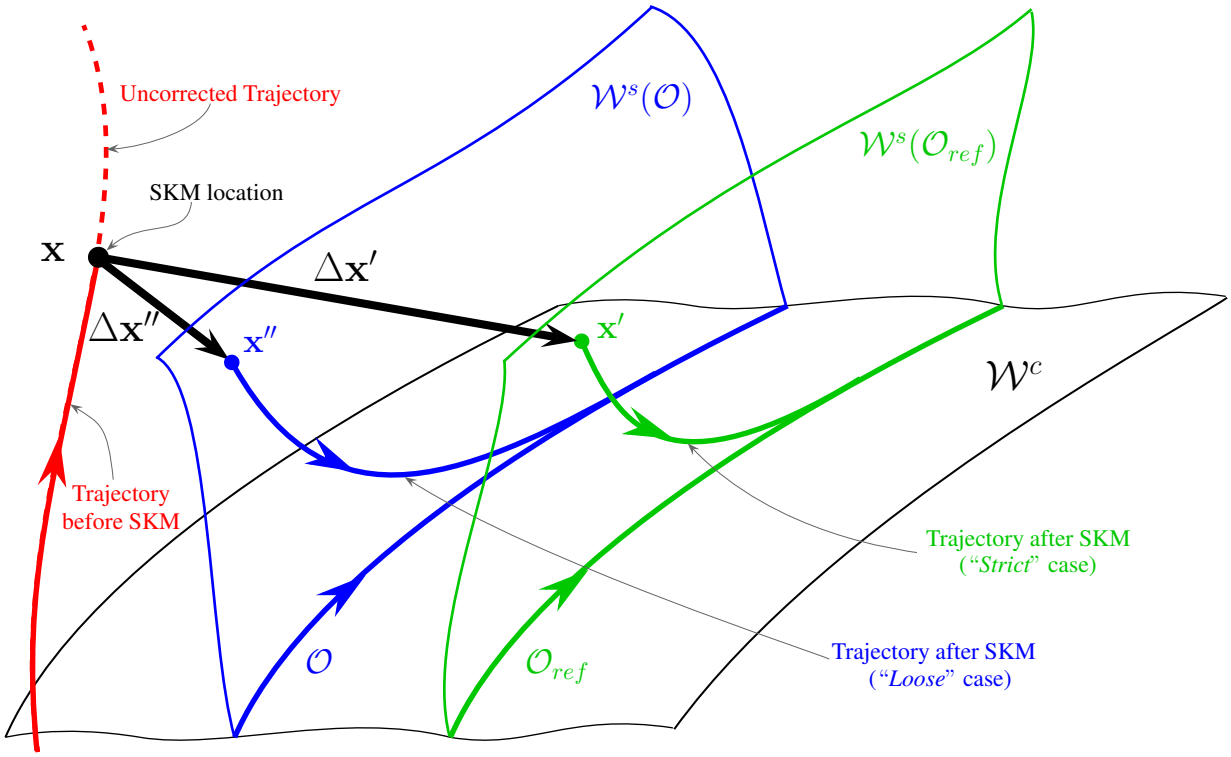

Figure 3.2: Conceptual sketch of the stationkeeping procedure. From the SKM location $\mathbf{x}$ off the invariant center manifold $\mathcal{W}^c$, two cases are shown. For the "*Strict*" case, the correction $\Delta\mathbf{x}'$, places the spacecraft on a point $\mathbf{x}'$ on the stable manifold of the reference orbit $\mathcal{W}^s(\mathcal{O}_{ref})$; the resulting trajectory converges to the reference orbit $\mathcal{O}_{ref} \in \mathcal{W}^c$ (in green). For the "*Loose*" requirements, the correction $\Delta\mathbf{x}''$, places the spacecraft on a point $\mathbf{x}''$ on the stable manifold of a neighboring orbit $\mathcal{W}^s(\mathcal{O})$ (in blue).

manifold structure that characterizes the neighborhood $\mathcal{X}_L \subset \mathbb{R}^6$ of L. Moreover, when analyzing the linearized dynamics, the tangent space associated with each phase point $\mathbf{x} \in \mathcal{X}_L$ maintains a partially hyperbolic structure similar to that of L and can be written as

$$T_{\mathbf{x}}\mathbb{R}^6 = \mathcal{V}^s(\mathbf{x}) \oplus \mathcal{V}^c(\mathbf{x}) \oplus \mathcal{V}^u(\mathbf{x}), \tag{3.3}$$

where $\mathcal{V}^s$, $\mathcal{V}^c$, and $\mathcal{V}^u$ are respectively the stable, center, and unstable linear subspaces calculated at $\mathbf{x}$. Note that the point $\mathbf{x}$ need not be on a particular orbit on $\mathcal{W}^c$ or on any other manifold for the splitting to hold. The splitting in Eq. (3.3) can also be written as

$$T_{\mathbf{x}}\mathbb{R}^6 = \mathcal{V}^{cs}(\mathbf{x}) \oplus \mathcal{V}^u(\mathbf{x}), \tag{3.4}$$

where $\mathcal{V}^{cs}(\mathbf{x}) = \mathcal{V}^s(\mathbf{x}) \oplus \mathcal{V}^c(\mathbf{x})$. Let us now consider points on the invariant center manifold $\mathcal{W}^{cs}$. At a point $\mathbf{x} \in \mathcal{W}^{cs}$, the vector field $\mathbf{f}(\mathbf{x})$ can be written as a linear combination of the vectors spanning $\mathcal{V}^{cs}(\mathbf{x})$ with no components in the $\mathcal{V}^u(\mathbf{x})$ direction. In other words, points on the invariant center-stable manifold $\mathcal{W}^{cs}$ satisfy the tangency condition

$$\mathbf{x} \in \mathcal{W}^{cs} \implies \mathbf{f}(\mathbf{x}) \in \mathcal{V}^{cs}(\mathbf{x}). \tag{3.5}$$

The tangency condition in Eq. (3.5) can alternatively be posed as the orthogonality condition

$$\langle \mathbf{f}(\mathbf{x}), \mathbf{w} \rangle = 0, \quad \forall \mathbf{w} \in [\mathcal{V}^{cs}(\mathbf{x})]^{\perp}, \tag{3.6}$$

[2] where the notation $[\mathcal{V}]^{\perp}$ indicates the orthogonal complement of the subspace $\mathcal{V}$. The SK procedure to place points on $\mathcal{W}^{cs}$ will require to satisfy such orthogonality condition.

[2] In this chapter, the notation '$\mathbf{v}$' is reserved for velocity vectors, therefore we use the notation '$\mathbf{w}$' to indicate general vectors belonging to certain subspaces.

Finally, the directions of the vectors spanning the linear subspaces $\mathcal{V}(\mathbf{x})$ can be approximated via different methods. For periodic orbits, Floquet theory (FT) is correct and is utilized to computed the so called Floquet modes (24). The use of Floquet modes has also been extended to quasiperiodic orbits; such extension is theoretically unjustifiable, therefore in certain circumstances Floquet modes may not be reliable at all. For this reason, we propose FTLA as an alternative means for approximating the linear subspaces. Numerical guidelines about the domain of application of our method will be provided in the example section.

3.2 Finite-Time Lyapunov Analysis and Application to CR3BP

In this section we apply FTLA specifically to the Earth-Moon CR3BP and present the algorithm for stationkeeping.

3.2.1 FTLA Applied to Earth-Moon CR3BP

In order to apply FTLA to the Earth-Moon CR3BP, we start by considering a region of the Euclidean six-dimensional state space ($n = 6$) that neighbors a collinear libration point. We indicate such region with $\mathcal{X}_L \subset \mathbb{R}^6$. Our objective is to reliably approximate the tangent space splitting in Eq. (3.3) at points $\mathbf{x} \in \mathcal{X}_L$. The nonlinear system $\dot{\mathbf{x}} = \mathbf{f}(\mathbf{x})$ to analyze has been provided in

Eq. (3.1) and the Jacobian matrix associated with it is

$$D\mathbf{f}(\mathbf{x}) = \begin{bmatrix} 0 & 0 & 0 & 1 & 0 & 0 \\ 0 & 0 & 0 & 0 & 1 & 0 \\ 0 & 0 & 0 & 0 & 0 & 1 \\ 3A_4 - A_1 + 1 & 3A_3 y & 3A_3 z & 0 & 2 & 0 \\ 3A_3 y & 3A_2 y^2 - A_1 + 1 & 3A_2 yz & -2 & 0 & 0 \\ 3A_3 z & 3A_2 yz & 3A_2 z^2 - A_1 & 0 & 0 & 0 \end{bmatrix} \tag{3.7}$$

where

$$\begin{aligned} A_1 &= \frac{\mu_G}{r_2^3} - \frac{\mu_G - 1}{r_1^3}, \\ A_2 &= \frac{\mu_G}{r_2^5} - \frac{\mu_G - 1}{r_1^5}, \\ A_3 &= \frac{\mu_G(\mu_G + x - 1)}{r_2^5} - \frac{(\mu_G - 1)(\mu_G + x)}{r_1^5}, \\ A_4 &= \frac{\mu_G(\mu_G + x - 1)^2}{r_2^5} - \frac{(\mu_G - 1)(\mu_G + x)^2}{r_1^5}. \end{aligned} \tag{3.8}$$

For the tangent space splitting to exist at a point $\mathbf{x}$, we require such point to be finite-time partially hyperbolic. We adapted the definition from 2.4.1 in chapter 1, to specifically fit the CR3BP application. Note that the following properties need to hold for a specific point $\mathbf{x}$ and not for a set of points.

Definition 3.2.1. *A point $\mathbf{x} \in \mathcal{X}_L$, is **finite-time partially hyperbolic** for* (2.1) *with respect to the Euclidean metric, with convergence time constant $\Delta\mu^{-1}$, resolvable over $\Delta\mu(\overline{T} - t_s)$ convergence time constants, if there exist non-negative integers n^s, n^c and n^u, with $n^s + n^c + n^u = n = 6$, a start time t_s, and a maximum averaging time $\overline{T}$, with $0 \leq t_s < \overline{T}$, such that the following properties are satisfied. We use the notation $\mathcal{T} = (t_s, \overline{T}]$.*

1. *T-Uniform Spectral Gaps – There exist $\beta > \alpha > 0$ such that, uniformly on $\mathcal{T}$, the forward and backward FTLE spectra are separated by gaps of size $\Delta\mu = \beta - \alpha$ into $n^s = 1$, $n^c = 4$ and $n^u = 1$ dimensional subsets as illustrated in Fig. 3.3 and specified by*

$$\begin{aligned} &\mu_1^+ \le -\beta \le -\alpha \le \mu_2^+, \qquad \mu_5^+ \le \alpha \le \beta \le \mu_6^+, \\ &-\mu_1^- \le -\beta \le -\alpha \le -\mu_2^-, \quad -\mu_5^- \le \alpha \le \beta \le -\mu_6^-. \end{aligned} \tag{3.9}$$

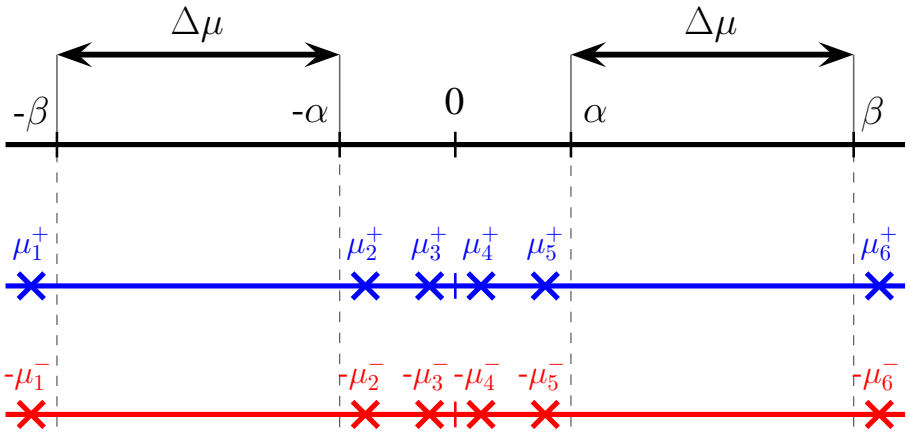

Figure 3.3: Spectra of forward and backward Lyapunov exponents in forward and backward time illustrating a partially hyperbolic spectrum, the constants α and β bounding the stable, center, and unstable spectral subsets, and the spectral gap $\Delta\mu$. The forward (resp. backward) exponents are indicated by "$^+$" (resp. "$^-$") superscripts.

2. *Tangent Space Splitting – For each averaging time $T \in \mathcal{T}$, there is a splitting*

$$\begin{aligned} T_{\mathbf{x}}\mathbb{R}^6 &= \mathcal{E}^s(T,\mathbf{x}) \oplus \mathcal{E}^c(T,\mathbf{x}) \oplus \mathcal{E}^u(T,\mathbf{x}), \\ &= \mathcal{E}^{cs}(T,\mathbf{x}) \oplus \mathcal{E}^u(T,\mathbf{x}). \end{aligned} \tag{3.10}$$

where

$$\mathcal{E}^s(T,\mathbf{x}) = \mathcal{L}^+_{n^s}(T,\mathbf{x}) = span\{\mathbf{l}^+_1(T,\mathbf{x})\},$$
$$\mathcal{E}^u(T,\mathbf{x}) = \mathcal{L}^-_{n^s+n^c+1}(T,\mathbf{x}) = span\{\mathbf{l}^-_6(T,\mathbf{x})\},$$

$$\begin{aligned}
&\mathcal{E}^{cs}(T,\mathbf{x}) = \mathcal{L}^+_{n^s+n^c}(T,\mathbf{x}) = span\{\mathbf{l}^+_1(T,\mathbf{x}),\mathbf{l}^+_2(T,\mathbf{x}),\mathbf{l}^+_3(T,\mathbf{x}),\mathbf{l}^+_4(T,\mathbf{x}),\mathbf{l}^+_5(T,\mathbf{x})\},\\
&\mathcal{E}^{cu}(T,\mathbf{x}) = \mathcal{L}^-_{n^s+1}(T,\mathbf{x}) = span\{\mathbf{l}^-_2(T,\mathbf{x}),\mathbf{l}^-_3(T,\mathbf{x}),\mathbf{l}^-_4(T,\mathbf{x}),\mathbf{l}^-_5(T,\mathbf{x}),\mathbf{l}^-_6(T,\mathbf{x})\},\\
&[\mathcal{E}^{cs}(T,\mathbf{x})]^\perp = span\{\mathbf{l}^+_6(T,\mathbf{x})\},\quad [\mathcal{E}^{cu}(T,\mathbf{x})]^\perp = span\{\mathbf{l}^-_1(T,\mathbf{x})\},
\end{aligned} \tag{3.11}$$

$$\mathcal{E}^c(T,\mathbf{x}) = [[\mathcal{E}^c(T,\mathbf{x})]^\perp]^\perp,$$
$$[\mathcal{E}^c(T,\mathbf{x})]^\perp = [[\mathcal{E}^{cs}(T,\mathbf{x})]^\perp \oplus [\mathcal{E}^{cu}(T,\mathbf{x})]^\perp]^\perp = span\{\mathbf{l}^+_6(T,\mathbf{x}),\mathbf{l}^-_1(T,\mathbf{x})\}.$$

The structure of the forward and backward FTLE spectra, as in Fig. 3.3, are required on an interval of averaging times $(t_s,\overline{T}]$ where the interval $[0,t_s]$ is excluded to avoid the initial transient period during which 'non-modal behavior' can influence the FTLEs.

Subspaces Convergence towards Fixed Subspaces

The splitting of the tangent space (3.10) at $\mathbf{x}$ is a good approximation of (3.3) only if the finite-time subspaces (3.11) have converged enough towards their invariant counterparts $\mathcal{V}(\mathbf{x})$. As described in section 2.3.3, the finite-time Lyapunov subspaces $\mathcal{L}(T,\mathbf{x})$ converge indeed towards fixed subspaces $\mathcal{L}(\mathbf{x})$ at a rate at least proportional to $e^{-\Delta\mu T}$ and so do the subspaces $\mathcal{E}^s(T,\mathbf{x})$, $\mathcal{E}^c(T,\mathbf{x})$, $\mathcal{E}^u(T,\mathbf{x})$, $\mathcal{E}^{cs}(T,\mathbf{x})$ and $\mathcal{E}^{cu}(T,\mathbf{x})$ with respect to $\mathcal{V}^s(\mathbf{x})$, $\mathcal{V}^c(\mathbf{x})$, $\mathcal{V}^u(\mathbf{x})$, $\mathcal{V}^{cs}(\mathbf{x})$ and $\mathcal{V}^{cu}(\mathbf{x})$, respectively.

As a guideline, for the CR3BP, in order for the finite-time subspaces to approximate their ideal infinite-time limits accurately, the convergence time constants $\Delta\mu(\overline{T}-t_s)$ should be at least $7-8$.

Note that, since the FTLEs spectra are point-dependent, $\Delta\mu$, $\overline{T}$, and t_s are functions of $\mathbf{x}$.

Once appropriate values of the maximum averaging time $\overline{T}$ and the start time t_s are selected to meet the subspace convergence criterion, we can finally re-write the tangent space splitting as

$$\begin{aligned} T_{\mathbf{x}}\mathbb{R}^6 &= \mathcal{E}^s(\overline{T},\mathbf{x}) \oplus \mathcal{E}^c(\overline{T},\mathbf{x}) \oplus \mathcal{E}^u(\overline{T},\mathbf{x}), \\ &= \mathcal{E}^{cs}(\overline{T},\mathbf{x}) \oplus \mathcal{E}^u(\overline{T},\mathbf{x}). \end{aligned} \tag{3.12}$$

The last step is to rewrite the orthogonality condition for placing points on the invariant center-stable manifold $\mathcal{W}^{cs}$ in Eq. (3.6) in terms of FTLVs

$$\langle \mathbf{f}(\mathbf{x}), \mathbf{w} \rangle = 0, \quad \forall \mathbf{w} \in [\mathcal{E}^{cs}(\overline{T},\mathbf{x})]^{\perp} = span\{\mathbf{l}_6^+(\overline{T},\mathbf{x})\}. \tag{3.13}$$

Note that if our objective is to place the spacecraft on the center-stable manifold, we really need to compute only the forward FTLEs and FTLVs, saving therefore roughly half of the computational time.

3.2.2 Stationkeeping Computational Procedure

Let us take a point $\mathbf{x}^{(i)}$ (with $i = 1$) at which we wish to perform a stationkeeping maneuver. Since the point is off of $\mathcal{W}^{cs}$, we already know that the orthogonality condition (3.13) will not be met, namely, $\langle \mathbf{f}(\mathbf{x}^{(i)}), \mathbf{l}_6^+(\overline{T}^{(i)}, \mathbf{x}^{(i)}) \rangle \neq 0$. To place the point as close as possible to $\mathcal{W}^{cs}$, we need to proceed iteratively by applying the following algorithm:

1. Compute $\mathbf{f}(\mathbf{x}^{(i)})$.
2. Compute the FTLEs $\mu(T, \mathbf{x}^{(i)})$ for $T > 0$ and select a maximum averaging time $\overline{T}^{(i)}$ so that

the product $\Delta\mu^{+}(\mathbf{x}^{(i)}) \cdot \overline{T}^{(i)}$ is large enough to guarantee a good subspace convergence.

3. Compute the FTLVs $\mathrm{l}^{+}(\overline{T}^{(i)}, \mathbf{x}^{(i)})$ and form the center-stable subspace and its orthogonal complement (resp. $\mathcal{E}^{cs}(\overline{T}^{(i)}, \mathbf{x}^{(i)})$ and $[\mathcal{E}^{cs}(\overline{T}^{(i)}, \mathbf{x}^{(i)})]^{\perp}$).

4. **If** the angle $\angle(\mathbf{f}(\mathbf{x}^{(i)}), \mathcal{E}^{cs}(\overline{T}^{(i)}, \mathbf{x}^{(i)})) < \alpha_1$, $\mathbf{x}^{(i)} \in \mathcal{W}^{cs}(\overline{T}^{(i)})$, **stop** the algorithm. (Typical values for α_1 are within $[10^{-7}, 10^{-5}]$ degrees).

   Else, **go to** next step.

5. Compute the next point $\mathbf{x}^{(i+1)}$ so that $\langle \mathbf{f}(\mathbf{x}^{(i+1)}), \mathbf{l}_6^{+}(\overline{T}^{(i)}, \mathbf{x}^{(i)}) \rangle = 0$.

6. Use $\mathbf{x}^{(i+1)}$ as the new initial point. **Go to** step 1.

Figure 3.4 shows a conceptual simplified drawing of four iterations of the described algorithm (i.e., $N = 4$). To visualize the iterative process, the represented center-stable subspaces and manifold are 2-dimensional. With each iteration, $\mathbf{x}^{(i)}$ is closer to $\mathcal{W}^{cs}$ and the angular distance of $\mathbf{f}(\mathbf{x}^{(i)})$ from $\mathcal{E}^{cs}(\overline{T}^{(i)}, \mathbf{x}^{(i)})$ is less. The vector field at $\mathbf{f}(\mathbf{x}^{(4)})$ lies on the Lyapunov approximation of the center-stable subspace $\mathcal{E}^{cs}(\overline{T}^{(4)}, \mathbf{x}^{(4)})$, tangent to the center-stable manifold $\mathcal{W}^{cs}$ at $\mathbf{x}^{(4)}$.

The orthogonality condition in step 5, $\langle \mathbf{f}(\mathbf{x}^{(i+1)}), \mathbf{l}_6^{+}(\overline{T}^{(i)}, \mathbf{x}^{(i)}) \rangle = 0$, is indeed 1 equation in 6 unknowns, namely, the 6 coordinates of $\mathbf{x}^{(i+1)}$. We treat each iteration $\mathbf{x}^{(i)} \rightarrow \mathbf{x}^{(i+1)}$ as a fictitious stationkeeping maneuver, and assuming that a SKM happens instantaneously, the spacecraft position vector $\mathbf{p}$ remains unchanged during the course of the maneuver, while the velocity vector $\mathbf{v}$ changes by the quantity $\delta\mathbf{v}$.

$$\begin{aligned} \mathbf{p}^{(i+1)} &= \mathbf{p}^{(i)}, \\ \mathbf{v}^{(i+1)} &= \mathbf{v}^{(i)} + \delta\mathbf{v}^{(i)}. \end{aligned} \tag{3.14}$$

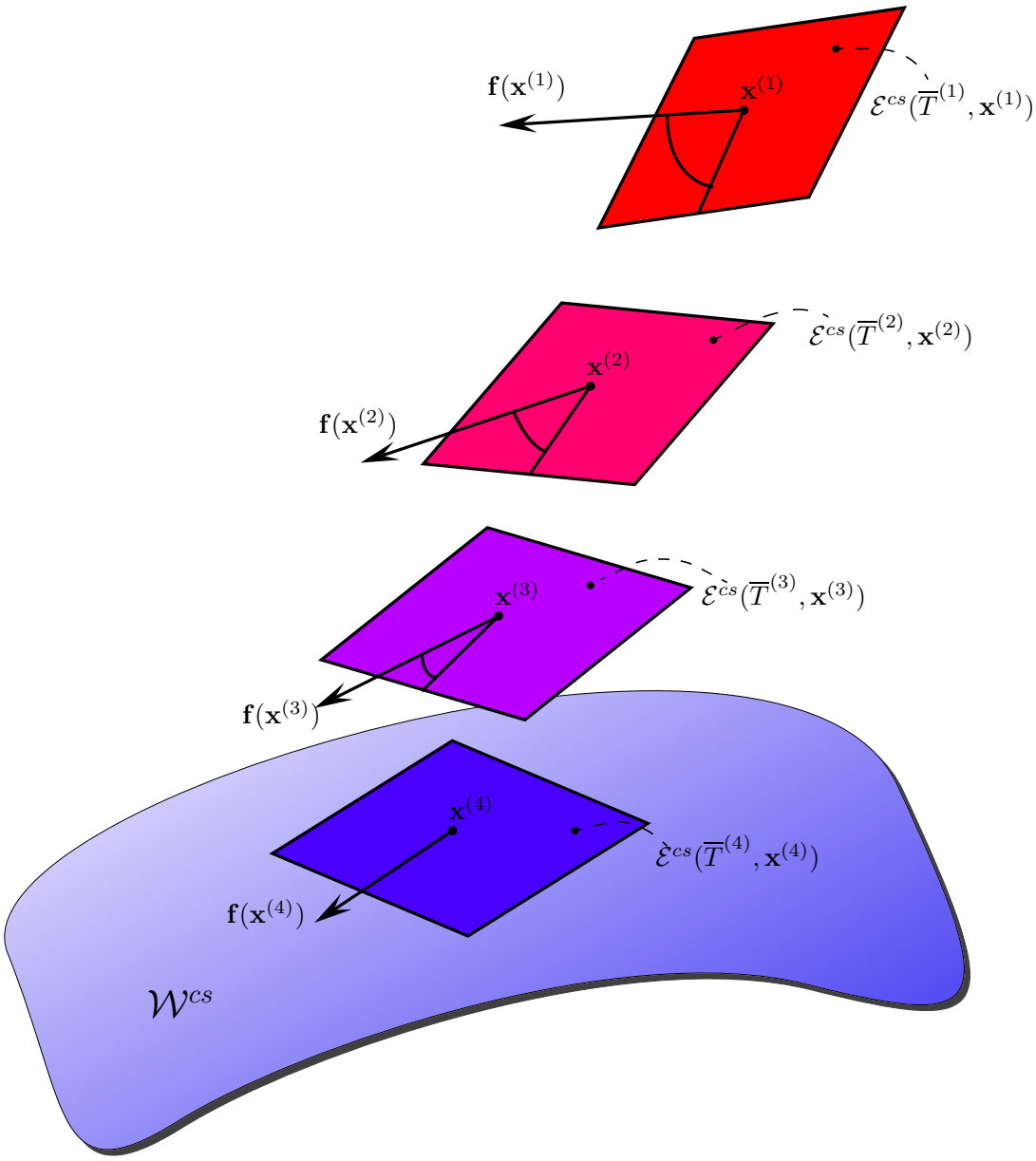

Figure 3.4: Placing a point on a fictional 2-dimensional center-stable manifold using iterations of the algorithm.

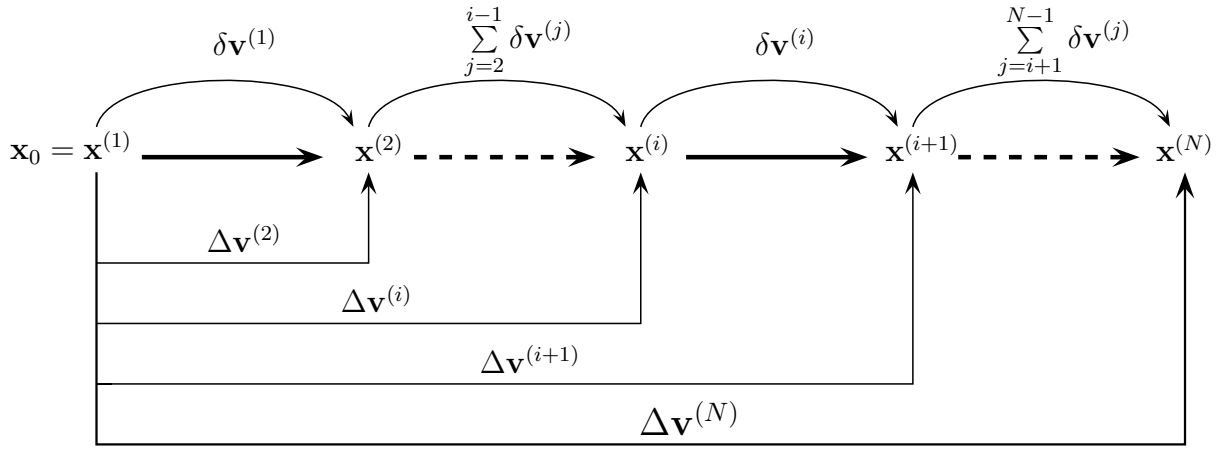

Figure 3.5: Sequence of iterations for placing a point onto the center-stable manifold.

The unknowns are thus reduced to the 3 coordinates of the velocity vector $\mathbf{v}^{(i+1)}$ and can be found by solving the following constrained minimization problem

$$\begin{aligned} &\textit{min}(J), \quad J = ||\Delta\mathbf{v}^{(i+1)}||^2, \\ &\textit{subject to} \quad \langle \mathbf{f}(\mathbf{x}^{(i+1)}), \mathbf{l}_6^+(\overline{T}^{(i)}, \mathbf{x}^{(i)}) \rangle = 0, \end{aligned} \tag{3.15}$$

where $\Delta\mathbf{v}^{(i+1)} = \mathbf{v}^{(i+1)} - \mathbf{v}_0$, with $\mathbf{v}_0 = \mathbf{v}^{(1)}$ being the velocity vector of the initial point $\mathbf{x}^{(1)}$. Note that we minimize the Delta-v between the final point at the present iteration and the initial point. If we denote with N the iteration number at which the algorithm stops, then $||\Delta\mathbf{v}^{(N)}||$ represents the total velocity-change required for real the maneuver. From the geometric perspective, $||\Delta\mathbf{v}^{(N)}||$ represents the distance between the points in the phase space, before and after the maneuver. A schematic of a few iterations of the algorithm is given in Fig. 3.5.

$$\mathbf{x}^{(N)} = \mathbf{x}^{(1)} + \left[0, 0, 0, \left[\Delta\mathbf{v}^{(N)}\right]^T\right]^T. \tag{3.16}$$

The averaging time $\overline{T}^{(i)}$ used to compute FTLEs and FTLVs need not be constant for all the iterations. In fact, the closer a point gets to the manifold $\mathcal{W}^{cs}$, the longer the resulting trajectory can be integrated without leaving the phase space region around the libration point, thus guaranteeing

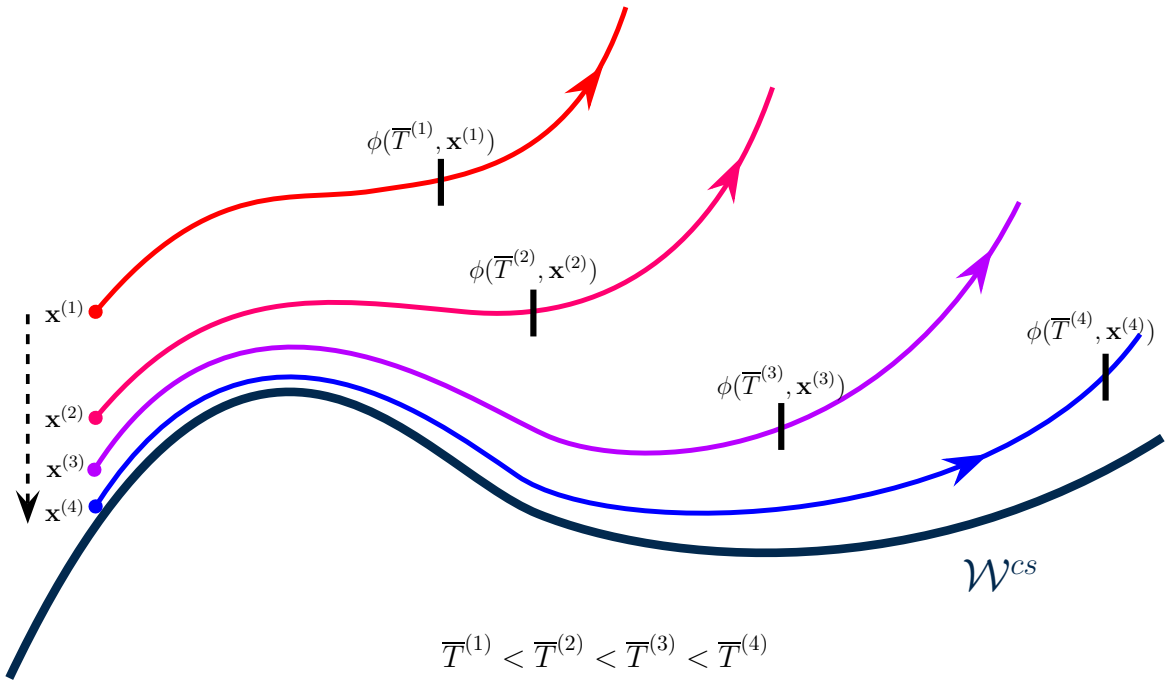

Figure 3.6: Representation of the trajectories departing the phase points $\mathbf{x}^{(i)}$ with $i = 1, 2, 3, 4$. The arrow indicates the direction in which the iterations are moving, that is, towards $\mathcal{W}^{cs}$. The closer $\mathbf{x}^{(i)}$ is to the invariant manifold, the longer the trajectory can be integrated sampling a consistent dynamical behavior. In this instance we have $\overline{T}^{(1)} < \overline{T}^{(2)} < \overline{T}^{(3)} < \overline{T}^{(4)}$.

a faster subspace convergence. If the trajectory left the region of the state around the libration point that is being considered, non-consistent dynamical behavior may be sampled, rendering the FTLEs and FTLVs information not uniform and thus not reliable. From simulations we normally find $\overline{T}^{(1)} < \overline{T}^{(2)} < \ldots < \overline{T}^{(i)} < \overline{T}^{(i+1)} < \overline{T}^{(N)}$ as illustrated for instance in Fig. 3.6. As already mentioned, the procedure does not explicitly call for a reference orbit $\mathcal{O}_{ref}$, so there is no guarantee that the point will be placed exactly on the reference orbit's stable manifold $\mathcal{W}^s(\mathcal{O}_{ref})$. Nevertheless, we will show that such stationkeeping strategy is effective to maintain the spacecraft in a close neighborhood of $\mathcal{O}_{ref}$.

3.3 Accuracy Assessment

In this section we will assess the accuracy of the approximations of the linear subspaces in Eq. (3.3). We will distinguish between the following cases:

- points on periodic orbits, $\mathbf{x} \in \mathcal{W}^c$,
- points on quasiperiodic orbits, $\mathbf{x} \in \mathcal{W}^c$.

In the first segment we will deal with periodic orbits; we will introduce the Floquet theory applied to the CR3BP and then use its results to validate FTLA. The second part of the section focuses on quasiperiodic orbits. The extension of Floquet modes to quasiperiodic orbits is presented and its limitations in approximating the local subspaces are outlined. A modification to the Floquet mode approach for the approximation of the linear subspaces is introduced and compared to FTLA.

3.3.1 Points on periodic orbits

For points on periodic orbits (Horizontal Lyapunov, Vertical Lyapunov, and Halo orbits), Floquet theory is applicable and the linear subspaces in (3.3) can be determined from the monodromy matrix. The monodromy matrix $M(\mathbf{x})$, for $\mathbf{x}$ on a periodic orbit, is the transition matrix at $t = T_p$ where T_p is the orbit period, namely

$$M(\mathbf{x}) = \Phi(T_p, \mathbf{x}). \tag{3.17}$$

The eigenvalues and eigenvectors of the monodromy matrix are also referred to as Floquet multi-

pliers and vectors and are used to define the splitting of the tangent space. We indicate with $\sigma_i(\mathbf{x})$ the eigenvalues and with $\mathbf{f}_i(\mathbf{x})$ the eigenvectors of $M(\mathbf{x})$, where $i = 1, ..., 6$. For the CR3BP, the eigenvalues are reciprocal in pairs, namely, $\sigma_1\sigma_2 = \sigma_3\sigma_4 = \sigma_5\sigma_6 = 1$. For the analyzed orbits, one can show that σ_1, σ_2, σ_3, σ_4 are real, with $\sigma_1 > 1$, $\sigma_2 < 1$, $\sigma_3 = \sigma_4 = 1$ and σ_5, σ_6 are conjugate complex with null real part. Therefore σ_1 is associated with the unstable mode $\mathbf{f}_1$, σ_2 with the stable mode $\mathbf{f}_2$, and σ_3, σ_4, σ_5, σ_6 are associated to the center modes $\mathbf{f}_3$, $\mathbf{f}_4$, $\mathbf{f}_5$, $\mathbf{f}_6$. Since $\mathbf{f}_5$, $\mathbf{f}_6$ are complex conjugate, we substitute them with the real and the imaginary parts of $\mathbf{f}_5$. The Floquet eigenvalues are equal to the natural logarithm of the multipliers. The splitting of the tangent space at $\mathbf{x}$ is written in terms of Floquet subspaces $\mathcal{F}(\mathbf{x})$

$$T_{\mathbf{x}}\mathbb{R}^6 = \mathcal{F}^s(\mathbf{x}) \oplus \mathcal{F}^c(\mathbf{x}) \oplus \mathcal{F}^u(\mathbf{x}), \tag{3.18}$$

where

$$\begin{aligned} \mathcal{F}^s(\mathbf{x}) &= span\{\mathbf{f}_2(\mathbf{x})\}, \\ \mathcal{F}^u(\mathbf{x}) &= span\{\mathbf{f}_1(\mathbf{x})\}, \\ \mathcal{F}^c(\mathbf{x}) &= span\{\mathbf{f}_3(\mathbf{x}), \mathbf{f}_4(\mathbf{x}), Re[\mathbf{f}_5(\mathbf{x})], Im[\mathbf{f}_5(\mathbf{x})]\}. \end{aligned} \tag{3.19}$$

As opposed to the finite-time Lyapunov subspaces $\mathcal{L}(T, \mathbf{x})$, which are approximations to invariant subspaces and whose accuracy increases with T, Floquet subspaces are theoretically Φ-invariant; when computed, there will be some numerical error. The applicability of Floquet theory to points on periodic orbits allows a quantitative accuracy assessment of the subspaces calculated via FTLA.

FTLA subspaces vs. Floquet subspaces for L_1 and L_3 orbits.

We present the case for points on several periodic orbits around L_1 and L_3. The periodic or-

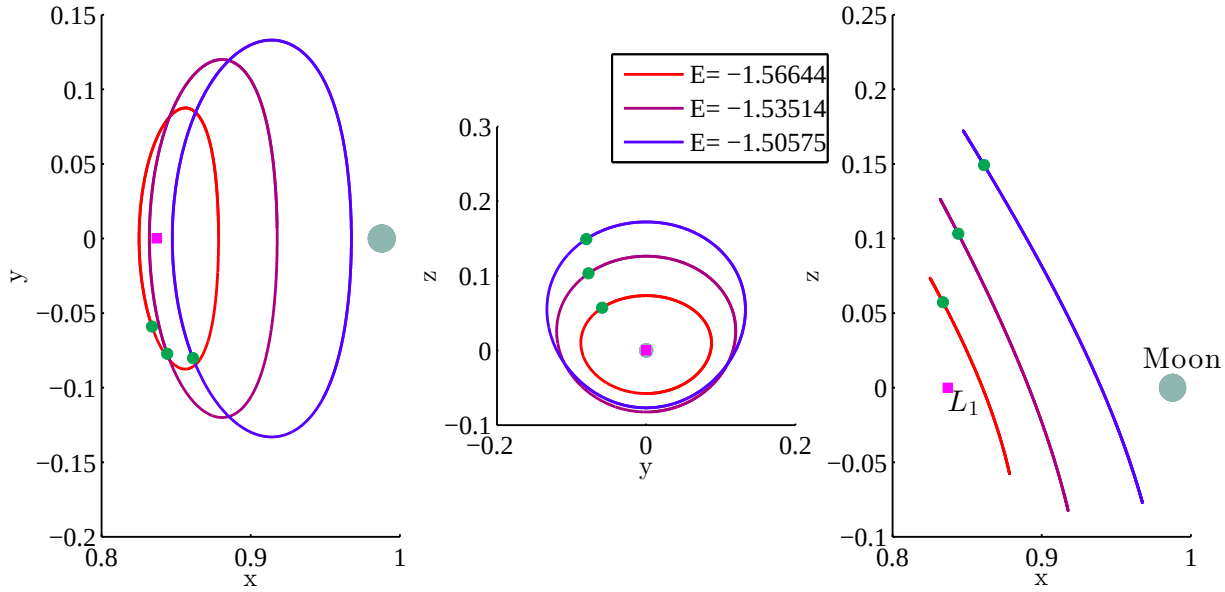

Figure 3.7: Spatial representation of Halo orbits around L_1: $\mathcal{O}_1$, $\mathcal{O}_2$, $\mathcal{O}_3$.

bits that we are going to analyze are grouped in three families: Halo orbits around L_1, Horizontal Lyapunov orbits around L_1, and Horizontal Lyapunov orbits around L_3. The spatial representation of the orbits are shown in Fig. 3.7, 3.8, and 3.9, while their characteristic parameters, such as type, specific energy E, and period T_p are reported in Table 3.1. The orbits have been computed using AUTO (12).

For each orbit $\mathcal{O}$, we choose a point $\mathbf{x}(\mathcal{O})$ on it and proceed to calculate the forward and backward FTLEs spectra for an interval $(0, \pm\overline{T}]$. Although we consider only one point per orbit, the FTLEs are uniform for all the points belonging to the same periodic orbit. The coordinates of the considered state points are shown in Table 3.2 and the values of the maximum averaging time $\overline{T}$, the start time t_s, the exponent gap $\Delta\mu(\mathbf{x})$, and the FTLA subspace convergence rate $\Delta\mu(\mathbf{x})(\overline{T} - t_s)$ are reported in Table 3.3. Figures 3.10, 3.11, and 3.12, show the forward and backward FTLE spectra for $\mathbf{x}_{\mathcal{O}_2}$, $\mathbf{x}_{\mathcal{O}_9}$, and $\mathbf{x}_{\mathcal{O}_9}$, respectively. The FTLEs for the remaining state points are shown in Fig. 3.13 and 3.14. For all the test cases, the forward and backward FTLEs spectra are divided into three subsets of dimension $n^s = 1$, $n^c = 4$, and $n^u = 1$, as previously anticipated.

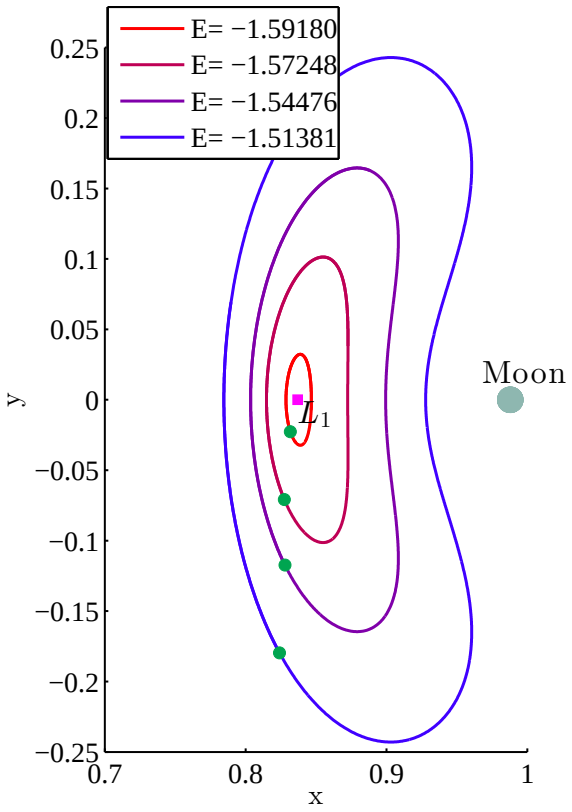

Figure 3.8: Spatial representation of Lyapunov Horizontal orbits around L_1: $\mathcal{O}_4$, $\mathcal{O}_5$, $\mathcal{O}_6$, $\mathcal{O}_7$.

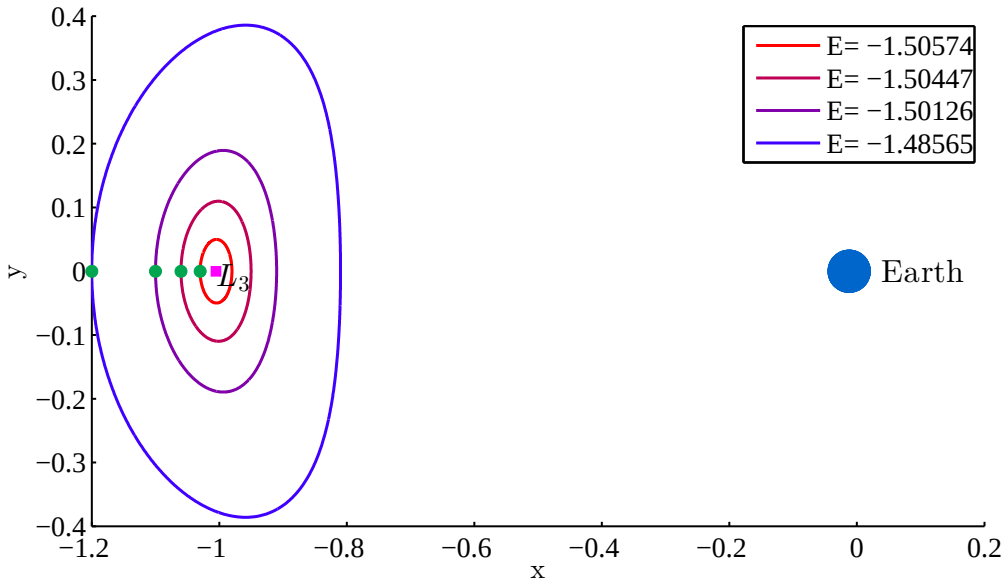

Figure 3.9: Spatial representation of Lyapunov Horizontal orbits around L_3: $\mathcal{O}_8$, $\mathcal{O}_9$, $\mathcal{O}_{10}$, $\mathcal{O}_{11}$.

Table 3.1: Periodic orbits around L_1 and L_3. For each orbit, the type, the specific energy, and the period are provided.

Orbit	Type	Lib. Point	Energy	Period-T_p
$\mathcal{O}_1$	Halo	L_1	-1.566441	2.772595
$\mathcal{O}_2$	Halo	L_1	-1.535143	2.782238
$\mathcal{O}_3$	Halo	L_1	-1.505751	2.594624
$\mathcal{O}_4$	Lyap. Horiz.	L_1	-1.593296	2.708469
$\mathcal{O}_5$	Lyap. Horiz.	L_1	-1.573706	2.868191
$\mathcal{O}_6$	Lyap. Horiz.	L_1	-1.545721	3.199118
$\mathcal{O}_7$	Lyap. Horiz.	L_1	-1.514429	3.854977
$\mathcal{O}_8$	Lyap. Horiz.	L_3	-1.505742	6.218416
$\mathcal{O}_9$	Lyap. Horiz.	L_3	-1.504466	6.218506
$\mathcal{O}_{10}$	Lyap. Horiz.	L_3	-1.501266	6.218730
$\mathcal{O}_{11}$	Lyap. Horiz.	L_3	-1.485648	6.219821

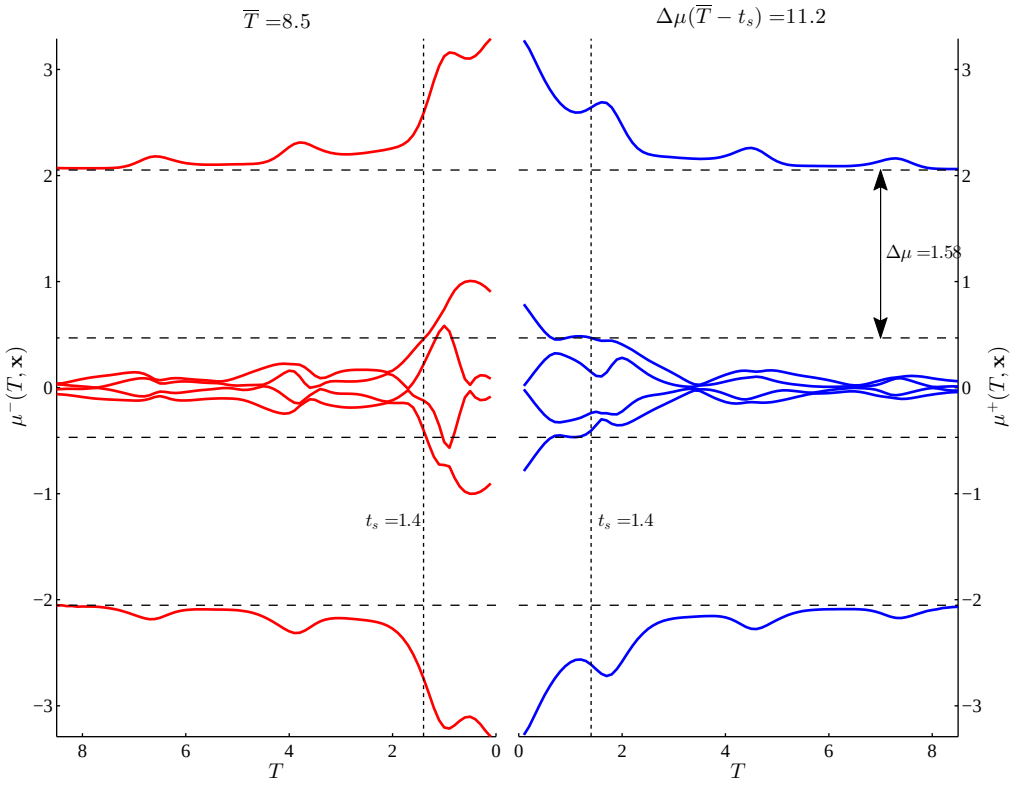

Figure 3.10: Finite-time Lyapunov exponents for $\mathbf{x}_{\mathcal{O}_2}$

Table 3.2: Coordinates of the points on the periodic orbits of Table 3.1.

Point	x	y	z
	v_x	v_y	v_z
$\mathbf{x}_{\mathcal{O}_1}$	$8.338337001 \cdot 10^{-1}$	$-7.725191617 \cdot 10^{-2}$	$5.724985963 \cdot 10^{-2}$
	$-4.687541907 \cdot 10^{-2}$	$1.385628934 \cdot 10^{-1}$	$9.013438369 \cdot 10^{-2}$
$\mathbf{x}_{\mathcal{O}_2}$	$8.440746578 \cdot 10^{-1}$	$-5.894828229 \cdot 10^{-2}$	$1.032428385 \cdot 10^{-2}$
	$-6.602693613 \cdot 10^{-2}$	$1.863195429 \cdot 10^{-1}$	$1.289161863 \cdot 10^{-1}$
$\mathbf{x}_{\mathcal{O}_3}$	$8.613174729 \cdot 10^{-1}$	$-8.020438943 \cdot 10^{-2}$	$1.492741754 \cdot 10^{-1}$
	$-8.312986278 \cdot 10^{-2}$	$2.143430550 \cdot 10^{-1}$	$1.391015775 \cdot 10^{-1}$
$\mathbf{x}_{\mathcal{O}_4}$	$8.317530684 \cdot 10^{-1}$	$-2.263443255 \cdot 10^{-2}$	$0.000000000 \cdot 10^{0}$
	$-1.709868103 \cdot 10^{-2}$	$5.287486568 \cdot 10^{-2}$	$0.000000000 \cdot 10^{0}$
$\mathbf{x}_{\mathcal{O}_5}$	$8.274870386 \cdot 10^{-1}$	$-7.086008362 \cdot 10^{-2}$	$0.000000000 \cdot 10^{0}$
	$-6.435743484 \cdot 10^{-2}$	$1.548004353 \cdot 10^{-1}$	$0.000000000 \cdot 10^{0}$
$\mathbf{x}_{\mathcal{O}_6}$	$8.278814484 \cdot 10^{-1}$	$-1.172621129 \cdot 10^{-1}$	$0.000000000 \cdot 10^{0}$
	$-1.094240742 \cdot 10^{-1}$	$2.225284771 \cdot 10^{-1}$	$0.000000000 \cdot 10^{0}$
$\mathbf{x}_{\mathcal{O}_7}$	$8.240826743 \cdot 10^{-1}$	$-1.797014005 \cdot 10^{-1}$	$0.000000000 \cdot 10^{0}$
	$-1.461510345 \cdot 10^{-1}$	$2.688061876 \cdot 10^{-1}$	$0.000000000 \cdot 10^{0}$
$\mathbf{x}_{\mathcal{O}_8}$	$-1.030000000 \cdot 10^{0}$	$0.000000000 \cdot 10^{0}$	$0.000000000 \cdot 10^{0}$
	$0.000000000 \cdot 10^{0}$	$5.009918840 \cdot 10^{-2}$	$0.000000000 \cdot 10^{0}$
$\mathbf{x}_{\mathcal{O}_9}$	$-1.060000000 \cdot 10^{0}$	$0.000000000 \cdot 10^{0}$	$0.000000000 \cdot 10^{0}$
	$0.000000000 \cdot 10^{0}$	$1.096065876 \cdot 10^{-1}$	$0.000000000 \cdot 10^{0}$
$\mathbf{x}_{\mathcal{O}_{10}}$	$-1.100000000 \cdot 10^{0}$	$0.000000000 \cdot 10^{0}$	$0.000000000 \cdot 10^{0}$
	$0.000000000 \cdot 10^{0}$	$1.877734070 \cdot 10^{-1}$	$0.000000000 \cdot 10^{0}$
$\mathbf{x}_{\mathcal{O}_{11}}$	$-1.200000000 \cdot 10^{0}$	$0.000000000 \cdot 10^{0}$	$0.000000000 \cdot 10^{0}$
	$0.000000000 \cdot 10^{0}$	$3.782441690 \cdot 10^{-1}$	$0.000000000 \cdot 10^{0}$

Table 3.3: Maximum averaging time $\overline{T}$, start time t_s, FTLEs gap $\Delta\mu(\mathbf{x})$, and subspaces rate of convergence $\Delta\mu(\mathbf{x})(\overline{T}-t_s)$ for the points listed in Table 3.2. The last column provides an estimate for the averaging time that is needed to get $\alpha^s = 10^{-5}$.

Point	$\overline{T}$	t_s	$\Delta\mu(\mathbf{x})$	$\Delta\mu(\mathbf{x})(\overline{T}-t_s)$	$T_{(\alpha^c=10^{-5})}$
$\mathbf{x}_{\mathcal{O}_1}$	7.0	1.4	2.14	11.9	6.0
$\mathbf{x}_{\mathcal{O}_2}$	8.5	1.4	1.58	11.2	7.5
$\mathbf{x}_{\mathcal{O}_3}$	13.0	3.0	0.81	8.1	13.0
$\mathbf{x}_{\mathcal{O}_4}$	6.0	1.4	2.59	11.9	5.0
$\mathbf{x}_{\mathcal{O}_5}$	7.0	1.4	2.04	11.9	6.0
$\mathbf{x}_{\mathcal{O}_6}$	8.5	1.5	1.44	10.1	7.0
$\mathbf{x}_{\mathcal{O}_7}$	10.5	2.6	0.96	7.6	10.5
$\mathbf{x}_{\mathcal{O}_8}$	90	12	0.16	12.3	80
$\mathbf{x}_{\mathcal{O}_9}$	90	12	0.15	12.0	80
$\mathbf{x}_{\mathcal{O}_{10}}$	90	12	0.16	12.3	80
$\mathbf{x}_{\mathcal{O}_{11}}$	90	12	0.15	11.9	80

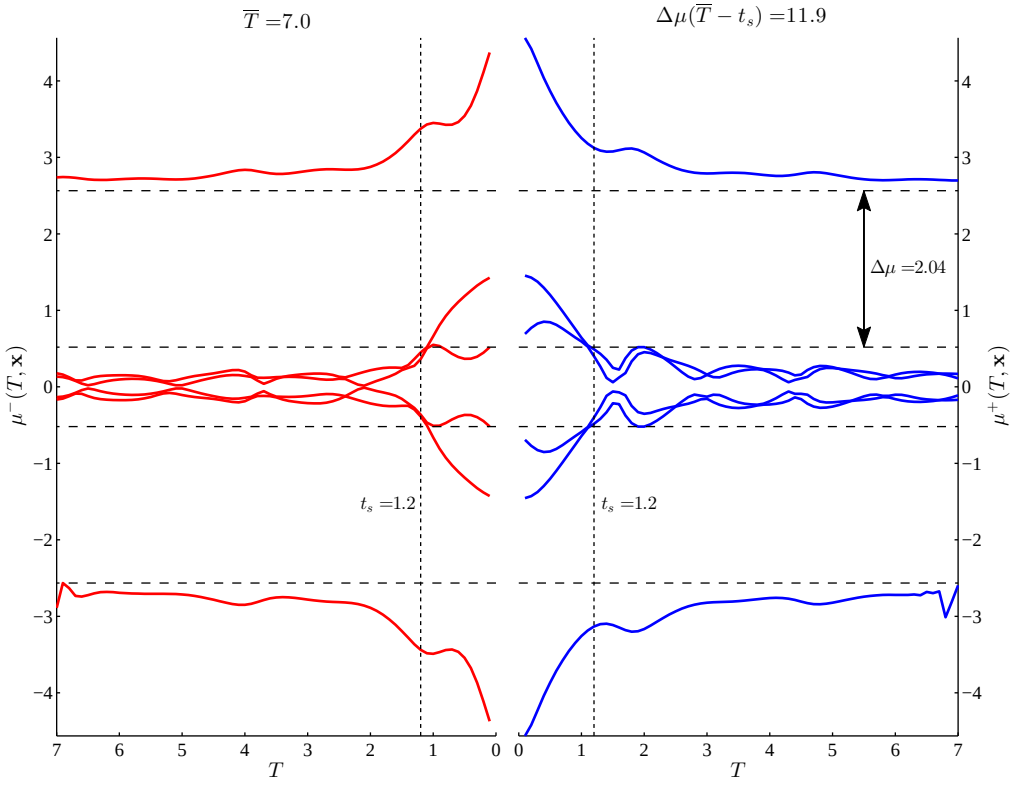

Figure 3.11: Finite-time Lyapunov exponents for $\mathbf{x}_{\mathcal{O}_5}$

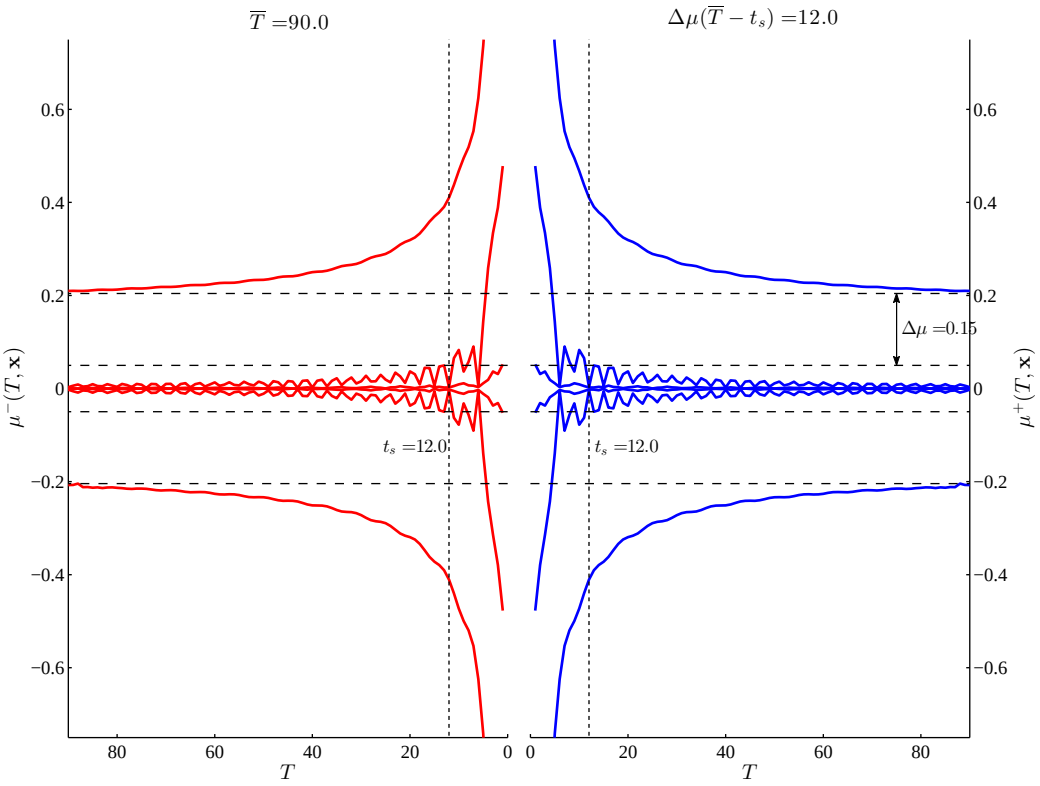

Figure 3.12: Finite-time Lyapunov exponents for $\mathbf{x}_{\mathcal{O}_9}$.

The FTLA subspaces (see Eq. (3.11)) are calculated for a range of averaging times T and are compared to the Floquet subspaces by computing the largest principal angles

$$\begin{aligned}
\alpha^s(T,\mathbf{x}) &= \angle\left(\mathcal{E}^s(T,\mathbf{x}),\mathcal{F}^s(\mathbf{x})\right), \\
\alpha^c(T,\mathbf{x}) &= \angle\left(\mathcal{E}^c(T,\mathbf{x}),\mathcal{F}^c(\mathbf{x})\right), \\
\alpha^u(T,\mathbf{x}) &= \angle\left(\mathcal{E}^u(T,\mathbf{x}),\mathcal{F}^u(\mathbf{x})\right),
\end{aligned} \tag{3.20}$$

between stable, center, and unstable subspaces. Figures 3.15, 3.16, 3.17, 3.18, and 3.19 show the value for these angles. As the averaging time T for FTLA increases, the angles between the Floquet and FTLA subspaces decrease at the expected exponential rates, showing that the FTLA subspaces accurately approximate the invariant subspaces for sufficiently large T. In general, points on different orbits have a different FTLE gap $\Delta\mu$ associated with them, therefore, in order to achieve a similar degree of accuracy (i.e., the value of the α angles), the FTLA subspaces must be computed using appropriate averaging times. As an example, we report in the last column of Table 3.3 the approximate values of the averaging times that are needed to reach $\alpha^c = 10^{-5}$. Note that points on orbits around L_3 have spectral gaps $\Delta\mu$ that are one order of magnitude smaller than the gaps associated with orbits around L_1. Thus, to obtain a similar value for $\alpha^c = 10^{-5}$, one needs to use for L_3 orbits, averaging times that are one order of magnitude greater than the ones relative to points on L_1 orbits. Note that the plots associated with the points on the L_3-orbits seem to have only two lines. In fact, the trends for α^s and α^u coincide, thus the green and the red lines are indistinguishable from one another. The reason is because the selected points lie on the $x - v_y$ plane, which is a plane of symmetry for the orbits. Therefore, the forward and backward trajectories are symmetrical and so are the directions of $\mathcal{E}^s(T,\mathbf{x})$ and $\mathcal{E}^u(T,\mathbf{x})$.

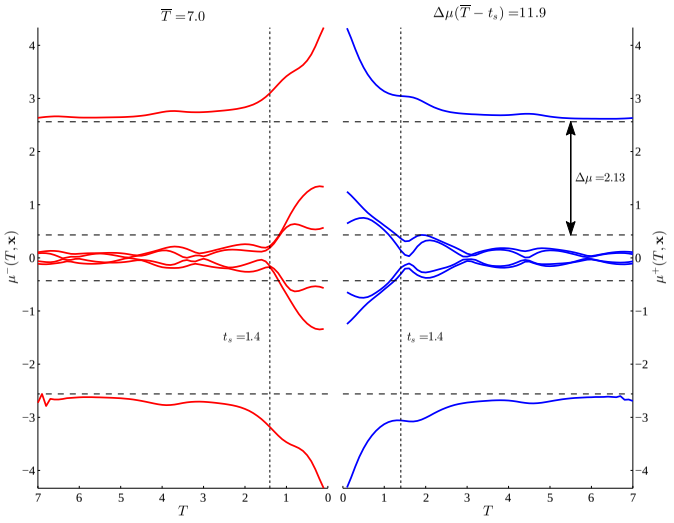

(a) Finite-time Lyapunov exponents for $\mathbf{x}_{\mathcal{O}_1}$

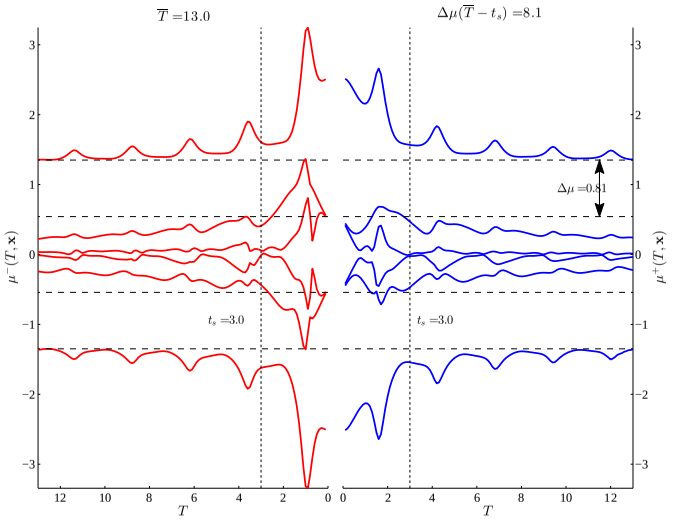

(b) Finite-time Lyapunov exponents for $\mathbf{x}_{\mathcal{O}_3}$

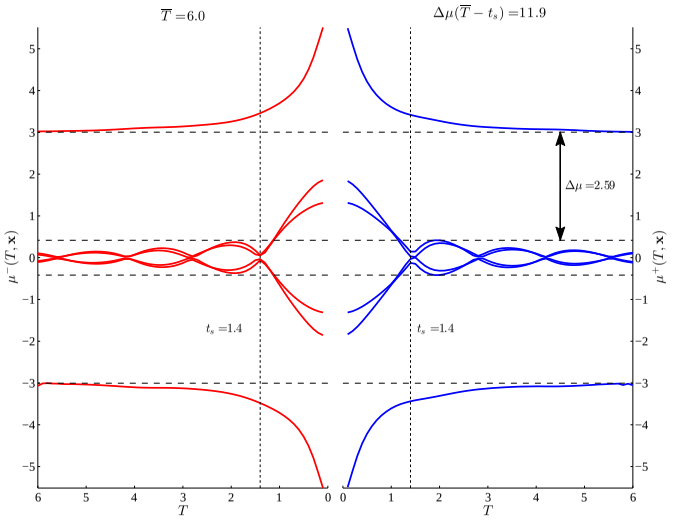

(c) Finite-time Lyapunov exponents for $\mathbf{x}_{\mathcal{O}_4}$

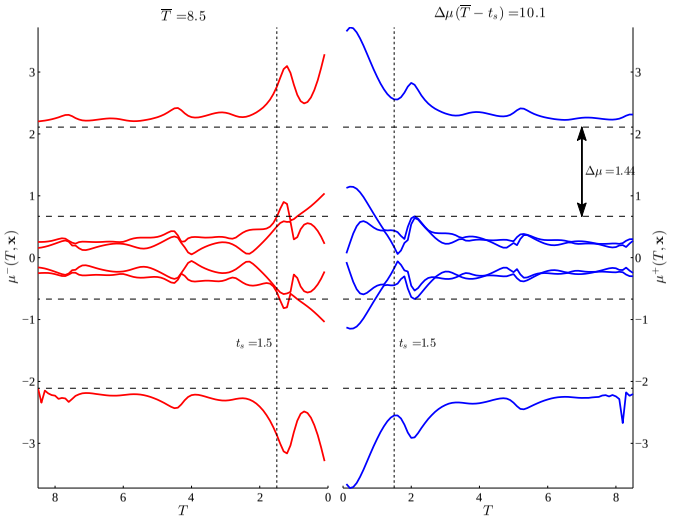

(d) Finite-time Lyapunov exponents for $\mathbf{x}_{\mathcal{O}_6}$

Figure 3.13: Finite-time Lyapunov exponents for $\mathbf{x}_{\mathcal{O}_1}$ (a), $\mathbf{x}_{\mathcal{O}_3}$ (b), $\mathbf{x}_{\mathcal{O}_4}$ (c), and $\mathbf{x}_{\mathcal{O}_6}$ (d).

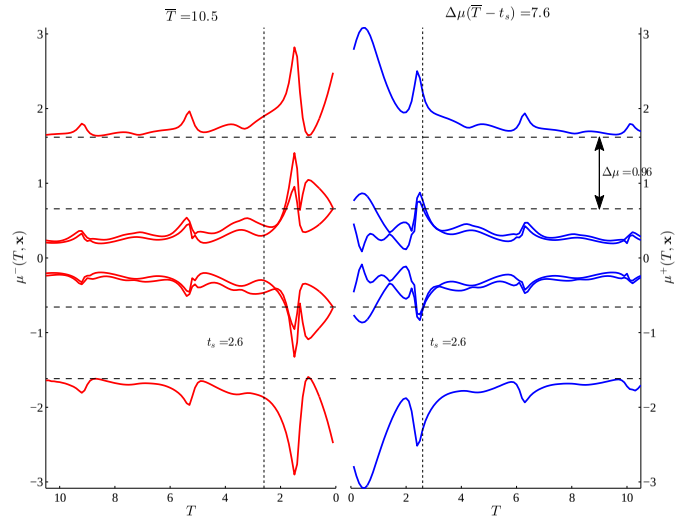

(a) Finite-time Lyapunov exponents for $\mathbf{x}_{\mathcal{O}_7}$

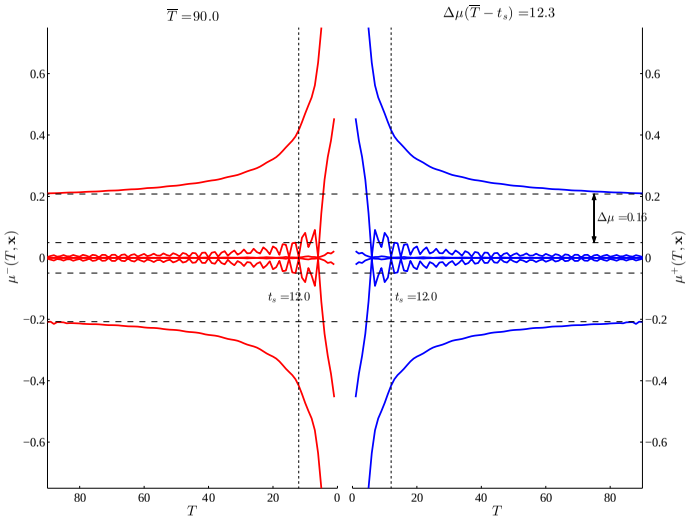

(b) Finite-time Lyapunov exponents for $\mathbf{x}_{\mathcal{O}_8}$

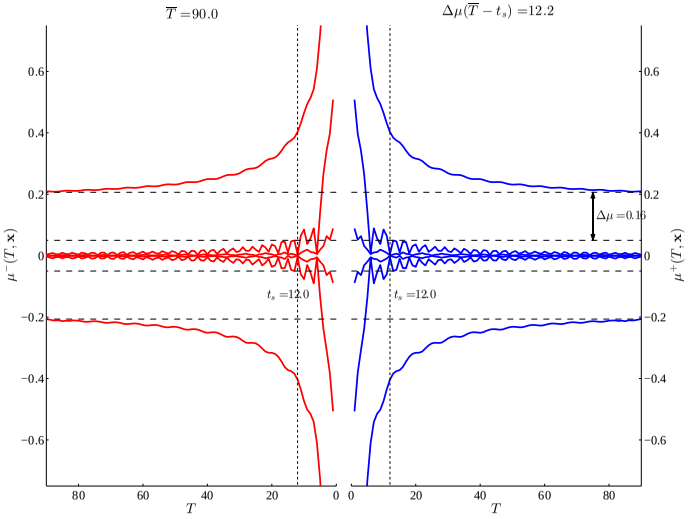

(c) Finite-time Lyapunov exponents for $\mathbf{x}_{\mathcal{O}_{10}}$

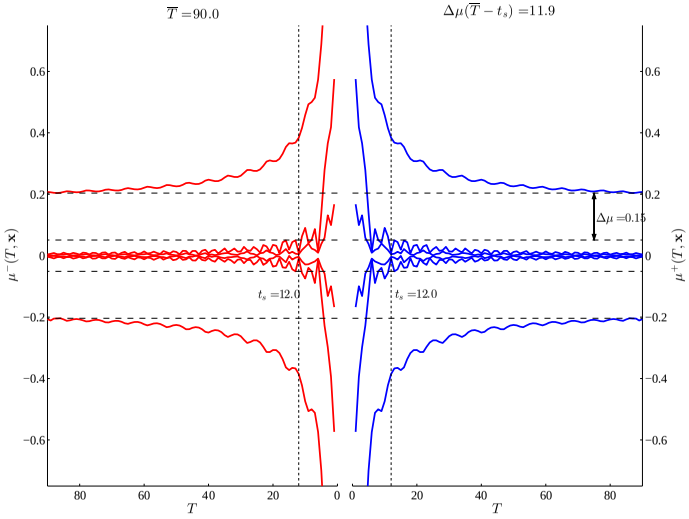

(d) Finite-time Lyapunov exponents for $\mathbf{x}_{\mathcal{O}_{11}}$

Figure 3.14: Finite-time Lyapunov exponents for $\mathbf{x}_{\mathcal{O}_7}$ (a), $\mathbf{x}_{\mathcal{O}_8}$ (b), $\mathbf{x}_{\mathcal{O}_{10}}$ (c), and $\mathbf{x}_{\mathcal{O}_{11}}$ (d).

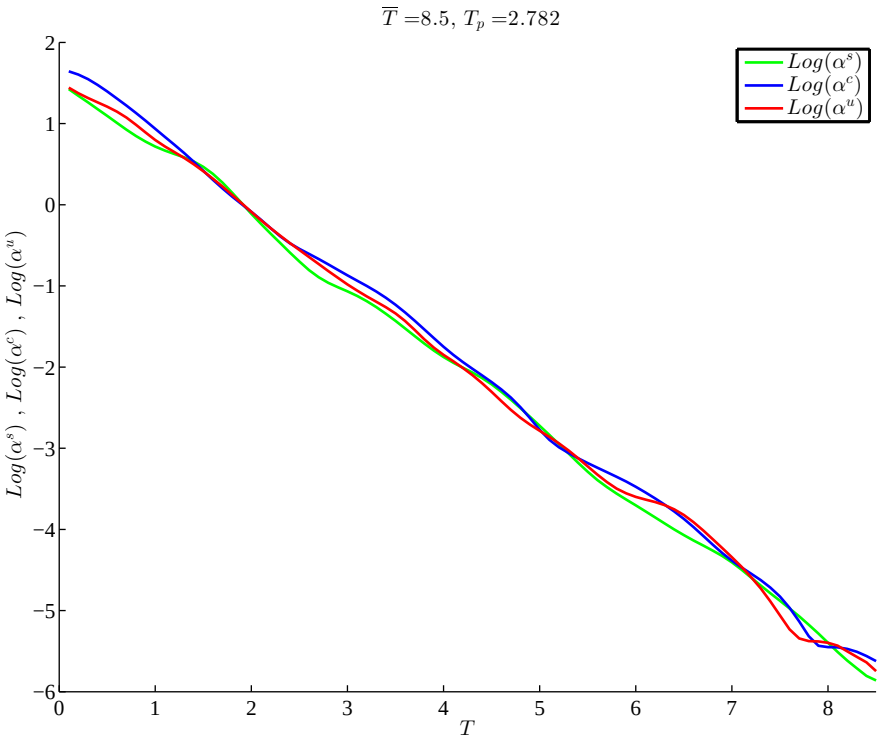

Figure 3.15: Base-10 logarithm of the angles between Floquet and FTLA subspaces at increasing averaging times T for $\mathbf{x}_{\mathcal{O}_2}$.

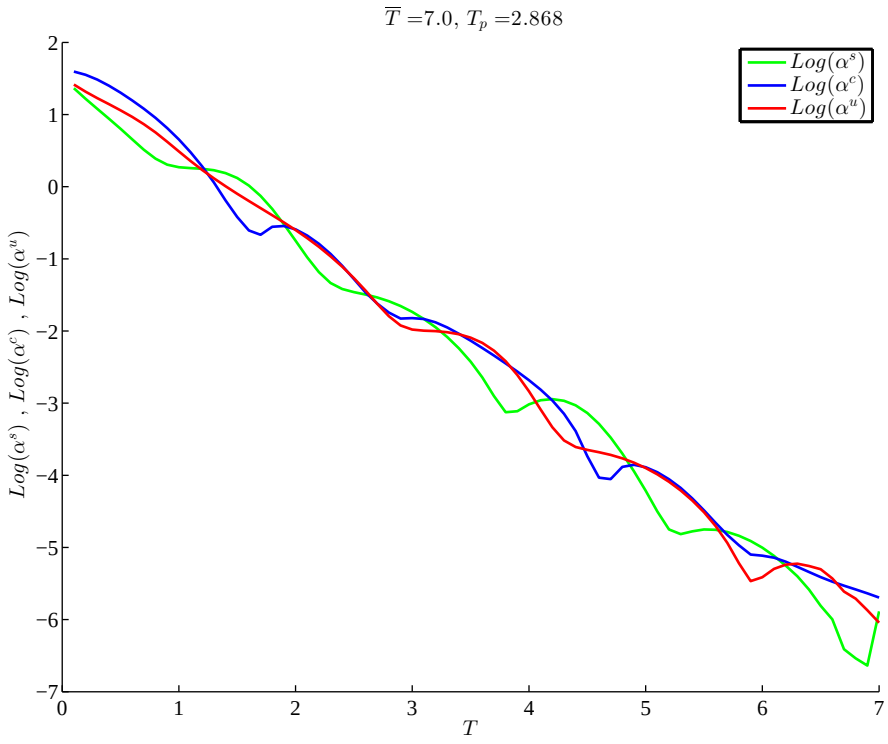

Figure 3.16: Base-10 logarithm of the angles between Floquet and FTLA subspaces at increasing averaging times T for $\mathbf{x}_{\mathcal{O}_5}$.

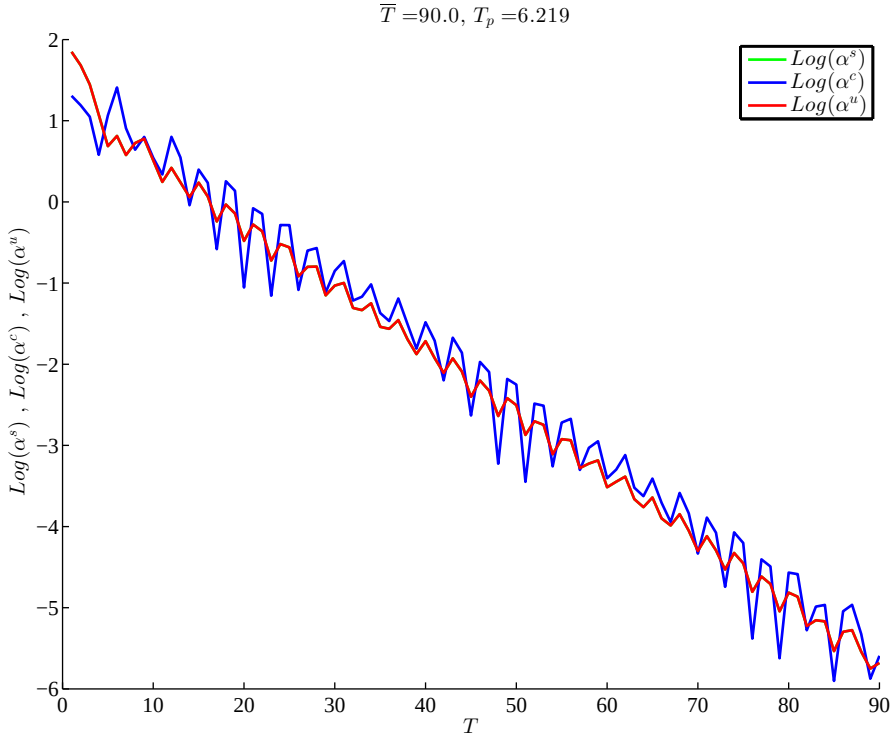

Figure 3.17: Base-10 logarithm of the angles between Floquet and FTLA subspaces at increasing averaging times T for $\mathbf{x}_{\mathcal{O}_9}$. The values of α^s (green line) and α^u (red line) coincide, thus their values appear indistinguishable. The reason for this behavior is due to the symmetry of the Lyapunov Horizontal orbits and to the fact that $\mathbf{x}_{\mathcal{O}_9}$ lies on the $x - v_y$ plane.

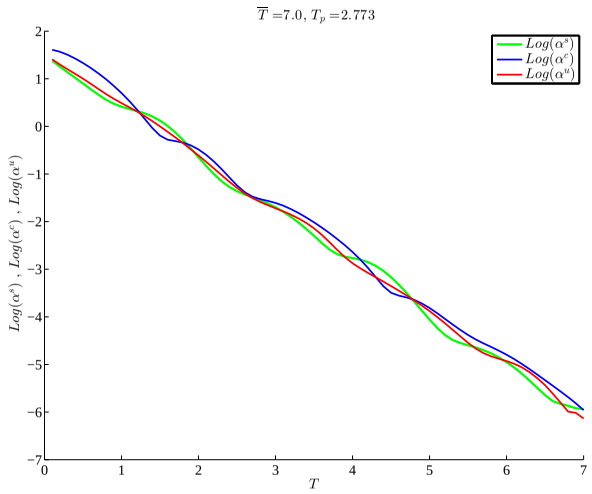

(a) α-angles for $\mathbf{x}_{\mathcal{O}_1}$

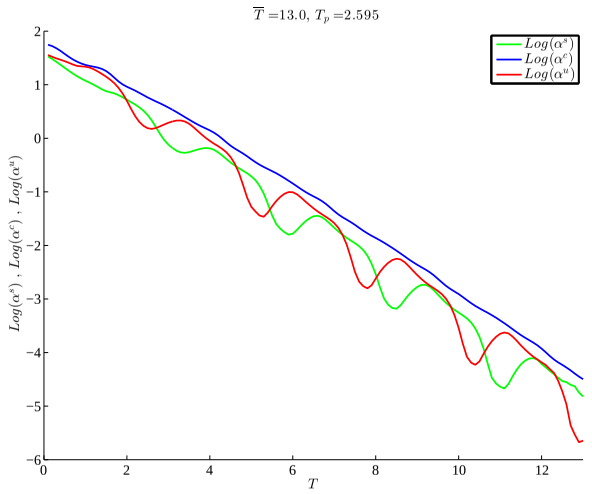

(b) α-angles for $\mathbf{x}_{\mathcal{O}_3}$

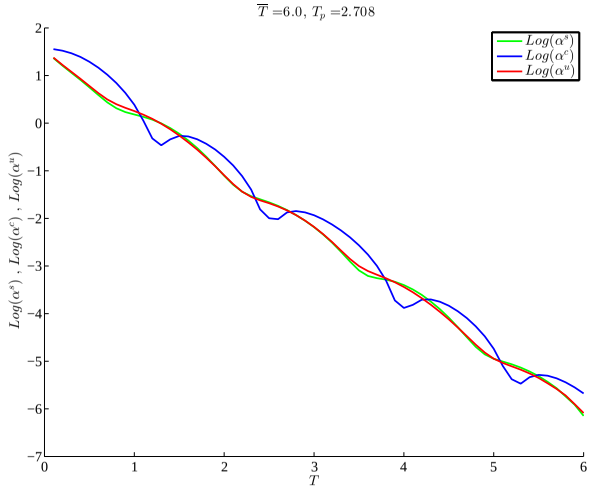

(c) α-angles for $\mathbf{x}_{\mathcal{O}_4}$

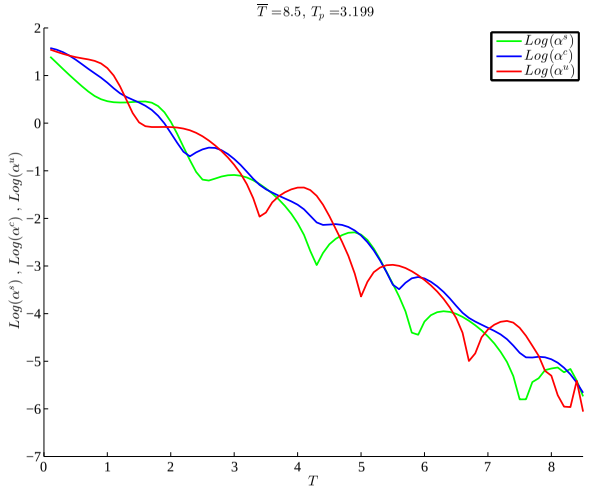

(d) α-angles for $\mathbf{x}_{\mathcal{O}_6}$

Figure 3.18: Base-10 logarithm of the angles between Floquet and FTLA subspaces at increasing averaging times T for $\mathbf{x}_{\mathcal{O}_1}$ (a), $\mathbf{x}_{\mathcal{O}_3}$ (b), $\mathbf{x}_{\mathcal{O}_4}$ (c), and $\mathbf{x}_{\mathcal{O}_6}$ (d).

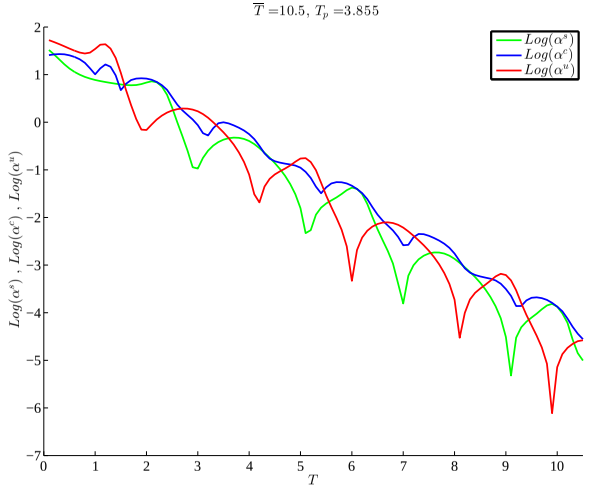

(a) α-angles for $\mathbf{x}_{\mathcal{O}_7}$

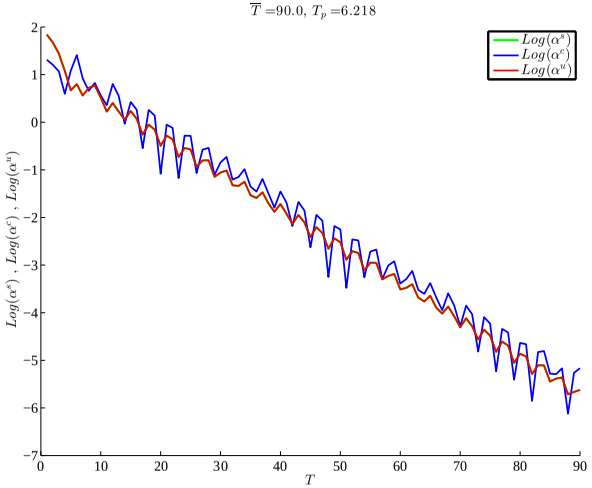

(b) α-angles for $\mathbf{x}_{\mathcal{O}_8}$

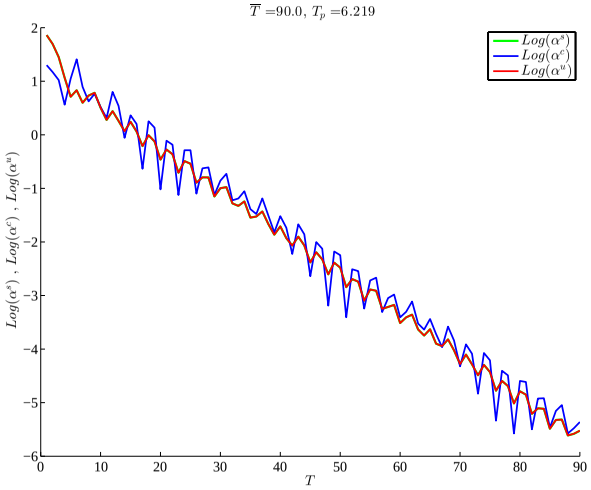

(c) α-angles for $\mathbf{x}_{\mathcal{O}_{10}}$

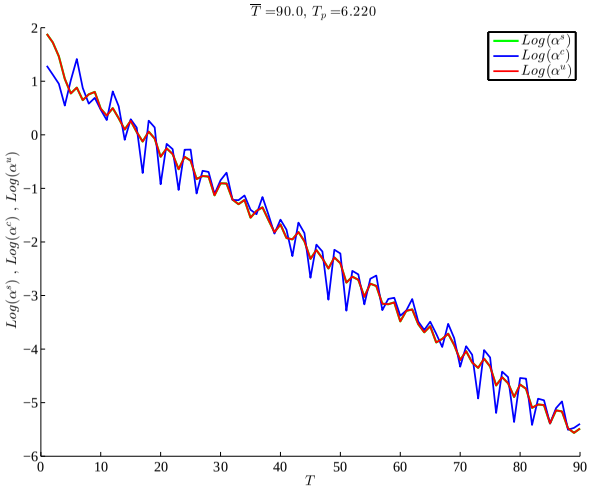

(d) α-angles for $\mathbf{x}_{\mathcal{O}_{11}}$

Figure 3.19: Base-10 logarithm of the angles between Floquet and FTLA subspaces at increasing averaging times T for $\mathbf{x}_{\mathcal{O}_7}$ (a), $\mathbf{x}_{\mathcal{O}_8}$ (b), $\mathbf{x}_{\mathcal{O}_{10}}$ (c), and $\mathbf{x}_{\mathcal{O}_{11}}$ (d). In subplots (b), (c), and (d) the values of α^s and α^u coincide, thus only 2 lines are clearly distinguishable.

3.3.2 Points on quasiperiodic orbits

EFA subspaces vs. FTLA subspaces

When considering points on aperiodic orbits, Floquet theory is in principle not applicable. Nevertheless, stationkeeping methods, such as the method which is based on the cancellation of the unstable component of the error vector proposed by (24), utilize vectors calculated in a similar fashion to Floquet vectors. We refer to such vectors as Extended Floquet Modes and to the methodology as Extended Floquet Analysis (EFA). In EFA, the monodromy matrix is substituted by $\tilde{M}(\mathbf{x}) = \Phi(T_r, \mathbf{x})$, where the revolution time T_r is the time associated with a first-return map and replaces the period. The EFA subspaces are denoted with $\tilde{\mathcal{F}}(T_r, \mathbf{x})$ and are computed in a similar fashion to (3.20), using the eigenvalues and the eigenvectors $\tilde{\mathbf{f}}_i(T_r, \mathbf{x})$ of $\tilde{M}(\mathbf{x})$. We use the '$\sim$' symbol to indicate that the subspaces only approximate the sought-after invariant subspaces.

$$\begin{aligned}
\tilde{\mathcal{F}}^s(T_r, \mathbf{x}) &= span\{\tilde{\mathbf{f}}_2(T_r, \mathbf{x})\}, \\
\tilde{\mathcal{F}}^u(T_r, \mathbf{x}) &= span\{\tilde{\mathbf{f}}_1(T_r, \mathbf{x})\}, \\
\tilde{\mathcal{F}}^c(T_r, \mathbf{x}) &= span\{\tilde{\mathbf{f}}_3(T_r, \mathbf{x}), \tilde{\mathbf{f}}_4(T_r, \mathbf{x}), Re[\tilde{\mathbf{f}}_5(T_r, \mathbf{x})], Im[\tilde{\mathbf{f}}_5(T_r, \mathbf{x})]\}.
\end{aligned} \tag{3.21}$$

For points on periodic orbits, EFA coincides with Floquet theory and is therefore exact, to the accuracy of the numerics; as demonstrated in the last section, FTLA can be viewed as an alternative and as reliable method to computing the subspaces, provided that the product $\Delta\mu(\mathbf{x})(\overline{T} - t_s)$ is large enough. For points on quasiperiodic orbits, the approximations obtained through EFA are not always accurate. Their accuracy is shown to depend on the following properties:

1. *The degree of recurrence of the orbit, δ.*

   We define the degree of recurrence of an orbit, calculated at a point $\mathbf{x}$, as the distance $\delta(\mathbf{x}) = ||\mathbf{x} - \phi(T_r, \mathbf{x})||$ between $\mathbf{x}$ and the point at which the orbit first returns to a particular Poincaré

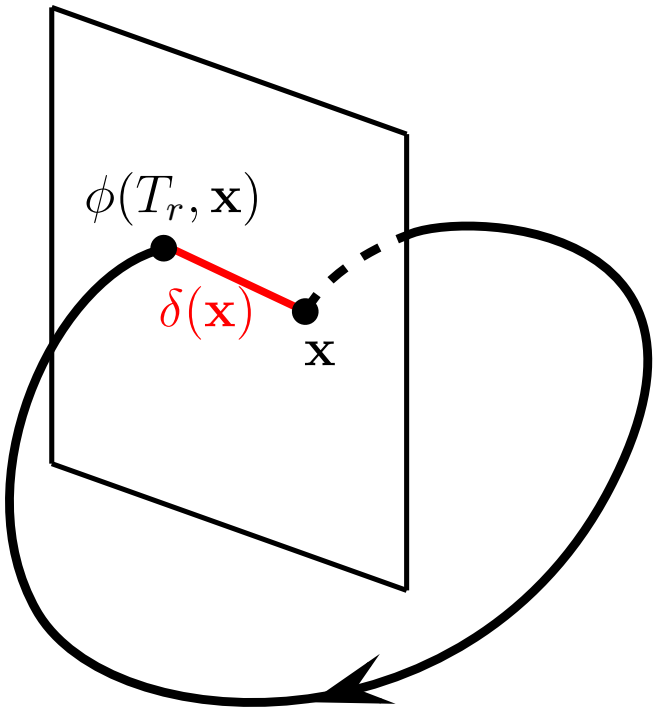

Figure 3.20: Degree of recurrence $\delta(\mathbf{x})$.

section, as shown in Fig. 3.20. Among the infinite number of Poincaré sections that can be selected, at each $\mathbf{x}$, we choose a section normal to $\mathbf{f}(\mathbf{x})$. T_r is the first-return time and it coincides with the period T_p if $\delta = 0$. As soon as $\delta > 0$, Floquet theory does not apply anymore and we will show that, the accuracy of the EFA subspaces decreases as δ increases.

2. *The direction of integration for calculating the EFA subspaces.*

   For periodic orbits, we have that $\phi(+T_p, \mathbf{x}) = \phi(-T_p, \mathbf{x}) = \mathbf{x}$, so the monodromy matrix provides consistent information in terms of eigenvalues and eigenvectors whether it is calculated forward or backward in time. Thus, the computation of the Floquet subspaces is not affected by the direction of integration. For aperiodic orbits, instead, the direction of integration becomes fundamental. In fact, one should define different δ and T_r whether the evolution of the orbit is taken forward or backward in time; as a result, we have two pairs of degree of recurrence-revolution time (δ^+, T_r^+) and (δ^-, T_r^-). δ^+, δ^-, T_r^+, T_r^- are all positive

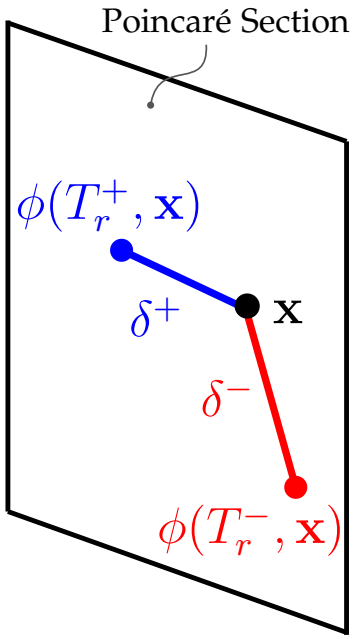

Figure 3.21: Poincaré section with initial point $\mathbf{x}$, forward $\phi(+T_r^+, \mathbf{x})$ and backward $\phi(+T_r^+, \mathbf{x})$ phase points, and corresponding degrees of recurrence δ^+ and δ^-. For clarity of representation, the forward and backward trajectories departing from $\mathbf{x}$ are not shown.

quantities. In general, the phase points that are reached forward and backward in time are different from each other and do not coincide with the initial point $\mathbf{x}$ as illustrated in Fig. 3.21.

$$\begin{aligned} &\phi(+T_r^+, \mathbf{x}) \neq \phi(-T_r^-, \mathbf{x}) \\ &\phi(+T_r^+, \mathbf{x}) \neq \mathbf{x}, \\ &\phi(-T_r^-, \mathbf{x}) \neq \mathbf{x}. \end{aligned} \tag{3.22}$$

The backward and forward state transition matrices, (resp. $\tilde{M}^+(\mathbf{x}) = \Phi(T_r^+, \mathbf{x})$ and $\tilde{M}^-(\mathbf{x}) = \Phi(-T_r^-, \mathbf{x})$) have different eigenvalues and eigenvectors due to the different time direction (which inverts the multipliers and changes the signs of the real parts of the eigenvalues) and due to lack of periodicity. This implies that, at any point $\mathbf{x}$ on an aperiodic orbit, the EFA

subspaces computed using the eigenvectors of $\tilde{M}^+$ (i.e., $\tilde{\mathcal{F}}^+$) differ from the ones computed from $\tilde{M}^-$ (i.e., $\tilde{\mathcal{F}}^-$). In particular, we will demonstrate that the most accurate EFA subspaces make use of the eigenvectors of both $\tilde{M}^+$ and $\tilde{M}^-$ and are computed following a FTLA-like procedure as shown in (3.11), where the forward and backward FTLVs (i.e., $\mathrm{l}^{\pm}$) are substituted with the eigenvectors of $\tilde{M}^{\pm}$ (i.e., $\tilde{\mathbf{f}}^{\pm}$). When considering both the forward and backward integrations, the EFA subspaces in Eq. (3.21) become

$$\begin{aligned}
\tilde{\mathcal{F}}^{s\pm}(T_r^{\pm}, \mathbf{x}) &= span\{\tilde{\mathbf{f}}_2^{\pm}(T_r^{\pm}, \mathbf{x})\}, \\
\tilde{\mathcal{F}}^{u\pm}(T_r^{\pm}, \mathbf{x}) &= span\{\tilde{\mathbf{f}}_1^{\pm}(T_r^{\pm}, \mathbf{x})\}, \\
\tilde{\mathcal{F}}^{c\pm}(T_r^{\pm}, \mathbf{x}) &= span\{\tilde{\mathbf{f}}_3^{\pm}(T_r^{\pm}, \mathbf{x}), \tilde{\mathbf{f}}_4^{\pm}(T_r^{\pm}, \mathbf{x}), Re[\tilde{\mathbf{f}}_5^{\pm}(T_r^{\pm}, \mathbf{x})], Im[\tilde{\mathbf{f}}_5^{\pm}(T_r^{\pm}, \mathbf{x})]\}.
\end{aligned} \tag{3.23}$$

where the '$\pm$' sign specifies the integration direction.

3. *The rate of convergence of subspaces at a point on the orbit.*

   Inspired by the concept of Lyapunov subspace convergence presented in 3.2.1, let us consider the product between the spectral gap and the revolution time $K = \Delta\mu(\mathbf{x})T_r$. The larger K is, the faster the EFA subspaces converge to their invariant counterparts, and therefore the accuracy of the results is higher. In practice, we utilize FTLA subspaces to judge the accuracy of EFA subspaces, on the assumptions that the FTLA subspaces have significantly converged to the invariant Lyapunov subspaces and that the EFA subspaces are computed similarly to the FTLA subspaces, namely the appropriate eigenvectors of $\tilde{M}^{\pm}(\mathbf{x})$ are used, as in Eq. (3.11).

To illustrate the effect of the listed properties, let us consider several points on quasiperiodic orbits about both L_1 and L_3. At each point $\mathbf{x}$ we calculate the FTLA and EFA approximations of the stable subspaces. The EFA stable subspaces are computed using the eigenvectors of $\tilde{M}^+$, namely $\tilde{\mathcal{F}}^{s+} = span\{\tilde{\mathbf{f}}_{\mathbf{2}}^+\}$. As a means of assessing the accuracy of the EFA approximations, we compute

the angle $\tilde{\alpha}^{s+} = \angle(\tilde{\mathcal{F}}^{s+}(T_r^+, \mathbf{x}), \mathcal{E}^s(\overline{T}, \mathbf{x}))$, assuming that the FTLA subspaces have converged enough to their invariant counterparts. Figure 3.22 shows how $\tilde{\alpha}^{s+}$ varies as a function of δ^+ (see Property 1) and K (see Property 3). Each point on the plot represents the angle between subspaces at a different point on a quasiperiodic orbit. The colored plane linearly interpolates the results and shows that the angles, and thus the accuracy of the EFA approximations, decrease with increasing values of K and decreasing values of δ^+. In other words, the EFA subspaces are more accurate for points on orbits that are closer to being periodic and/or have larger spectral gap and revolution times associated with them. Moreover, given a similar degree of recurrence (i.e., δ), the angles for points on orbits about L_1 are generally smaller than the ones referring to points on orbits about L_3. This is due to the characteristic rate of convergence associated with the libration points themselves. In fact, at libration points, the rate of convergence of the subspaces can be approximated with $K \simeq K_L = \|\lambda_{max}(L)\| T_{p_L}$, where $\|\lambda_{max}(L)\|$ and T_{p_L} are the maximum eigenvalue and the characteristic period of L, respectively. As can be seen from Fig. 3.23, $K_{L_1} > K_{L_2} > K_{L_3}$, for values of the gravitational parameter $\mu_G < 0.04$. In particular, for the Earth-Moon system ($\mu_G = 0.01215$), we have $K_{L_1} \approx 8$ and $K_{L_3} \approx 1$, which translates into orbits around L_1 having a greater rate of convergence with respect to orbits around L_3 with a similar degree of recurrence.

Φ-subspaces vs. FTLA subspaces

Once the degree of recurrence δ ceases to be zero, the EFA subspaces are accurate enough only if they are computed following a FTLA-like approach. In particular, as soon as $\delta > 0$, the revolution time T_r ceases to have the fundamental role that the period T_p has in Floquet theory. In fact, the revolution time is only relevant in forming the product $K = \Delta\mu(\mathbf{x})T_r$, which is the key factor to subspace convergence. As a matter of fact, when dealing with points on aperiodic orbits, one could simply abandon the concept of EFA and simply calculate the subspaces directly from the state transition matrices $\Phi(\pm T, \mathbf{x})$, where the revolution time is substituted with the averaging time

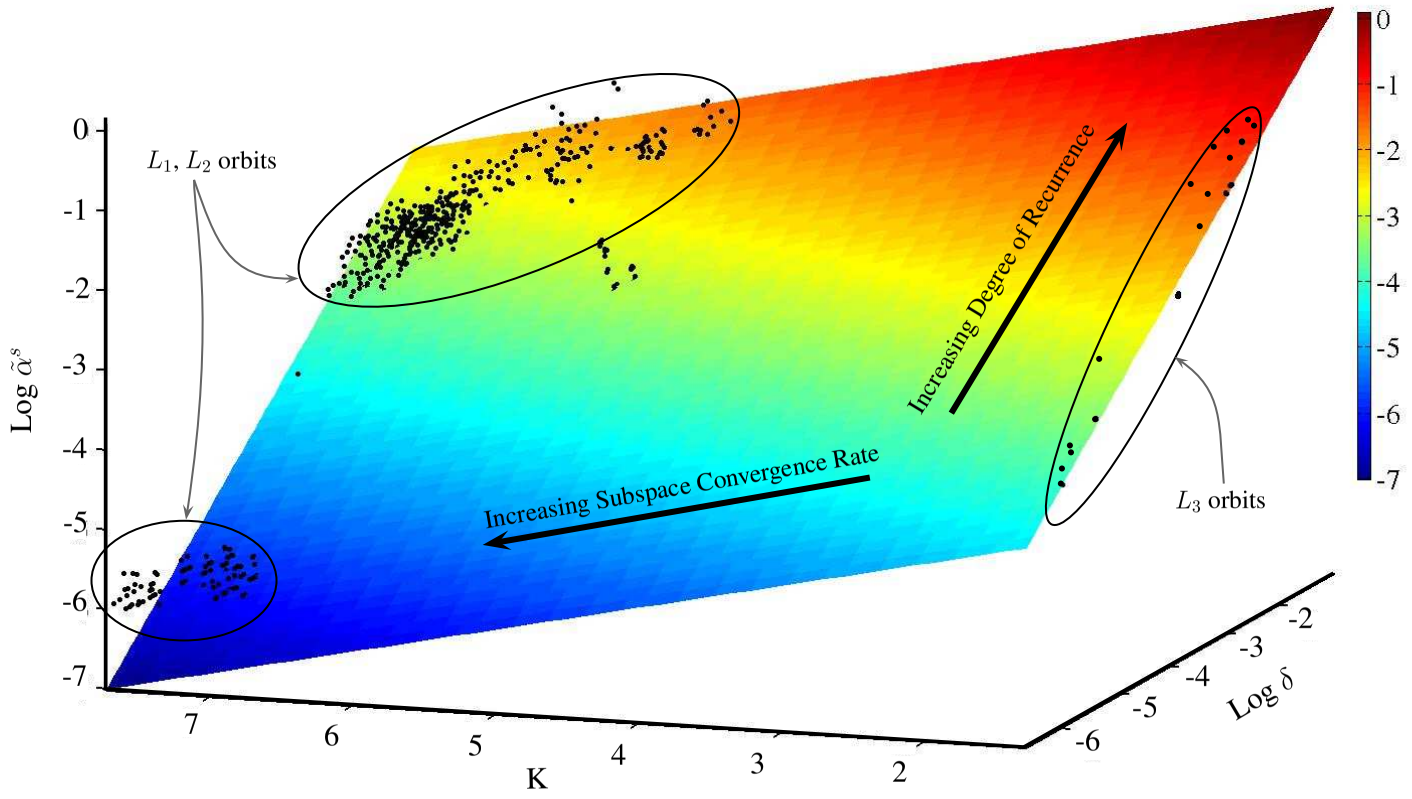

Figure 3.22: Logarithm in base 10 of the angle between stable subspaces computed with FTLA and EFA at points on orbits around L_1 and L_3. EFA produces more precise results when considering points on nearly-periodic orbits (NPO) with respect to points on quasiperiodic orbits (QPO). The angles are generally lower for points on orbits around L_1 because of a bigger subspace convergence rates associated with such orbits.

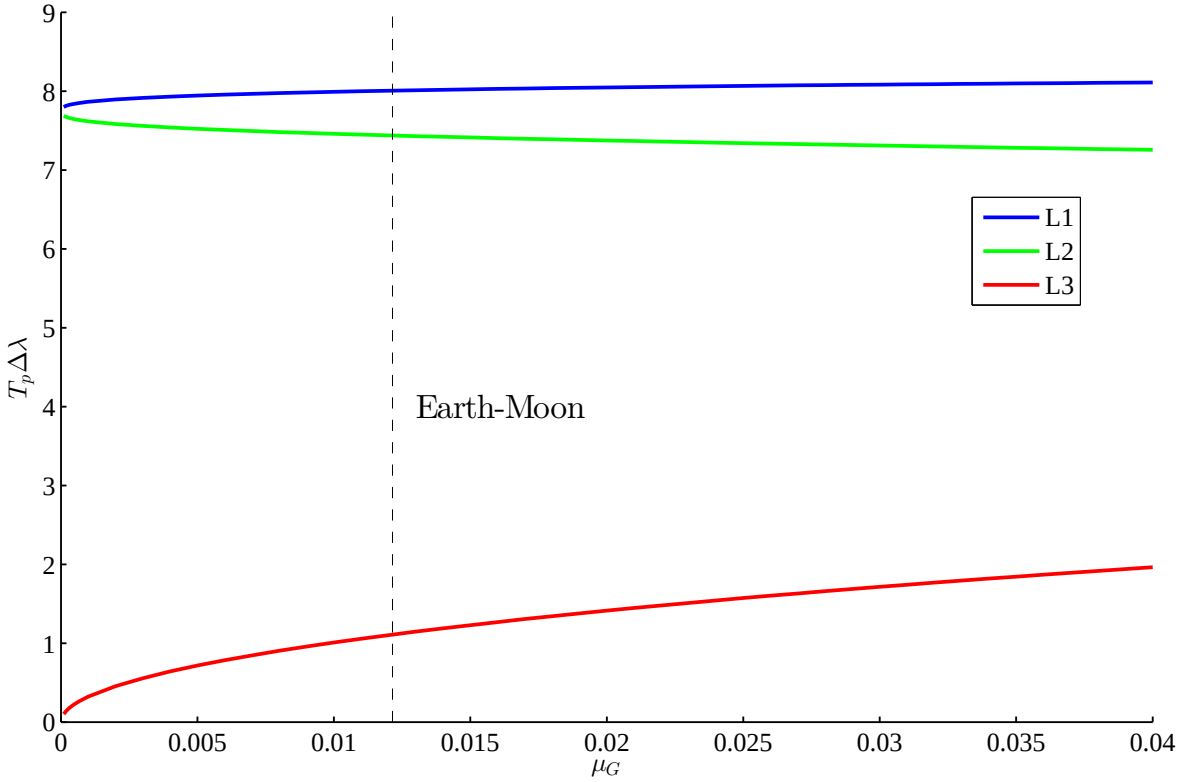

Figure 3.23: Characteristic rate of subspace convergence of libration collinear points for gravitational parameter values $\mu_G < 0.04$.

T, which has to be chosen, combined with the gap in the exponents, to provide enough subspace convergence. In particular, T need not be equal or even similar to T_r. We indicate the Φ-subspaces with $\mathcal{P}$ (for 'Phi') and we define them in a similar fashion to the EFA subspaces in Eq. (3.23)

$$\begin{aligned}
\mathcal{P}^{s\pm}(T,\mathbf{x}) &= span\{\mathbf{p}_2^{\pm}(T,\mathbf{x})\},\\
\mathcal{P}^{u\pm}(T,\mathbf{x}) &= span\{\mathbf{p}_1^{\pm}(T,\mathbf{x})\},\\
\mathcal{P}^{c\pm}(T,\mathbf{x}) &= span\{\mathbf{p}_3^{\pm}(T,\mathbf{x}), \mathbf{p}_4^{\pm}(T,\mathbf{x}), Re[\mathbf{p}_5^{\pm}(T,\mathbf{x})], Im[\mathbf{p}_5^{\pm}(T,\mathbf{x})]\}.
\end{aligned} \tag{3.24}$$

where $\mathbf{p}^{\pm}$ are the eigenvectors of $\Phi(\pm T,\mathbf{x})$. Notice that, for $T = T_r^{\pm}$ the Φ-subspaces coincide with the EFA ones. The Φ-subspaces can be seen as equivalent to the FTLA subspaces, with the major difference that the former ones are computed using the eigenvectors $\Phi(\pm T,\mathbf{x})$, while the latter ones make use of the eigenvectors of $\Phi(\pm T,\mathbf{x})^T\Phi(\pm T,\mathbf{x})$, or of $\Phi(\pm T,\mathbf{x})\Phi(\pm T,\mathbf{x})^T$. We will demonstrate that, under certain circumstances, both the approaches lead to numerically similar results. While there is a solid theoretical justification for using FTLA, this cannot be stated so far when it comes to considering the eigenspaces of Φ. Moreover, even when the two approaches lead to equivalent results, working with the orthogonal matrices (i.e., $\Phi(\pm T,\mathbf{x})^T\Phi(\pm T,\mathbf{x})$)could be numerically advantageous. In this subsection we will stick to showing the numerical results given by the two methods without trying to justify the theoretical correctness of the Φ-eigenvectors subspaces.

We will now compare the Φ-subspaces with the FTLA ones. The comparison is carried out as follows: we consider points on some quasiperiodic orbits around L_1 and L_3. At such points we compute the FTLEs, extract the gap information and determine a maximum averaging time $\overline{T}$ so that $\mu(\mathbf{x})\overline{T}$ is large enough to satisfy the subspace convergence condition. We then form the FTLA subspaces $\mathcal{E}(T,\mathbf{x})$ and the Φ-subspaces $\mathcal{P}^{\pm}(T,\mathbf{x})$ for $T \in (0,\overline{T}]$. From previous analysis on periodic orbits, we consider $\mathcal{E}(\overline{T},\mathbf{x})$ good approximations of the invariant subspaces $\mathcal{V}(\mathbf{x})$. We proceed by calculating the largest principal angles β between $\mathcal{P}^{\pm}(T,\mathbf{x})$ and the converged

subspaces $\mathcal{E}(\overline{T}, \mathbf{x})$. We limit our analysis to the stable and unstable subspaces.

$$\begin{aligned}
\beta^{s+}(T, \mathbf{x}) &= \angle\left(\mathcal{P}^{s+}(T, \mathbf{x}), \mathcal{E}^{s}(\overline{T}, \mathbf{x})\right), \\
\beta^{s-}(T, \mathbf{x}) &= \angle\left(\mathcal{P}^{s-}(T, \mathbf{x}), \mathcal{E}^{s}(\overline{T}, \mathbf{x})\right), \\
\beta^{u+}(T, \mathbf{x}) &= \angle\left(\mathcal{P}^{u+}(T, \mathbf{x}), \mathcal{E}^{u}(\overline{T}, \mathbf{x})\right), \\
\beta^{u-}(T, \mathbf{x}) &= \angle\left(\mathcal{P}^{u-}(T, \mathbf{x}), \mathcal{E}^{u}(\overline{T}, \mathbf{x})\right).
\end{aligned} \tag{3.25}$$

Notice that, while $\mathcal{E}^s$ and $\mathcal{E}^u$ are uniquely defined, $\mathcal{P}^s$ and $\mathcal{P}^u$ have an additional '+' or '-' depending on the direction of integration used to calculate the state transition matrix Φ. When $T = T_r^+$, we obtain $\mathcal{P}^{s+}(T_r^+, \mathbf{x}) = \tilde{\mathcal{F}}^{s+}(T_r^+, \mathbf{x})$ and thus $\beta^{s+}(T_r^+, \mathbf{x}) = \tilde{\alpha}^{s+}(\mathbf{x})$, which is the same angle plotted in Fig. 3.22. Similar conclusions can be drawn for the other subspaces. For comparison purposes let us also define the following angles between FTLA subspaces

$$\begin{aligned}
\gamma^{s}(T, \mathbf{x}) &= \angle\left(\mathcal{E}^{s}(T, \mathbf{x}), \mathcal{E}^{s}(\overline{T}, \mathbf{x})\right), \\
\gamma^{u}(T, \mathbf{x}) &= \angle\left(\mathcal{E}^{u}(T, \mathbf{x}), \mathcal{E}^{u}(\overline{T}, \mathbf{x})\right).
\end{aligned} \tag{3.26}$$

All β and γ angles are computed for $T \in (0, \overline{T}]$. Similarly to the periodic case, the quasiperiodic orbits and the analyzed points on them are reported in Tables 3.4, 3.5, and 3.6. We consider eight quasiperiodic orbits, labeled from $\tilde{\mathcal{O}}_1$ through $\tilde{\mathcal{O}}_8$. Orbits $\tilde{\mathcal{O}}_1$, $\tilde{\mathcal{O}}_2$, $\tilde{\mathcal{O}}_3$, $\tilde{\mathcal{O}}_4$, and $\tilde{\mathcal{O}}_5$ are around L_1, while $\tilde{\mathcal{O}}_6$, $\tilde{\mathcal{O}}_7$ and $\tilde{\mathcal{O}}_8$ are around L_3. Figures 3.24 and 3.25 show the logarithm in base 10 of the β angles for the points $\mathbf{x}_{\tilde{\mathcal{O}}_4}$ (orbit around L_1) and $\mathbf{x}_{\tilde{\mathcal{O}}_6}$ (orbit around L_3), respectively. In particular, β^{s+} is displayed in the top-left corner (blue curve), β^{u-} is in the top-right corner (green curve), β^{s-} in the bottom-left corner (red curve), and β^{u+} is shown in the bottom-right corner (purple curve). The black-dotted curves represent the logarithm in base 10 of γ^s (left subplots) and of γ^u (right subplots). The plots of the β angles for the remaining points can be found in Fig. 3.29, while the FTLEs for all points are shown in Fig. 3.30, 3.31. From the figures we can conclude that:

Table 3.4: Quasiperiodic orbits around L_1 and L_3 with associated specific energy.

Orbit	Type	Lib. Point	Energy
$\tilde{\mathcal{O}}_1$	Quasihalo	L_1	-1.578103
$\tilde{\mathcal{O}}_2$	Quasihalo	L_1	-1.569051
$\tilde{\mathcal{O}}_3$	Lissajous	L_1	-1.553985
$\tilde{\mathcal{O}}_4$	Quasihalo	L_1	-1.540802
$\tilde{\mathcal{O}}_5$	Quasihalo	L_1	-1.533448
$\tilde{\mathcal{O}}_6$	Quasi Lyap. Horiz.	L_3	-1.503069
$\tilde{\mathcal{O}}_7$	Quasi Lyap. Horiz.	L_3	-1.502444
$\tilde{\mathcal{O}}_8$	Quasi Lyap. Horiz.	L_3	-1.500774

Table 3.5: Coordinates of the points on the quasiperiodic orbits of Table 3.4.

Point	x	y	z
	v_x	v_y	v_z
$\mathbf{x}_{\tilde{\mathcal{O}}_1}$	$8.647474307 \cdot 10^{-1}$	$4.838781982 \cdot 10^{-2}$	$-2.454016248 \cdot 10^{-2}$
	$1.252773079 \cdot 10^{-2}$	$-1.521654620 \cdot 10^{-1}$	$9.935781384 \cdot 10^{-5}$
$\mathbf{x}_{\tilde{\mathcal{O}}_2}$	$8.578526876 \cdot 10^{-1}$	$9.324349952 \cdot 10^{-2}$	$-2.435399232 \cdot 10^{-2}$
	$6.819680113 \cdot 10^{-2}$	$-1.358020826 \cdot 10^{-2}$	$-9.454421303 \cdot 10^{-2}$
$\mathbf{x}_{\tilde{\mathcal{O}}_3}$	$8.716260479 \cdot 10^{-1}$	$1.499214880 \cdot 10^{-2}$	$5.143108711 \cdot 10^{-2}$
	$4.847735840 \cdot 10^{-2}$	$-1.170544503 \cdot 10^{-1}$	$2.392455166 \cdot 10^{-1}$
$\mathbf{x}_{\tilde{\mathcal{O}}_4}$	$8.283709976 \cdot 10^{-1}$	$-1.403606055 \cdot 10^{-6}$	$1.123099414 \cdot 10^{-1}$
	$-1.571467529 \cdot 10^{-3}$	$2.414537876 \cdot 10^{-1}$	$-2.702619439 \cdot 10^{-2}$
$\mathbf{x}_{\tilde{\mathcal{O}}_5}$	$8.834841951 \cdot 10^{-1}$	$1.235200559 \cdot 10^{-1}$	$4.579375218 \cdot 10^{-2}$
	$9.156308040 \cdot 10^{-2}$	$4.729740930 \cdot 10^{-5}$	$-2.180539119 \cdot 10^{-1}$
$\mathbf{x}_{\tilde{\mathcal{O}}_6}$	$-9.300568185 \cdot 10^{-1}$	$0.000000000 \cdot 10^{0}$	$3.398214257 \cdot 10^{-3}$
	$2.026103287 \cdot 10^{-6}$	$-1.546303971 \cdot 10^{-1}$	$2.971082650 \cdot 10^{-3}$
$\mathbf{x}_{\tilde{\mathcal{O}}_7}$	$-9.400868392 \cdot 10^{-1}$	$7.949997775 \cdot 10^{-2}$	$1.724630144 \cdot 10^{-2}$
	$3.462450078 \cdot 10^{-2}$	$-1.282241787 \cdot 10^{-1}$	$3.385000243 \cdot 10^{-2}$
$\mathbf{x}_{\tilde{\mathcal{O}}_8}$	$-9.265506734 \cdot 10^{-1}$	$-1.209629699 \cdot 10^{-1}$	$3.757372231 \cdot 10^{-2}$
	$-5.106540349 \cdot 10^{-2}$	$-1.499459267 \cdot 10^{-1}$	$-1.950155754 \cdot 10^{-2}$

Table 3.6: Maximum averaging time $\overline{T}$, start time t_s, FTLEs gap $\Delta\mu(\mathbf{x})$, subspaces rate of convergence $\Delta\mu(\mathbf{x})(\overline{T}-t_s)$, and forward and backwards revolution times T_r^+, T_r^- for the points listed in Table 3.5.

Point	$\overline{T}$	t_s	$\Delta\mu(\mathbf{x})$	$\Delta\mu(\mathbf{x})(\overline{T}-t_s)$	T_r^+	T_r^-
$\mathbf{x}_{\tilde{\mathcal{O}}_1}$	7.0	1.4	2.14	12.0	2.805	2.807
$\mathbf{x}_{\tilde{\mathcal{O}}_2}$	7.0	1.4	2.03	11.3	2.829	2.842
$\mathbf{x}_{\tilde{\mathcal{O}}_3}$	7.0	1.2	1.77	10.3	2.988	2.961
$\mathbf{x}_{\tilde{\mathcal{O}}_4}$	8.0	1.8	1.79	11.1	2.793	2.797
$\mathbf{x}_{\tilde{\mathcal{O}}_5}$	9.0	1.4	1.53	11.6	2.828	2.771
$\mathbf{x}_{\tilde{\mathcal{O}}_6}$	65	12.0	0.17	9.1	6.219	6.218
$\mathbf{x}_{\tilde{\mathcal{O}}_7}$	70	11.5	0.16	9.3	6.220	6.220
$\mathbf{x}_{\tilde{\mathcal{O}}_8}$	65	11.5	0.16	8.7	6.221	6.220

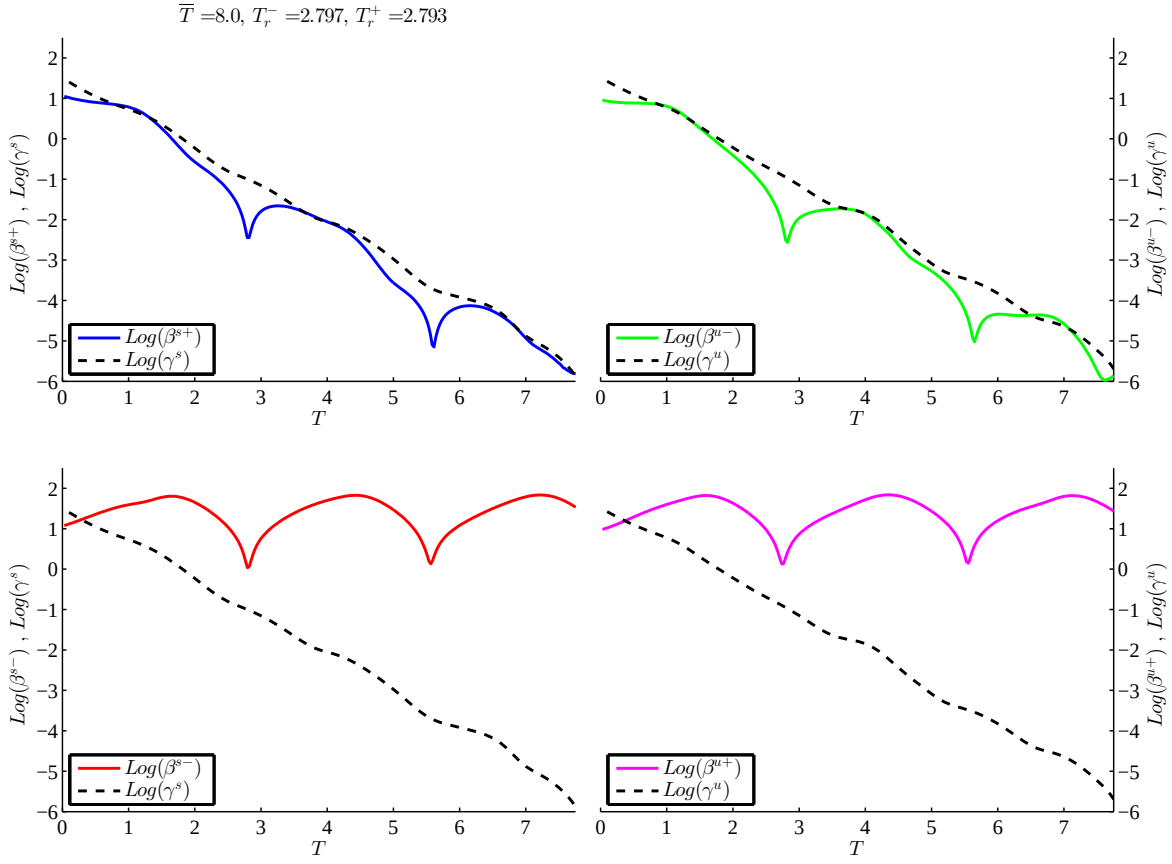

Figure 3.24: Base-10 logarithm of the angles between the stable and unstable FTLA and Φ-subspaces at increasing averaging times T for $\mathbf{x}_{\tilde{\mathcal{O}}_4}$. In particular, β^{s+} is plotted in the top-left subplot, β^{s-} in the bottom-left subplot, β^{u-} in the top-right subplot, and β^{u+} in the top-left subplot. The figure also shows γ^s (dotted-black curves) in the left subplots and γ^u (dotted-black curves) in the right subplots.

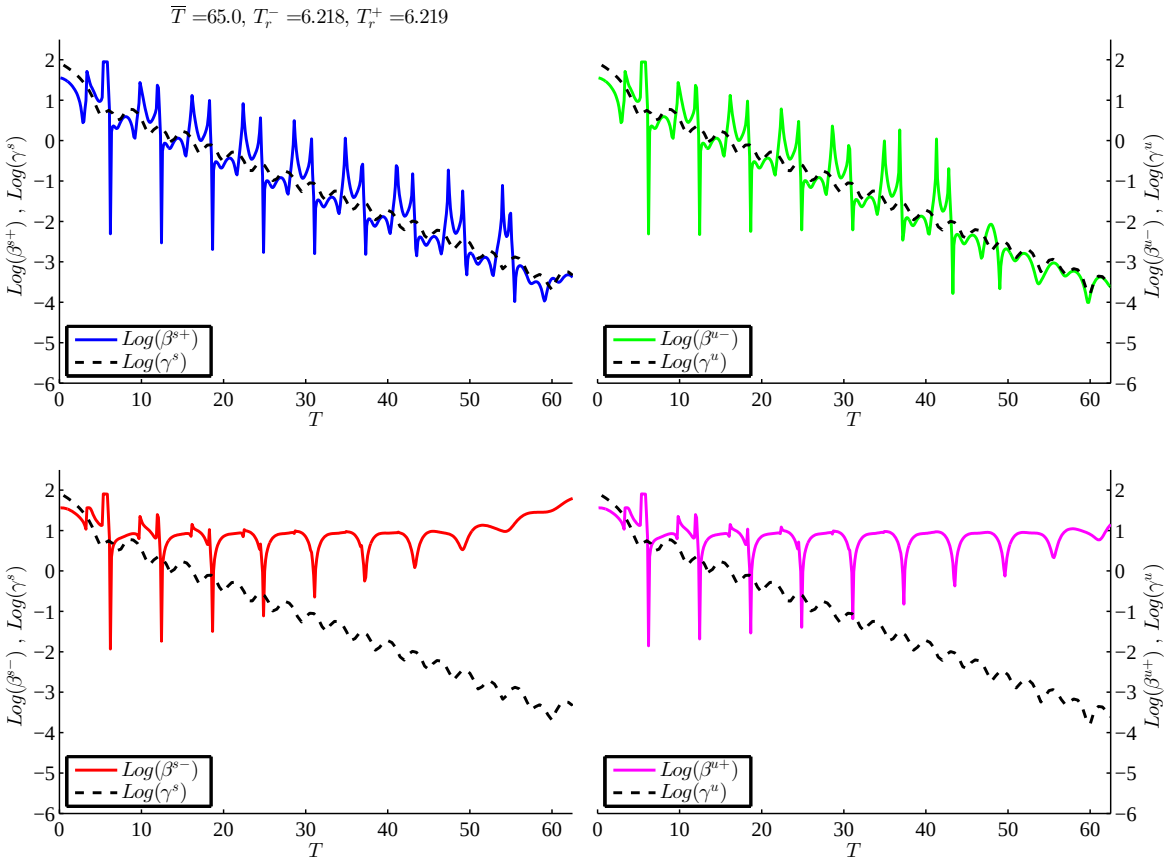

Figure 3.25: Base-10 logarithm of the angles between Floquet and FTLA subspaces at increasing averaging times T for $\mathbf{x}_{\tilde{\mathcal{O}}_6}$. In particular, β^{s+} is plotted in the top-left subplot, β^{s-} in the bottom-left subplot, β^{u-} in the top-right subplot, and β^{u+} in the top-left subplot. The figure also shows γ^s (dotted-black curves) in the left subplots and γ^u (dotted-black curves) in the right subplots.

- The angles $\beta^{s+}(T, \mathbf{x})$ and $\beta^{u-}(T, \mathbf{x})$ exponentially decrease as T is increased. If we neglect the intermediate negative peaks, the trend is very similar to the ones the characterizes γ^s and γ^u, respectively. This means that the subspaces $\mathcal{P}^{s+}(T, \mathbf{x})$ and $\mathcal{P}^{u-}(T, \mathbf{x})$ essentially provide the same information given by $\mathcal{E}^s(T, \mathbf{x})$ and $\mathcal{E}^u(T, \mathbf{x})$ because they converge to $\mathcal{E}^s(\overline{T}, \mathbf{x})$ and $\mathcal{E}^u(\overline{T}, \mathbf{x})$ at similar rates of convergence.

- The values of the angles $\beta^{s-}(T, \mathbf{x})$ and $\beta^{u+}(T, \mathbf{x})$ fluctuate as T varies, but their average values remain almost constant. The subspaces $\mathcal{P}^{s-}(T, \mathbf{x})$ and $\mathcal{P}^{u+}(T, \mathbf{x})$ do not converge to $\mathcal{E}^s(\overline{T}, \mathbf{x})$ and $\mathcal{E}^u(\overline{T}, \mathbf{x})$, and they are not reliable approximations of the local invariant stable and unstable directions.

- All angles have downwards peaks in correspondence to $T = kT_r^{\pm}$ with $k \in \mathbb{Z}^+$. An explanation for this behavior will be given later on.

We have demonstrated that, when it comes to points on quasiperiodic orbits, the Φ-subspaces are reliable approximations of the $\mathcal{E}(\overline{T}, \mathbf{x})$ subspaces, and hence of the invariant subspaces, if and only if we compute them using a FTLA-like procedure. This means that i) the proper eigenvectors of either $\Phi(+T, \mathbf{x})$ or $\Phi(-T, \mathbf{x})$ must be used, and ii) the averaging time T needs to be chosen so that there is enough subspace convergence and in turn, small β angles. In particular, for the stable and unstable local directions we have

$$\begin{aligned} &\mathcal{P}^{s+}(T, \mathbf{x}) \approx \mathcal{E}^s(T, \mathbf{x}), \\ &\mathcal{P}^{s-}(T, \mathbf{x}) \neq \mathcal{E}^s(T, \mathbf{x}), \\ &\mathcal{P}^{u+}(T, \mathbf{x}) \neq \mathcal{E}^u(T, \mathbf{x}), \\ &\mathcal{P}^{u-}(T, \mathbf{x}) \approx \mathcal{E}^u(T, \mathbf{x}). \end{aligned} \tag{3.27}$$

To explain the presence and the meaning of the downward peaks in the β angles, it is beneficial to consider again points on periodic orbits. To be consistent with the previous section, we show the

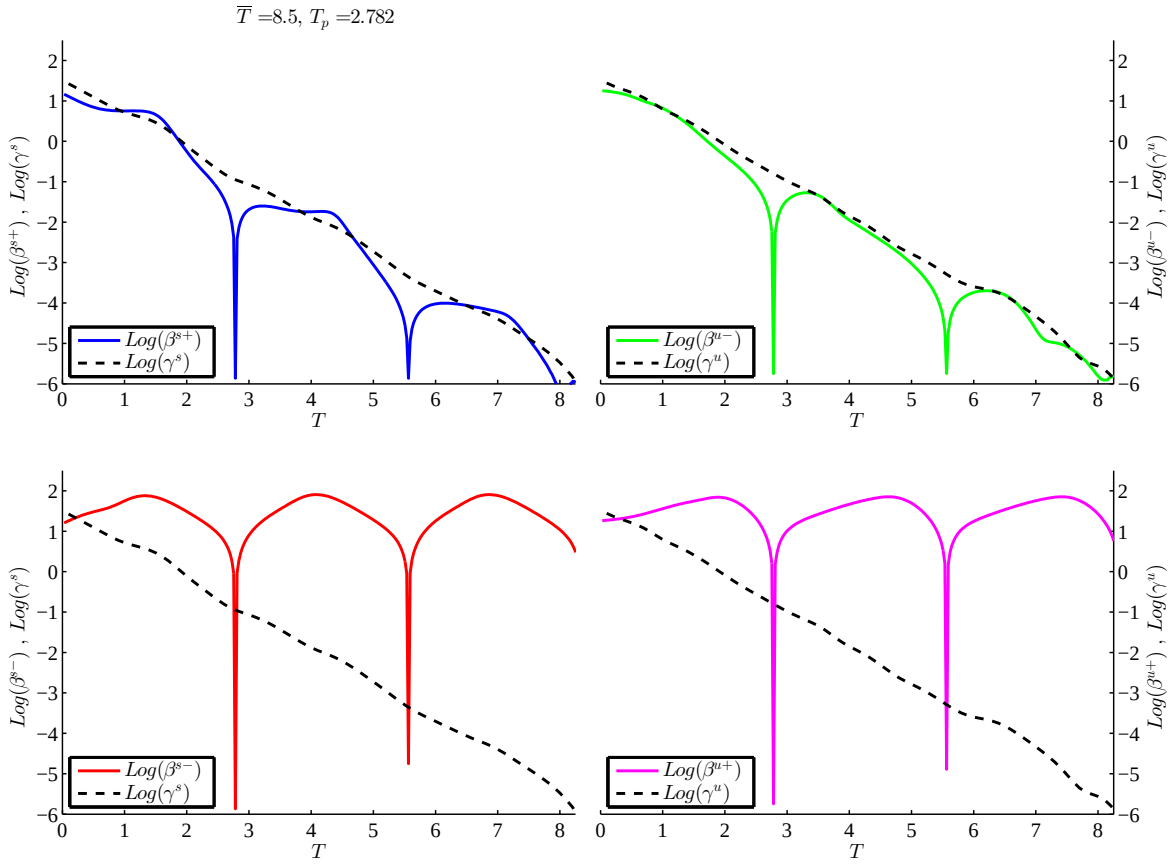

Figure 3.26: Periodic Orbit around L_1: Base-10 logarithm of the angles between the stable and unstable FTLA subspaces and Φ-subspaces at increasing averaging times T for $\mathbf{x}_{\mathcal{O}_2}$.

results associated with the subspaces computed at $\mathbf{x}_{\mathcal{O}_2}$, $\mathbf{x}_{\mathcal{O}_5}$ (on periodic orbits around L_1) and at $\mathbf{x}_{\mathcal{O}_9}$ (on a periodic orbit around L_3). The results are shown in Fig. 3.26, 3.27, and 3.28. The state transition matrices $\Phi(\pm T, \mathbf{x})$ computed at averaging times T that are positive integer multiples of the period T_p (i.e., $T = kT_p$, $k \in \mathbb{Z}^+$) produce the same information given by the monodromy matrix $M = \Phi(T_p, \mathbf{x})$. That is, for points on periodic orbits, the Φ-subspaces computed at $T = \pm kT_p$ coincide with the Floquet subspaces $\mathcal{P}^{\pm}(\pm kT_p, \mathbf{x}) = \mathcal{F}(\mathbf{x})$. Therefore, at $T = \pm kT_p$, $\beta^{s\pm}(T, \mathbf{x}) = \beta^{u\pm}(T, \mathbf{x}) = 0$, or equivalently, $Log(\beta^{s\pm}(T, \mathbf{x})) = Log(\beta^{u\pm}(T, \mathbf{x})) \to -\infty$. (The values at the peaks are not exactly $-\infty$ because of numerical imprecisions.)

For the quasiperiodic case, the negative peaks appear at $T = kT_r^{\pm}$ but their depth is significantly reduced. This is particularly true for $k = 1$, namely, at $T = T_r^{\pm}$, when the Φ-subspaces coincide

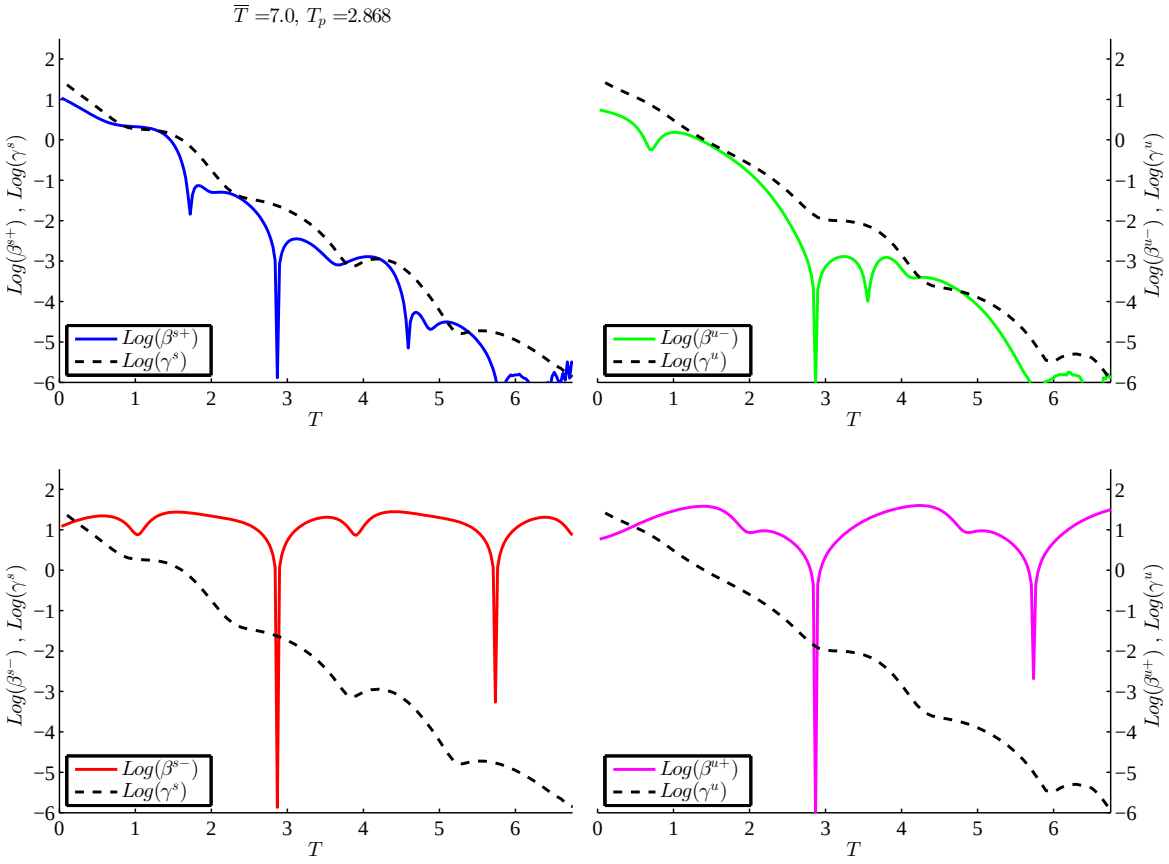

Figure 3.27: Periodic Orbit around L_1: Base-10 logarithm of the angles between the stable and unstable FTLA subspaces and Φ-subspaces at increasing averaging times T for $\mathbf{x}_{\mathcal{O}_5}$..

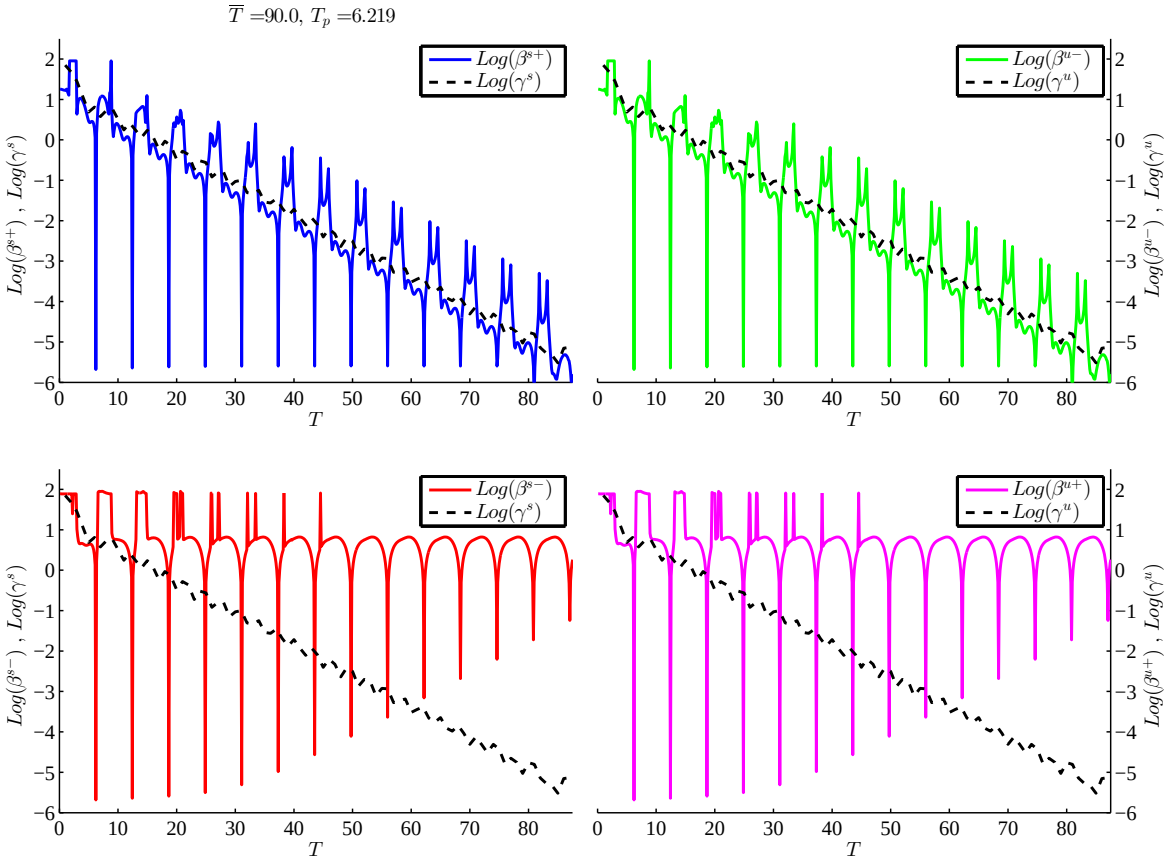

Figure 3.28: Periodic Orbit around L_3: Base-10 logarithm of the angles between the stable and unstable FTLA subspaces and Φ-subspaces at increasing averaging times T for $\mathbf{x}_{\mathcal{O}_9}$.

with the EFA subspaces $\tilde{\mathcal{F}}^{\pm}(T_r^{\pm}, \mathbf{x})$. The reduction in the magnitude of the peaks is linked to the degrees of recurrences $\delta^+(\mathbf{x})$ and $\delta^-(\mathbf{x})$. The larger the degrees of recurrence, the less accentuated the peaks are. In fact, as we stated earlier, the EFA subspaces at points on orbits with high degrees of recurrences, are not reliable approximations of the invariant linear directions. Moreover, the peaks are very narrow, thus, the integration has to stopped precisely at $T = kT_r^{\pm}$. Finally we can conclude that there is no real advantage in using the EFA subspaces, unless $T_r^{\pm}$ happen to be large enough to lead to a significant subspace convergence and the direction of integration follows the FTLA-subspaces methodology.

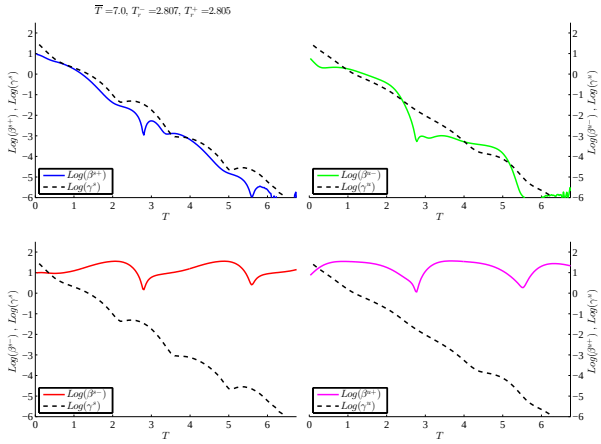

(a) β-angles for $\mathbf{x}_{\tilde{\mathcal{O}}_1}$

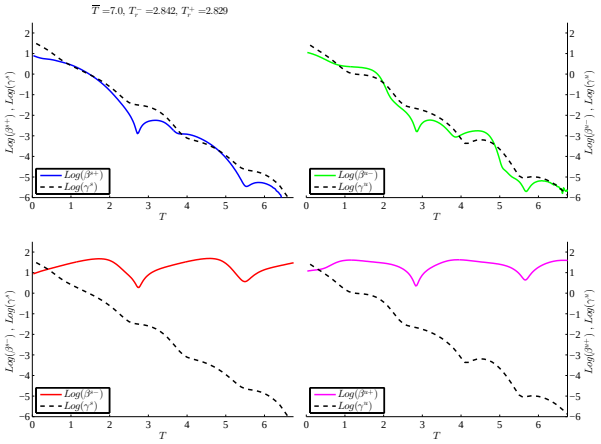

(b) β-angles for $\mathbf{x}_{\tilde{\mathcal{O}}_2}$

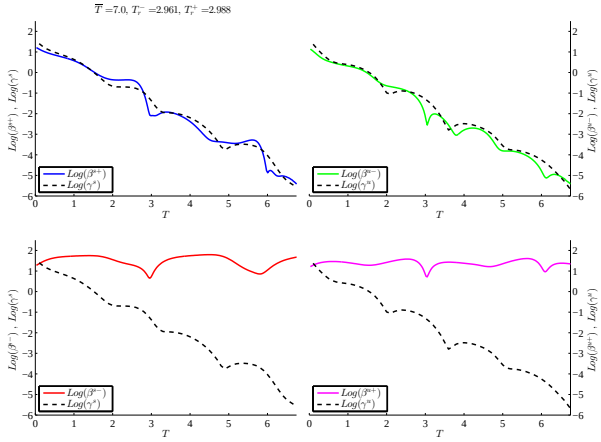

(c) β-angles for $\mathbf{x}_{\tilde{\mathcal{O}}_3}$

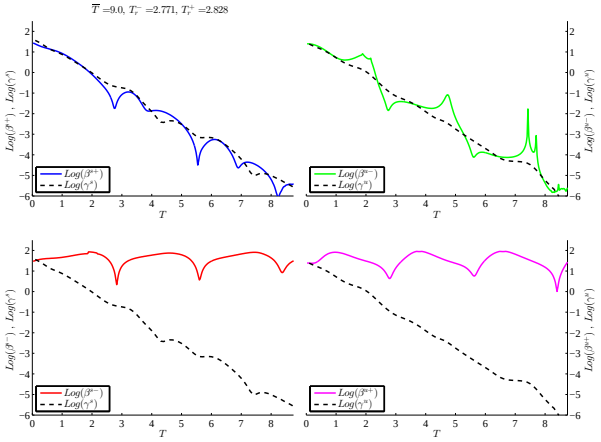

(d) β-angles for $\mathbf{x}_{\tilde{\mathcal{O}}_5}$

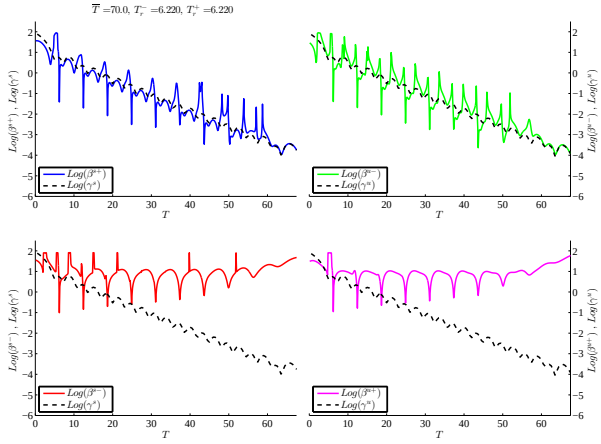

(e) β-angles for $\mathbf{x}_{\tilde{\mathcal{O}}_7}$

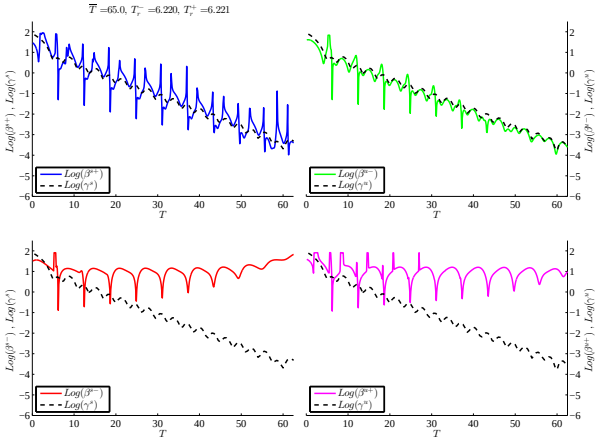

(f) β-angles for $\mathbf{x}_{\tilde{\mathcal{O}}_8}$

Figure 3.29: Base-10 logarithm of the angles between Φ-subspaces and converged FTLA subspaces at increasing averaging times T for $\mathbf{x}_{\tilde{\mathcal{O}}_1}$ (a), $\mathbf{x}_{\tilde{\mathcal{O}}_2}$ (b), $\mathbf{x}_{\tilde{\mathcal{O}}_3}$ (c), and $\mathbf{x}_{\tilde{\mathcal{O}}_5}$ (d), $\mathbf{x}_{\tilde{\mathcal{O}}_7}$ (e), and $\mathbf{x}_{\tilde{\mathcal{O}}_8}$ (f).

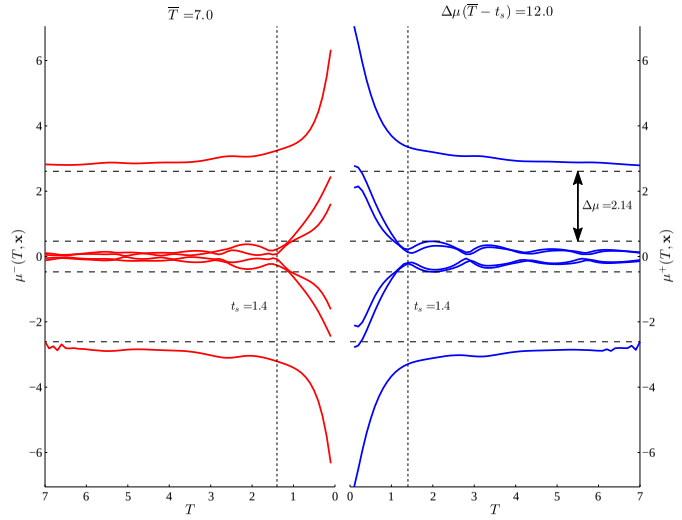

(a) Finite-time Lyapunov exponents for $\mathbf{x}_{\tilde{\mathcal{O}}_1}$

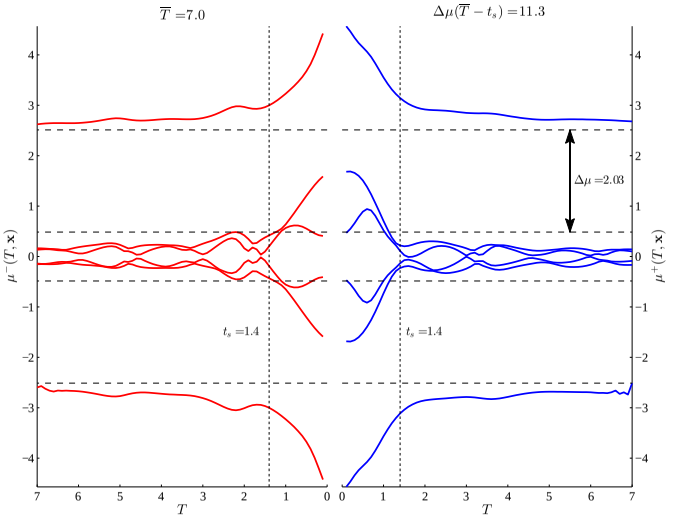

(b) Finite-time Lyapunov exponents for $\mathbf{x}_{\tilde{\mathcal{O}}_2}$

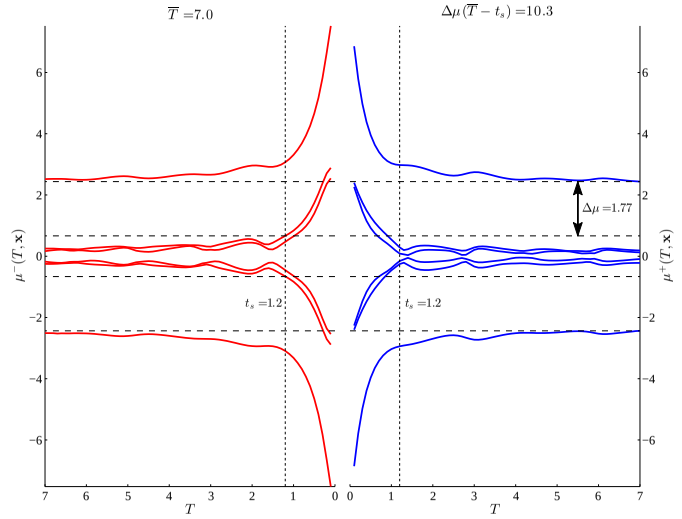

(c) Finite-time Lyapunov exponents for $\mathbf{x}_{\tilde{\mathcal{O}}_3}$

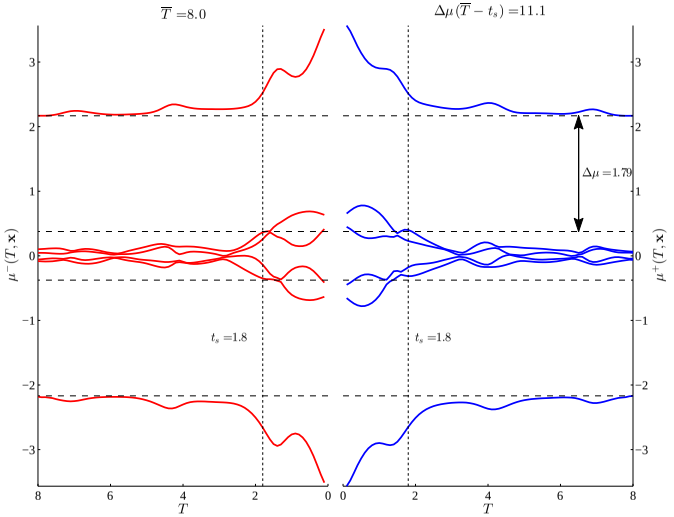

(d) Finite-time Lyapunov exponents for $\mathbf{x}_{\tilde{\mathcal{O}}_4}$

Figure 3.30: Finite-time Lyapunov exponents for $\mathbf{x}_{\tilde{\mathcal{O}}_1}$ (a), $\mathbf{x}_{\tilde{\mathcal{O}}_2}$ (b), $\mathbf{x}_{\tilde{\mathcal{O}}_3}$ (c), and $\mathbf{x}_{\tilde{\mathcal{O}}_4}$ (d).

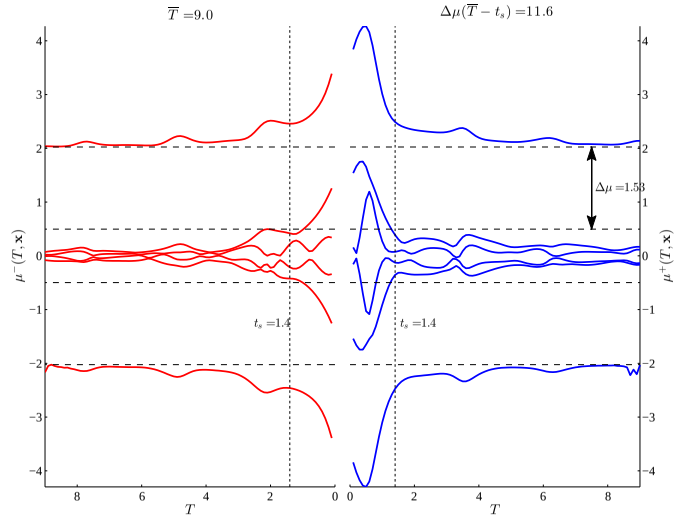

(a) Finite-time Lyapunov exponents for $\mathbf{x}_{\tilde{\mathcal{O}}_5}$

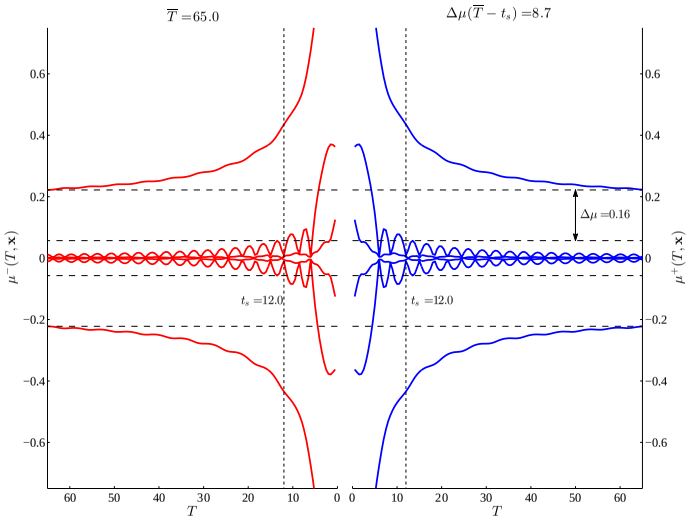

(b) Finite-time Lyapunov exponents for $\mathbf{x}_{\tilde{\mathcal{O}}_6}$

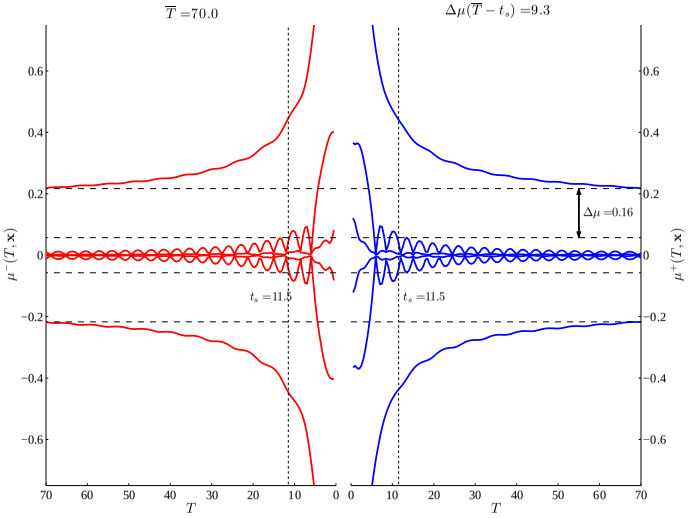

(c) Finite-time Lyapunov exponents for $\mathbf{x}_{\tilde{\mathcal{O}}_7}$

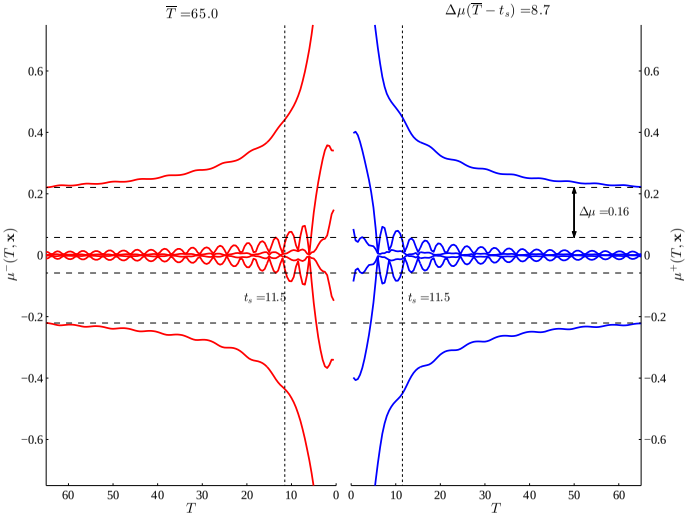

(d) Finite-time Lyapunov exponents for $\mathbf{x}_{\tilde{\mathcal{O}}_8}$

Figure 3.31: Finite-time Lyapunov exponents for $\mathbf{x}_{\tilde{\mathcal{O}}_5}$ (a), $\mathbf{x}_{\tilde{\mathcal{O}}_6}$ (b), $\mathbf{x}_{\tilde{\mathcal{O}}_7}$ (c), and $\mathbf{x}_{\tilde{\mathcal{O}}_8}$ (d).

Table 3.7: Adoptable approaches for approximating the linear subspaces forming the tangent space splitting at $\mathbf{x}$

Method	Subspaces	E.vects of	Fixed time	Periodic	Aperiodic
FLOQUET	$\mathcal{F}$	$\Phi(\pm T_p, \mathbf{x})$	yes	yes	no
EFA	$\tilde{\mathcal{F}}^{\pm}$	$\Phi(\pm T_r^{\pm}, \mathbf{x})$	yes	yes	no
Φ	$\mathcal{P}^{\pm}$	$\Phi(\pm T, \mathbf{x})$	no	yes	yes
FTLA	$\mathcal{E}$	$\Phi(\pm T, \mathbf{x})^T \Phi(\pm T, \mathbf{x})$	no	yes	yes

Review of Methodologies

Table 3.7 summarizes the various approaches that can be adopted for approximating the linear subspaces that form the tangent splitting at a state point $\mathbf{x}$.

When considering points on periodic orbits, Floquet analysis is applicable and in principle is exact, although all methods can be used. In fact, for periodic orbits, the Φ-subspaces coincide with the EFA subspaces and with the Floquet ones. EFA and FTLA yield approximations for the aperiodic case. In EFA, the useful information is extracted from the transition matrix computed at the revolution times (i.e. $T_r^{\pm}$). The values of $T_r^{\pm}$ are fixed and so is the rate of subspaces convergence K. If K happens to be large enough, and if the directions of integration are properly chosen, the EFA subspaces are accurate. Should K not be sufficiently large, the forward and backward in time transition matrices should be integrated for longer times. Finally, our numerical results show that if Φ, rather than $\Phi^T Phi$ or its transpose is used, in what otherwise is the FTLA methodology, accuracy similar to that of FTLA is achieved. In fact, the accuracy of FTLA subspaces does not depend on the periodicity of the orbits, but only on the rate of convergence of the finite-time subspaces towards the invariant ones. Therefore, as long as the convergence requirement is met, we can apply FTLA to reliably approximate the tangent space splitting at points on both periodic and aperiodic orbits.

3.4 Examples of Stationkeeping

We will now present five examples to show the application of FTLA to stationkeeping. The first two test cases focus on performing a single stationkeeping maneuver; the FTLA results are compared to the ones obtained using EFA subspaces. Since the SK algorithm presented in 3.2.2 calls for forward-in-time integration only, the EFA subspaces that we will use are $\tilde{\mathcal{F}}^{+}(T_r^{+}, \mathbf{x})$. The following two test cases describe mission-like scenarios where multiple SKM are performed. The purpose of these test cases is to show the results obtained via FTLA, for orbits about L_1 and L_3. The last example provides some insightful results for stationkeeping for orbits about L_1 when the worst case scenario, in terms of navigation and maneuver execution errors, is considered.

3.4.1 Single Stationkeeping Maneuver

In this subsection we present the results for a single stationkeeping maneuver, computed according to the algorithm presented in 3.2.2. We analyze two test cases, one representative of the general behavior of orbits around L_1 and the other representative of the general behavior of orbits about L_3. For each case, we start by considering a quasiperiodic reference orbit $\mathcal{O}_{ref}$. We choose a point on $\mathcal{O}_{ref}$, $\mathbf{x}_{ref} = (\mathbf{p}_{ref}^T, \mathbf{v}_{ref}^T)^T$, perturb it by adding the vector $(\delta\mathbf{p_0}^T, \delta\mathbf{v_0}^T)^T$ thus obtaining $\mathbf{x}_{pert} = ((\mathbf{p}_{ref} + \delta\mathbf{p_0})^T, (\mathbf{v}_{ref} + \delta\mathbf{v_0})^T)^T$. The perturbation vectors $(\delta\mathbf{p_0}^T, \delta\mathbf{v_0}^T)^T$ are specifically chosen to show the behavior of the system after the maneuver. The perturbed point $\mathbf{x}_{pert}$ is off $\mathcal{O}_{ref}$ and its stable manifold $\mathcal{W}^s(\mathcal{O}_{ref})$. We then apply the stationkeeping algorithm obtaining the velocity-correction $\Delta\mathbf{v}_{SKM} = \Delta\mathbf{v}^{(N)}$. As previously stated, our goal is to place the spacecraft as close as possible to the stable manifold of a neighboring orbit of $\mathcal{O}_{ref}$ which is part of the center-stable manifold $\mathcal{W}^{cs}$. To assess the quality of the maneuver, we propagate the trajectory forward in time using as initial state the corrected point $\mathbf{x}_{new} = \mathbf{x}_{pert} + (\mathbf{0}^T, \Delta\mathbf{v}_{SKM}^T)^T$ and monitor the difference in position and velocity between the new and the reference trajectories. The closer

$\mathbf{x}_{new}$ is to the invariant manifold $\mathcal{W}^{cs}$, the longer the trajectory that starts from it will stay in the neighborhood of the reference trajectory, delaying the need for a second SKM. The degree of success of a single SKM is thus quantified by the amount of time t_{prop} that the corrected trajectory spends near the reference orbit, before inevitably diverging from it. With 'near' we mean that the distance between the spacecraft and the reference trajectory is within the same order of magnitude of the initial perturbation. The value $||\Delta\mathbf{v}_{SKM}||$ is proportional to the fuel that is required to perform the maneuver. For a single SKM, though, this parameter alone is not enough to assess the quality of the maneuver. In fact, two maneuvers that require the same $||\Delta\mathbf{v}_{SKM}||$ may produce trajectories that start to diverge from the reference orbit at very different times. We use both FTLA subspaces and EFA subspaces to compute the correction $\mathbf{v}_{SKM}$; the results of the two methods will then be compared.

Test Case 1: quasiperiodic orbit about L_1

We choose as reference orbit the quasiperiodic orbit $\tilde{\mathcal{O}}_1$ and we consider a point on it $\mathbf{x}_{ref} = \mathbf{x}_{\tilde{\mathcal{O}}_1}$. For more details about $\tilde{\mathcal{O}}_1$ and $\mathbf{x}_{\tilde{\mathcal{O}}_1}$ see Tables 3.4 and 3.5. We choose the following position-velocity perturbations

$$\delta\mathbf{p_0} = (-7.271054665 \times 10^{-5}, -9.746843715 \times 10^{-5}, -4.617384625 \times 10^{-5})^T,$$
$$\delta\mathbf{v_0} = (-6.731267941 \times 10^{-6}, -6.101792617 \times 10^{-5}, 7.588584293 \times 10^{-5})^T,$$

with

$$||\delta\mathbf{p_0}|| = 50 \text{ km}, \ ||\delta\mathbf{v_0}|| = 10 \text{ cm/s}.$$

to obtained the perturbed state $\mathbf{x}_{pert}$. The delta-v corrections obtained via FTLA and EFA methods and that are applied to $\mathbf{x}_{pert}$ are

$$\text{FTLA: } \Delta\mathbf{v}_{SKM} = (2.101830638 \times 10^{-4}, 4.953142424 \times 10^{-5}, 3.571088655 \times 10^{-5})^T,$$
$$||\Delta\mathbf{v}_{SKM}|| = 22.4 \text{ cm/s}, \quad t_{prop} > 25 \text{ days},$$

$$\text{EFA: } \Delta\mathbf{v}_{SKM} = (2.094479352 \times 10^{-4}, 4.935744957 \times 10^{-5}, 3.558154143 \times 10^{-5})^T,$$
$$||\Delta\mathbf{v}_{SKM}|| = 22.3 \text{ cm/s}, \quad t_{prop} \approx 10 \text{ days}.$$

We denote with $||\delta\mathbf{p}|| = ||\mathbf{p}_{ref} - \mathbf{p}(\phi(t, \mathbf{x}_{new}))||$ and $||\delta\mathbf{v}|| = ||\mathbf{v}_{ref} - \mathbf{v}(\phi(t, \mathbf{x}_{new}))||$ the position and the velocity difference between the reference and the trajectory after the SK correction. The quantities are all plotted in Fig. 3.32 as functions of time. The red dashed lines in the plots represent the position and velocity differences in the case of the SKM not being applied. Although the $||\Delta\mathbf{v}_{SKM}||$ calculated with both the methods are nearly the same, $\mathbf{x}_{new}$ obtained utilizing FTLA subspaces is much closer to the center-stable manifold, given that the propagated trajectory remains in the neighborhood of the reference orbit for at least 2.5 times longer than the EFA trajectory. The average revolution time for the reference orbit is $T_r^+ \approx 12$ days, so if the FTLA method is used, the next SKM can potentially be performed after 2 revolutions, while if we computed the same maneuver using the EFA subspaces, there would be a need of a maneuver after less than a complete revolution.

Test Case 2: quasiperiodic orbit about L_3

We choose as reference orbit the quasiperiodic orbit $\tilde{\mathcal{O}}_6$ and we consider a point on it $\mathbf{x}_{ref} = \mathbf{x}_{\tilde{\mathcal{O}}_6}$. For more details about $\tilde{\mathcal{O}}_6$ and $\mathbf{x}_{\tilde{\mathcal{O}}_6}$ see Tables 3.4 and 3.5. We apply the following position-velocity

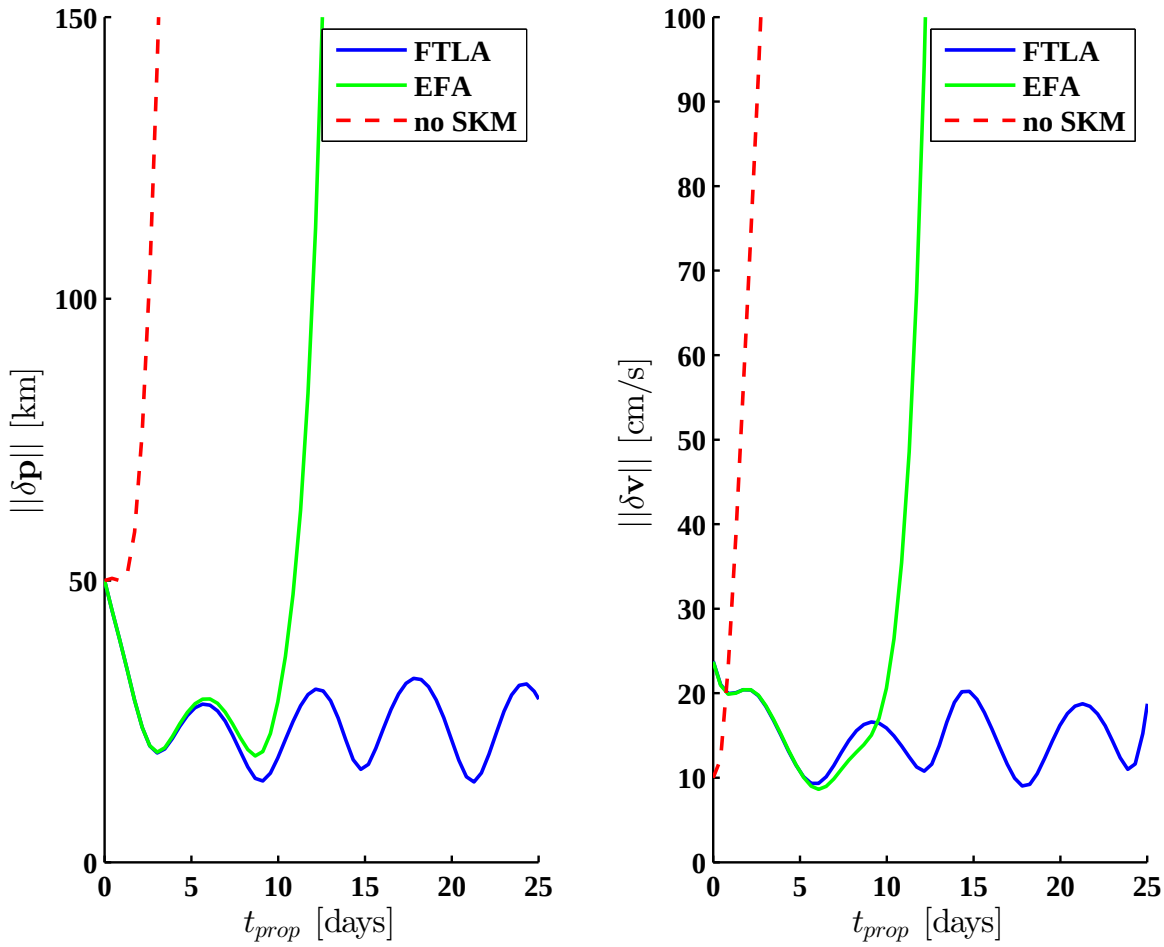

Figure 3.32: L_1 case: time evolution of position and velocity difference between the reference orbit and the trajectory after a single SKM. Position is measured in km and velocity is measured in cm/s. The blue solid curves refer to the trajectory after the correction computed via FTLA, the green solid curves refer to the EFA case, while the red dashed curves indicate the behavior in case the trajectory is not corrected.

perturbation

$$\delta\mathbf{p_0} = [8.078286363 \times 10^{-5}, 8.208626458 \times 10^{-5}, -6.045591801 \times 10^{-5}]^T,$$
$$\delta\mathbf{v_0} = [6.9992757550 \times 10^{-5}, 6.799589073 \times 10^{-5}, -2.175126166 \times 10^{-6}]^T,$$

with

$$||\delta\mathbf{p_0}|| = 50 \text{ km}, \ ||\delta\mathbf{v_0}|| = 10 \text{ cm/s},$$

The delta-v corrections obtained via FTLA and EFA methods and that are applied to $\mathbf{x}_{pert}$ are

$$\text{FTLA: } \Delta\mathbf{v}_{SKM} = (-1.444389142 \times 10^{-4}, -2.270532578 \times 10^{-4}, 5.846387372 \times 10^{-6})^T,$$
$$||\Delta\mathbf{v}_{SKM}|| = 27.6 \text{ cm/s}, \quad t_{prop} > 85 \text{ days},$$

$$\text{EFA: } \Delta\mathbf{v}_{SKM} = (-1.006868771 \times 10^{-2}, -3.270049303 \times 10^{-2}, 1.209522631 \times 10^{-3})^T,$$
$$||\Delta\mathbf{v}_{SKM}|| = 3508 \text{ cm/s}, \quad t_{prop} \approx 0 \text{ days}.$$

For the L_3 case, the two methods produce very different values of $||\Delta\mathbf{v}_{SKM}||$, with the one calculated via FTLA about 130 times lower than the one computed through EFA. The EFA results are clearly less accurate as can be seen from the $||\delta\mathbf{p}||$ and $||\delta\mathbf{v}||$ plots in Fig. 3.33. In fact, the corrected trajectory (green curves) instantaneously departs from the reference trajectory and from the phase space region around L_3. The EFA results are such that it would be less detrimental to not perform a SK maneuver at all (see the dashed lines in the plots). FTLA on the other hand (blue curves), guarantees that, after the maneuver, the spacecraft remains in the neighborhood of the reference trajectory for more than two months. The reason behind the poor accuracy of the EFA subspaces is that the revolution time associated with $\mathbf{x}_{pert}$ is on the order of $T_r^+ = 6.22$ time units, which is not enough to produce a successful convergence of the subspaces. In fact, the averaging

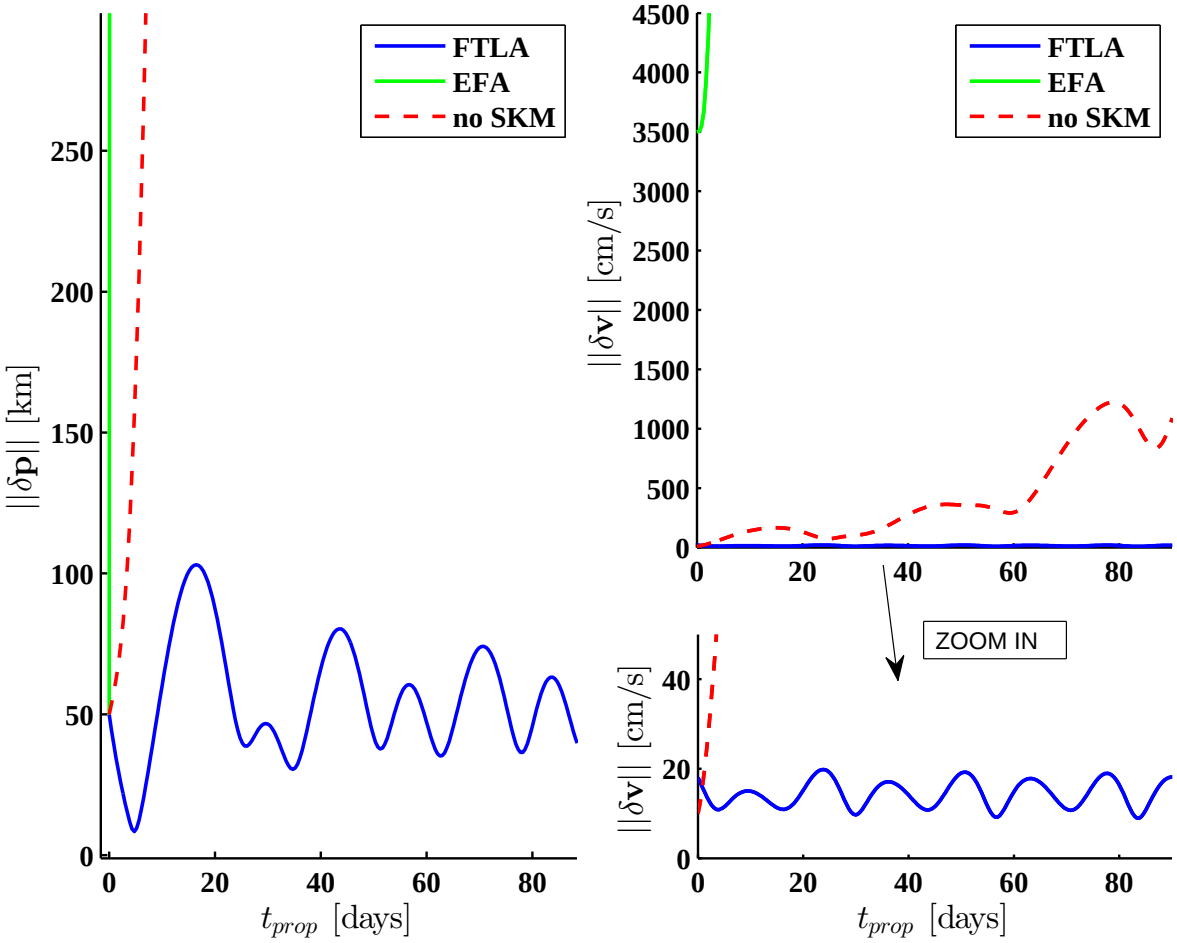

Figure 3.33: L_3 case: time evolution of position and velocity difference between the reference trajectory and the trajectory after a single SKM. Position is measured in km and velocity is measured in cm/s. The blue solid curves refer to the trajectory after the correction computed via FTLA, the green solid curves refer to the EFA case, while the red dashed curves indicate the behavior in case the trajectory is not corrected.

times used to calculate the FTLA is $\overline{T} = 85$, producing a subspace convergence rate of around an order of magnitude greater than the one associated with the EFA subspaces.

3.4.2 Multiple Stationkeeping Maneuvers

In this section we test FTLA and present results for multiple SKM. Consistently with the previous section, we show some mission scenarios for a spacecraft orbiting in the neighborhood of L_1, and some mission scenarios for the L_3 case. In order to make the simulations more meaningful, and inspired by the work presented in (18), we introduce some random errors which are divided in two categories:

- *Navigation Errors* (ϵ_n). The true position and velocity of a spacecraft cannot be determined with absolute accuracy due to inherent errors linked with the measurement of these quantities. The navigation errors are therefore introduced to account for such discrepancies and they affect both the position and the velocity coordinates. They are applied before the starting point of the algorithm in 3.2.2, namely,

$$\begin{aligned} \mathbf{x}^{(1)} &= \mathbf{x}^{(1)} + \epsilon_n, \\ \epsilon_n &= [\mathbf{p}_{\epsilon_n}^T, \mathbf{v}_{\epsilon_n}^T]^T. \end{aligned} \tag{3.28}$$

  The components of the $\mathbf{p}_{\epsilon_n}$ and $\mathbf{v}_{\epsilon_n}$ vectors are randomly generated using a normal probability distribution centered at 0 and with standard deviations $\sigma_{\mathbf{p}_n}$ and $\sigma_{\mathbf{v}_n}$, respectively. Values for $\sigma_{\mathbf{p}_n}$ and $\sigma_{\mathbf{v}_n}$ will be given in the examples.

- *Maneuver Execution Errors* (ϵ_m). The maneuver execution errors account for the differences between the designed $\Delta\mathbf{v}_{SKM}$ vector and the actual one delivered by the thrusters. These errors affect only the velocity coordinates and are implemented after the algorithm in 3.2.2

so that

$$\Delta \mathbf{v}_{SKM} = \Delta \mathbf{v}^{(N)} + \epsilon_m, \tag{3.29}$$

where once again the three components of ϵ_m are randomly generated using a normal probability distribution centered at 0, with standard deviations σ_m. The maneuver execution errors will in general change the magnitude and direction of $\Delta \mathbf{v}_{SKM}$.

Test Case 3: Stationkeeping for L_1 orbit.

In this test case we simulate several scenarios. Each mission starts from the same point of Test Case 1 in 3.4.1, which belongs to the quasihalo orbit $\tilde{\mathcal{O}}_1$. Each simulation consists of 40 revolutions around L_1; this number is chosen so that the spacecraft will be able to explore several regions of the surface of the torus containing $\tilde{\mathcal{O}}_1$. We implement 3 different stationkeeping strategies:

(a) 2 SKM per revolution, performed when the spacecraft crosses the x-z plane, plus a SKM at the initial point, for a total of 81 SKM.

(b) 2 SKM per revolution, performed when the spacecraft v_y component is null (i.e., when $|y|$ is maximum), plus a SKM at the initial point, for a total of 81 SKM.

(c) 4 SKM per revolution, combining the locations of the two previous cases, plus a SKM at the initial point, for a total of 161 SKM.

For each of the three stationkeeping strategies, we use 3 different levels of navigation and maneuver execution errors:

1. $\sigma_{\mathbf{p}_n} = 1.0\ km$, $\sigma_{\mathbf{v}_n} = 1.0\ cm/s$, $\sigma_m = 1.0\%\ of\ \Delta\mathbf{v}^{(N)}$ (high errors).

2. $\sigma_{\mathbf{p}_n} = 0.1\ km$, $\sigma_{\mathbf{v}_n} = 0.1\ cm/s$, $\sigma_m = 0.1\%\ of\ \Delta\mathbf{v}^{(N)}$ (realistic errors).

3. $\sigma_{\mathbf{p}_n} = \sigma_{\mathbf{v}_n} = \sigma_m = 0$ (no errors).

To account for the randomness of the errors, cases a-1, b-1, c-1, a-2, b-2, and c-2 are simulated 100 times. The results of the simulations are shown in Tables 3.8 and 3.9. The results are presented in terms of total delta-v requirement normalized per year ($||\Delta\mathbf{v}||/yr$) and average delta-v per stationkeeping maneuver ($||\Delta\mathbf{v}_{SKM}||_{avg}$). The delta-v requirements decrease as the applied errors decrease. For a fixed error level, the 4-point strategy (c) demands a lower total delta-v than the other two stationkeeping strategies, despite requiring twice as many SKM.

As an example, we provide more detailed results for a representative one of the simulations of case b-2, namely, the SKM are performed twice per revolution in correspondence to the maximum value of $|y|$ and the navigation and execution maneuver errors are set to 'Realistic' level. Figure 3.34 shows the resulting quasiperiodic orbit with the 81 stationkeeping locations marked by green dots. The average time between two consecutive maneuvers is about 6 days for a total mission duration of about 15 months. Figure 3.35 shows the required $||\Delta\mathbf{v}||$ for each of the performed stationkeeping maneuver, with a $||\Delta\mathbf{v}_{SKM}||_{avg}$ of 2.3 cm/s and a $||\Delta\mathbf{v}||/yr$ of 1.4 m/s. As a purely indicative benchmark, we want to mention that the observed errors during the Artemis mission to Earth-Moon L_1 were comparable with the 'Realistic' level of our simulations and the total delta-v required was about $||\Delta\mathbf{v}||/yr = 2.4$ m/s, with SKM performed roughly every 7 days.

Test Case 4: Stationkeeping for L_3 orbit.

For the L_3 test case, we select the quasiperiodic orbit $\tilde{\mathcal{O}}_3$, starting each time from the point $\mathbf{x}_{\tilde{\mathcal{O}}_3}$, whose coordinates were given in Test Case 2 in 3.4.1. We simulate a 20-revolution scenario using

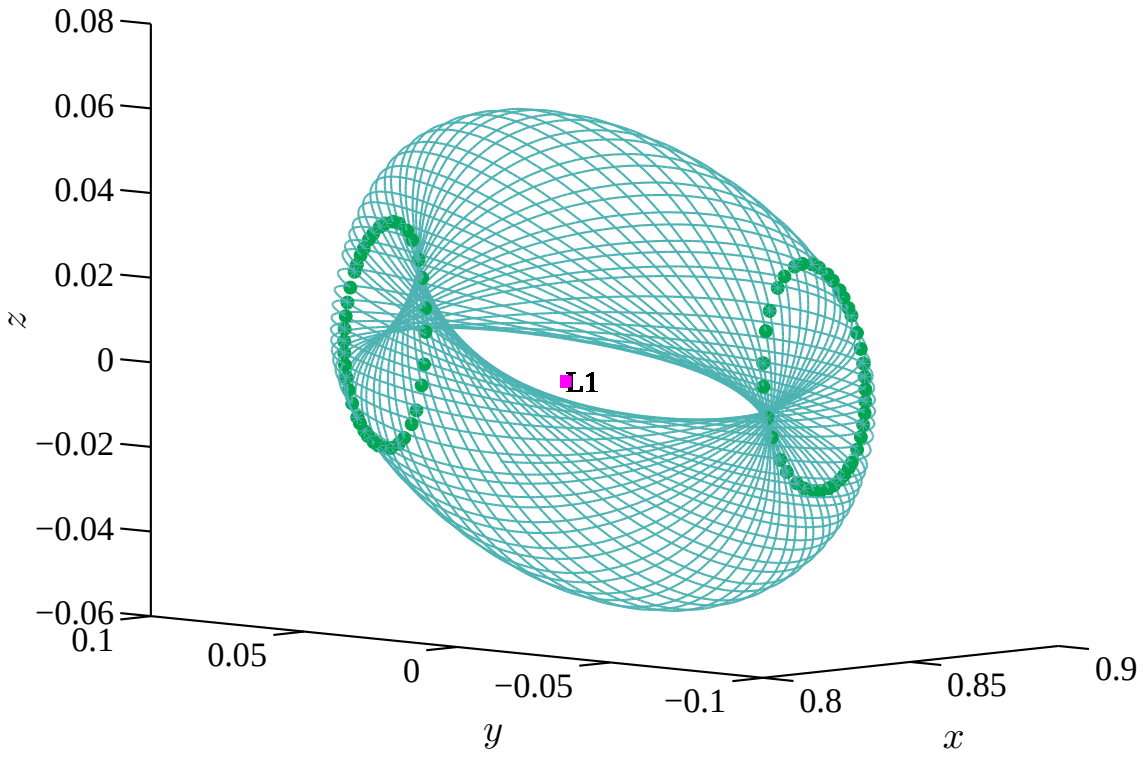

Figure 3.34: L_1 case: stationkeeping maneuvers about the quasihalo orbit $\tilde{\mathcal{O}}_1$. The mission is designed to have 40 revolutions in order to span most of the surface of the torus. The 81 SKM are performed roughly every 6 days. The SKM locations are indicated by the green dots.

Table 3.8: Yearly delta-v requirement in m/s for simulated stationkeeping missions about $\tilde{\mathcal{O}}_1$.

Total $||\Delta \mathrm{v}||$ per year of mission in [m/s]

Errors	SKM Location		
	(a) x-z plane	(b) max$\|y\|$	(c) 4 points
1.High	14.97 ± 2.04	14.39 ± 1.81	4.64 ± 0.43
2.Realistic	1.51 ± 0.55	1.41 ± 0.12	0.46 ± 0.05
3.Null	≈ 0.00	≈ 0.00	≈ 0.00

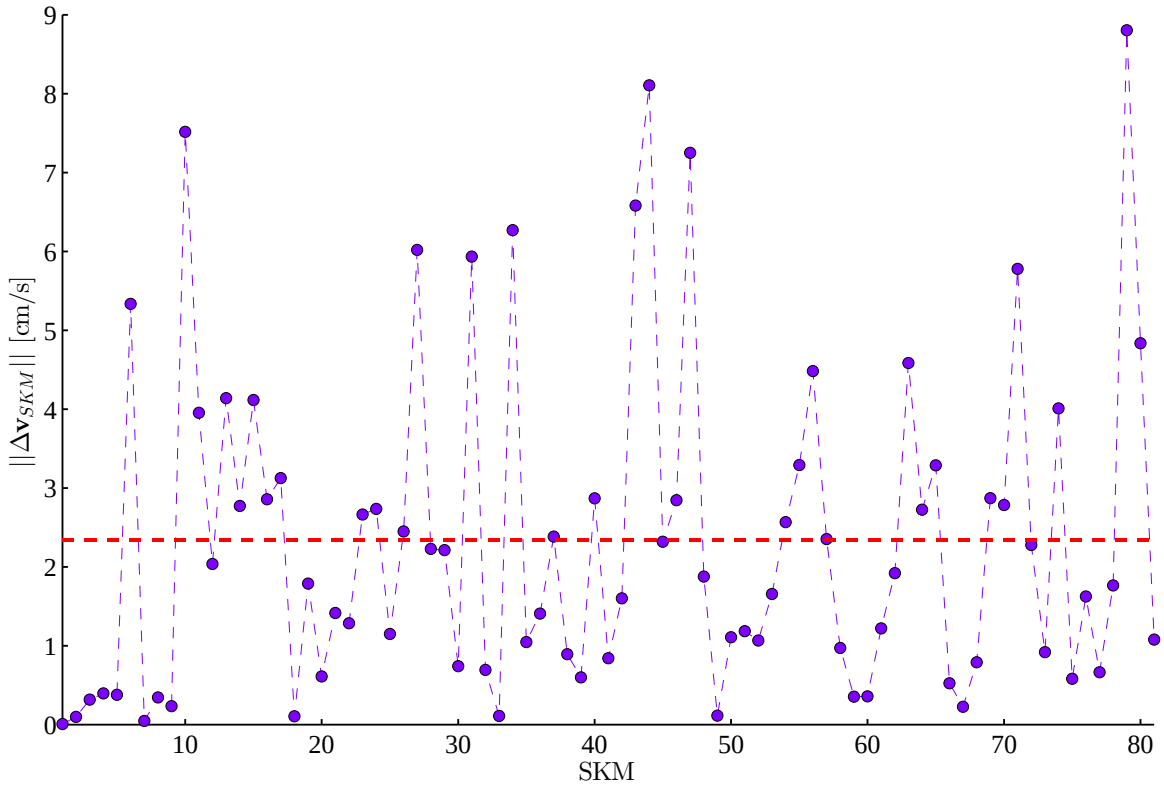

Figure 3.35: SKM profile for a simulated mission about the quasihalo orbit $\tilde{\mathcal{O}}_1$. The $||\Delta \mathbf{v}_{SKM}||$ are measured in cm/s; the stationkeeping maneuvers are performed at $max|y|$ with realistic levels of navigation and maneuver execution errors (i.e., b-2 case). The dotted line represents the average $||\Delta \mathbf{v}_{SKM}||$, which in this particular mission simulation is equal to 2.34 cm/s.

Table 3.9: Average delta-v requirement per SKM in cm/s for simulated stationkeeping missions about $\tilde{\mathcal{O}}_1$.

Average $||\Delta \mathbf{v}_{SKM}||$ in [cm/s]

Errors	SKM Location		
	(a) x-z plane	(b) max$\|y\|$	(c) 4 points
1.High	24.38	23.57	3.80
2.Realistic	2.46	2.31	0.38
3.Null	≈ 0.00	≈ 0.00	≈ 0.00

Table 3.10: Yearly delta-v requirement in m/s for simulated stationkeeping missions about $\tilde{\mathcal{O}}_3$.

Total $\|\|\Delta\mathrm{v}\|\|$ per year of mission in [m/s]		
Errors	SKM Location	
	(d) 1 SKM/1 rev	(e) 1 SKM/3 revs
1.High	0.20 ± 0.04	0.55 ± 0.14
2.Realistic	0.03 ± 0.01	0.06 ± 0.02
3.Null	≈ 0.00	≈ 0.00

Table 3.11: Average delta-v requirement per SKM in cm/s for simulated stationkeeping missions about $\tilde{\mathcal{O}}_3$.

Average $\|\|\Delta\mathrm{v}_{SKM}\|\|$ in [cm/s]		
Errors	SKM Location	
	(d) 1 SKM/1 rev	(e) 1 SKM/3 revs
1.High	1.51	12.29
2.Realistic	0.21	1.27
3.Null	≈ 0.00	0.01

2 different stationkeeping strategies:

(d) 1 SKM per revolution, performed when the spacecraft crosses the x-z and $x < x(L_3)$, plus a SKM at the initial point, for a total of 21 SKM.

(e) 1 SKM every 3 revolutions, performed when the spacecraft crosses the x-z and $x < x(L_3)$, plus a SKM at the initial point, for a total of 8 SKM.

The navigation and execution maneuver error levels are the same for the L_1 case and the results are summarized in Tables 3.10 and 3.11.

Figures 3.36 and 3.37 show the trajectory with the SKM locations and the $||\Delta\mathbf{v}_{SKM}||$ profile for the 20 SKM of a representative simulation of case d-1 (1 SKM per revolution with high levels of navigation and maneuver execution errors). The average time between 2 consecutive SKM is 27

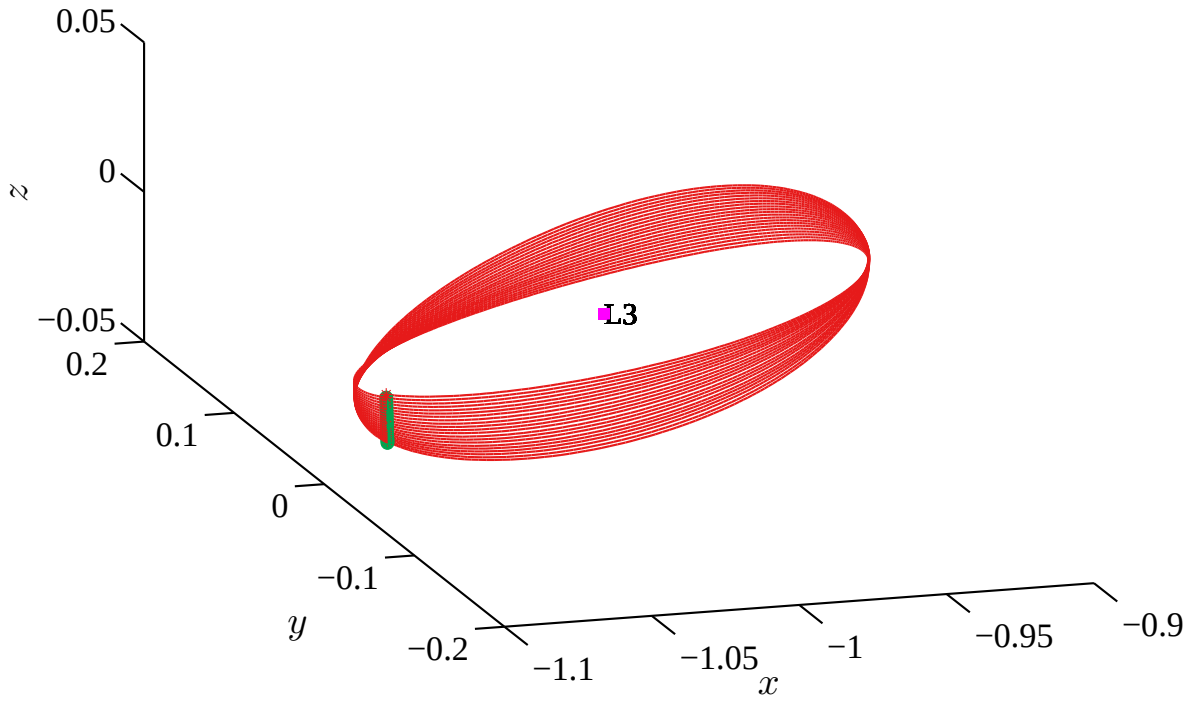

Figure 3.36: L_3 case: stationkeeping maneuvers about the quasiperiodic orbit $\tilde{\mathcal{O}}_3$. The simulation consists of 20 revolutions and 21 SKM are performed roughly every 27 days. The SKM locations are indicated by the green dots.

days, with a $||\Delta \mathbf{v}_{SKM}||_{avg}$ of 1.4 cm/s. The yearly delta-v requirement is about 0.2 m/s.

Test Case 5: Stationkeeping for L_1 orbits using extreme errors.

In this test case, we simulate stationkeeping for some orbits around L_1. Unlike test cases 3 and 4, at each SKM, the navigation and maneuver execution errors are not Gaussian-distributed; their directions and magnitude are chosen to simulate an extreme scenario. In particular, the errors are always aligned with the local unstable direction at the point where the maneuver is performed (i.e., $\mathcal{E}^u(\mathbf{x})$). Because the true unstable direction $\mathcal{E}^u(\mathbf{x})$, which is assumed the worst-case direction, is not known, it is replaced with its finite-time approximation $\mathcal{E}^u(\overline{T}, \mathbf{x})$. The navigation error

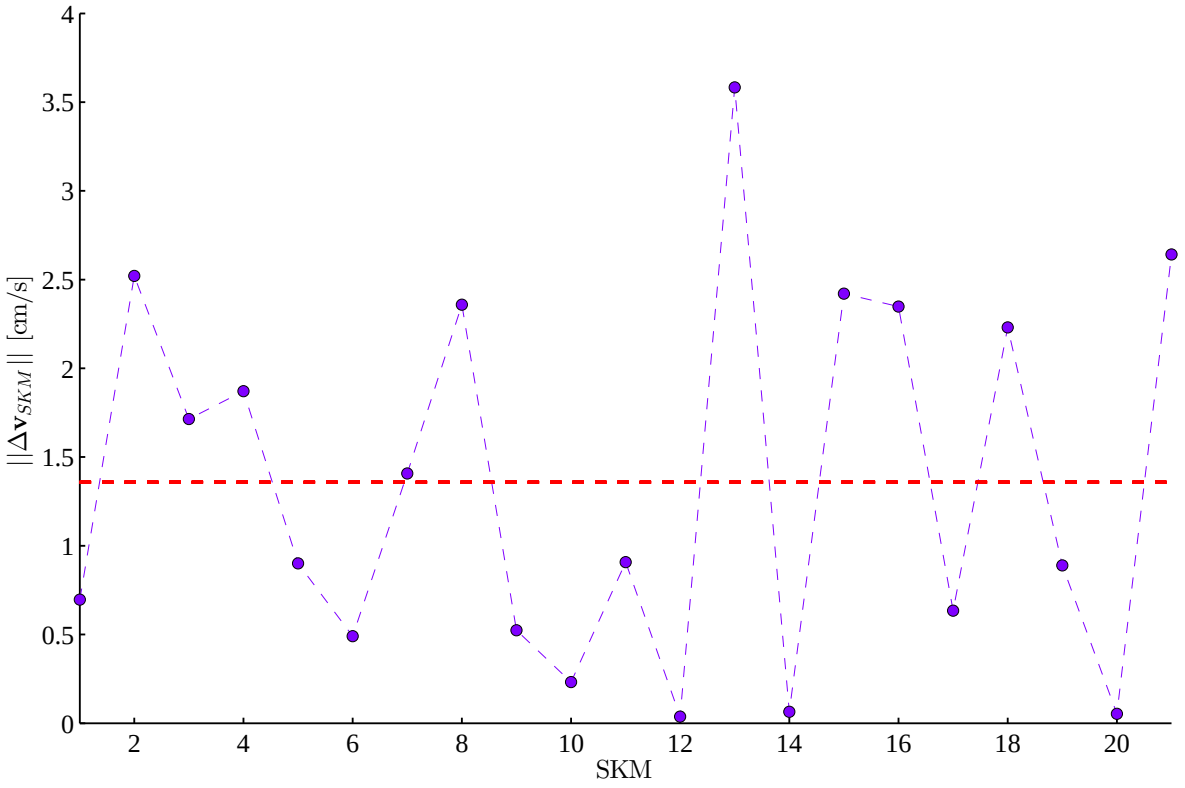

Figure 3.37: SKM profile for a simulated mission about the quasihalo orbit $\tilde{\mathcal{O}}_3$. The $||\Delta \mathbf{v}_{SKM}||$ are measured in cm/s; the stationkeeping maneuvers are performed at the intersection with the x-z plane when $x < x(L_3)$ with high levels of navigation and maneuver execution errors (i.e., d-1 case). The dotted line represents the average $||\Delta \mathbf{v}_{SKM}||$, which in this mission simulation is equal to 1.4 cm/s.

$\epsilon^{\mathbf{u}}_{\mathbf{n}} := \epsilon_{\mathbf{n}} \in \mathcal{E}^u(\overline{T}, \mathbf{x})$ has position and velocity components $\mathbf{p}_{\epsilon^u_n}$ and $\mathbf{v}_{\epsilon^u_n}$ calculated so that

$$\begin{cases} ||\mathbf{p}_{\epsilon^u_n}|| = 3\sigma_{\mathbf{p}_n} \\ ||\mathbf{v}_{\epsilon^u_n}|| \leq 3\sigma_{\mathbf{v}_n} \end{cases} \quad \vee \quad \begin{cases} ||\mathbf{p}_{\epsilon^u_n}|| \leq 3\sigma_{\mathbf{p}_n} \\ ||\mathbf{v}_{\epsilon^u_n}|| = 3\sigma_{\mathbf{v}_n} \end{cases},$$

with $\sigma_{\mathbf{p}_n} = 0.1$ km and $\sigma_{\mathbf{v}_n} = 0.1$ cm/s, based on the 'Realistic' error levels considered in test case 3. There are two choices for the orientation of $\epsilon^{\mathbf{u}}_{\mathbf{n}}$; not having an a priori knowledge of which orientation will determine a larger $||\Delta\mathbf{v}^{(N)}||$, the orientation is randomly picked for each SKM. The maneuver execution error ($\epsilon^{\mathbf{u}}_{\mathbf{m}}$) lies on the local projection of the unstable subspace onto the velocity space containing $\mathbf{x}$. Its magnitude is picked to be 1% of $||\Delta\mathbf{v}^{(N)}||$. Of the 2 possible orientations of $\epsilon^{\mathbf{u}}_{\mathbf{m}}$, we choose the one that maximizes $||\Delta\mathbf{v}_{SKM}||$ (see Eq. (3.29)). Figure 3.38 shows a schematic of the aforementioned errors. To facilitate the understanding, we limit the representation to a fictitious three-dimensional phase space in which the position space is monodimensional ($\hat{\mathbf{p}}$ axis) and the velocity space is two-dimensional ($\hat{\mathbf{v}}_\mathbf{1}$ and $\hat{\mathbf{v}}_\mathbf{2}$ axes). Starting from $\mathbf{x}$, we perturb in the unstable direction $\mathcal{E}^u(\overline{T}, \mathbf{x})$ (red thick solid line) by the navigation error $\epsilon^{\mathbf{u}}_{\mathbf{n}} = [\mathbf{p}^T_{\epsilon^u_n}, \mathbf{v}^T_{\epsilon^u_n}]^T$ (purple vector). The velocity-correction $\Delta\mathbf{v}^{(N)}$ (blue vector) is then calculated at $\mathbf{x} + \epsilon^{\mathbf{u}}_{\mathbf{n}}$ and applied back at $\mathbf{x}$. The maneuver execution error $\epsilon^{\mathbf{u}}_{\mathbf{m}}$ (orange vector) is aligned with the projection of $\mathcal{E}^u(\overline{T}, \mathbf{x})$ on the local velocity subspace (red solid thin line) and added to $\Delta\mathbf{v}^{(N)}$ to form the final delta-v $\Delta\mathbf{v}_{SKM}$ (green vector) which is applied to the spacecraft. Note that $\Delta\mathbf{v}^{(N)}$, $\epsilon^{\mathbf{u}}_{\mathbf{m}}$, and $\Delta\mathbf{v}_{SKM}$ are contained in planes parallel to the one spanned by $\{\hat{\mathbf{v}}_\mathbf{1}, \hat{\mathbf{v}}_\mathbf{2}\}$.

The simulations are carried out for seven reference orbits of four different types: halo, quasihalo, Lyapunov horizontal, and Lissajous. The orbits are all in the neighborhood of L_1. The details for such orbits, which also include the x, y, and z amplitudes and specific energy, are summarized in Table 3.12. The x-amplitude of an orbit is defined as $A_x = 0.5(x_{max} - x_{min})$, where x_{max} and x_{max} are the maximum and minimum x-coordinates, respectively. Analogously, we can define A_y and A_z. We present the results of the stationkeeping simulations in terms of average annual delta-v

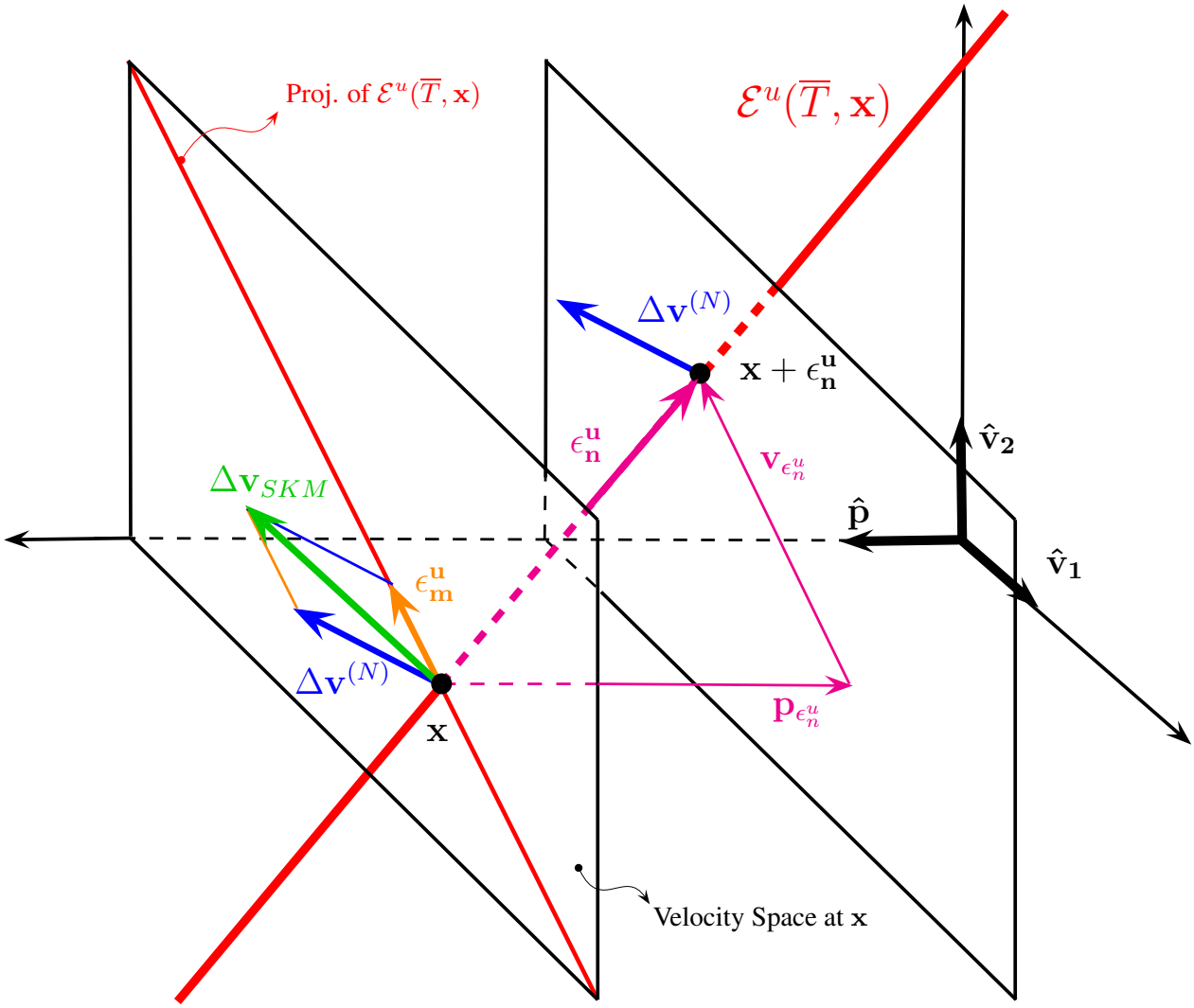

Figure 3.38: Fictitious 3D space with 1D position space and 2D velocity space in which the navigation and maneuver execution errors are illustrated.

Table 3.12: The table includes the types of the reference orbits used in the simulations, their specific energy, and their spatial amplitudes A_x, A_y, and A_z, measured in kilometers. The last three columns contain the maximum absolute variation in amplitude $|\delta A_x|$,$|\delta A_y|$, and $|\delta A_z|$, between the reference and the simulated orbits, measured in km. The per cent variations, relative to the reference orbits' amplitudes, are given in parentheses.

Ref. Orbit	Energy	A_x	A_y	A_z	$\lvert\delta A_x\rvert$(%)	$\lvert\delta A_y\rvert$(%)	$\lvert\delta A_z\rvert$(%)
I-Halo	-1.582	7,234	25,268	12,887	73 (1.0%)	200 (0.8%)	247 (1.9%)
II-Lyap.Hor.	-1.572	11,122	38,959	0	62 (0.6%)	173 (0.4%)	0 (–)
III-Quasihalo	-1.569	11,475	39,470	31,084	24 (0.2%)	51(0.1%)	91 (0.3%)
IV-Lyap.Hor.	-1.561	14,741	49,601	0	49 (0.3%)	134 (0.3%)	0 (–)
V-Lissajous	-1.554	14,227	45,402	50,732	171 (1.2%)	507(1.1%)	131 (0.3%)
VI-Quasihalo	-1.541	16,180	47,791	41,006	15 (0.1%)	42 (0.1%)	88 (0.2%)
VII-Quasihalo	-1.533	18,085	51,431	44,815	65 (0.4%)	374 (0.7%)	28 (0.1%)

budget measured in m/s as a function of the time between successive stationkeeping maneuvers, which has been set to vary from 1 day to 7 days. As shown in Fig. 3.39, given any reference trajectory, the yearly fuel consumption has a minimum in correspondence to a time between SKM between 2 and 3 days. Fixing a time between maneuvers, the annual fuel consumption increases as the energy associated with the orbit decreases and appears not to depend on the type of orbit the spacecraft is shadowing.

To assess the efficiency of the stationkeeping, we finally compare the dimension of the corrected orbits, that is, the actual orbits the spacecraft is on, with the dimension of the orbits of reference. The idea is that, if the stationkeeping procedure is successful, the reference and real orbits will be close to each other. To do so, we first consider the absolute values of the difference in amplitudes between the actual and the reference trajectory, which are indicated with $|\delta A_x|$, $|\delta A_y|$, and $|\delta A_z|$, and are reported in Table 3.12. Note that the amplitudes of the corrected trajectories are, in each direction, always within 2.0% of the reference ones. Two orbits can have the same spatial amplitudes, but still be very far from each other. For this reason, it is important to also consider the maximum difference between the maximum (and minimum) coordinates that define the "spatial boundaries"

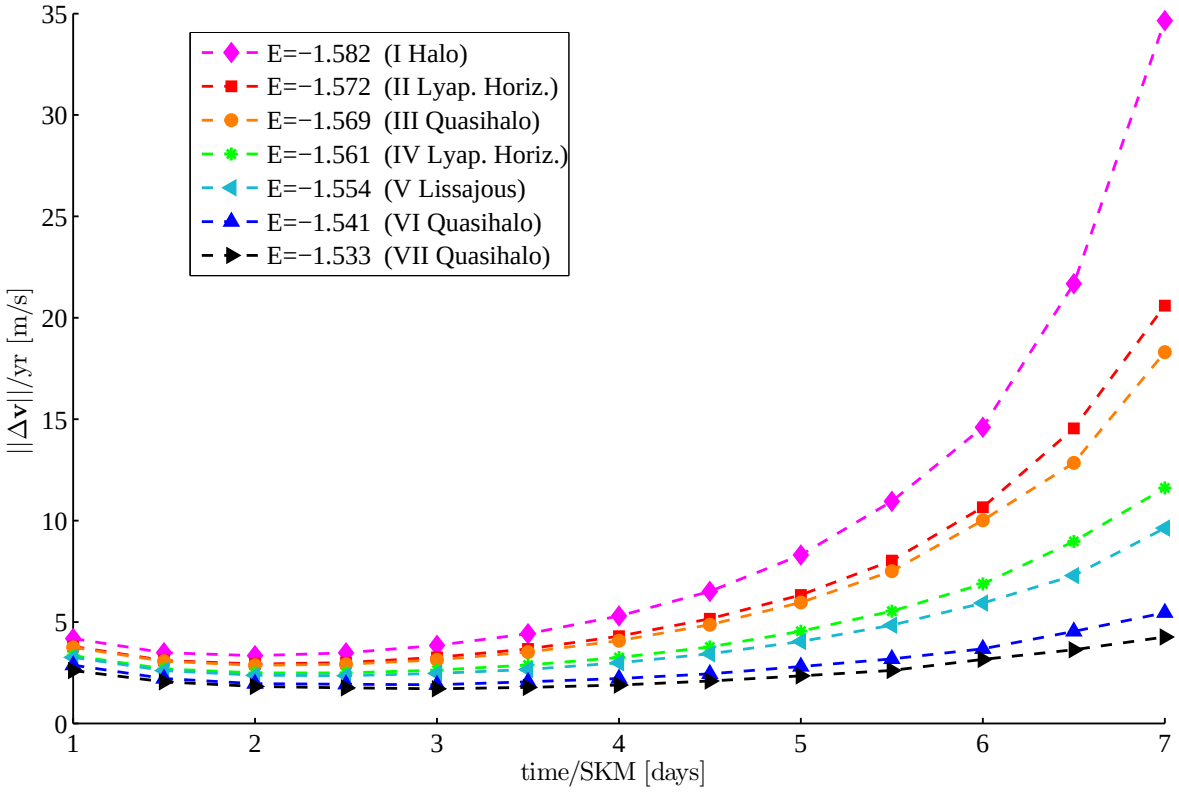

Figure 3.39: Delta-v yearly budget in m/s for six different orbits. The minima of the curves represent the times between two successive SKM that minimize the yearly fuel consumption.

Table 3.13: Maximum difference between the maximum (and minimum) coordinates that define the "spatial boundaries" of the orbits, for the trajectories corrected via FTLA stationkeeping procedure when compared to the reference trajectories of Table 3.12. In parentheses, the per cent errors relative to the amplitude of the orbit in the corresponding direction.

Ref. Orbit	$\lvert\delta x_{min}\rvert$(%)	$\lvert\delta x_{max}\rvert$(%)	$\lvert\delta y_{min}\rvert$(%)	$\lvert\delta y_{max}\rvert$(%)	$\lvert\delta z_{min}\rvert$(%)	$\lvert\delta z_{max}\rvert$(%)
I-Halo	51 (0.7%)	95 (1.3%)	200 (0.8%)	201 (0.8%)	232 (1.8%)	262 (2.0%)
II-Lyap.Hor.	40 (0.4%)	85 (0.8%)	187 (0.5%)	159 (0.4%)	0 (–)	0 (–)
III-Quasihalo	71 (0.6%)	51 (0.4%)	62 (0.2%)	70 (0.2%)	126 (0.4%)	56 (0.2%)
IV-Lyap.Hor.	23 (0.2%)	77 (0.5%)	136 (0.3%)	133 (0.3%)	0 (–)	0 (–)
V-Lissajous	149 (1.0%)	194 (1.4%)	552 (1.2%)	462 (1.0%)	171 (0.3%)	92 (0.2%)
VI-Quasihalo	10 (0.1%)	27 (0.2%)	49 (0.1%)	35 (0.1%)	138 (0.3%)	38 (0.1%)
VII-Quasihalo	132 (0.7%)	41 (0.2%)	447 (0.9%)	42 (0.1%)	21 (<0.1%)	35 (0.1%)

of the orbits. Such differences are indicated with $|\delta x_{min}|$, $|\delta x_{max}|$, $|\delta y_{min}|$, $|\delta y_{max}|$, $|\delta z_{min}|$, and $|\delta z_{max}|$ and are reported in Table 3.13 along with the per cent displacement relative to the spatial amplitude in the corresponding direction. Similarly to the amplitude relative differences, also the maximum relative boundary displacements never exceed 2.0%. In case a reference orbit is not provided, but only some bounds in the excursion of the orbit are given (i.e., its amplitudes), as it is for the JWST (74), one could use the FTLA stationkeeping information to preliminary design one or more orbits that fulfill those mission requirements.

3.5 Limits of Finite-Time Lyapunov Analysis Applicability to Earth-Moon CR3BP

Although stationkeeping via FTLA has been shown reliable and more precise than the extended Floquet analysis for aperiodic orbits, there are some limitations to its applicability. In particular, for orbits around the libration point L_1, FTLA fails when the time interval between maneuvers and/or the magnitude of the errors are too high. When the magnitude of the errors are kept within a realistic range, even the worst case scenario can be handled for maneuvers that occur at most

every 7-8 days between each other. Regardless of the magnitude of the errors and of the type of reference orbits, our methodology cannot be applied to stationkeeping for orbits whose specific energies are higher than approximately -1.52 for the L_1 case. The reasons for this failure are not completely clear at this stage, but we hypothesize that the fact that a high energy level allows more of the phase space to be explored, higher-energy trajectories are less controllable when it comes to stationkeeping via the described algorithm. In fact, simply placing the spacecraft on a center-stable manifold of an orbit, does not guarantee that the destination trajectory (although the energy is preserved) is in the neighborhood of the reference one, or even in the phase space region of interest. A common failing case is that of a spacecraft orbiting around L_1 which is placed on a center-stable manifold of an orbit around another libration point (typically L_2). To avoid such scenarios, we recommend applying the algorithm only to orbits with specific energies less than -1.52. For orbits around L_3, the time interval between maneuvers can be greatly extended due to the less unstable nature of the phase space around L_3. Based on simulation results, we recommend to apply FTLA to orbits with $E \leq -1.50$.

Chapter 4

Solving Partially Hyper-Sensitive Optimal Control Problems Using Manifold Structure

The chapter is organized as follows. We first provide a brief description of a partially hyper-sensitive optimal control problem (PHOCP). We then describe the application of finite-time Lyapunov analysis to it. The following section describes in great detail the strategy used for approximating the solution to partially hyper-sensitive optimal control problems. Lastly, we show the results of the approach when applied to a specific example.

This chapter is an adaptation of work that was published as ref.(5), co-authored with Dr. Erkut Aykutluğ and Prof. Kenneth D. Mease. My specific contributions are in sections 4.3, 4.3.3, 4.3.4, and 4.4.

4.1 Optimal Control Problem and Associated Hamiltonian Boundary-Value Problem

We consider the Lagrangian optimal control problem: determine the control function u on the time interval $[0, t_f]$ that minimizes the cost function

$$\mathrm{J} = \int_0^{t_f} L(x(t), u(t))dt \tag{4.1}$$

$$\begin{aligned} \text{subject to} \qquad & \dot{x} = f(x, u) \\ & x(0) = x_0,\ x(t_f) = x_f \end{aligned}$$

where we assume that the vector field, $f(x, u)$, and $L(x, u)$ are smooth in both x and u, and that t_f is given. The state vector $x(t) \in \mathbb{R}^k$ and the control $u(t) \in \mathbb{R}^m$. The first-order necessary conditions for optimality lead to the Hamiltonian boundary-value problem (HBVP)

$$\begin{aligned} \dot{x} &= \frac{\partial H^*}{\partial \lambda} \\ \dot{\lambda} &= -\frac{\partial H^*}{\partial x} \\ x(0) = x_0, \quad &\text{and} \quad x(t_f) = x_f, \end{aligned} \tag{4.2}$$

where $\lambda(t) \in \mathbb{R}^k$ is the costate vector and $H^* = L(x, u^*) + \lambda^T f(x, u^*)$ is the Hamiltonian evaluated at the optimal control $u^*(x(t), \lambda(t)) = \arg\min H(x(t), \lambda(t), u(t))$. We assume u^* is a smooth function of x and λ. The augmented state $\mathbf{x} = (x^T, \lambda^T)^T$

$$\dot{\mathbf{x}} = \mathbf{h}(\mathbf{x}) \tag{4.3}$$

where $\mathbf{h}(\mathbf{x}) = (\partial H/\partial \lambda, -\partial H/\partial x)^T$ is the Hamiltonian vector field[1]. The linearized dynamics

$$\dot{\mathbf{v}} = D\mathbf{h}(\mathbf{x})\mathbf{v}. \tag{4.4}$$

are analyzed to characterize the timescales and associated phase space geometry for the flow of (4.3).

4.1.1 Hyper-Sensitivity

If numerical solution of an OCP proves difficult and reducing the final time alleviates the difficulty, hyper-sensitivity should be investigated. By observing how the solution evolves as t_f is varied, the relevant phase space region can be identified. Using finite-time Lyapunov analysis, as described in the next section, on a grid of phase points in this region, the spectrum of exponential rates can be determined. If the spectrum uniformly separates into fast-stable, slow, and fast-unstable subsets, and the 'fast' rates are indeed fast relative to the time interval of interest, then hyper-sensitivity is confirmed. To describe the general case, let k be the dimension of the state dynamics; then it follows that $n = 2k$ is the dimension of the associated Hamiltonian system. The spectrum also reveals the equal dimensions, n^s and n^u, of the fast-stable and fast-unstable behavior, respectively. If $n^s + n^u = n$, then the OCP is completely hyper-sensitive. If $n^s + n^u < n$, then the OCP is partially hyper-sensitive.

[1]We use the notation 'x' to indicate the state vector only, while the Hamiltonian phase space vector, which comprises both the state and costate vectors, is indicated with boldface '$\mathbf{x}$'.

4.2 Finite-Time Lyapunov Analysis Applied to PHOCP

In the present context, the goal of FTLA is to determine if the nonlinear Hamiltonian system, $\dot{\mathbf{x}} = \mathbf{h}(\mathbf{x})$, has, at each point $\mathbf{x}$ in a neighborhood $\mathcal{X} \subset \mathbb{R}^n$ of the solution of interest, a tangent space splitting $T_{\mathbf{x}}\mathbb{R}^n = \mathcal{V}^s(\mathbf{x}) \oplus \mathcal{V}^c(\mathbf{x}) \oplus \mathcal{V}^u(\mathbf{x})$, where all the vectors in the fast-stable subspace $\mathcal{V}^s(\mathbf{x})$ contract exponentially fast in forward time and all the vectors in the fast-unstable subspace $\mathcal{V}^u(\mathbf{x})$ contract exponentially fast in backward time, and all the vectors in the slow (i.e., center) subspace $\mathcal{V}^c(\mathbf{x})$ change more slowly, under the linearized Hamiltonian flow. Note that in the finite-time setting, we use the terms stable and unstable for simplicity, even though fast contracting and fast expanding are more appropriate. Also we use the term center for the subspace associated with the FTLEs of small, but not necessarily zero, magnitude. In the asymptotic theory of partially hyperbolic sets (6; 32), the splitting is invariant, however, when defined in terms of finite-time Lyapunov exponents and vectors (FTLE/Vs), the splitting only approximates an invariant splitting. Associated with the splitting is a manifold structure as depicted in Fig. 4.1.

4.3 Solution Approximation Approach

The approach for approximating the solution to partially hyper-sensitive optimal control problems comes from observing that such solution shadows for most of the time some trajectory on the invariant center manifold $\mathcal{W}^c$. The shadowed trajectory σ can be found as the intersection between the center-stable and center-unstable manifolds that contain σ.

$$\sigma = \mathcal{W}^{cs}(\sigma) \cap \mathcal{W}^{cu}(\sigma) \tag{4.5}$$

where $\mathcal{W}^{cs}(\sigma)$ and $\mathcal{W}^{cu}(\sigma)$ denote the center-stable and the center-unstable containing σ. Such manifolds have equal dimensions

$$dim(\mathcal{W}^{cs}(\sigma)) = n^s + 1 = n^u + 1 = dim(\mathcal{W}^{cu}(\sigma)), \tag{4.6}$$

and they are submanifolds of the global center-stable and center-unstable invariant manifolds, namely,

$$\begin{aligned} &\mathcal{W}^{cs}(\sigma) \subset \mathcal{W}^{cs}, \quad dim(\mathcal{W}^{cs}) = n^c + n^s, \\ &\mathcal{W}^{cu}(\sigma) \subset \mathcal{W}^{cu}, \quad dim(\mathcal{W}^{cu}) = n^c + n^u. \end{aligned} \tag{4.7}$$

The optimal solution has an initial boundary layer that shadows a trajectory on the center-stable manifold $\mathcal{W}^{cs}(\sigma)$. Analogously, the final boundary-layer segment of the optimal solution shadows a trajectory contained on the center-unstable manifold $\mathcal{W}^{cu}(\sigma)$. The shadowed trajectory on $\mathcal{W}^{cs}(\sigma)$ will approach asymptotically the centrer-manifold trajectory σ forward in time, while the shadowed trajectory on $\mathcal{W}^{cu}(\sigma)$ will approach σ backward in time. The strategy therefore utilizes the shadowed trajectories on the three manifolds to approximate the optimal solution. Figure 4.1 shows the initial boundary-layer trajectory on the center-stable manifold $\mathcal{W}^{cs}(\sigma)$ (in blue), the central trajectory σ on the center manifold $\mathcal{W}^{c}$ (in black), and the final boundary layer on the center-unstable manifold $\mathcal{W}^{cu}(\sigma)$ (in red).

The goal is to formulate conditions to compute, in the phase space, the initial condition $\mathbf{x}(t_0)$ and the final condition $\mathbf{x}(t_f)$, such that the initial and final segments departing from such points lie on $\mathcal{W}^{cs}(\sigma)$ and $\mathcal{W}^{cu}(\sigma)$ respectively.

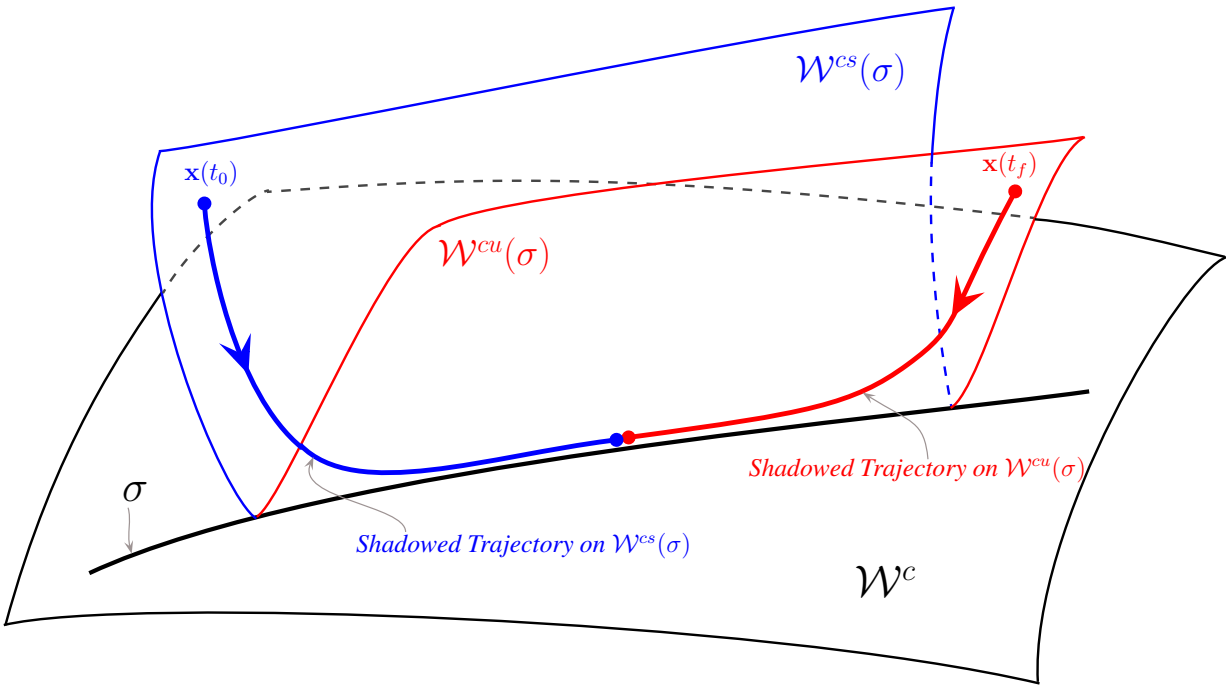

Figure 4.1: Geometry of the solution to partially hyper-sensitive optimal control problem in the Hamiltonian phase space. The center manifold $\mathcal{W}^c$ is even-dimensional and the black curve σ represents the shadowed trajectory on it. The solution is comprised of two shadowed trajectory segments, the first on the center-stable manifold of σ, $\mathcal{W}^{cs}(\sigma)$ (blue curve) and the second the center-stable manifold of σ, $\mathcal{W}^{cu}(\sigma)$ (red curve).

4.3.1 Matching on Slow Manifold

The initial and final conditions are points in $\mathbb{R}^n$ and

$$\begin{aligned} \mathbf{x}(t_0) &= (x(t_0)^T, \lambda(t_0)^T)^T, \\ \mathbf{x}(t_f) &= (x(t_f)^T, \lambda(t_f)^T)^T, \end{aligned} \tag{4.8}$$

where $x(t_0)$ and $x(t_f)$ are the known k-dimensional initial and final states, while $\lambda(t_0)$ and $\lambda(t_f)$ represent the k-dimensional unknown initial and final costates, respectively. The initial costate $\lambda(t_0)$ must be chosen so that the initial phase point $\mathbf{x}(t_0)$ lies on the center-stable manifold $\mathcal{W}^{cs}(\sigma)$, while the final costate $\lambda(t_f)$ must be chosen so that the final phase point $\mathbf{x}(t_f)$ is on the center-unstable manifold $\mathcal{W}^{cu}(\sigma)$. This leaves us with $k + k = n$ degrees of freedom, which correspond

to the coordinates of the boundary costates $\lambda(t_0)$ and $\lambda(t_f)$.

For the initial boundary layer, we suppress the fast unstable behavior forward in time, that is, we choose the initial costate $\lambda(t_0)$ so that the initial phase point $\mathbf{x}(t_0)$ is on the $(n^s + n^c)$-dimensional center-manifold $\mathcal{W}^{cs}$, which contains the center-stable manifold $\mathcal{W}^{cs}(\sigma)$, which, in turn, contains the trajectory σ on the center manifold. The remaining $k - n^u$ degrees of freedom are used to control the trajectory on $\mathcal{W}^{cs}$ and in particular, what trajectory it will approach on the center manifold $\mathcal{W}^c$. Similarly, choosing the unknown final costate $\lambda(t_f)$ so that the final phase point $\mathbf{x}(t_f)$ is on the center-unstable manifold $\mathcal{W}^{cu}$, suppresses the fast unstable behavior for backward time integration, and leaves $k-n^s$ degrees of freedom to control the final boundary-layer trajectory and in particular, what trajectory it will approach on the center manifold. These degrees of freedom are used to match the forward and backward trajectories, within a specified tolerance, and construct a composite (approximate) solution.

More specifically, of the k unknown initial conditions, n^u are specified to place $\mathbf{x}(t_0)$ on $\mathcal{W}^{cs}$, whereas the remaining $k - n^u$ determine which trajectory will be approached on $\mathcal{W}^c$ (ideally, that would be σ). Similarly, of the k unknown final conditions, n^s are specified to place $\mathbf{x}(t_f)$ on $\mathcal{W}^{cu}$, while the remaining $k - n^s$ determine which trajectory will be approached on $\mathcal{W}^c$ (ideally, that would still be σ). This means that $k - n^u$ initial conditions and $k - n^s$ final conditions are adjusted to achieve matching on $\mathcal{W}^c$ at a selected matching time $t_m \in (0, t_f)$. Since the matching time $t = t_m$ is finite, the forward and backward trajectories will not meet exactly on the center manifold, nor will they end at the same exact point. Therefore, we allow a discontinuity in the solution at $t = t_m$. Such discontinuity is inevitable, but it will be specified to be within a certain tolerance. Denoting with $\mathbf{x}(t_m)^+ = \phi(t_m, \mathbf{x}(t_0))$ the end point of the forward trajectory and with $\mathbf{x}(t_m)^- = \phi(-(t_f - t_m), \mathbf{x}(t_f))$ the end point of the backward trajectory at time $t = t_m$, we define

the matching distance as

$$d_m = ||\mathbf{x}(t_m)^+ - \mathbf{x}(t_m)^-|| < tol_{d_m} \tag{4.9}$$

where tol_{d_m} is a prescribed matching distance tolerance. In this context and throughout this chapter, ϕ is not intended as the exact mapping as seen in 2.1, but it refers to the approximate mapping given by the particular numerical integrator that is used. Figure 4.2 shows the forward and backward trajectories meeting on the center manifold. The matching distance has been exaggerated for representation purposes. Rather than determining all k unknown conditions either at the initial

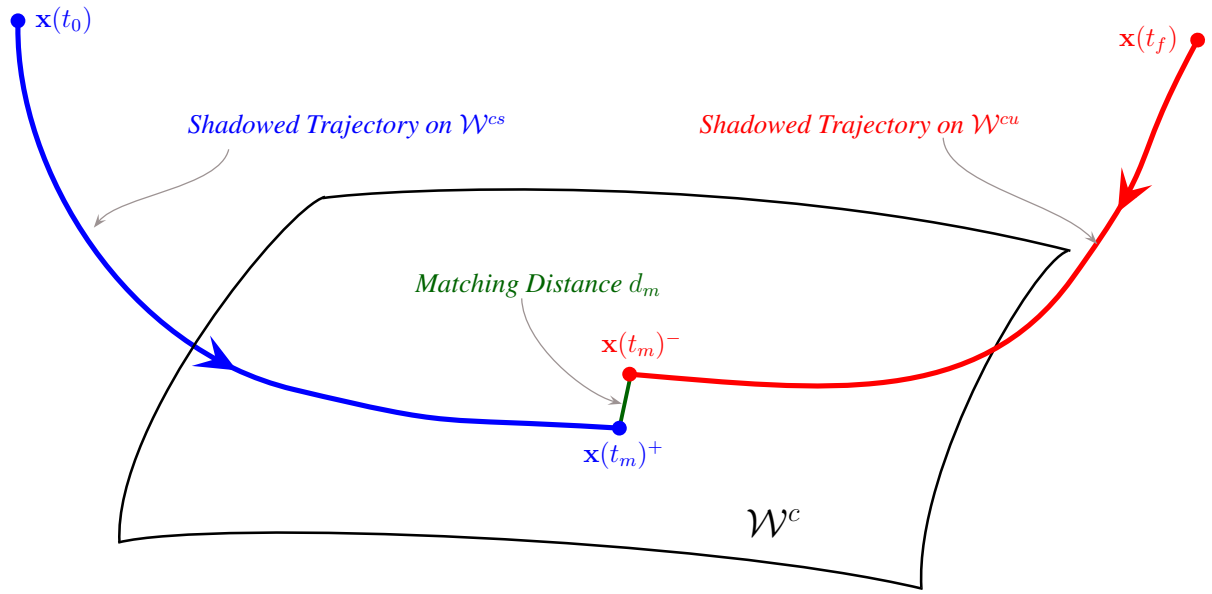

Figure 4.2: Shadowed trajectories on center-stable manifold $\mathcal{W}^{cs}$ (blue curve) and on center-unstable manifold $\mathcal{W}^{cu}$ (red curve) meeting on the center manifold $\mathcal{W}^c$. The distance between the end points of the forward trajectory ($\mathbf{x}(t_m)^+$) and of the backward trajectory ($\mathbf{x}(t_m)^-$) is denoted with d_m. The magnitude of d_m is purposely exaggerated to illustrate the concept.

time or the final time such that the boundary conditions at the other end are satisfied, which would be very difficult due to the hyper-sensitivity, we determine $k - n^u$ and $k - n^s$ boundary conditions at each end, so that a solution is constructed by matching somewhere in the middle, and approximately on the center manifold $\mathcal{W}^c$. The remaining n^u and n^s unknown boundary conditions at each

end are determined such that the fast-unstable motion is suppressed in the direction of integration. This strategy was first proposed by S.-H. Lam, circa 1990.

4.3.2 Computing Boundary Conditions on Invariant Manifolds

Assume the columns of a matrix B form a basis for the tangent space $T_{\mathbf{x}}\mathbb{R}^n$ at each phase point $\mathbf{x}$, consistent with the partially hyperbolic Lyapunov spectrum. Further, let us assume the structure

$$B(\mathbf{x}) = [B^s(\mathbf{x})\ B^c(\mathbf{x})\ B^u(\mathbf{x})], \tag{4.10}$$

where $B^s(\mathbf{x}) \in \mathbb{R}^{n\times n^s}$, $B^c(\mathbf{x}) \in \mathbb{R}^{n\times n^c}$, and $B^u(\mathbf{x}) \in \mathbb{R}^{n\times n^u}$ contain the column vectors that span the stable, center and unstable subspaces, respectively. At each phase point $\mathbf{x}$, the vector $\mathbf{h}(\mathbf{x})$ can be expressed as

$$\dot{\mathbf{x}} = \mathbf{h}(\mathbf{x}) = B^s(\mathbf{x})w_s(\mathbf{x}) + B^c(\mathbf{x})w_c(\mathbf{x}) + B^u(\mathbf{x})w_u(\mathbf{x}), \tag{4.11}$$

where $w_s(\mathbf{x})$, $w_c(\mathbf{x})$ and $w_u(\mathbf{x})$ are determined by

$$\begin{aligned} w_s(\mathbf{x}) &= [B^s(\mathbf{x})]^\dagger \mathbf{h}(\mathbf{x}), \\ w_c(\mathbf{x}) &= [B^c(\mathbf{x})]^\dagger \mathbf{h}(\mathbf{x}), \\ w_u(\mathbf{x}) &= [B^u(\mathbf{x})]^\dagger \mathbf{h}(\mathbf{x}). \end{aligned} \tag{4.12}$$

with $[B^s(\mathbf{x})]^\dagger \in \mathbb{R}^{n^s\times n}$, $[B^c(\mathbf{x})]^\dagger \in \mathbb{R}^{n^c\times n}$ and $[B^u(\mathbf{x})]^\dagger \in \mathbb{R}^{n^u\times n}$ composed of the appropriate rows of $B(\mathbf{x})^{-1}$, respectively.

Placing the Initial Point on $\mathcal{W}^{cs}$

To place the initial phase point on the center-stable manifold, $\mathcal{W}^{cs}$, we impose the condition

$$w_u = 0$$

that is, the unstable dynamics are suppressed.

Assuming that there is a splitting of the tangent space at $\mathbf{x}(t_0) = \mathbf{x}_0$, such that

$$T_{\mathbf{x}_0}\mathbb{R}^n = \mathcal{V}^{cs}(\mathbf{x}_0) \oplus [\mathcal{V}^{cs}(\mathbf{x}_0)]^{\perp},$$

where $\mathcal{V}^{cs}(\mathbf{x}_0)$ represents the center-stable linear subspace at $\mathbf{x}_0$, which is the direct sum of stable and center linear subspaces $\mathcal{V}^{cs}(\mathbf{x}_0) = \mathcal{V}^{s}(\mathbf{x}_0) \oplus \mathcal{V}^{c}(\mathbf{x}_0)$. $[\mathcal{V}^{cs}(\mathbf{x}_0)]^{\perp}$ is the orthogonal complement of $\mathcal{V}^{cs}(\mathbf{x}_0)$. If $\mathbf{x}_0$ were on the center-stable manifold $\mathcal{W}^{cs}$, we would have that $w_u(\mathbf{x}_0) = 0$ and then the following condition would hold

$$< \mathbf{h}(\mathbf{x}_0), \mathbf{w} >= 0, \ \forall \mathbf{w} \in [\mathcal{V}^{cs}(\mathbf{x}_0)]^{\perp}. \tag{4.13}$$

We can approximate the subspace $\mathcal{V}^{cs}(\mathbf{x}_0)$ with the finite-time Lyapunov subspace $\mathcal{E}^{cs}(\mathbf{x}_0)$, can be obtained by using the finite-time Lyapunov vectors

$$\mathcal{E}^{cs}(T, \mathbf{x}_0) = span\{\mathbf{l}_1^{+}(T, \mathbf{x}_0), \cdots, \mathbf{l}_{n^s+n^c}^{+}(T, \mathbf{x}_0)\}$$

and an approximation of the subspace $[\mathcal{V}^{cs}(\mathbf{x}_0)]^{\perp}$ is

$$[\mathcal{E}^{cs}(T, \mathbf{x}_0)]^{\perp} = span\{\mathbf{l}_{n^s+n^c+1}^{+}(T, \mathbf{x}_0), \cdots, \mathbf{l}_{n}^{+}(T, \mathbf{x}_0)\}.$$

Equation 4.13 provides the n^u conditions that are needed for placing the initial point on $\mathcal{W}^{cs}$.

Placing the Final Point on $\mathcal{W}^{cu}$

The procedure for placing the final point on the center-unstable invariant manifold is similar to what described in the last paragraph. Assume that at $\mathbf{x}(t_f) = \mathbf{x}_f$, there is a splitting of the tangent space

$$T_{\mathbf{x}_f}\mathbb{R}^n = \mathcal{V}^{cu}(\mathbf{x}_f) \oplus [\mathcal{V}^{cu}(\mathbf{x}_f]^{\perp},$$

where $\mathcal{V}^{cu}(\mathbf{x}_f) = \mathcal{V}^{u}(\mathbf{x}_f) \oplus \mathcal{V}^{c}(\mathbf{x}_f)$ and $[\mathcal{V}^{cu}(\mathbf{x}_f)]^{\perp}$ is its orthogonal complement. If $\mathbf{x}_f$ were on the center-unstable manifold, i.e., if $w_s(\mathbf{x}_f) = 0$, then the following condition would hold

$$< \mathbf{h}(\mathbf{x}_f), \mathbf{w} >= 0, \ \forall \mathbf{w} \in [\mathcal{V}^{cu}(\mathbf{x}_f)]^{\perp}. \tag{4.14}$$

Approximations to subspaces $\mathcal{V}^{cu}(\mathbf{x}_f)$ and $[\mathcal{V}^{cu}(\mathbf{x}_f)]^{\perp}$ can be obtained by using finite-time Lyapunov vectors

$$\mathcal{E}^{cu}(T, \mathbf{x}_f) = span\{\mathbf{l}^{-}_{n^s+1}(T, \mathbf{x}_f), \cdots, \mathbf{l}^{-}_{n}(T, \mathbf{x}_f)\}$$

and

$$[\mathcal{E}^{cu}(T, \mathbf{x}_f)]^{\perp} = span\{\mathbf{l}^{-}_{1}(T, \mathbf{x}_f), \cdots, \mathbf{l}^{-}_{n^s}(T, \mathbf{x}_f)\}.$$

Using these finite-time Lyapunov subspaces and the orthogonality conditions in Eq. (4.13) and (4.14), one can choose the unknown boundary conditions to locate the initial and final phase points approximately on the appropriate invariant manifolds. Then the Hamiltonian system can

be integrated forward or backward in time to reach the center invariant manifold, matching on it. However, because the boundary conditions are only approximately on the invariant manifolds, that is, $\mathbf{x}(t_0) \notin \mathcal{W}^{cs}$ and $\mathbf{x}(t_f) \notin \mathcal{W}^{cu}$, the trajectories will depart from the manifolds. The procedure in the next subsection re-initializes the integration to keep the trajectory close to the invariant manifold.

4.3.3 Re-Initialization Procedure

In this subsection we describe the re-initialization procedure that repeatedly places the evolving phase trajectory in the proximity of $\mathcal{W}^{cs}$. For the initial segment of the solution, we are ideally computing a trajectory on $\mathcal{W}^{cs}$. However, because the initialization of $\mathbf{x}(t_0)$ on $\mathcal{W}^{cs}$ is only approximate, the trajectory will start off of $\mathcal{W}^{cs}$ and depart farther with time due to the residual fast-unstable component of the vector field.

At $t = 0$, assuming that the orthogonality conditions are satisfied exactly, a fast-unstable component of the vector field will remain. The fast-unstable component of the vector field that cannot be suppressed is

$$w_u(\mathbf{x}_0) = [B^u(\mathbf{x}_0)]^\dagger \hat{B}^{cs}(T, \mathbf{x}_0)\mathbf{h}(\mathbf{x}_0)$$

where

$$\hat{B}^{cs}(T, \mathbf{x}_0) = \hat{B}^s(T, \mathbf{x}_0)[\hat{B}^s(T, \mathbf{x}_0)]^\dagger + \hat{B}^c(T, \mathbf{x}_0)[\hat{B}^c(T, \mathbf{x}_0)]^\dagger.$$

When we map this component forward in time, we get

$$w_u(t) = \Phi_u(t, \mathbf{x}_0)([B^u(\mathbf{x}_0)]^\dagger \hat{B}^{cs}(T, \mathbf{x}_0)\mathbf{h}(\mathbf{x}_0)).$$

To force the trajectory to follow $\mathcal{W}^{cs}$ more closely, the phase is re-initialized periodically to bring it closer to $\mathcal{W}^{cs}$ and reduce w_u. Let $[0, t_m]$ be subdivided into intervals $[t_{i-1}, t_i],\ i = 1, ..., j$, where $t_0 = 0$ and $t_j = t_m$. By imposing $w_u(t_i) = 0$, for $i = 1, \cdots, j$, and updating the current phase point $\phi(\mathbf{x}(t_i), \Delta t_i)$ to $\mathbf{x}(t_{i+1})$, with Δt_i being the propagation time $\Delta t_i = t_i - t_{i-1}$, we place the phase point closer to the invariant manifold at each t_i. Figure 4.3 illustrates the re-initialization procedure for $i = 1, 2, 3, 4$. The initial guess $\mathbf{x}^0$ is placed approximately on $\mathcal{W}^{cs}$ (initialization). From the resulting phase point $\mathbf{x}(t_0)$, the trajectory is propagated forward in time for Δt_1, reaching the point $\phi(\mathbf{x}(t_0), \Delta t_1)$. Now we apply another FTLA correction (re-initialization) in order to bring back the point close to $\mathcal{W}^{cs}$. The procedure is repeated until the matching time is reached and the trajectory has approached the center manifold $\mathcal{W}^{c}$. In the figure the continuous line represents the shadowed trajectory on $\mathcal{W}^{c}$, while the dashed lines represent the approximate solution to the optimal control problem. As it can be seen, the re-initialization procedure introduces discontinuities in the solution (in the figure their size is purposely exaggerated) and the trajectory approximation is the union of all the dashed segments. The magnitude of the discontinuities could be reduced by increasing the frequency of the corrections (i.e., by decreasing Δt_i). In fact, the unstable component $w_u(t_i + \Delta t_i)$ exponentially increases with time. This would yield to smaller but more numerous discontinuities. On the other hand, one could decide to fix the propagation times Δt_i and thus the number of discontinuities, and reduce their magnitude by increasing the averaging time T used to compute the finite-time Lyapunov vectors and exponents. Both by increasing T and by decreasing Δt_i will increase the computational time required to perform the re-initialization procedure, therefore a trade-off between these quantities must be found.

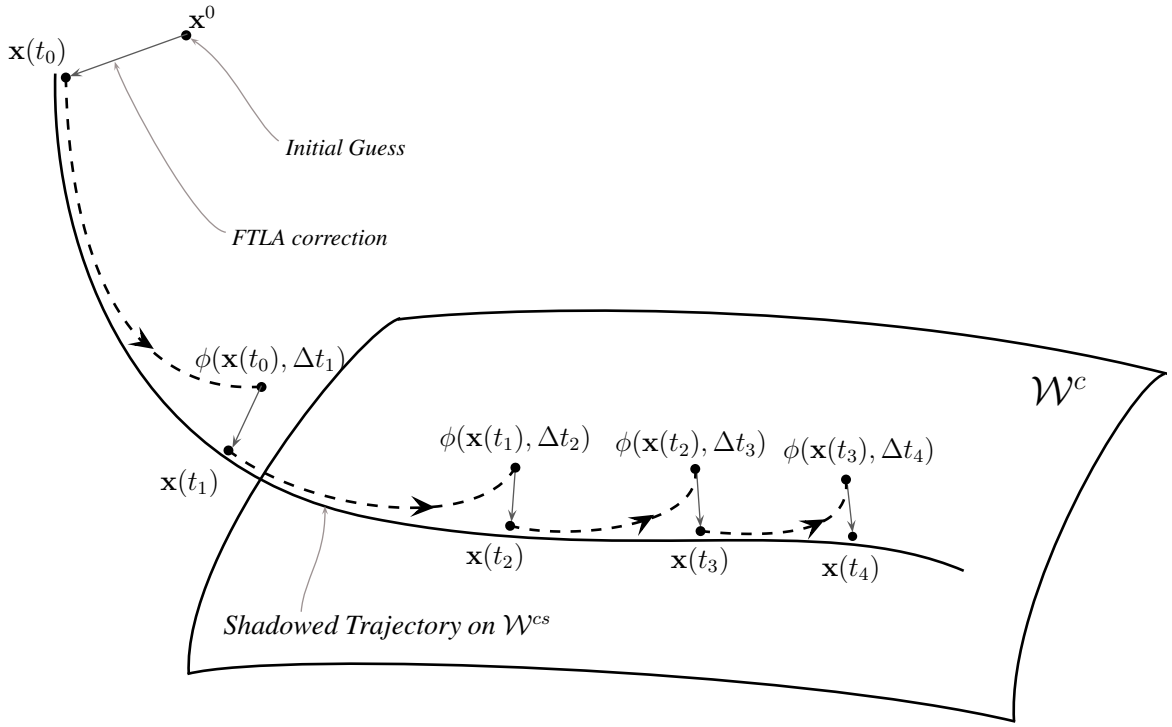

Figure 4.3: Illustration of the re-initialization procedure for the forward segment of the trajectory. The trajectory approximation is discontinuous and it is comprised of the union of the dashed segments. The solid line represents the shadowed trajectory on $\mathcal{W}^{cs}$. $\phi(\mathbf{x}(t_i), \Delta t_i)$ and $\mathbf{x}(t_{i+1})$, $i = 1, 2, 3, 4$, denote the phase space points right before and after the i-th re-initialization.

For the segment of the trajectory that shadows the center-unstable manifold, the re-initialization procedure is analogous, with the only difference being that the propagation happens backward in time and that in this case we are imposing the suppression of the stable component of the vector field $w_s(t_i) = 0$ with $i = N - 1, ..., j$, $t_N = t_f$, and $t_j = t_m$.

4.3.4 Computational Algorithm

The following is the algorithm for computing the approximate solution to the partially hypersensitive optimal control problem. The initial and final states $x(t_0)$ and $x(t_f)$ are given. Select a matching time $t_m \in [0, t_f]$.

Part (a): Forward trajectory segment

1. Initial guess $\mathbf{x}^0$: select $\mathbf{x}^0$ so that $x^0 = x(t_0)$. The k initial costate components are arbitrarily chosen.

2. Placing initial point on $\mathcal{W}^{cs}$: fix $k - n^u$ costate components and determine the remaining n^u costate components by applying steps 1-6 of the algorithm described in 3.2.2.

3. Divide $[0, t_m]$ into intervals $\Delta t_i = t_i - t_{i-1}$ where $i = 1, ..., j$, $t_0 = 0$, and $t_j = t_m$.

4. **For** $i = 1, ..., j$

   Propagation: from $\mathbf{x}(t_{i-1})$, integrate forward in time to obtain $\phi(\mathbf{x}(t_{i-1}), \Delta t_i)$.

   Re-initialization: apply Step 2, Part (a) and obtain $\mathbf{x}(t_i)$.

5. Repeat Steps 1-4, Part (a) for several initial guesses (a $(k - n^u)$-dimensional grid where the $k - n^u$ initial costate components are predetermined) thus obtaining a $(k - n^u)$-parameter family of forward trajectories. For each initial guess, store the values of the phase point $\mathbf{x}(t_m)^+$ (the plus sign indicates that we got to the point by forward integration).

Part (b): Backward trajectory segment

1. Final guess $\mathbf{x}^f$: select $\mathbf{x}^f$ so that $x^f = x(t_f)$. The k initial costate components are arbitrarily chosen.

2. Placing final point on $\mathcal{W}^{cu}$: fix $k - n^s$ costate components and determine the remaining n^s costate components by applying steps 1-6 of the algorithm described in 3.2.2.

3. Divide $[t_m, t_f]$ into intervals $\Delta t_i = t_i - t_{i-1}$ where $i = N, ..., j$, $t_N = t_f$, and $t_j = t_m$.

4. **For** $i = 1, ..., j$

   Propagation: from $\mathbf{x}(t_i)$, integrate backward in time to obtain $\phi(\mathbf{x}(t_i), -\Delta t_i)$.

   Re-initialization: apply Step 2, Part (b) and obtain $\mathbf{x}(t_{i-1})$.

5. Repeat Steps 1-4, Part (b) for several initial guesses (a $(k - n^s)$-dimensional grid where the $k - n^s$ initial costate components are predetermined) thus obtaining a $(k - n^s)$-parameter family of forward trajectories. For each final guess, store the values of the phase point $\mathbf{x}(t_m)^-$ (the minus sign indicates that we got to the point by forward integration) .

Part (c): Matching distance

1. Compute the matching distance $d_m = ||\mathbf{x}(t_m)^+ - \mathbf{x}(t_m)^-||$ for each pair of $\mathbf{x}(t_m)^+$ and $\mathbf{x}(t_m)^-$.

2. Find $d_{m_{min}} = min(d_m)$ and select the pair of initial-final points ($\mathbf{x}(t_0)$, $\mathbf{x}(t_f)$) that led to $d_{m_{min}}$.

3. **If** $d_{m_{min}} < tol_{d_m}$ **then** stop.
   Else, refine grids for initial and final points centered around ($\mathbf{x}(t_0)$, $\mathbf{x}(t_f)$) found in Step 2, Part (c) and repeat the whole procedure starting from Step 1, Part (a).

Notice that the orthogonality conditions to be solved in Step 2, Part (a) and Step 2, Part (b) are given in Eq. (4.13) and (4.14), respectively.

4.4 Test Case: Minimum Energy Control of Spring-Mass-Damper System

We illustrate the approach for the optimal control problem associated with a nonlinear mass-damper-spring mechanical system. A sketch of the system is provided in Fig. 4.4. The mass m is connected to a damper with characteristic constant c, and to a nonlinear spring with coefficients k_1 and k_2. x_1 represents the coordinate along the direction of motion of the mass and is

measured from the rest length of the spring. x_2 is the mass velocity along x_1. Finally, $u(t)$ is the control force which is applied in the x_1 direction. The goal of the optimization problem is to minimize the control effort to move the mass from an initial to a final position in a specified time t_f.

$$\begin{aligned} \text{min} \quad J &= \tfrac{1}{2}\int_0^{t_f} u^2 dt \\ \text{such that} \quad \dot{x_1} &= x_2 \\ m\dot{x_2} &= -k_1 x_1 - k_2 x_1^3 - c x_2 + u \\ x_1(0) &= 2.4, \quad x_2(0) = 0.0, \\ x_1(t_f) &= -2.4, \quad x_2(t_f) = 0.0, \end{aligned} \tag{4.15}$$

The first-order necessary conditions lead to the Hamiltonian boundary-value problem

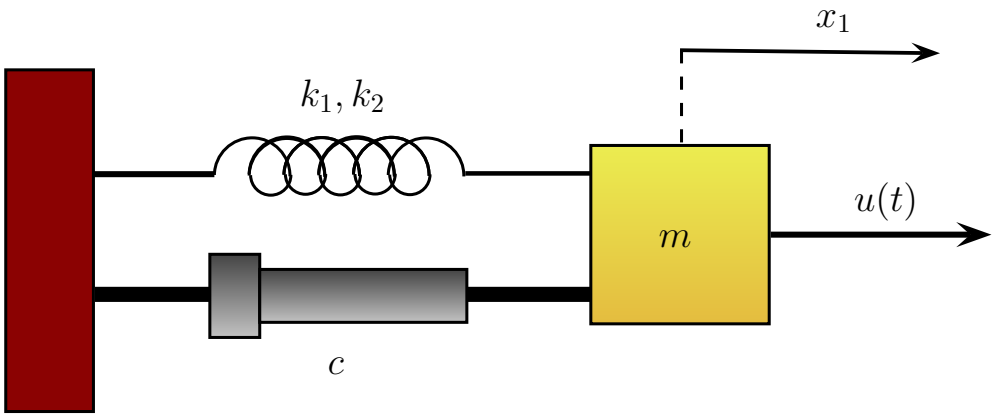

Figure 4.4: Nonlinear spring-mass-damper system as a set up for the optimal control problem. The mass m is connected to a damper with characteristic constant c, and to a nonlinear spring with coefficients k_1 and k_2. x_1 represents the coordinate along the direction of motion of the mass. $u(t)$ is the control force which is applied along x_1.

$$
\begin{aligned}
\dot{x}_1 &= x_2 \\
m\dot{x}_2 &= -k_1 x_1 - k_2 x_1^3 - c x_2 - \tilde{\lambda}_2 \\
\dot{\lambda}_1 &= \tilde{\lambda}_2 (k_1 + 3k_2 x_1^2) \\
m\dot{\tilde{\lambda}}_2 &= -\lambda_1 + c\tilde{\lambda}_2
\end{aligned}
\tag{4.16}
$$

where λ_1 and λ_2 are the costate components associated with x_1 and x_2; furthermore we can rewrite the costate associated with x_2 as $\lambda_2 = m\tilde{\lambda}_2$; see ((41)). The boundary conditions are those on the state given above.

This system has two-timescale behavior when the mass m is sufficiently small. For the numerical results, we use $k_1 = 1$, $k_2 = 0.1$, $c = 1.265$, $m = 0.1$ and $t_f = 2.0$. When the final time is long relative to fast contraction and expansion rates, but not the slow contraction and expansion rates, the optimal control problem is partially hyper-sensitive with $k = 2$, $n = 4$, $n^s = n^u = 1$, and $n^c = 2$. We select a matching time $t_m = t_f/2 = 1.0$. The interval $[0, t_f]$ is divided in $N = 20$ equal segments of duration $\Delta t = 0.1$ each. Since $n^u = 1$ and $n^s = 1$, we have at each end 1 initial costate component that is determined by solving the orthogonality conditions. The remaining $k - n^u + k - n^s = 2$ costate components are the degrees of freedom that are controlled to generate one-parameter families of initial and final boundary trajectories. In particular, for each re-initialization, namely, at each time t_i, we fix $\lambda_1(t_i)$ and compute $\lambda_2(t_i)$ by solving the orthogonality conditions. During the integration of the forward segment of the trajectory we impose

$$
\langle \mathbf{h}(\mathbf{x}(t_i)), \mathbf{l}_4^+(T, \mathbf{x}(t_i)) \rangle = 0, \tag{4.17}
$$

while during the integration of the backward segment we need to solve

$$
\langle \mathbf{h}(\mathbf{x}(t_i)), \mathbf{l}_1^-(T, \mathbf{x}(t_i)) \rangle = 0. \tag{4.18}
$$

The orthogonality conditions can be applied several times to place the phase point closer to the appropriate manifold. As already described in Chapter 1, the solution of such orthogonality conditions is indeed an iterative procedure. At each iteration, the FTLEs gap between the slow and fast exponents becomes more uniform as the phase point gets closer to the center-stable (resp. center-unstable) manifold. When the gap between the slow and fast exponents is uniform for longer times, longer averaging times can be used in finite-time Lyapunov analysis, which leads to better approximation of the ideal asymptotic FTLEs/FTLVs. For the numerical results, an averaging time $T \leq 1.0$ was used in all cases. We select the initial and final costate components $\lambda_1(t_0) = \lambda_1^0$ and $\lambda_1(t_f) = \lambda_1^f$ to generate the two one-parameter families of forward and backward trajectories. These families of trajectories are shown in Fig. 4.5 and 4.6. The blue curves represent the forward segments, while the red curves depict the backward ones. The matching on the center manifold occurs for unique values of $\lambda_1(0)$ and $\lambda_1(t_f)$ which are computed through the technique described in the previous section. Starting from a broad set of values for the initial and final costates, the distance between the end points of each forward and backward trajectory is calculated. Figure 4.7 shows the values of the distance d_m between the end of the forward and backward trajectories for $\lambda_1(t_0) = \lambda_1^0 \in [0.2, 1.4]$ and $\lambda_1(t_f) = \lambda_1^f \in [9.2, 12.0]$. In this example using $\lambda_1(0) = 0.7863$ and $\lambda_1(t_f) = 10.3542$, the forward and backward trajectories are matched with an error less than 0.0001. Figure 4.8 shows the approximation of the optimal solution in 6 two-dimensional projections of the four-dimensional phase space. The blue and red curves represent the portions of the solution that shadows the trajectory on center-stable manifold and on the center-unstable manifold, respectively. The black circular dots are the initial and final points, while the black triangles represent the phase points $\mathbf{x}(t_i)$ after each re-initialization. Figures 4.9, 4.10 and 4.11 show the forward FTLEs for the points from $\mathbf{x}(t_0)$ through $\mathbf{x}(t_{10})^+$, while Figs. 4.12, 4.13 and 4.14 show the backward FTLEs for the points from $\mathbf{x}(t_f)$ through $\mathbf{x}(t_{10})^-$. For each point, the values of the maximum averaging time $\overline{T}$, the FTLEs gap $\Delta\mu$ and the rate of subspace convergence $\Delta\mu(\overline{T} - t_s)$ are reported on the plots. For all the points, we selected $t_s = 0$. As per property 3 of Definition 2.4.1,

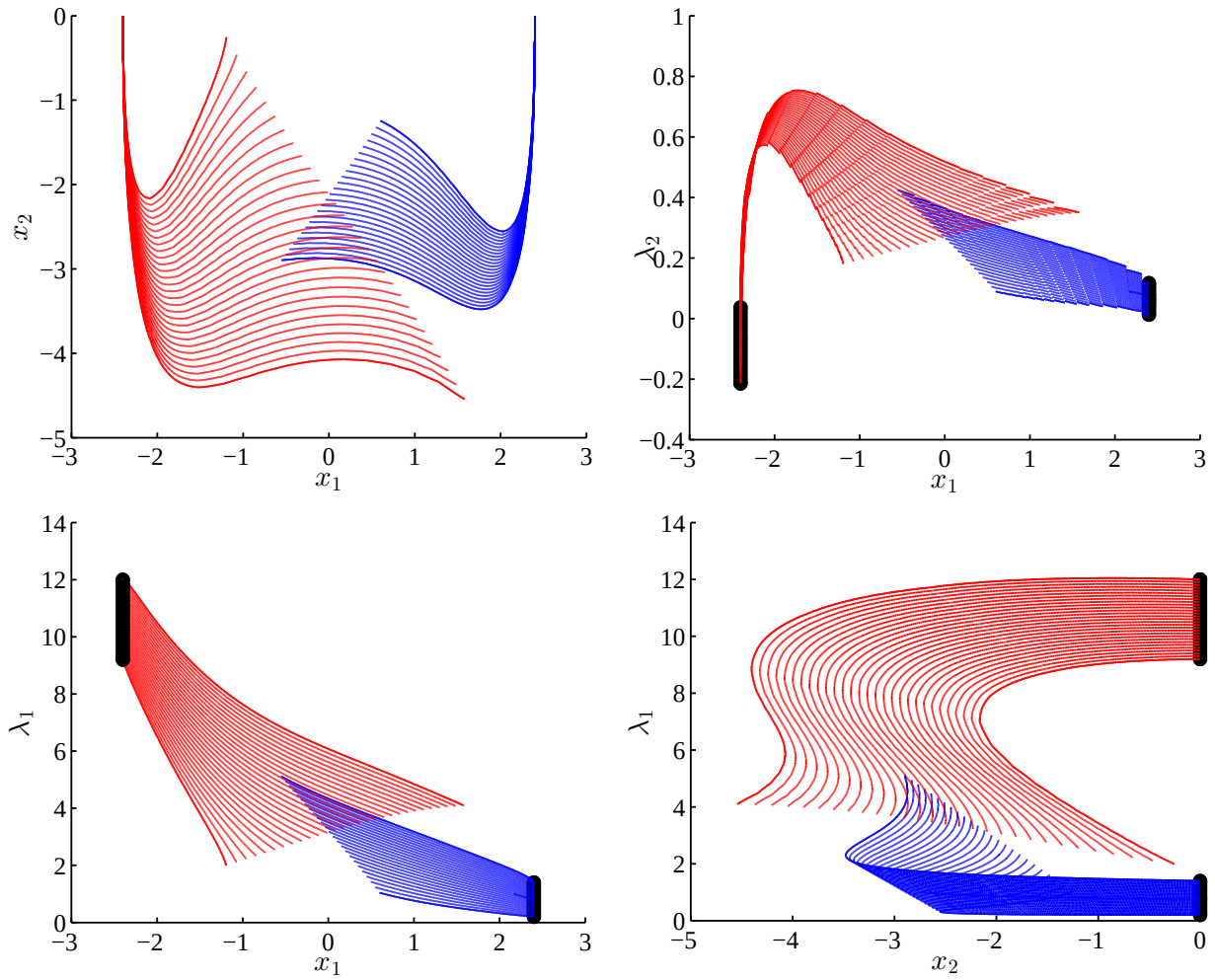

Figure 4.5: One-parameter families of forward (blue curves) and backward (red curves) trajectories for $\lambda_1(t_0) = \lambda_1^0 \in [0.2, 1.4]$ and $\lambda_1(t_f) = \lambda_1^f \in [9.2, 12.0]$. The four plots show the trajectories in the $x_1 - x_2$ plane (top left), in the $x_1 - \lambda_2$ plane (top right), in the $x_1 - \lambda_1$ plane (bottom left), and in the $x_2 - \lambda_1$ plane (bottom right).

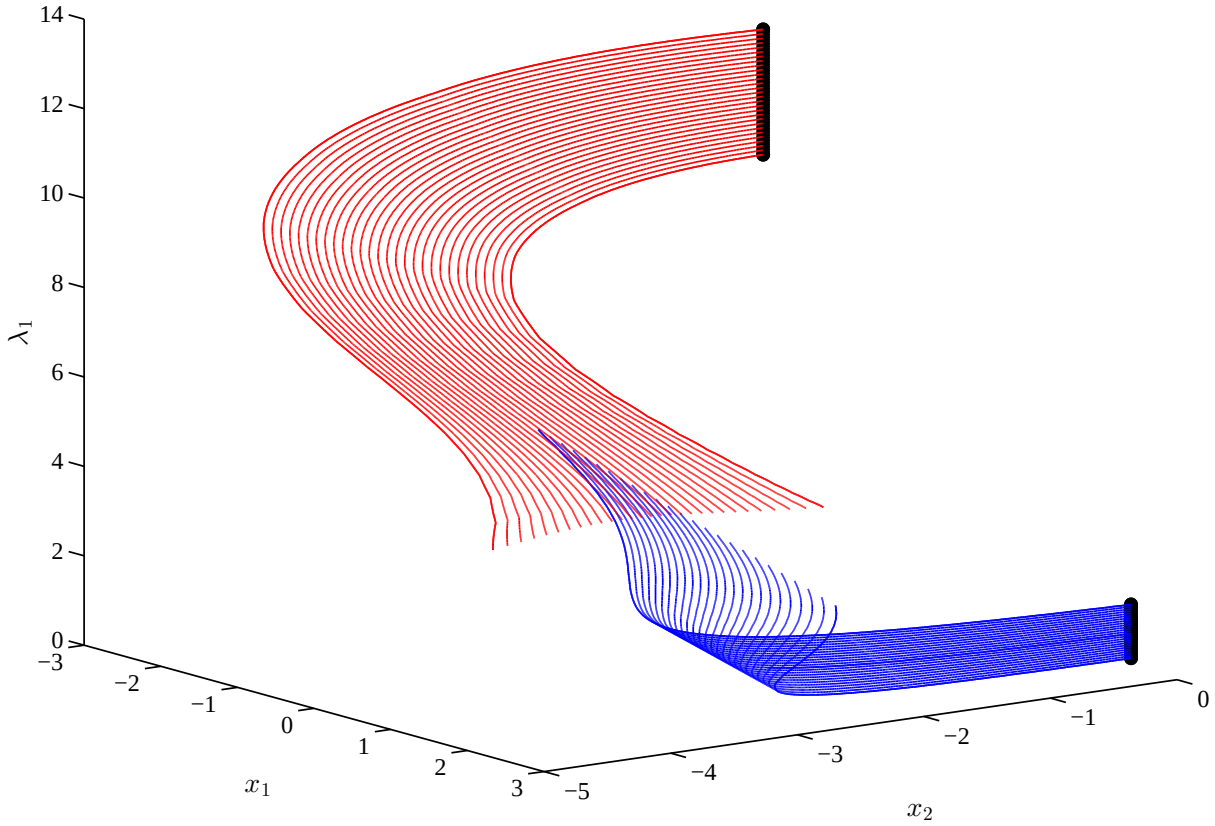

Figure 4.6: Projection in the $x_1 - x_2 - \lambda_1$ space of one-parameter families of forward (blue curves) and backward (red curves) trajectories for $\lambda_1^0 \in [0.2, 1.4]$ and $\lambda_1^f \in [9.2, 12.0]$. The black dots represent the initial and final points.

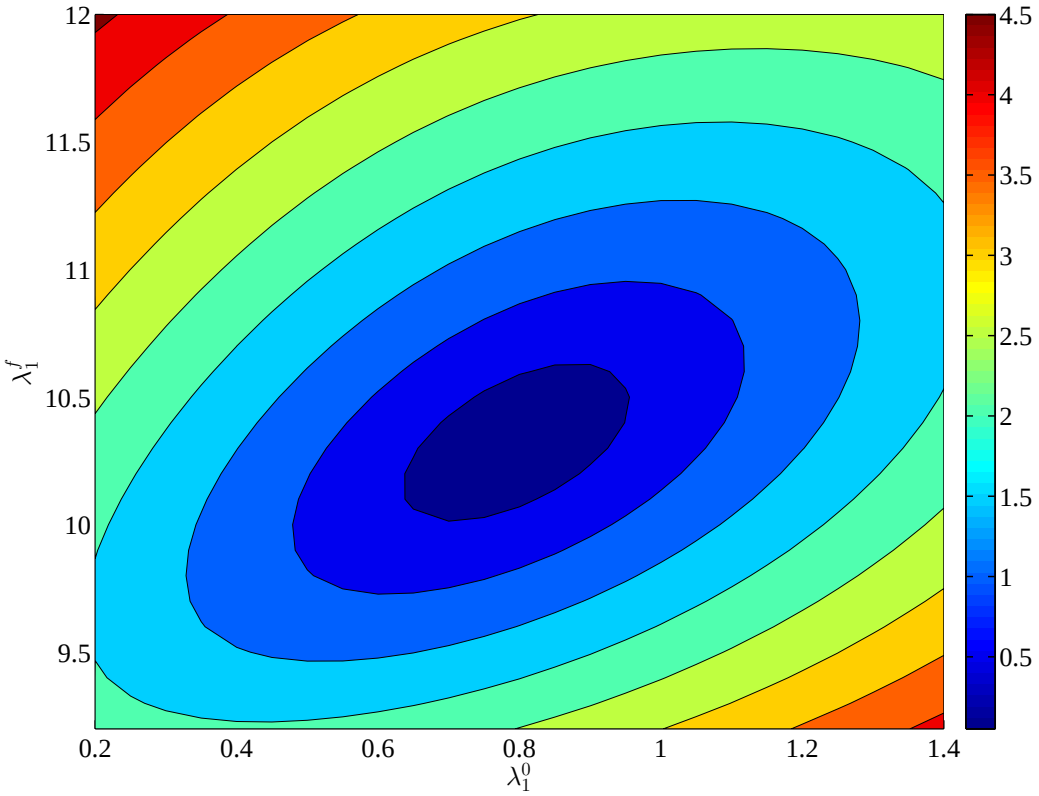

Figure 4.7: Distance d_m from ends of backward and forward trajectories for $\lambda_1^0 \in [0.2, 1.4]$ and $\lambda_1^f \in [9.2, 12.0]$.

we determine that $\nu = 13$ and $\sigma = 1$, which yield to fast and slow time constants $\nu^{-1} = 0.077$ and $\sigma^{-1} = 1$, respectively. Since $t_f = 2$, $t_f \gg \nu^{-1}$ and $t_f < \sigma^{-1}$, we confirm that there is slow-fast behavior in the tangent linear dynamics relative to the time interval of interest (see 2.4.3). Finally, tables 4.1 and 4.2 show the values of the phase points before and after each re-initialization (note that only λ_2 changes). The last column of each table reports the number of iterations necessary to satisfy the orthogonality conditions as described in Step 2, Part (a) and (b) of the computational algorithm. A Matlab® code sample of the procedure is provided in Appendix B.

Accuracy Assessment

To assess the accuracy of the optimal solution obtained via FTLA, we compared it to the solution obtained by two other methods. The first method is identical to our method except that the basis for the partially hyperbolic tangent space splitting is constructed from eigenvectors of $Dh(\mathbf{x})$ rather than OCP finite-time Lyapunov vectors. The second method is to use the general purpose optimal control problem solver GPOPS ((56)). For the particular set of parameters chosen for this example, we consider the GPOPS solution to be accurate, therefore we use it as a means of assessing the accuracy of our results. The three solutions are displayed in Fig. 4.15 and the three control profiles $u(t)$ are displayed in Fig. 4.16. Re-initialization with $\Delta t_i = 0.1$ is used for both the FTLA method and the eigenvector method. The FTLA and GPOPS solutions are indistinguishable, whereas the eigenanalysis solution is less accurate. Furthermore, for larger x_1, the eigenvector method is not applicable, because the eigenvalues and eigenvectors become complex and do not reveal the two timescales.

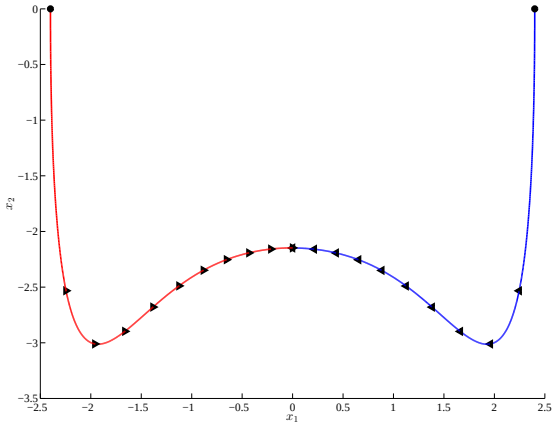

(a) Trajectory projected on the x_1-x_2 plane.

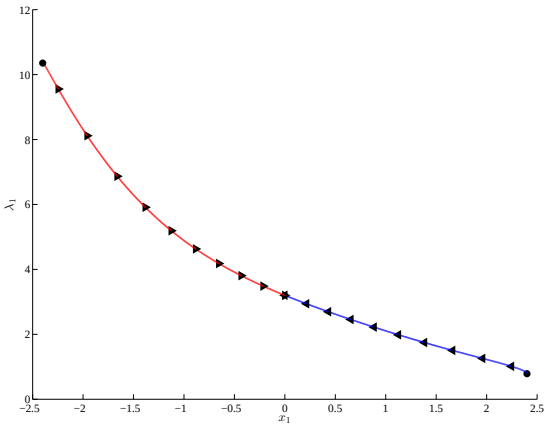

(b) Trajectory projected on the x_1-λ_1 plane.

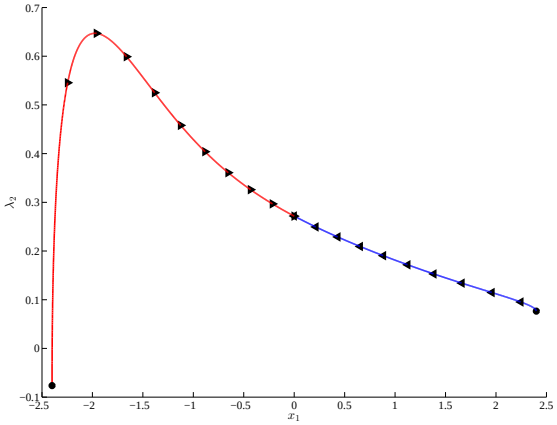

(c) Trajectory projected on the x_1-λ_2 plane.

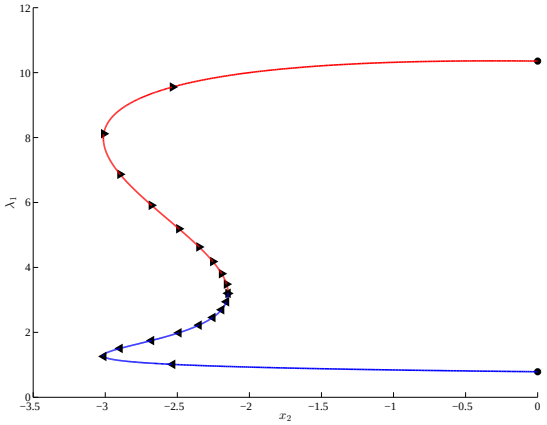

(d) Trajectory projected on the x_2-λ_1 plane.

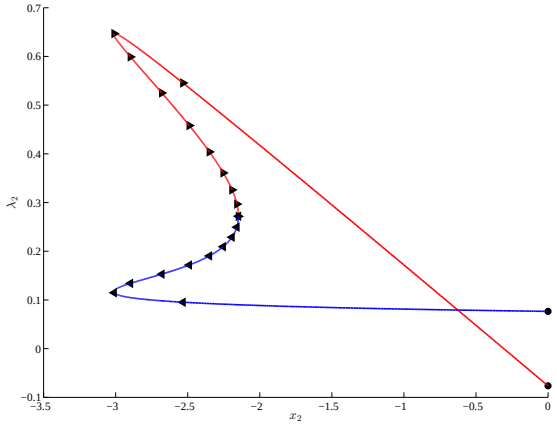

(e) Trajectory projected on the x_2-λ_2 plane.

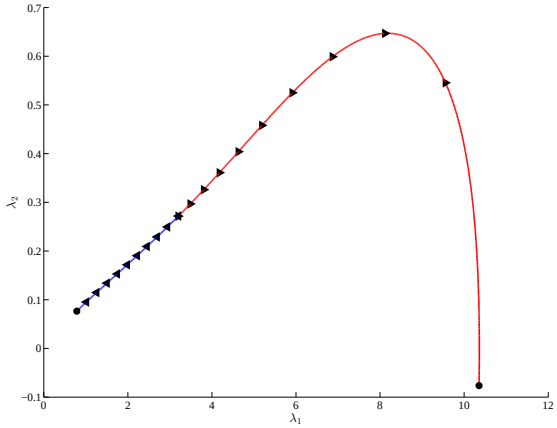

(f) Trajectory projected on the λ_1-λ_2 plane.

Figure 4.8: Six projections of the FTLA approximation of the optimal trajectory in the state space. The blue curves represent the portions of the solution that shadows the trajectory on center-stable manifold, while the red curves represent the portions of the solution that shadows the trajectory on center-unstable manifold. The black circular dots are the initial and final points, while the black triangles represent the phase points $\mathbf{x}(t_i)$ after each re-initialization.

Table 4.1: State and costate variables before and after each re-initialization on the forward segment of the trajectory that approximates the optimal solution. The last column indicates the number of iterations necessary for satisfying the manifold conditions.

Point	time	x_1	x_2	λ_1	λ_2	Iter. #
$\mathbf{x}^0$		2.400000	0.000000	0.786300	0.000000	
$\mathbf{x}(t_0)$	t_0=0.0	2.400000	0.000000	0.786300	0.076478	(8)
$\phi(\mathbf{x}(t_0), \Delta t_1)$		2.245330	-2.533144	1.012862	0.095328	
$\mathbf{x}(t_1)$	t_1=0.1	2.245330	-2.533144	1.012862	0.095329	(1)
$\phi(\mathbf{x}(t_1), \Delta t_2)$		1.959359	-3.010807	1.257264	0.114721	
$\mathbf{x}(t_2)$	t_2=0.2	1.959359	-3.010807	1.257264	0.114722	(1)
$\phi(\mathbf{x}(t_2), \Delta t_3)$		1.661872	-2.897855	1.503588	0.133989	
$\mathbf{x}(t_3)$	t_3=0.3	1.661872	-2.897855	1.503588	0.133990	(1)
$\phi(\mathbf{x}(t_3), \Delta t_4)$		1.382945	-2.679825	1.746507	0.152966	
$\mathbf{x}(t_4)$	t_4=0.4	1.382945	-2.679825	1.746507	0.152967	(1)
$\phi(\mathbf{x}(t_4), \Delta t_5)$		1.124871	-2.489736	1.985211	0.171709	
$\mathbf{x}(t_5)$	t_5=0.5	1.124871	-2.489736	1.985211	0.171710	(1)
$\phi(\mathbf{x}(t_5), \Delta t_6)$		0.883301	-2.349828	2.220928	0.190396	
$\mathbf{x}(t_6)$	t_6=0.6	0.883301	-2.349828	2.220928	0.190397	(2)
$\phi(\mathbf{x}(t_6), \Delta t_7)$		0.653429	-2.254136	2.456160	0.209303	
$\mathbf{x}(t_7)$	t_7=0.7	0.653429	-2.254136	2.456160	0.209304	(2)
$\phi(\mathbf{x}(t_7), \Delta t_8)$		0.431323	-2.193044	2.694593	0.228816	
$\mathbf{x}(t_8)$	t_8=0.8	0.431323	-2.193044	2.694593	0.228818	(2)
$\phi(\mathbf{x}(t_8), \Delta t_9)$		0.213914	-2.159242	2.941270	0.249453	
$\mathbf{x}(t_9)$	t_9=0.9	0.213914	-2.159242	2.941270	0.249457	(2)
$\phi(\mathbf{x}(t_9), \Delta t_{10})$		-0.001293	-2.148532	3.202927	0.271914	
$\mathbf{x}(t_{10})^+$	t_{10}=1.0	-0.001293	-2.148532	3.202927	0.271921	(2)

Table 4.2: State and costate variables before and after each re-initialization on the backward segment of the trajectory that approximates the optimal solution. The last column indicates the number of iterations necessary for satisfying the manifold conditions.

Point	time	x_1	x_2	λ_1	λ_2	Iter. #
$\mathbf{x}^f$		-2.400000	0.000000	10.354200	0.000000	
$\mathbf{x}(t_f)$	t_f=2.0	-2.400000	0.000000	10.354200	-0.076400	(7)
$\phi(\mathbf{x}(t_f), -\Delta t_{20})$		-2.245358	-2.532665	9.556018	0.545485	
$\mathbf{x}(t_{19})$	t_{19}=1.9	-2.245358	-2.532665	9.556018	0.545486	(1)
$\phi(\mathbf{x}(t_{19}), -\Delta t_{19})$		-1.959445	-3.010148	8.116274	0.646906	
$\mathbf{x}(t_{18})$	t_{18}=1.8	-1.959445	-3.010148	8.116274	0.646906	(1)
$\phi(\mathbf{x}(t_{18}), -\Delta t_{18})$		-1.662028	-2.897110	6.868202	0.599058	
$\mathbf{x}(t_{17})$	t_{17}=1.7	-1.662028	-2.897110	6.868202	0.599058	(1)
$\phi(\mathbf{x}(t_{17}), -\Delta t_{17})$		-1.383180	-2.679015	5.913475	0.524922	
$\mathbf{x}(t_{16})$	t_{16}=1.6	-1.383180	-2.679015	5.913475	0.524922	(1)
$\phi(\mathbf{x}(t_{16}), -\Delta t_{16})$		-1.125189	-2.488867	5.190240	0.458089	
$\mathbf{x}(t_{15})$	t_{15}=1.5	-1.125189	-2.488867	5.190240	0.458089	(1)
$\phi(\mathbf{x}(t_{15}), -\Delta t_{15})$		-0.883709	-2.348901	4.629082	0.404008	
$\mathbf{x}(t_{14})$	t_{14}=1.4	-0.883709	-2.348901	4.629082	0.404007	(1)
$\phi(\mathbf{x}(t_{14}), -\Delta t_{14})$		-0.653933	-2.253152	4.179006	0.360891	
$\mathbf{x}(t_{13})$	t_{13}=1.3	-0.653933	-2.253152	4.179006	0.360890	(1)
$\phi(\mathbf{x}(t_{13}), -\Delta t_{13})$		-0.431928	-2.192003	3.805276	0.325923	
$\mathbf{x}(t_{12})$	t_{12}=1.2	-0.431928	-2.192003	3.805276	0.325921	(2)
$\phi(\mathbf{x}(t_{12}), -\Delta t_{12})$		-0.214626	-2.158144	3.484146	0.296735	
$\mathbf{x}(t_{11})$	t_{11}=1.1	-0.214626	-2.158144	3.484146	0.296733	(2)
$\phi(\mathbf{x}(t_{11}), -\Delta t_{11})$		-0.000467	-2.148473	3.202939	0.271867	
$\mathbf{x}(t_{10})^-$	t_{10}=1.0	-0.000467	-2.148473	3.202639	0.271862	(3)

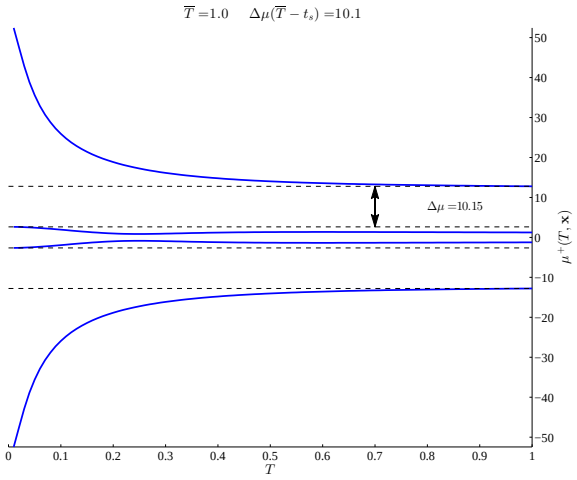

(a) Forward FTLEs for $\mathbf{x}(t_0)$

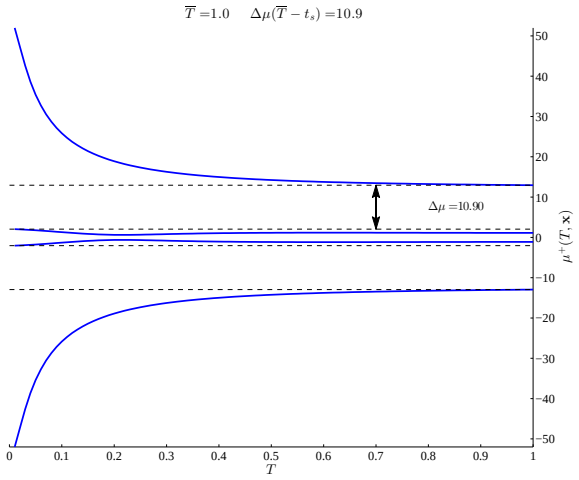

(b) Forward FTLEs for $\mathbf{x}(t_1)$

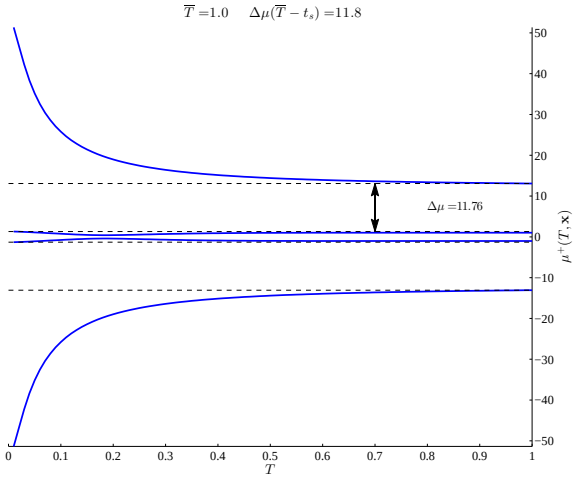

(c) Forward FTLEs for $\mathbf{x}(t_2)$

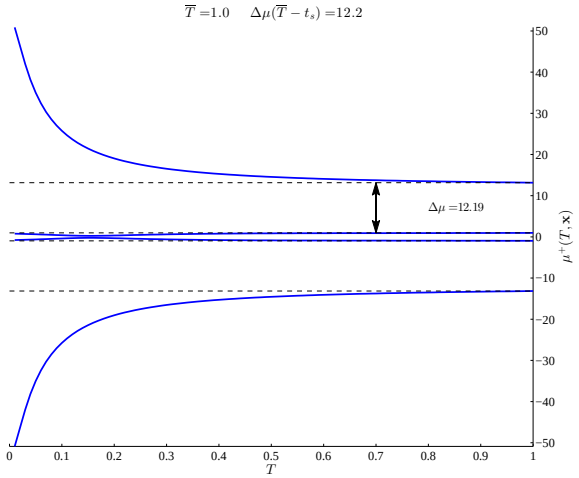

(d) Forward FTLEs for $\mathbf{x}(t_3)$

Figure 4.9: Forward finite-time Lyapunov exponents for $\mathbf{x}(t_0)$ (a), $\mathbf{x}(t_1)$ (b), $\mathbf{x}(t_2)$ (c), and $\mathbf{x}(t_3)$ (d).

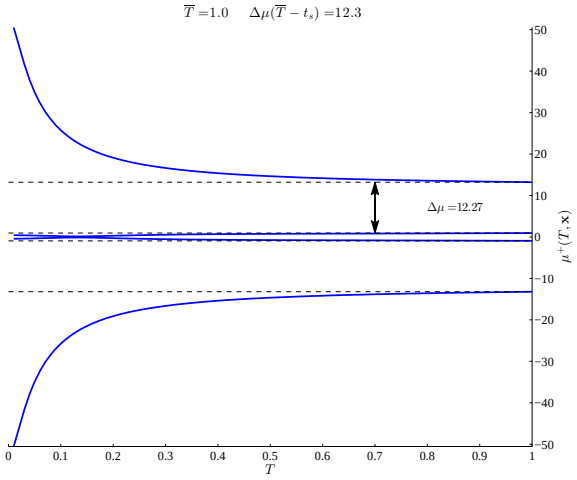

(a) Forward FTLEs for $\mathbf{x}(t_4)$

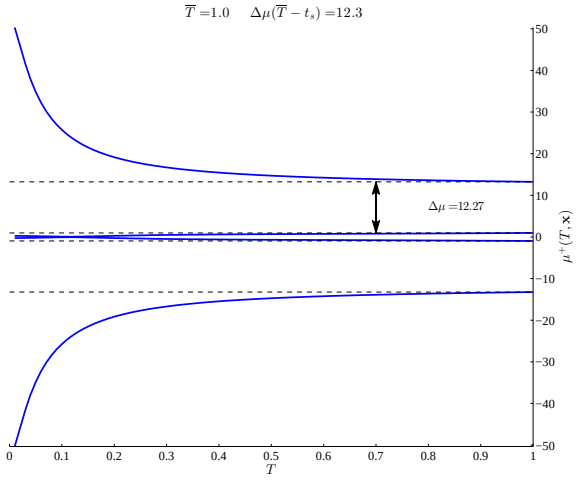

(b) Forward FTLEs for $\mathbf{x}(t_5)$

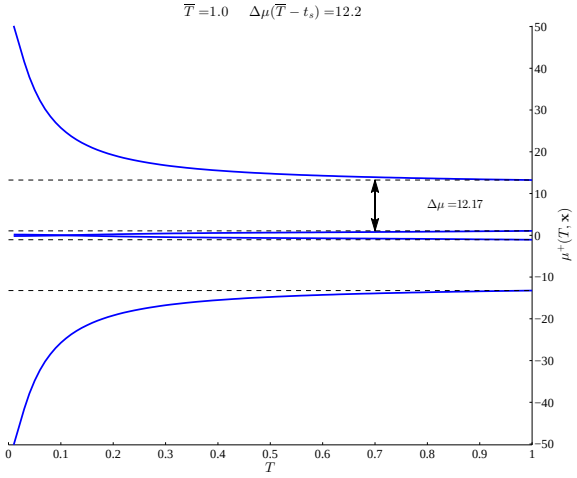

(c) Forward FTLEs for $\mathbf{x}(t_6)$

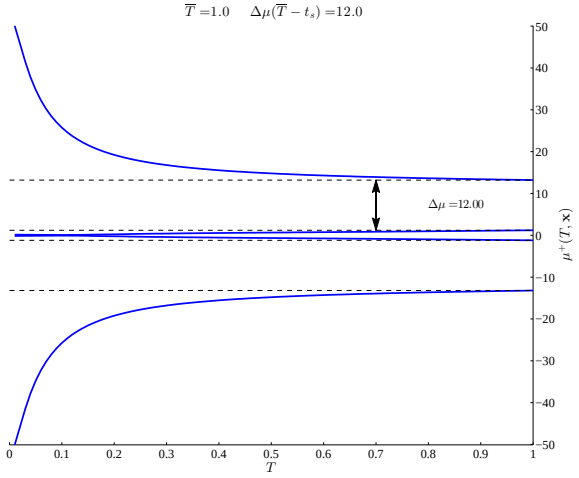

(d) Forward FTLEs for $\mathbf{x}(t_7)$

Figure 4.10: Forward finite-time Lyapunov exponents for $\mathbf{x}(t_4)$ (a), $\mathbf{x}(t_5)$ (b), $\mathbf{x}(t_6)$ (c), and $\mathbf{x}(t_7)$ (d).

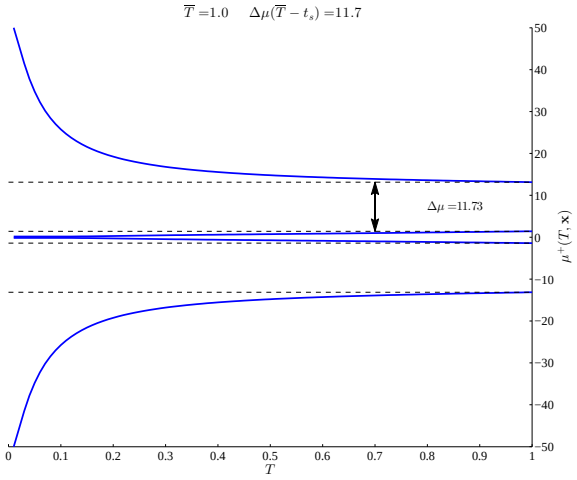

(a) Forward FTLEs for $\mathbf{x}(t_8)$

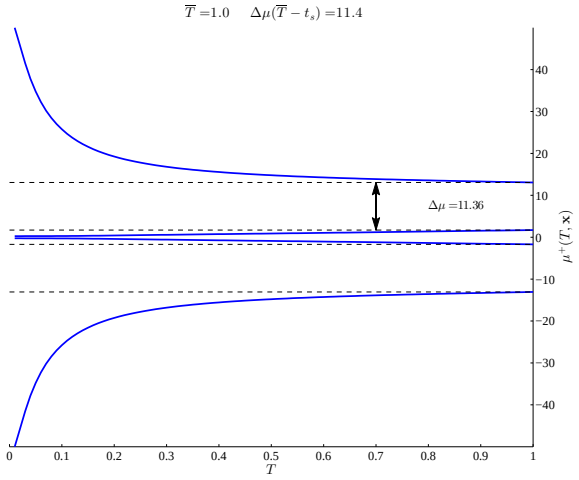

(b) Forward FTLEs for $\mathbf{x}(t_9)$

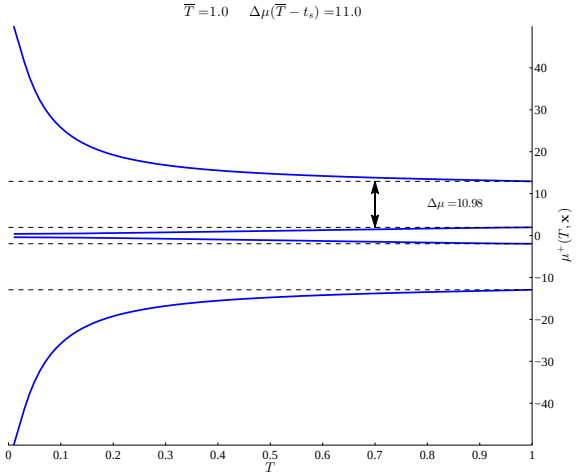

(c) Forward FTLEs for $\mathbf{x}(t_{10})^+$

Figure 4.11: Forward finite-time Lyapunov exponents for $\mathbf{x}(t_8)$ (a), $\mathbf{x}(t_9)$ (b), and $\mathbf{x}(t_{10})^+$ (c).

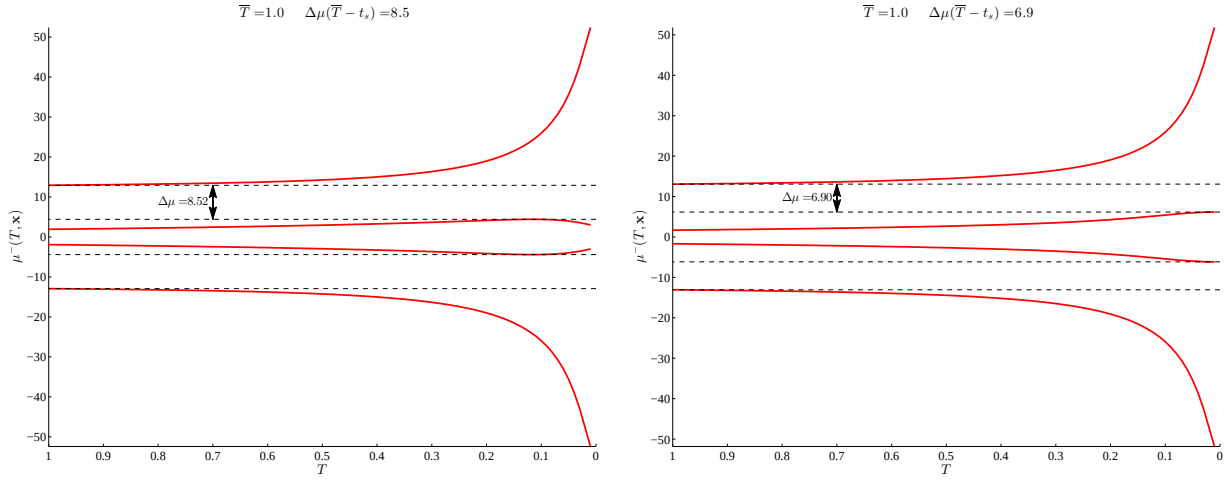

(a) Backward FTLEs for $\mathbf{x}(t_f)$

(b) Backward FTLEs for $\mathbf{x}(t_{19})$

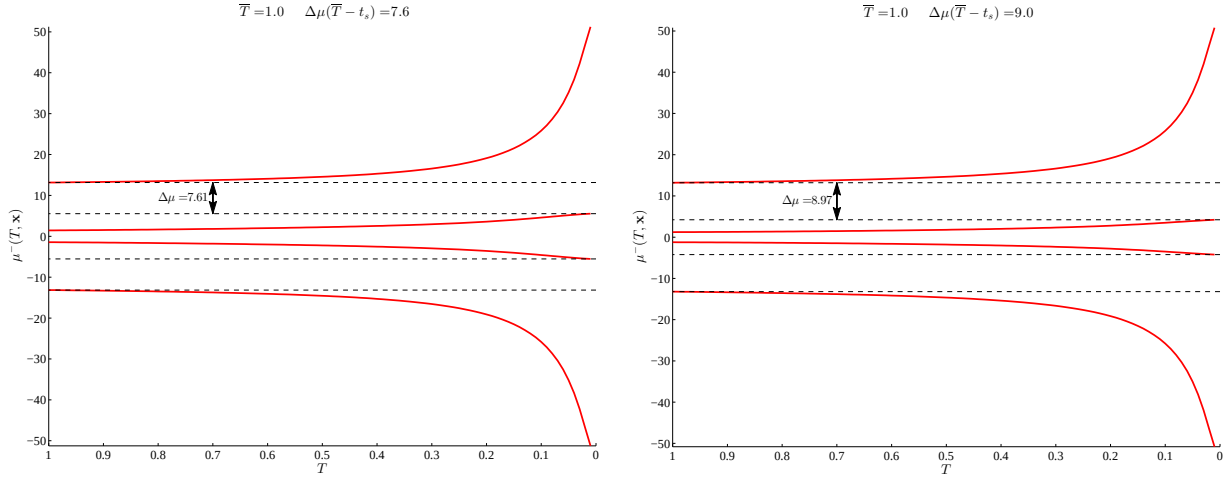

(c) Backward FTLEs for $\mathbf{x}(t_{18})$

(d) Backward FTLEs for $\mathbf{x}(t_{17})$

Figure 4.12: Backward finite-time Lyapunov exponents for $\mathbf{x}(t_f)$ (a), $\mathbf{x}(t_{19})$ (b), $\mathbf{x}(t_{18})$ (c), and $\mathbf{x}(t_{17})$ (d).

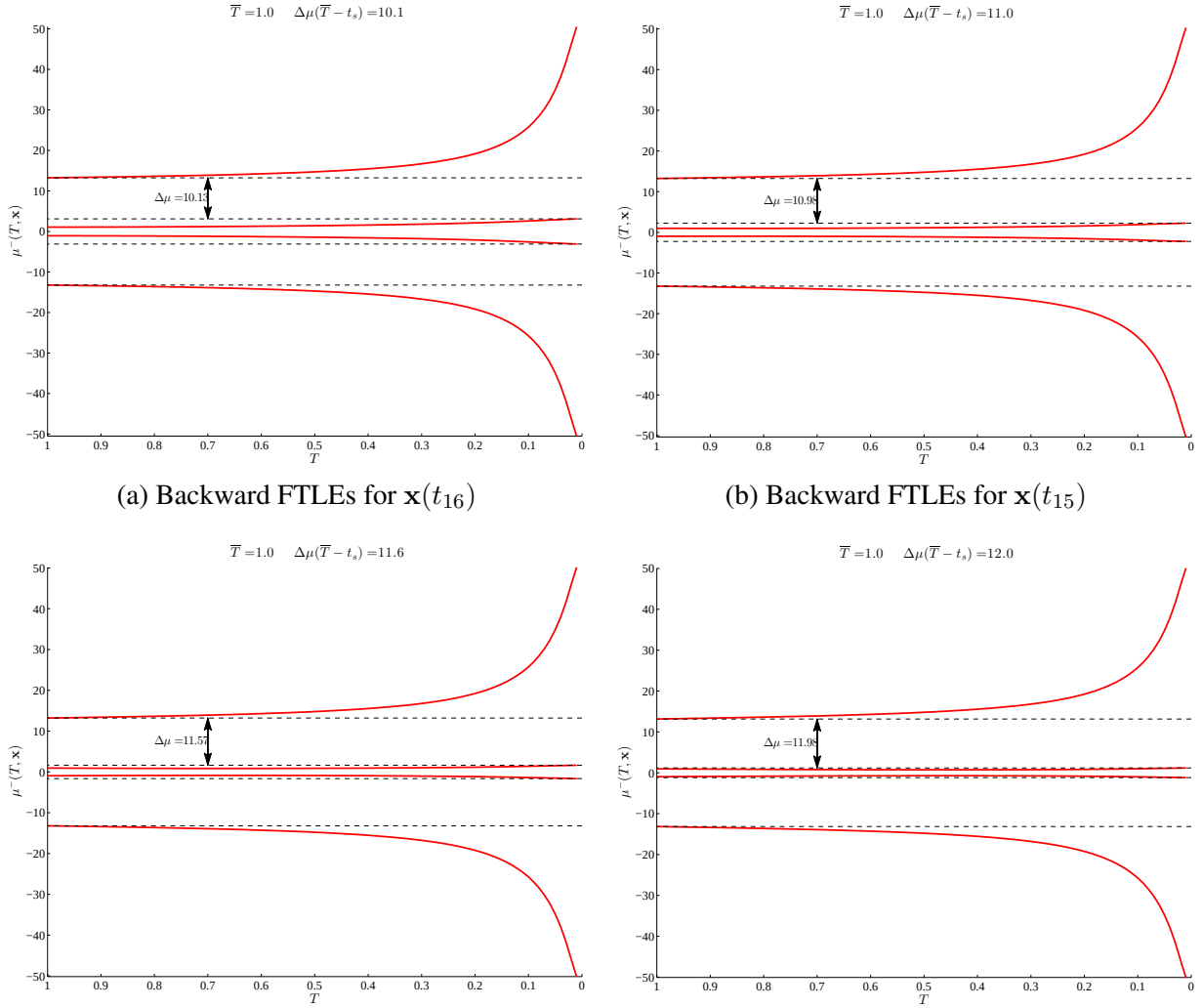

(a) Backward FTLEs for $\mathbf{x}(t_{16})$

(b) Backward FTLEs for $\mathbf{x}(t_{15})$

(c) Backward FTLEs for $\mathbf{x}(t_{14})$

(d) Backward FTLEs for $\mathbf{x}(t_{13})$

Figure 4.13: Backward finite-time Lyapunov exponents for $\mathbf{x}(t_{16})$ (a), $\mathbf{x}(t_{15})$ (b), $\mathbf{x}(t_{14})$ (c), and $\mathbf{x}(t_{13})$ (d).

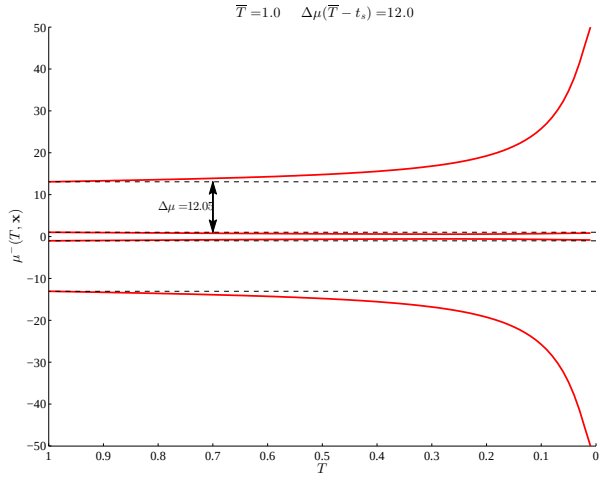

(a) Backward FTLEs for $\mathbf{x}(t_{12})$

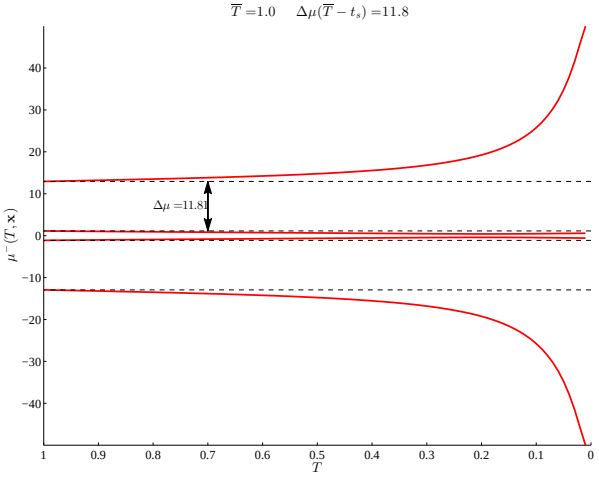

(b) Backward FTLEs for $\mathbf{x}(t_{11})$

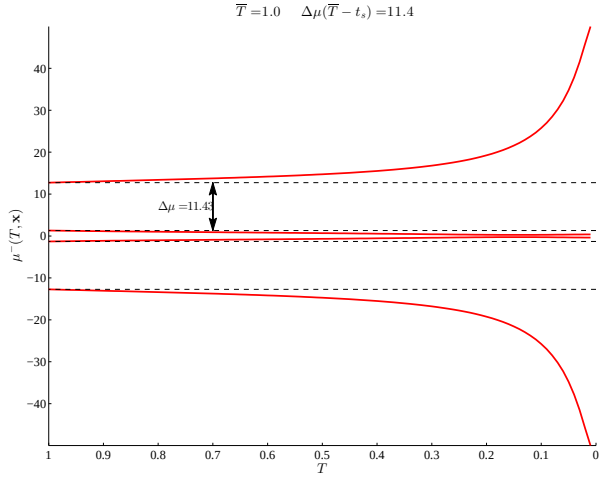

(c) Backward FTLEs for $\mathbf{x}(t_{10})^-$

Figure 4.14: Backward finite-time Lyapunov exponents for $\mathbf{x}(t_{12})$ (a), $\mathbf{x}(t_{11})$ (b), and $\mathbf{x}(t_{10})^-$ (c).

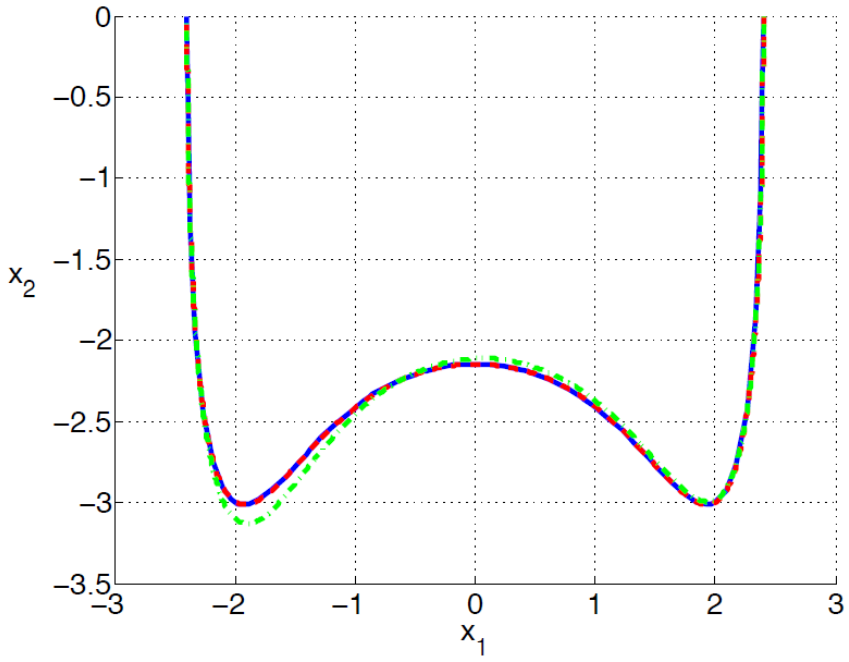

Figure 4.15: x_1-x_2 projection of the solution obtained via FTLA (solid blue curve), via eigenvector method (dashed green curve), and via GPOPS (dashed red curve). The FTLA and GPOPS solutions appear indistinguishable.

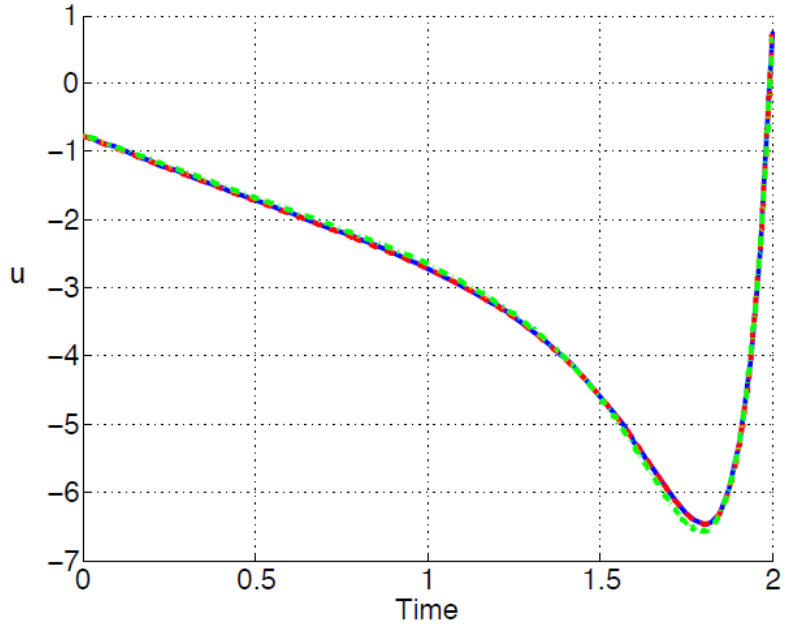

Figure 4.16: Control profile $u(t)$ obtained via FTLA (solid blue curve), via eigenvector method (dashed green curve), and via GPOPS (dashed red curve). The FTLA and GPOPS control profiles appear indistinguishable.

Chapter 5

Conclusions and Future Work

The main goal of this work was to contribute to the advancement of a methodology to diagnose the timescale structure in the tangent space for time-invariant nonlinear dynamical systems and extend its applications to problems in diverse fields. The timescale information, as well as the manifold structure were obtained by finite-time Lyapunov exponents and vectors and were utilized as tools to approach two research problems:

- Determining the manifold structure around libration points in the circular-restricted three-body problem and use the information to formulate a strategy for stationkeeping of spacecraft.
- Proposing a strategy for approximating the solution of partially hyper-sensitive optimal control problems.

5.1 Spacecraft Stationkeeping in the Circular Restricted Three-Body Problem via Finite-Time Lyapunov Analysis

Finite-time Lyapunov analysis was applied to the dynamics of a spacecraft in the circular restricted three-body problem. It was demonstrated that accurate information on stable and unstable directions relevant to stationkeeping and orbit insertion can be obtained. For periodic orbits, the information from finite-time Lyapunov analysis is consistent with that from Floquet analysis, provided a sufficiently long averaging time is used for the former. The benefit of Lyapunov analysis is that it is not limited to periodic orbits. It was demonstrated by simulation that the directions of the tangent subspaces at a point on a quasiperiodic orbit can be determined with greater accuracy if compared to the existent methodology. This is especially true when points on orbits around the L_3 libration point are considered. FTLA is independent of orbit periodicity and the accuracy of the tangent structure approximation is only a function of the convergence rate of the approximated linear subspaces towards their asymptotic counterparts.

A stationkeeping strategy using FTLA was then proposed. The proposed stationkeeping method produces numerical results similar to the ones of a realistic mission, it does not require an a priori knowledge of a reference orbit, and gives insight into the geometric structure of the problem, though remaining relatively simple compared to the Target Point methods.

Ideas for future work include applying FTLA to more complex gravitational models, and refining the numerical algorithms to perhaps extend its applicability to even more families of orbits. An interesting idea for future work would also be to integrate FTLA to the Target Point method, in a similar fashion to what is seen in (64).

5.2 Solving Partially Hyper-Sensitive Optimal Control Problems Using Manifold Structure

Finite-time Lyapunov exponents and vectors were used to provide a means of diagnosis hyper-sensitivity and determining the associated manifold structure for optimal control problems that are affected by partial hyper-sensitivity. The proposed approach required determining the unknown boundary conditions such that the solution end points lie on certain invariant manifolds and matching of forward and backward segments of the trajectory on the center manifold. The proposed strategy, which has great potential since it overcomes the problems encountered by using classic indirect methods, was demonstrated to work for a low-order optimal control problem. Future work recommendations include applying the FTLA-based strategy to more complex optimal control problems and improving the numerical algorithm for matching the forward and backward segments of the trajectory.

Bibliography

[1] A. Adrover, S. Cerbelli and M. Giona, *Exterior algebra-based algorithms to estimate Lyapunov spectra and stretching statistics in high-dimensional and distributed systems*, International Journal of Bifucration and Chaos 12(2) (2002) 353–368.

[2] A. Adrover, F. Creta, M. Giona, M. Valorani and V. Vitacolonna, *Natural tangent dynamics with recurrent biorthonormalizations: A geometric computational approach to dynamical systems exhibiting slow manifolds and periodic/chaotic limit sets*, Physica D 213(2) (2006) 121 – 146.

[3] E. Aykutluğ and K. D. Mease, *Approximate Solution of Hypersensitive Optimal Control Problems Using Finite-Time Lyapunov Analysis*, American Control Conference, St. Louis, Missouri, June 2009.

[4] E. Aykutluğ, *Finite-Time Lyapunov Analysis of Invariant Manifolds in Nonlinear Dynamical Systems*, Dissertation, University of California, Irvine (2011).

[5] E. Aykutuluğ, M. Maggia, and K. D. Mease, *Solving Partially Hyper-Sensitive Optimal Control Problems Using Manifold Structure,* Conference Paper, NOLCOS International Federation of Automatic Controls, Toulouse, 4–6 September 2013.

[6] L. Barreira and Y. B. Pesin, *Lyapunov Exponents and Smooth Ergodic Theory*, University Lecture Series, Vol. 23, American Mathematical Society, Providence, 2002.

[7] M. Belló, G. Gómez, and J. J. Masdemont. *Invariant Manifolds, Lagrangian Trajectories and Space Mission Design* in: Space Manifold Dynamics, Springer, pp. 1–96, 2010.

[8] H. W. Broer, A. Hagen, and G. Vegter, *Numerical continuation of normally hyperbolic invariant manifolds*, Nonlinearity 20 (2007) 1499-1534.

[9] R. Buizza and T. N. Palmer, *The singular-vector structure of the atmospheric global circulation*, J. Atmos. Sci. 52(9) (1995) 1434–1456.

[10] L. Dieci and E. S. Van Vleck, *Lyapunov spectral intervals: theory and computation*, SIAM J. Numerical Analysis 40(2) (2002) 516–542.

[11] E. J. Doedel, V. A. Romanov, R. C. Paffenroth, H. B. Keller, D. J. Dichmann, J. Galán-Vioque, and A. Vanderbauwhede. *Elemental Periodic Orbits associated with the Libration Points in the Circular Restricted 3-Body Problem,* International Journal of Bifurcation and Chaos, 17 (2007), No. 8, 2625–2677.

[12] E. J. Doedel, AUTO, ftp://ftp.cs.concordia.ca/pub/doedel/auto.

[13] R. Doerner, B. Hübinger, W. Martienssen, S. Grossmann, and S. Thomae, *Stable manifolds and predictability of dynamical systems*, Chaos, Solitons, and Fractals 10(11) (1999) 1759–1782.

[14] J. P. England, B. Krauskopf, and H. M. Osinga, *Computing two-dimensional global invariant manifolds in slow-fast systems*, Int. J. Bifurcation and Chaos 17(3) (2007) 805–822.

[15] S. V. Ershov and A. B. Potapov, *On the concept of stationary Lyapunov basis*, Physica D 118 (1998) 167–198.

[16] N. Fenichel, *Geometric singular perturbation theory for ordinary differential equations*, J. Diffirential Equations 31 (1979) 53–g, E98.

[17] D. C. Folta, T. A. Pavlak, A. F. Haapala, K. C. Howell, M. A. Woodard. *Earth-Moon Libration Point Stationkeeping: Theory, Modeling, and Operations,* Acta Astronautica, 94 (2014), No. 1, 421–433.

[18] D. C. Folta, M. A. Woodard, and D. Cosgrove *Stationkeeping of the First Earth-Moon Libration Orbiters: the Artemis Mission* 21st AAS/AIAA Space Flight Mechanics Meeting New Orleans, Louisiana (2011).

[19] C. Froeschle, E. Lega and R. Gonczi, *Fast Lyapunov indicators: application to asteroidal motion*, Celestial Mechanics and Dynamical Astronomy 67 (1997) 41–62.

[20] C. W. Gear, T. J. Kaper, I. G. Kevrekidis, and A. Zagaris, *Projecting to a slow manifold: Singularly perturbed systems and legacy codes*, SIAM J. Applied Dynamical Systems 4 (2005) 711–732.

[21] K. Geist, U. Parlitz and W. Lauterborn, *Comparison of different methods for computing Lyapunov exponents*, Progress of Theoretical Physics 83(5) (1990) 875 – 893.

[22] I. Goldhirsch, P.-L. Sulem, and S. A. Orszag, *Stability and Lyapunov stability of dynamical systems : a differential approach and a numerical method*, Physica D 27 (1987) 311–337.

[23] G. H. Golub and C. F. Van Loan, *Matrix Computations*, 3rd Edition, The Johns Hopkins University Press, Baltimore, 1996.

[24] G. Gómez, J. Llibre, R. Martínez, and C. Simó. *Station Keeping of Libration Point Orbits,* Technical Report ESOC Contract 5648/83/D/JS(SC), 1985.

[25] G. Gómez, J. Masdemont, and C. Simó. *Study of the Transfer from the Earth to a Halo Orbit Around the Equilibrium Point L1,* Celestial Mechanics and Dynamical Astronomy, 56 (1993) 541-562.

[26] G. Gómez, K. Howell, J. Masdemont, C. and Simó, *Station-Keeping Strategies for Translunar Libration Point Orbits,* AAS/AIAA Spaceflight Mechanics 1998, Advances in the Astronautical Sciences, Vol. 99, Part II, J. Middour, L. Sackett, L. D'Amario, and D. Byrnes (editors), (1998), pp. 949-967.

[27] J. M. Greene and J.-S. Kim, *Introduction of a metric tensor into linearized evolution equations*, Physica D 36 (1989) 83–91.

[28] J. Guckenheimer and P. Holmes, *Nonlinear Oscillations, Dynamical Systems, and Bifurcations of Vector Fields*, Springer-Verlag, New York, 1983, p. 127.

[29] J. Guckenheimer and C. Kuehn, *Computing slow manifolds of saddle type*, SIAM J. Appl. Dyn. Syst. 8(3) (2009) 854–879.

[30] G. Haller, *Finding finite-time invariant manifolds in two-dimensional velocity fields*, Chaos 10(1) (2000) 99–108.

[31] G. Haller, *A variational theory of hyperbolic Lagrangian coherent structures*, Physica D 240 (2011) 574–598.

[32] B. Hasselblatt and Y. B. Pesin. *Partially Hyperbolic Dynamical Systems.* in: B. Haselblatt and A. Katok (Eds.), Handbook of Dynamical Systems, Vol. 1B, Elsevier, New York, 2005.

[33] K. C. Howell, B. Barden, and M. Lo. *Application of Dynamical Systems Theory to Trajectory Design for a Libration Point Mission,* Journal of Astronautics Science, 45 (1997), No. 2, 161-178.

[34] A. Isidori, *Nonlinear Control Systems*, 3rd Edition, Springer-Verlag, New York, 1995, p. 21.

[35] C. K. R. T. Jones, *Geometric Singular Perturbation Theory*, in R. Johnson (Ed.), Dynamical Systems, Lecture Notes in Math 1609, Springer, Berlin, 1995.

[36] H. G. Kaper and T. J. Kaper, *Asymptotic analysis of two reduction methods for systems of chemical reactions*, Physica D 165 (2002) 66–93.

[37] A. Katok and B. Hasselblatt, *Introduction to the Modern Theory of Dynamical Systems*, Cambridge University Press, New York, 1995.

[38] T. M. Keeter. *Station-Keeping Strategies for Libration Point Orbits: Target Point and Floquet Mode Approaches.* Ph.D. Dissertation, Purdue University, 1994.

[39] E. Kolemen, N. J. Kasdin and P. Gurfi *Quasi-Periodic Orbits of the Restricted Three-Body Problem Made Easy*, AIP Conference Proceedings, Vol. 886, (2007), pp. 68–77.

[40] W. S. Koon, M. W. Lo, J. E. Marsden, and S. D. Ross. *Heteroclinic Connections between Periodic Orbits and Resonance Transitions in Celestial Mechanics,* Chaos, 10 (2000), No. 2, 427-469.

[41] P. V. Kokotovic, H. K. Khalil, and J. O'Reilly, *Singular Perturbation Methods in Control: Analysis and Design*, Academic Press, New York, 1986.

[42] S. H. Lam, *Singular perturbation for stiff equations using numerical computations*, Lectures in Applied Mathematics 24 (1986) 3–19.

[43] S. H. Lam and D. A. Goussis, *The CSP method for simplifying kinetics*, Int. J. Chemical Kinetics 26 (1994) 461–486.

[44] B. Legras and R. Vautard, *A guide to Lyapunov vectors*, in: Predictability, Vol. 1, ed. T. Palmer, ECWF Seminar, Reading, UK, 1996 135–146.

[45] F. Lekien and S. D. Ross, *The computation of finite-time Lyapunov exponents on unstructured meshes and for non-Euclidean manifolds*, Chaos 20(1) (2010) 017505.

[46] E. N. Lorenz, *The local structure of a chaotic attractor in 4-dimension*, Physica D 13 (1984) 90–104.

[47] A. M. Lyapunov, *The general problem of stability of motion*, Intern. J. of Control, 55(3) (1992) 531–773. (reprint of Lyapunov's 1892 Thesis).

[48] U. Maas and S. B. Pope, *Simplifying chemical kinetics: intrinsic low-dimensional manifolds in composition space*, Combustion and Flame 88 (1992) 239–264.

[49] C. Marschler, J. Sieber, R. Berkemer, A. Kawamoto, and J. Starke, *Implicit methods for equation-free analysis: convergence results and analysis of emergent waves in microscopic traffic models*, SIAM J. Applied Dynamical Systems 13 (2014) 1202–1238.

[50] Maggia, M. and Mease, K.D., *Flow Structure Identification for Nonlinear Dynamical Systems via Finite-Time Lyapunov Analysis,* Math. Model. Nat. Phenom. Vol. 10, (2015), No. 3, pp. 91–104.

[51] K. D. Mease, U. Topcu, E. Aykutluğ, and M. Maggia. *Characterizing Two-Timescale Nonlinear Dynamics Using Finite-Time Lyapunov Exponents and Vectors,* Communications in Nonlinear Science and Numerical Simulation, Vol. 36, (2016), pp. 148–174.

[52] K. D. Mease, S. Bharadwaj, and S. Iravanchy, *Timescale analysis for nonlinear dynamical systems*, J. Guidance, Control and Dynamics 26 (2003) 318–330.

[53] K. D. Mease, *Multiple timescales in nonlinear flight mechanics: diagnosis and modeling*, Applied Mathematics and Computation 164 (2005) 627–648.

[54] V. Oseledec, *A multiplicative ergodic theorem: Lyapunov characteristic numbers for dynamical systems*, Trans. Moscow Math. Soc. 19 (1968) 197–231.

[55] T. A. Pavlak and K. C. Howell *Strategy for Optimal, Long-Term Stationkeeping of Libration Point Orbits in the Earth-Moon System* AIAA SPACE 2012 Conference and Exposition, Pasadena, CA (2012).

[56] A. V. Rao, D. A. Benson, C. L. Darby, M. A. Patterson, C. Francolin, I. Sanders, and G. T. Huntington *Algorithm 902: Gpops, a matlab software for solving multiple-phase optimal control problems using the gauss pseudospectra method,* ACM Trans. Math. Software, 37(2), (2010).

[57] A. V. Rao and K. D. Mease, *Dichotomic basis approach to solving hyper-sensitive optimal control problems*, Automatica 35 (1999) 633–642.

[58] A. V. Rao and K. D. Mease, *Eigenvector approximate dichotomic basis method for solving hyper-sensitive optimal control problems*, Optimal Control Applications and Methods 21 (2000) 1–19.

[59] B. Rasmussen and L. Dieci, *A geometrical method for the approximation of invariant tori*, J. Computational and Applied Mathematics 216 (2008) 388–412.

[60] Z. Ren and S. B. Pope, *The geometry of reaction trajectories and attracting manifolds in composition space*, Combustion Theory and Modeling 10(3) (2006) 361–388.

[61] M. R. Roussel and S. J. Fraser, *Geometry of the steady-state approximation: perturbation and accelerated convergence methods*, J. Chem. Phys. 93(3) (1990) 1072–1081.

[62] P. J. Schmid, *Nonmodal Stability Theory*, Annu. Rev. Fluid Mech. 39 (2007) 129-162.

[63] S. C. Shadden, F. Lekien, and J. E. Marsden, *Definition and properties of Lagrangian coherent structures from finite-time Lyapunov exponents in two-dimensional aperiodic flows*, Physica D 212 (2005) 271–304.

[64] C. R. Short and K. C. Howell. *Flow Control Segment and Lagrangian Coherent Structure Approaches for Application in Multi-Body Problems,* Acta Astronautica 94 (2014), 562–607.

[65] C. Simó, G. Gómez, J. Llibre, and R. Martínez. *Station Keeping of a Quasiperiodic Halo Orbit Using Invariant Manifolds,* Proceedings of the Second International Symposium on Spacecraft Flight Dynamics, Darmstadt, FR Germany, 20-23 October 1986 (ESA SP-255, Dec. 1986).

[66] V. Szebehely. *Theory of Orbits: The Restricted Problem of Three Bodies,* Academic Press, New York, 1967.

[67] S.-K. Tin, N. Kopell, and C. K. R. T. Jones, *Invariant manifolds and singularly perturbed boundary value problems*, SIAM J. Numer. Anal. 31 (1994) 1558-1576.

[68] U. Topcu and K. D. Mease, *Using Lyapunov vectors and dichotomy to solve hyper-sensitive optimal control problems.* Proceedings of the 45^{th} IEEE Conference on Decision and Control, San Diego, CA, USA, (2006).

[69] J. A. Vastano and R. D. Moser, *Short-time Lyapunov exponent analysis and the transition to chaos in Taylor-Couette flow*, J. Fluid Mechanics 233 (1991) 83–118.

[70] B. F. Villac, *Using FLI maps for preliminary spacecraft trajectory design in multi-body environments*, Celestial Mechanics and Dynamical Astronomy 102(1-3) (2008) 29-48.

[71] C. L. Wolfe and R. M. Samelson, *An efficient method of recovering Lyapunov vectors from singular vectors*, Tellus 59A (2007) 355–366.

[72] S. Yoden and M. Nomura. *Finite-Time Lyapunov Stability Analysis and Its Application to Atmospheric Predictability*, J. Atmospheric Sciences 50 (1993), No. 11, 1531–1543.

[73] L.-S. Young, *Ergodic Theory of Differentiable Dynamical Systems*, in: *Real and Complex Dynamics*, eds. Branner and Hiorth, NATO ASI Series, Kluwer Academic Publishers, 1995, 201–226.

[74] NASA - James Webb Space Telescope Website `https://jwst.nasa.gov/`

[75] NASA - SOHO Website `https://www.nasa.gov/mission_pages/soho/index.html`

[76] NASA - ARTEMIS Website `https://www.nasa.gov/artemis`

Appendix A

Subspace Convergence

Proposition A.0.3 below gives the exponential rate at which the finite-time Lyapunov subspaces, introduced in Section 2.3.2 and expressed in terms of the FTLVs, evolve with increasing T toward their asymptotic limits, under hypotheses in which these limits exist. The proposition concerns forward time only, but is easily adaptable to backward time. Most of the ideas in Proposition A.0.3 and its proof can be found in (15; 22). The new element here is that convergence of a particular Lyapunov subspace is addressed explicitly, rather than the convergence of individual Lyapunov vectors, although the proof still relies on the evolution of individual Lyapunov vectors and requires uniformly distinct FTLEs. See (31) for an alternative approach for a special case of a co-dimension one subspace.

Definition A.0.1. *The Lyapunov spectrum is strongly non-degenerate at a point* $\mathbf{x}$*, if there exists positive constants* t_s *and* δ *such that the spectral gap between each neighboring pair of forward FTLEs,* $\mu^+_{i+1}(T, \mathbf{x}) - \mu^+_i(T, \mathbf{x})$*,* $i = 1, \ldots, n-1$*, is greater than* δ *for all* $T > t_s$ *and likewise for the backward exponents.*

To consider the convergence of a Lyapunov subspace $\mathcal{L}^+_j(T, \mathbf{x})$ with T, we focus on a particular

spectral gap and bound it for use in the proposition that follows.

Definition A.0.2. *[Spectral Gap Lower Bound] For a specified $t_s \geq 0$, the lower bound on the spectral gap $\Delta\mu_j^+(\mathbf{x})$ between neighboring forward FTLEs $\mu_j^+(T,\mathbf{x})$ and $\mu_{j+1}^+(T,\mathbf{x})$, for a particular $j \in \{1,2,\ldots,n-1\}$, is*

$$\Delta\mu_j^+(\mathbf{x}) := \inf_{T>t_s} (\mu_{j+1}^+(T,\mathbf{x}) - \mu_j^+(T,\mathbf{x})). \tag{A.1}$$

Similarly the spectral gap bound $\Delta\mu_k^-(\mathbf{x})$ between neighboring backward FTLEs $\mu_{k-1}^-(T,\mathbf{x})$ and $\mu_k^-(T,\mathbf{x})$ is defined as

$$\Delta\mu_k^-(\mathbf{x}) := \inf_{T>t_s} (\mu_{k-1}^-(T,\mathbf{x}) - \mu_k^-(T,\mathbf{x})). \tag{A.2}$$

Proposition A.0.3. *Consider the dynamical system (2.1) on a compact invariant subset $\mathcal{Y}$ of the state space $\mathbb{R}^n$. At a Lyapunov regular point $\mathbf{x} \in \mathcal{Y}$ for which there exists $t_s \geq 0$ and $\delta > 0$ such that the Lyapunov spectrum is strongly non-degenerate for $T > t_s$ and for which there is a nonzero lower bound $\Delta\mu_j^+(\mathbf{x})$ on the spectral gap for a specific value of j, the subspace $\mathcal{L}_j^+(T,\mathbf{x})$ approaches the fixed subspace $\mathcal{L}_j^+(\mathbf{x})$, defined in Section 2.3.1 in terms of the asymptotic Lyapunov exponent $\mu_j^+(\mathbf{x})$. There exists a constant $T_1 > t_s$ such that the approach is at an exponential rate characterized, for every sufficiently small $\Delta T > 0$, by*

$$dist(\mathcal{L}_j^+(T,\mathbf{x}), \mathcal{L}_j^+(T+\Delta T,\mathbf{x})) \leq K e^{-\Delta\mu_j^+(\mathbf{x})\cdot T}, \tag{A.3}$$

for all $T \geq T_1$, where $K > 0$ is ΔT and T_1 dependent but T independent. Similarly, as T increases, the subspace $\mathcal{L}_k^-(T,\mathbf{x})$ approaches the fixed subspace $\mathcal{L}_k^-(\mathbf{x})$ at a rate proportional to $exp(-\Delta\mu_k^-(\mathbf{x})\cdot T)$.

Proof of Proposition A.0.3: Using (2.14) we have

$$\begin{aligned}
&\text{dist}(\mathcal{L}_j^+(T,\mathbf{x}),\mathcal{L}_j^+(T+\Delta T,\mathbf{x})) = \|L_j^+(T,\mathbf{x})^T L_{j'}^+(T+\Delta T,\mathbf{x})\|_2 \\
&= \left\| \begin{bmatrix} \mathbf{l}_1^+(T,\mathbf{x})^T \\ \mathbf{l}_2^+(T,\mathbf{x})^T \\ \vdots \\ \mathbf{l}_j^+(T,\mathbf{x})^T \end{bmatrix} \begin{bmatrix} \mathbf{l}_{j+1}^+(T+\Delta T,\mathbf{x}) & \cdots & \mathbf{l}_n^+(T+\Delta T,\mathbf{x}) \end{bmatrix} \right\|_2 \\
&= \left\| \begin{bmatrix} \langle \mathbf{l}_1^+(T,\mathbf{x}), \mathbf{l}_{j+1}^+(T+\Delta T,\mathbf{x})\rangle & \cdots & \langle \mathbf{l}_1^+(T,\mathbf{x}), \mathbf{l}_n^+(T+\Delta T,\mathbf{x})\rangle \\ \vdots & & \vdots \\ \langle \mathbf{l}_j^+(T,\mathbf{x}), \mathbf{l}_{j+1}^+(T+\Delta T,\mathbf{x})\rangle & \cdots & \langle \mathbf{l}_j^+(T,\mathbf{x}), \mathbf{l}_n^+(T+\Delta T,\mathbf{x})\rangle \end{bmatrix} \right\|_2
\end{aligned} \tag{A.4}$$

Using a result from (22), we have for $T > 0$ to 1^{st}-order in the time increment ΔT

$$\mathbf{l}_m^+(T+\Delta T) = (1+c\Delta T)\mathbf{l}_m^+(T) + \Delta T \sum_{i=1(i\neq m)}^{n} \frac{\left[(\mathbf{n}_i^+)^T(A^T+A)\mathbf{n}_m^+\right]\mathbf{l}_i^+}{e^{(\mu_m^+-\mu_i^+)T} - e^{(\mu_i^+-\mu_m^+)T}}, \tag{A.5}$$

where $A = D\mathbf{f}(\mathbf{x})$ is the system matrix of the linearized dynamics (2.2), $\mathbf{n}_i^+$ is a vector from the SVD of the transition matrix $\Phi(T,\mathbf{x})$ as defined in Section 2.3.2, c is a constant that is inconsequential in the following developments and is thus left unspecified, the $\mathbf{x}$ dependence has been suppressed, and all exponents and vectors in the summation on the right-hand-side are evaluated at $(T,\mathbf{x})$. It follows that the inner products in (A.4) are

$$\langle \mathbf{l}_k^+(T,\mathbf{x}), \mathbf{l}_m^+(T+\Delta T,\mathbf{x})\rangle = \Delta T \frac{\left[(\mathbf{n}_k^+)^T(A^T+A)\mathbf{n}_m^+\right]}{e^{(\mu_m^+-\mu_k^+)T} - e^{(\mu_k^+-\mu_m^+)T}}. \tag{A.6}$$

Because $k \in \{1,\ldots,j\}$ and $m \in \{j+1,\ldots,n\}$, we have for $T > t_s$ that $\exp[(\mu_k^+(T,\mathbf{x}) - \mu_m^+(T,\mathbf{x}))T] \leq \exp[-\Delta\mu_j^+(\mathbf{x})T]$. Let $\overline{a} = \max_{x\in\mathcal{Y}} \max_{i\in\{1,2,\ldots,n\}} |\lambda_i(A^T+A)|$, the maximum

eigenvalue magnitude of $A^T + A$ over the set $\mathcal{Y}$. And let $\alpha = \exp(-2\Delta\mu_j^+(\mathbf{x})T_1)$ for some $T_1 > t_s$. Then for $T \geq T_1 > 0$ we have

$$|\langle \mathbf{l}_k^+(T, \mathbf{x}), \mathbf{l}_m^+(T + \Delta T, \mathbf{x})\rangle| \leq \frac{\overline{a}\Delta T}{1-\alpha} e^{-\Delta\mu_j^+(\mathbf{x})T}. \tag{A.7}$$

Upper-bounding the 2-norm by the Frobenius norm and taking $K = \sqrt{j(n-j)}\ \frac{\overline{a}\Delta T}{1-\alpha}$, the bound in the proposition follows. This bound is conservative, due to the use of the Frobenius norm, but it shows the exponential rate of convergence. Using the bound (A.3), one can show that the sequence of iterates for $T = T_1, T_1 + \Delta T, T_1 + 2\Delta T, \ldots$, is Cauchy. Moreover this is true for every sufficiently small ΔT. Because the space of j-dimensional subspaces in $T_{\mathbf{x}}\mathbb{R}^n$, a Grassmannian, with the distance given in (2.14) as the metric, is complete, we conclude that $\mathcal{L}_j^+(T, \mathbf{x})$ approaches a fixed subspace. This subspace is $\mathcal{L}_j^+(\mathbf{x})$ defined in Section 2.3.1, because all vectors in it have exponents less than or equal to $\mu_j^+(\mathbf{x})$ and one can show that any vector not in the subspace must have a larger exponent. The constant K can be smaller by increasing T_1 at the expense of delaying the applicability of the bound. ■

Appendix B

MATLAB® Code for Solving Partially Hypersensitive Optimal Control Problems

B.1 Main File

breaklines

```
%%%%%%%%%%%%%%%%%%%%%%%%%%%%%%%%%%%%%%%%%%%%%%%%%%%%%%%%%%%%%%%%%%%%%%%%%%%%%%%%
%%%   Mass-Damper-Spring (MCK)                                              %%%
%%%   Partially Hypersensitive OCP                                          %%%
%%%   Determination of Optimal Solution                                     %%%
%%%                                                                         %%%
%%%   Marco Maggia                                                          %%%
%%%   Dept. of Mechanical & Aerospace Eng.                                  %%%
%%%   University of California, Irvine                                      %%%
%%%   2013                                                                  %%%
%%%%%%%%%%%%%%%%%%%%%%%%%%%%%%%%%%%%%%%%%%%%%%%%%%%%%%%%%%%%%%%%%%%%%%%%%%%%%%%%

% clc
clear all
close all
cprintf('comment','~~~~~~~~~~~~~~~~~~~~~~~~~~~~~~~~~~~~~~~~~~~~~~~~~~~~~~~~~~~~~~~~~~~~~~~~~~~~~~~~\n')
cprintf('comment','~~~~~~~~~~~~~~~~~~~~~~~~~~~~~~~~~~~~~~~~~~~~~~~~~~~~~~~~~~~~~~~~~~~~~~~~~~~~~~~~\n')
cprintf('comment','~~~~~~~~~~~~~~~~~~~~~~~~~~~~~~~~~~~~~~~~~~~~~~~~~~~~~~~~~~~~~~~~~~~~~~~~~~~~~~~~\n')
cprintf('comment','~~~~~~~~~~~~~~~~~~~~~~~~~~~~~~~~~~~~~~~~~~~~~~~~~~~~~~~~~~~~~~~~~~~~~~~~~~~~~~~~\n\n')

tic
global n m k1 k2 c ns nc nu
global options flag

func_name = 'func_MCK_integration';
% System dimension
```

```
n = 4;
ns = 1;
nc = 2;
nu = n-(ns+nc);

% System Parameters
    % Mass
    m  = 0.1;
    % Linear spring coefficient
    k1 = 1;
    % Nonlinear spring coefficient
    k2 = 0.1;
    % Damping coefficient
    c  = 4*sqrt(k1*m);
    % Final Time
    tf=2;

% Initial values for x1 and x2
x1_0 = 2.4;
x2_0 = 0.0;
% Final values for x1 and x2
x1_f =-2.4;
x2_f = 0.0;

% First attempt for x3_0,x4_0 and x3_f,x4_f
% The initial sets for x30 and x3f must have at least 3 elements each.
x30 = 0.2:0.05:1.4;
x3f = 9.2:0.1:12.0;

% x30 = 7.86e-01;
% x3f = 1.0354e+01;

kn_x30 = size(x30)*[0 1]';
kn_x3f = size(x3f)*[0 1]';

NNN = 50;
NN = 10;
N = round(tf/2*NN);

T_fwd =  1.0; % Must be >0
T_bwd = -1.0; % Must be <0

% Tolerances for orthogonality condition
tol_err4_0 = 10^-5;
tol_err4_f = 10^-5;
tol_ang = 1E-5; %[deg]
tol_prop = 5;

% Integration options (tolerances)
options = odeset('RelTol',1e-9,'AbsTol',1e-10);

% method='X0' --> only X0 determination
% method='XF' --> only XF determination
% method='both' --> both X0 & XF determination
method = 'both';

% fig_traj = 'on' --> figures showing trajectories are on
fig_traj = 'on';

% it-num = 'on' --> shows iterations
it_num = 'on';

% solver='fms'
% solver='manual'
solver = 'manual';
```

```
text_points = fopen('FTLA_M.txt','w');
fprintf(text_points,' x01              x02              x03              x04\n\n');

for Define_Initial_and_Final_Regions=1

if strcmp(method,'X0') || strcmp(method,'both')
    % Determination of X0
    k=1;
    k_stop_0i=k+1;

% Finding Left Bound for X0
cprintf('red','Left Bound for x30\n\n')
%%%%%%%%%%%%%%%%%%%%%%%%%%%%%%%%%%%%%%%%%%%%%%%%%%%%%%%%%%%%%%%%%%%%%%%%%%%%%%%%
    while k~=k_stop_0i
        J=0;
        x3_0 = x30(1,k);
        x4_0 = 0;
        X0 =[x1_0 x2_0 x3_0 x4_0]';

        jmax=10;
        x0(:,1) = X0;

        x_fwd = zeros(n,N);
        x_fwd_prop = zeros(n,N);
        dist_fwd = zeros(N,1);

        for i=1:N+1

            j=1;
            err4_0 = 1;

            while (err4_0>tol_err4_0 || err_theta>tol_ang) && j<jmax

                if  strcmp(it_num,'on')
                    fprintf(' x0 = [%.13f,  %.13f,  %.13f,  %.13f]
(%d)\n',x0(1,j),x0(2,j),x0(3,j),x0(4,j),j-1)
                end
                % Vector field at current position
                V(1,1) = x0(2,j);
                V(2,1) = (1/m)*(-k1*x0(1,j) - k2*x0(1,j)^3 - c*x0(2,j) - x0(4,j)*(1/m));
                V(3,1) = x0(4,j)*(1/m)*(k1 + 3*k2*x0(1,j)^2);
                V(4,1) = -x0(3,j) + c*x0(4,j)*(1/m);

                T=T_fwd;
                [~,l4p] = func_FTLV(x0(:,j),T,NNN);

                l4p_1 = l4p(1,1);
                l4p_2 = l4p(2,1);
                l4p_3 = l4p(3,1);
                l4p_4 = l4p(4,1);

                err_theta = norm(asin(V'*l4p));

                num = (-l4p_1*x0(2,j) + l4p_2*(1/m)*(k1*x0(1,j)+k2*x0(1,j)^3+c*x0(2,j)) +
l4p_4*x0(3,j));
                den = (l4p_3*(1/m)*(k1+3*k2*x0(1,j)^2) + l4p_4*c*(1/m) - l4p_2*(1/m)^2);

                x0(4,j+1) = num/den;
                x0(3,j+1) = x0(3,j);
                x0(2,j+1) = x0(2,j);
                x0(1,j+1) = x0(1,j);

                err4_0 = norm(x0(4,j+1)-x0(4,j))/norm(x0(4,j));
                j=j+1;
```

```
156             end
157             J=J+j-1;
158             if strcmp(it_num,'on')
159                 cprintf([0 153/255 0],'Reinit.# =%d/%d ',i,N+1)
160                 cprintf([200/255 0 0],'Lyap. It# = %d\n',j-1)
161                 for k=1:j
162 %                 cprintf('black','X_FWD_old=[%.6f, %.6f, %.6f, %.6f]      \n',x0(:,1))
163                   cprintf('comment','X_FWD_old=[%.6f, %.6f, %.6f, %.6f] (%d)\n',x0(:,k),k-1)
164                 end
165                 cprintf('black','X_FWD_new=[%.6f, %.6f, %.6f, %.6f] (%d)\n',x0(:,j),i)
166             end
167             x_fwd(:,i)=x0(:,j);
168 
169             if i>1
170                 dist_fwd(i-1) = norm(x_fwd(:,i)-x_fwd(:,i-1));
171                 N_k = i-1;
172             end
173             if i>2 && (dist_fwd(i-1)>dist_fwd(1) || norm(x_fwd_prop(:,i-2)-x_fwd(:,i-1))>tol_prop)
174                 k_stop_0i = k;
175                 k=k+1;
176                 break
177             end
178 
179             k_stop_0i = k;
180 
181             if i<N+1
182                 dt=1/NN;
183                 flag = 'sims';
184 
185                 [tt,xx] = ode45(func_name,[0 dt],x_fwd(:,i),options);
186 
187                 x_fwd_prop(:,i) = xx(end,1:n)';
188                 x0(:,1) = x_fwd_prop(:,i);
189 
190                 if strcmp(fig_traj,'on')
191                     figure(1),hold on,grid off
192                     subplot(2,2,1),hold on,grid off
193                     plot3(xx(:,1),xx(:,2),xx(:,3),'linewidth',1.0)
194 
195                     subplot(2,2,2),hold on,grid off
196                     plot3(xx(:,1),xx(:,4),xx(:,2),'linewidth',1.0)
197 
198                     subplot(2,2,3),hold on,grid off
199                     plot3(xx(:,1),xx(:,3),xx(:,4),'linewidth',1.0)
200 
201                     subplot(2,2,4),hold on,grid off
202                     plot3(xx(:,2),xx(:,3),xx(:,4),'linewidth',1.0)
203 
204 
205                     figure(101),hold on
206                     plot3(xx(:,1),xx(:,2),xx(:,3),'linewidth',1.0)
207                 end
208             end
209             if i==1 &&  strcmp(fig_traj,'on')
210                 figure(1),hold on,grid off
211                 subplot(2,2,1),hold on,grid off
212 
213 plot3(x_fwd(1,i),x_fwd(2,i),x_fwd(3,i),'linewidth',2.0,'color','k','marker','o','MarkerFaceColor',
214 'k')
215 
216                 subplot(2,2,2),hold on,grid off
217 
218 plot3(x_fwd(1,i),x_fwd(4,i),x_fwd(2,i),'linewidth',2.0,'color','k','marker','o','MarkerFaceColor',
219 'k')
220 
```

```
                subplot(2,2,3),hold on,grid off

plot3(x_fwd(1,i),x_fwd(3,i),x_fwd(4,i),'linewidth',2.0,'color','k','marker','o','MarkerFaceColor',
'k')

                subplot(2,2,4),hold on,grid off

plot3(x_fwd(2,i),x_fwd(3,i),x_fwd(4,i),'linewidth',2.0,'color','k','marker','o','MarkerFaceColor',
'k')


                figure(101),hold on

plot3(x_fwd(1,i),x_fwd(2,i),x_fwd(3,i),'linewidth',2.0,'color','k','marker','o','MarkerFaceColor',
'k')
            end
        end
        if strcmp(fig_traj,'on')
            set(gcf,'units','normalized','position',[0 0 0.8 0.8])
        end

        if strcmp(fig_traj,'on')
            figure(2),hold on,grid off
            set(gcf,'units','normalized','position',[0 0 0.8 0.8])
            plot(1:N_k,dist_fwd(1:N_k,1),'linewidth',1.0,'color','b')
            text(N_k,dist_fwd(N_k,1),['\lambda_1 = ', num2str(x3_0)])
        end
        if k==kn_x30+1
            k=k_stop_0i;
            x30 = [];
        end
    end

    k=kn_x30;
    k_stop_0f=k-1;
    cprintf('blue','Averaging Time ''T'' = %.2f\n',T_fwd)
    cprintf('blue','Total Reinitializations = %d\n',N+1)
    cprintf('blue','Total Lyap. Iterations  = %d\n\n',J)


    if size(x30)*[1 0]' ~= 0;

% Finding Right Bound for X0
fprintf('\n')
cprintf('red','Right Bound for x30\n\n')
%%%%%%%%%%%%%%%%%%%%%%%%%%%%%%%%%%%%%%%%%%%%%%%%%%%%%%%%%%%%%%%%%%%%%%%%%%%
    while k~=k_stop_0f
        J=0;
        x3_0 = x30(1,k);
        x4_0 = 0;
        X0 =[x1_0 x2_0 x3_0 x4_0]';

        jmax=10;
        x0(:,1) = X0;

        x_fwd = zeros(n,N);
        x_fwd_prop = zeros(n,N);
        dist_fwd = zeros(N,1);

        for i=1:N+1

            j=1;
            err4_0 = 1;

            while (err4_0>tol_err4_0 || err_theta>tol_ang) && j<jmax
```

```
286
287                     if  strcmp(it_num,'on')
288                         fprintf(' x0 = [%.13f,  %.13f,  %.13f,  %.13f]
289 (%d)\n',x0(1,j),x0(2,j),x0(3,j),x0(4,j),j-1)
290                     end
291                     % Vector field at current position
292                     V(1,1) = x0(2,j);
293                     V(2,1) = (1/m)*(-k1*x0(1,j) - k2*x0(1,j)^3 - c*x0(2,j) - x0(4,j)*(1/m));
294                     V(3,1) = x0(4,j)*(1/m)*(k1 + 3*k2*x0(1,j)^2);
295                     V(4,1) = -x0(3,j) + c*x0(4,j)*(1/m);
296
297                     T=T_fwd;
298                     [~,l4p] = func_FTLV(x0(:,j),T,NNN);
299
300                     l4p_1 = l4p(1,1);
301                     l4p_2 = l4p(2,1);
302                     l4p_3 = l4p(3,1);
303                     l4p_4 = l4p(4,1);
304
305                     err_theta = norm(asin(V'*l4p));
306
307                     num = (-l4p_1*x0(2,j) + l4p_2*(1/m)*(k1*x0(1,j)+k2*x0(1,j)^3+c*x0(2,j)) +
308 l4p_4*x0(3,j));
309                     den = (l4p_3*(1/m)*(k1+3*k2*x0(1,j)^2) + l4p_4*c*(1/m) - l4p_2*(1/m)^2);
310
311                     x0(4,j+1) = num/den;
312                     x0(3,j+1) = x0(3,j);
313                     x0(2,j+1) = x0(2,j);
314                     x0(1,j+1) = x0(1,j);
315
316                     err4_0 = norm(x0(4,j+1)-x0(4,j))/norm(x0(4,j));
317                     j=j+1;
318                 end
319                 J=J+j-1;
320                 if  strcmp(it_num,'on')
321                     cprintf([0 153/255 0],'Reinit.# =%d/%d ',i,N+1)
322                     cprintf([200/255 0 0],'Lyap. It# = %d\n',j-1)
323                     cprintf('black','X_FWD=[%.6f, %.6f, %.6f, %.6f] (%d)\n',x0(:,j),i)
324                 end
325
326                 x_fwd(:,i)=x0(:,j);
327
328                 if i>1
329                     dist_fwd(i-1) = norm(x_fwd(:,i)-x_fwd(:,i-1));
330                     N_k = i-1;
331                 end
332                 if i>2 && (dist_fwd(i-1)>dist_fwd(1) || norm(x_fwd_prop(:,i-2)-x_fwd(:,i-1))>tol_prop)
333                     k_stop_0f = k;
334                     k=k-1;
335                     break
336                 end
337
338                 k_stop_0f = k;
339
340                 if i<N+1
341                     dt=1/NN;
342                     flag = 'sims';
343
344                     [tt,xx] = ode45(func_name,[0 dt],x_fwd(:,i),options);
345
346                     x_fwd_prop(:,i) = xx(end,1:n)';
347                     x0(:,1) = x_fwd_prop(:,i);
348
349                     if strcmp(fig_traj,'on')
350                         figure(1),hold on,grid off
```

```
                    subplot(2,2,1),hold on,grid off
                    plot3(xx(:,1),xx(:,2),xx(:,3),'linewidth',1.0)

                    subplot(2,2,2),hold on,grid off
                    plot3(xx(:,1),xx(:,4),xx(:,2),'linewidth',1.0)

                    subplot(2,2,3),hold on,grid off
                    plot3(xx(:,1),xx(:,3),xx(:,4),'linewidth',1.0)

                    subplot(2,2,4),hold on,grid off
                    plot3(xx(:,2),xx(:,3),xx(:,4),'linewidth',1.0)

                    figure(101),hold on
                    plot3(xx(:,1),xx(:,2),xx(:,3),'linewidth',1.0)
                end
            end
            if i==1 &&  strcmp(fig_traj,'on')
                figure(1),hold on,grid off
                subplot(2,2,1),hold on,grid off

plot3(x_fwd(1,i),x_fwd(2,i),x_fwd(3,i),'linewidth',2.0,'color','k','marker','o','MarkerFaceColor',
'k')

                subplot(2,2,2),hold on,grid off

plot3(x_fwd(1,i),x_fwd(4,i),x_fwd(2,i),'linewidth',2.0,'color','k','marker','o','MarkerFaceColor',
'k')

                subplot(2,2,3),hold on,grid off

plot3(x_fwd(1,i),x_fwd(3,i),x_fwd(4,i),'linewidth',2.0,'color','k','marker','o','MarkerFaceColor',
'k')

                subplot(2,2,4),hold on,grid off

plot3(x_fwd(2,i),x_fwd(3,i),x_fwd(4,i),'linewidth',2.0,'color','k','marker','o','MarkerFaceColor',
'k')


                figure(101),hold on

plot3(x_fwd(1,i),x_fwd(2,i),x_fwd(3,i),'linewidth',2.0,'color','k','marker','o','MarkerFaceColor',
'k')
            end
        end
        if strcmp(fig_traj,'on')
            set(gcf,'units','normalized','position',[0 0 0.8 0.8])
        end
        if strcmp(fig_traj,'on')
            figure(2),hold on,grid off
            set(gcf,'units','normalized','position',[0 0 0.8 0.8])
            plot(1:N_k,dist_fwd(1:N_k,1),'linewidth',1.0,'color','b')
            text(N_k,dist_fwd(N_k,1),['\lambda_1 = ', num2str(x3_0)])
        end
    end

    cprintf('blue','Averaging Time ''T'' = %.2f\n',T_fwd)
    cprintf('blue','Total Reinitializations = %d\n',N+1)
    cprintf('blue','Total Lyap. Iterations  = %d\n\n',J)
    if k_stop_0i==1 && k_stop_0f==kn_x30
        x30 = x30(1,k_stop_0i:k_stop_0f);
    end
    if k_stop_0i==1 && k_stop_0f~=kn_x30
        x30 = x30(1,k_stop_0i:k_stop_0f+1);
    end
```

```
    if k_stop_0i~=1 && k_stop_0f==kn_x30
        x30 = x30(1,k_stop_0i-1:k_stop_0f);
    end
    if k_stop_0i~=1 && k_stop_0f~=kn_x30
        x30 = x30(1,k_stop_0i-1:k_stop_0f+1);
    end
    end
end

%%%%%%%%%%%%%%%%%%%%%%%%%%%%%%%%%%%%%%%%%%%%%%%%%%%%%%%%%%%%%%%%%%%%%%%%%%%%%%%%
cprintf('comment','~~~~~~~~~~~~~~~~~~~~~~~~~~~~~~~~~~~~~~~~~~~~~~~~~~~~~~~~~~~~~~~~~~\n')
%%%%%%%%%%%%%%%%%%%%%%%%%%%%%%%%%%%%%%%%%%%%%%%%%%%%%%%%%%%%%%%%%%%%%%%%%%%%%%%%

if strcmp(method,'XF') || strcmp(method,'both')
    % Determination of XF0
    k=1;
    k_stop_Fi=k+1;

% Finding Left Bound for XF
fprintf('\n')
cprintf('red','Left Bound for x3f\n\n')
%%%%%%%%%%%%%%%%%%%%%%%%%%%%%%%%%%%%%%%%%%%%%%%%%%%%%%%%%%%%%%%%%%%%%%%%%%%%%%%%
    while k~=k_stop_Fi
        J=0;
        x3_f = x3f(1,k);
        x4_f = 0;
        XF =[x1_f x2_f x3_f x4_f]';

        jmax=10;
        xf(:,1) = XF;

        x_bwd = zeros(n,N);
        x_bwd_prop = zeros(n,N);
        dist_bwd = zeros(N,1);

        for i=1:N+1

            j=1;
            err4_f = 1;

            while (err4_f>tol_err4_f || err_theta>tol_ang) && j<jmax

                if strcmp(it_num,'on')
                    fprintf(' xf = [%.13f,  %.13f,  %.13f,  %.13f]
(%d)\n',xf(1,j),xf(2,j),xf(3,j),xf(4,j),j-1)
                end
                % Vector field at current position
                V(1,1) = xf(2,j);
                V(2,1) = (1/m)*(-k1*xf(1,j) - k2*xf(1,j)^3 - c*xf(2,j) - xf(4,j)*(1/m));
                V(3,1) = xf(4,j)*(1/m)*(k1 + 3*k2*xf(1,j)^2);
                V(4,1) = -xf(3,j) + c*xf(4,j)*(1/m);

                T=T_bwd;
                [~,l1m] = func_FTLV(xf(:,j),T,NNN);

                l1m_1 = l1m(1,1);
                l1m_2 = l1m(2,1);
                l1m_3 = l1m(3,1);
                l1m_4 = l1m(4,1);

                err_theta = norm(asin(V'*l1m));

                num = (-l1m_1*xf(2,j) + l1m_2*(1/m)*(k1*xf(1,j)+k2*xf(1,j)^3+c*xf(2,j)) +
l1m_4*xf(3,j));
                den = (l1m_3*(1/m)*(k1+3*k2*xf(1,j)^2) + l1m_4*c*(1/m) - l1m_2*(1/m)^2);
```

```
481
482                     xf(4,j+1) = num/den;
483                     xf(3,j+1) = xf(3,j);
484                     xf(2,j+1) = xf(2,j);
485                     xf(1,j+1) = xf(1,j);
486
487                     err4_f = norm(xf(4,j+1)-xf(4,j))/norm(xf(4,j));
488                     j=j+1;
489
490                 end
491                 J=J+j-1;
492                 if strcmp(it_num,'on')
493                     cprintf([0 153/255 0],'Reinit.# =%d/%d ',i,N+1)
494                     cprintf([200/255 0 0],'Lyap. It# = %d\n',j-1)
495                     cprintf('black','X_BWD=[%.6f, %.6f, %.6f, %.6f] (%d)\n',xf(:,j),i)
496                 end
497
498                 x_bwd(:,i)=xf(:,j);
499
500                 if i>1
501                     dist_bwd(i-1) = norm(x_bwd(:,i)-x_bwd(:,i-1));
502                     N_k = i-1;
503                 end
504                 if i>2 && (dist_bwd(i-1)>dist_bwd(1) || norm(x_bwd_prop(:,i-2)-x_bwd(:,i-1))>tol_prop)
505                     k_stop_Fi = k;
506                     k=k+1;
507                     break
508                 end
509
510                 k_stop_Fi = k;
511
512                 if i<N+1
513                     dt=-1/NN;
514                     flag = 'sims';
515
516                     [tt,xx] = ode45(func_name,[0 dt],x_bwd(:,i),options);
517
518                     x_bwd_prop(:,i) = xx(end,1:n)';
519                     xf(:,1) = x_bwd_prop(:,i);
520
521                     if strcmp(fig_traj,'on')
522                         figure(1),hold on,grid off
523                         subplot(2,2,1),hold on,grid off
524                         plot3(xx(:,1),xx(:,2),xx(:,3),'linewidth',1.0,'color','r')
525
526                         subplot(2,2,2),hold on,grid off
527                         plot3(xx(:,1),xx(:,4),xx(:,2),'linewidth',1.0,'color','r')
528
529                         subplot(2,2,3),hold on,grid off
530                         plot3(xx(:,1),xx(:,3),xx(:,4),'linewidth',1.0,'color','r')
531
532                         subplot(2,2,4),hold on,grid off
533                         plot3(xx(:,2),xx(:,3),xx(:,4),'linewidth',1.0,'color','r')
534
535                         figure(101),hold on
536                         plot3(xx(:,1),xx(:,2),xx(:,3),'linewidth',1.0,'color','r')
537                     end
538                 end
539                 if i==1 && strcmp(fig_traj,'on')
540                     figure(1),hold on
541                     subplot(2,2,1),hold on,grid off
542
543 plot3(x_bwd(1,i),x_bwd(2,i),x_bwd(3,i),'linewidth',2.0,'color','k','marker','o','MarkerFaceColor',
544 'k')
545
```

```
                subplot(2,2,2),hold on,grid off

plot3(x_bwd(1,i),x_bwd(4,i),x_bwd(2,i),'linewidth',2.0,'color','k','marker','o','MarkerFaceColor',
'k')

                subplot(2,2,3),hold on,grid off

plot3(x_bwd(1,i),x_bwd(3,i),x_bwd(4,i),'linewidth',2.0,'color','k','marker','o','MarkerFaceColor',
'k')

                subplot(2,2,4),hold on,grid off

plot3(x_bwd(2,i),x_bwd(3,i),x_bwd(4,i),'linewidth',2.0,'color','k','marker','o','MarkerFaceColor',
'k')

                figure(101),hold on

plot3(x_bwd(1,i),x_bwd(2,i),x_bwd(3,i),'linewidth',2.0,'color','k','marker','o','MarkerFaceColor',
'k')
            end
        end
        if strcmp(fig_traj,'on')
            set(gcf,'units','normalized','position',[0 0 0.8 0.8])
        end
        if strcmp(fig_traj,'on')
            figure(3),hold on,grid off
            set(gcf,'units','normalized','position',[0 0 0.8 0.8])
            plot(1:N_k,dist_bwd(1:N_k,1),'linewidth',1.0,'color','r')
            text(N_k,dist_bwd(N_k,1),['\lambda_1 = ', num2str(x3_f)])
        end

        if k==kn_x3f+1
            k=k_stop_Fi;
            x3f = [];
        end
    end

    cprintf('blue','Averaging Time ''T'' = %.2f\n',T_bwd)
    cprintf('blue','Total Reinitializations = %d\n',N+1)
    cprintf('blue','Total Lyap. Iterations  = %d\n\n',J)

    k=kn_x3f;
    k_stop_Ff=k-1;

    if size(x3f)*[1 0]' ~= 0;

% Finding Right Bound for XF
fprintf('\n')
cprintf('red','Right Bound for x3f\n\n')
%%%%%%%%%%%%%%%%%%%%%%%%%%%%%%%%%%%%%%%%%%%%%%%%%%%%%%%%%%%%%%%%%%%%%%%%%%%%%%%%
    while k~=k_stop_Ff
        J=0;
        x3_f = x3f(1,k);
        x4_f = 0;
        XF =[x1_f x2_f x3_f x4_f]';

        jmax=10;
        xf(:,1) = XF;

        x_bwd = zeros(n,N);
        x_bwd_prop = zeros(n,N);
        dist_bwd = zeros(N,1);

        for i=1:N+1

```

```
611             j=1;
612             err4_f = 1;
613 
614             while (err4_f>tol_err4_f || err_theta>tol_ang) && j<jmax
615 
616                 if  strcmp(it_num,'on')
617                     fprintf(' xf = [%.13f,  %.13f,  %.13f,  %.13f]
618 (%d)\n',xf(1,j),xf(2,j),xf(3,j),xf(4,j),j-1)
619                 end
620                 % Vector field at current position
621                 V(1,1) = xf(2,j);
622                 V(2,1) = (1/m)*(-k1*xf(1,j) - k2*xf(1,j)^3 - c*xf(2,j) - xf(4,j)*(1/m));
623                 V(3,1) = xf(4,j)*(1/m)*(k1 + 3*k2*xf(1,j)^2);
624                 V(4,1) = -xf(3,j) + c*xf(4,j)*(1/m);
625 
626                 T=T_bwd;
627                 [~,l1m] = func_FTLV(xf(:,j),T,NNN);
628 
629                 l1m_1 = l1m(1,1);
630                 l1m_2 = l1m(2,1);
631                 l1m_3 = l1m(3,1);
632                 l1m_4 = l1m(4,1);
633 
634                 err_theta = norm(asin(V'*l1m));
635 
636                 num = (-l1m_1*xf(2,j) + l1m_2*(1/m)*(k1*xf(1,j)+k2*xf(1,j)^3+c*xf(2,j)) +
637 l1m_4*xf(3,j));
638                 den = (l1m_3*(1/m)*(k1+3*k2*xf(1,j)^2) + l1m_4*c*(1/m) - l1m_2*(1/m)^2);
639 
640                 xf(4,j+1) = num/den;
641                 xf(3,j+1) = xf(3,j);
642                 xf(2,j+1) = xf(2,j);
643                 xf(1,j+1) = xf(1,j);
644 
645                 err4_f = norm(xf(4,j+1)-xf(4,j))/norm(xf(4,j));
646                 j=j+1;
647 
648             end
649             J=J+j-1;
650             if strcmp(it_num,'on')
651                 cprintf([0 153/255 0],'Reinit.# =%d/%d ',i,N+1)
652                 cprintf([200/255 0 0],'Lyap. It# = %d\n',j-1)
653                 for k=1:j
654                     cprintf('comment','X_BWD_old=[%.6f, %.6f, %.6f, %.6f] (%d)\n',xf(:,k),k-1)
655                 end
656                 cprintf('black','X_BWD_new=[%.6f, %.6f, %.6f, %.6f] (%d)\n',xf(:,j),i)
657             end
658 
659             x_bwd(:,i)=xf(:,j);
660 
661             if i>1
662                 dist_bwd(i-1) = norm(x_bwd(:,i)-x_bwd(:,i-1));
663                 N_k = i-1;
664             end
665             if i>2 && (dist_bwd(i-1)>dist_bwd(1) || norm(x_bwd_prop(:,i-2)-x_bwd(:,i-1))>tol_prop)
666                 k_stop_Ff = k;
667                 k=k-1;
668                 break
669             end
670 
671             k_stop_Ff = k;
672 
673             if i<N+1
674                 dt=-1/NN;
675                 flag = 'sims';
```

```
676
677                     [tt,xx] = ode45(func_name,[0 dt],x_bwd(:,i),options);
678
679                     x_bwd_prop(:,i) = xx(end,1:n)';
680                     xf(:,1) = x_bwd_prop(:,i);
681
682                     if strcmp(fig_traj,'on')
683                         figure(1),hold on,grid off
684                         subplot(2,2,1),hold on,grid off
685                         plot3(xx(:,1),xx(:,2),xx(:,3),'linewidth',1.0,'color','r')
686
687                         subplot(2,2,2),hold on,grid off
688                         plot3(xx(:,1),xx(:,4),xx(:,2),'linewidth',1.0,'color','r')
689
690                         subplot(2,2,3),hold on,grid off
691                         plot3(xx(:,1),xx(:,3),xx(:,4),'linewidth',1.0,'color','r')
692
693                         subplot(2,2,4),hold on,grid off
694                         plot3(xx(:,2),xx(:,3),xx(:,4),'linewidth',1.0,'color','r')
695
696                         figure(101),hold on
697                         plot3(xx(:,1),xx(:,2),xx(:,3),'linewidth',1.0,'color','r')
698                     end
699                 end
700                 if i==1 && strcmp(fig_traj,'on')
701                     figure(1),hold on
702                     subplot(2,2,1),hold on,grid off
703
704 plot3(x_bwd(1,i),x_bwd(2,i),x_bwd(3,i),'linewidth',2.0,'color','k','marker','o','MarkerFaceColor',
705 'k')
706
707                     subplot(2,2,2),hold on,grid off
708
709 plot3(x_bwd(1,i),x_bwd(4,i),x_bwd(2,i),'linewidth',2.0,'color','k','marker','o','MarkerFaceColor',
710 'k')
711
712                     subplot(2,2,3),hold on,grid off
713
714 plot3(x_bwd(1,i),x_bwd(3,i),x_bwd(4,i),'linewidth',2.0,'color','k','marker','o','MarkerFaceColor',
715 'k')
716
717                     subplot(2,2,4),hold on,grid off
718
719 plot3(x_bwd(2,i),x_bwd(3,i),x_bwd(4,i),'linewidth',2.0,'color','k','marker','o','MarkerFaceColor',
720 'k')
721
722                     figure(101),hold on
723
724 plot3(x_bwd(1,i),x_bwd(2,i),x_bwd(3,i),'linewidth',2.0,'color','k','marker','o','MarkerFaceColor',
725 'k')
726                 end
727             end
728             if strcmp(fig_traj,'on')
729                 set(gcf,'units','normalized','position',[0 0 0.8 0.8])
730             end
731             if strcmp(fig_traj,'on')
732                 figure(3),hold on,grid off
733                 set(gcf,'units','normalized','position',[0 0 0.8 0.8])
734                 plot(1:N_k,dist_bwd(1:N_k,1),'linewidth',1.0,'color','r')
735                 text(N_k,dist_bwd(N_k,1),['\lambda_1 = ', num2str(x3_f)])
736             end
737         end
738
739         cprintf('blue','Averaging Time ''T'' = %.2f\n',T_bwd)
740         cprintf('blue','Total Reinitializations = %d\n',N+1)
```

```
741       cprintf('blue','Total Lyap. Iterations  = %d\n\n',J)
742
743       if k_stop_Fi==1 && k_stop_Ff==kn_x3f
744           x3f = x3f(1,k_stop_Fi:k_stop_Ff);
745       end
746       if k_stop_Fi==1 && k_stop_Ff~=kn_x3f
747           x3f = x3f(1,k_stop_Fi:k_stop_Ff+1);
748       end
749       if k_stop_Fi~=1 && k_stop_Ff==kn_x3f
750           x3f = x3f(1,k_stop_Fi-1:k_stop_Ff);
751       end
752       if k_stop_Fi~=1 && k_stop_Ff~=kn_x3f
753           x3f = x3f(1,k_stop_Fi-1:k_stop_Ff+1);
754       end
755       end
756   end
757
758
759   end
760
761   figure(1),hold on,grid off
762   subplot(2,2,1),hold on,grid off
763   xlab=xlabel('$x_1$');
764   ylab=ylabel('$x_2$');
765   zlab=zlabel('$\lambda_1$');
766   set([xlab,ylab,zlab],'FontSize', 16,'linewidth',2.0,'interpreter','latex','FontName',
767   'Times','FontWeight','normal');
768   set(gca,'FontSize', 14,'linewidth',1.0,'FontName', 'Times','FontWeight','normal');
769
770   subplot(2,2,2),hold on,grid off
771   xlab=xlabel('$x_1$');
772   ylab=ylabel('$\lambda_2$');
773   zlab=zlabel('$x_2$');
774   set([xlab,ylab,zlab],'FontSize', 16,'linewidth',2.0,'interpreter','latex','FontName',
775   'Times','FontWeight','normal');
776   set(gca,'FontSize', 14,'linewidth',1.0,'FontName', 'Times','FontWeight','normal');
777
778   subplot(2,2,3),hold on,grid off
779   xlab=xlabel('$x_1$');
780   ylab=ylabel('$\lambda_1$');
781   zlab=zlabel('$\lambda_2$');
782   set([xlab,ylab,zlab],'FontSize', 16,'linewidth',2.0,'interpreter','latex','FontName',
783   'Times','FontWeight','normal');
784   set(gca,'FontSize', 14,'linewidth',1.0,'FontName', 'Times','FontWeight','normal');
785
786   subplot(2,2,4),hold on,grid off
787   xlab=xlabel('$x_2$');
788   ylab=ylabel('$\lambda_1$');
789   zlab=zlabel('$\lambda_2$');
790   set([xlab,ylab,zlab],'FontSize', 16,'linewidth',2.0,'interpreter','latex','FontName',
791   'Times','FontWeight','normal');
792   set(gca,'FontSize', 14,'linewidth',1.0,'FontName', 'Times','FontWeight','normal');
793
794   set(gcf,'units','normalized','position',[0 0 0.8 0.9])
795   fillPage(gcf, 'papersize', [11.5 8.5], 'margins', [0.1 0.1 0.1 0.1]);
796
797
798   figure(101),hold on
799   xlab=xlabel('$x_1$');
800   ylab=ylabel('$x_2$');
801   zlab=zlabel('$\lambda_1$');
802   set([xlab,ylab,zlab],'FontSize', 16,'linewidth',2.0,'interpreter','latex','FontName',
803   'Times','FontWeight','normal');
804   set(gca,'FontSize', 14,'linewidth',1.0,'FontName', 'Times','FontWeight','normal');
805
```

```
set(gcf,'units','normalized','position',[0 0 0.8 0.9])
fillPage(gcf, 'papersize', [11.5 8.5], 'margins', [0.1 0.1 0.1 0.1]);


x30_lb = x30(1,1);
x30_ub = x30(1,end);
x3f_lb = x3f(1,1);
x3f_ub = x3f(1,end);
cprintf('black','x3_0 = [%.4e ; %.4e]  x3_f = [%.4e ; %.4e]\n',x30_lb,x30_ub,x3f_lb,x3f_ub)

if strcmp(solver,'fms')
    par =  [x1_0 x1_f;
             x2_0 x2_f
             Tfwd Tbwd];

    X0 = [0.5*(x30_lb+x30_ub); 0.5*(x3f_lb+x3f_ub)];
    options_fms = optimset('TolFun',11);

    tic
    [x,distance,exitflag] = fminsearch(@(x) func_PHOCP_fms(x,par),X0,options_fms);
    toc
    return
end

if strcmp(method,'X0') || strcmp(method,'XF')
    return
end
%%%%%%%%%%%%%%%%%%%%%%%%%%%%%%%%%%%%%%%%%%%%%%%%%%%%%%%%%%%%%%%%%%%%%%%%%%%%%%%%%%%%%%
%%%%%%%%%%%%%%%%%%%%%%%%%%%%%%%%%%%%%%%%%%%%%%%%%%%%%%%%%%%%%%%%%%%%%%%%%%%%%%%%%%%%%%
cprintf('comment','~~~~~~~~~~~~~~~~~~~~~~~~~~~~~~~~~~~~~~~~~~~~~~~~~~~~~~~~~~~~~~~~~~~~~~~~~~~~\n')
cprintf('comment','~~~~~~~~~~~~~~~~~~~~~~~~~~~~~~~~~~~~~~~~~~~~~~~~~~~~~~~~~~~~~~~~~~~~~~~~~~~~\n')
%%%%%%%%%%%%%%%%%%%%%%%%%%%%%%%%%%%%%%%%%%%%%%%%%%%%%%%%%%%%%%%%%%%%%%%%%%%%%%%%%%%%%%
%%%%%%%%%%%%%%%%%%%%%%%%%%%%%%%%%%%%%%%%%%%%%%%%%%%%%%%%%%%%%%%%%%%%%%%%%%%%%%%%%%%%%%

radius = 1;
r_x30 = abs(x30(1,1)-x30(1,end))/abs(x30(1,1));
r_x3f = abs(x3f(1,1)-x3f(1,end))/abs(x3f(1,1));
tol_r =1E-3;
tol_radius = 1E-3;

Nt_0 = 5;
Nt_f = 5;

% Grid refinement
while radius > tol_radius && (r_x30>tol_r || r_x3f>tol_r)

kmax_x30 = size(x30)*[0 1]';
kmax_x3f = size(x3f)*[0 1]';

% method='X0' --> only X0 determination
% method='XF' --> only XF determination
% method='both' --> both X0 & XF determination
method = 'both';

text_points = fopen('FTLA_M.txt','w');
fprintf(text_points,' x01              x02              x03              x04\n\n');

if strcmp(method,'X0') || strcmp(method,'both')

    % Determination of X0
    fprintf('\n')
    cprintf('red','Determination of X0. Distance = %.4f\n\n',radius)

    x_fwd = zeros(n,N,kmax_x30);
    J=0;
```

```
871
872     for k=1:kmax_x30
873
874         x3_0 = x30(1,k);
875         x4_0 = 0;
876         X0 =[x1_0 x2_0 x3_0 x4_0]';
877
878         jmax=10;
879         x0(:,1) = X0;
880
881         dist_fwd = zeros(N,1);
882         x_fwd_prop = zeros(n,N);
883
884         for i=1:N+1
885
886             j=1;
887             err4_0 = 1;
888
889             while (err4_0>tol_err4_0 || err_theta>tol_ang) && j<jmax
890                 if  strcmp(it_num,'on')
891                     fprintf(' x0 = [%.13f,  %.13f,  %.13f,  %.13f]
892 (%d)\n',x0(1,j),x0(2,j),x0(3,j),x0(4,j),j-1)
893                 end
894                 % Vector field at current position
895                 V(1,1) = x0(2,j);
896                 V(2,1) = (1/m)*(-k1*x0(1,j) - k2*x0(1,j)^3 - c*x0(2,j) - x0(4,j)*(1/m));
897                 V(3,1) = x0(4,j)*(1/m)*(k1 + 3*k2*x0(1,j)^2);
898                 V(4,1) = -x0(3,j) + c*x0(4,j)*(1/m);
899
900                 T=T_fwd;
901                 [~,l4p] = func_FTLV(x0(:,j),T,NNN);
902
903                 l4p_1 = l4p(1,1);
904                 l4p_2 = l4p(2,1);
905                 l4p_3 = l4p(3,1);
906                 l4p_4 = l4p(4,1);
907
908                 err_theta = norm(asin(V'*l4p));
909
910                 num = (-l4p_1*x0(2,j) + l4p_2*(1/m)*(k1*x0(1,j)+k2*x0(1,j)^3+c*x0(2,j)) +
911 l4p_4*x0(3,j));
912                 den = (l4p_3*(1/m)*(k1+3*k2*x0(1,j)^2) + l4p_4*c*(1/m) - l4p_2*(1/m)^2);
913
914                 x0(4,j+1) = num/den;
915                 x0(3,j+1) = x0(3,j);
916                 x0(2,j+1) = x0(2,j);
917                 x0(1,j+1) = x0(1,j);
918
919                 err4_0 = norm(x0(4,j+1)-x0(4,j))/norm(x0(4,j));
920                 j=j+1;
921             end
922             J=J+j-1;
923             if strcmp(it_num,'on')
924                 cprintf([0 153/255 0],'Reinit.# =%d/%d ',i,N+1)
925                 cprintf([200/255 0 0],'Lyap. It# = %d\n',j-1)
926                 cprintf('black','X_FWD=[%.6f, %.6f, %.6f, %.6f] (%d)\n',x0(:,j),i)
927             end
928             x_fwd(:,i,k)=x0(:,j);
929
930             if i>1
931                 dist_fwd(i-1,1) = norm(x_fwd(:,i,k)-x_fwd(:,i-1,k));
932             end
933
934             if i<N+1
935                 dt=1/NN;
```

```
936                     flag = 'sims';
937
938                     [tt,xx] = ode45(func_name,[0 dt],x_fwd(:,i,k),options);
939
940                     x_fwd_prop(:,i) = xx(end,1:n)';
941                     x0(:,1) = x_fwd_prop(:,i);
942
943                     if strcmp(fig_traj,'on')
944                         figure(1),hold on,grid off
945                         subplot(2,2,1),hold on,grid off
946                         plot3(xx(:,1),xx(:,2),xx(:,3),'linewidth',1.0)
947
948                         subplot(2,2,2),hold on,grid off
949                         plot3(xx(:,1),xx(:,4),xx(:,2),'linewidth',1.0)
950
951                         subplot(2,2,3),hold on,grid off
952                         plot3(xx(:,1),xx(:,3),xx(:,4),'linewidth',1.0)
953
954                         subplot(2,2,4),hold on,grid off
955                         plot3(xx(:,2),xx(:,3),xx(:,4),'linewidth',1.0)
956
957                         figure(101),hold on,grid off
958                         plot3(xx(:,1),xx(:,2),xx(:,3),'linewidth',1.0)
959                     end
960                 end
961                 if i==1 &&  strcmp(fig_traj,'on')
962                     figure(1),hold on
963                     subplot(2,2,1),hold on,grid off
964
965 plot3(x_fwd(1,i,k),x_fwd(2,i,k),x_fwd(3,i,k),'linewidth',2.0,'color','k','marker','o',
966 'MarkerFaceColor','k')
967
968                     subplot(2,2,2),hold on,grid off
969
970 plot3(x_fwd(1,i,k),x_fwd(4,i,k),x_fwd(2,i,k),'linewidth',2.0,'color','k','marker','o',
971 'MarkerFaceColor','k')
972
973                     subplot(2,2,3),hold on,grid off
974
975 plot3(x_fwd(1,i,k),x_fwd(3,i,k),x_fwd(4,i,k),'linewidth',2.0,'color','k','marker','o',
976 'MarkerFaceColor','k')
977
978                     subplot(2,2,4),hold on,grid off
979
980 plot3(x_fwd(2,i,k),x_fwd(3,i,k),x_fwd(4,i,k),'linewidth',2.0,'color','k','marker','o',
981 'MarkerFaceColor','k')
982
983
984                     figure(101),hold on
985
986 plot3(x_fwd(1,i,k),x_fwd(2,i,k),x_fwd(3,i,k),'linewidth',2.0,'color','k','marker','o',
987 'MarkerFaceColor','k')
988                 end
989             end
990             if strcmp(fig_traj,'on')
991                 set(gcf,'units','normalized','position',[0 0 0.8 0.8])
992             end
993             if strcmp(fig_traj,'on')
994                 figure(2),hold on,grid off
995                 set(gcf,'units','normalized','position',[0 0 0.8 0.8])
996                 plot(1:N,dist_fwd(:,1),'linewidth',1.0,'color','b')
997                 text(N,dist_fwd(N,1),['\lambda_1 = ', num2str(x3_0)])
998             end
999         end
1000 end
```

```
cprintf('blue','Averaging Time ''T'' = %.2f\n',T_fwd)
cprintf('blue','Total Reinitializations = %d\n',N+1)
cprintf('blue','Total Lyap. Iterations (Avg.) = %d\n\n',J/(Nt_0+1))

%%%%%%%%%%%%%%%%%%%%%%%%%%%%%%%%%%%%%%%%%%%%%%%%%%%%%%%%%%%%%%%%%%%%%%%%%%%%%%%%
%%%%%%%%%%%%%%%%%%%%%%%%%%%%%%%%%%%%%%%%%%%%%%%%%%%%%%%%%%%%%%%%%%%%%%%%%%%%%%%%


if strcmp(method,'XF') || strcmp(method,'both')

    % Determination of XF
    cprintf('red','Determination of XF. Distance = %.4f\n\n',radius)
    x_bwd = zeros(n,N,kmax_x3f);
    J=0;

    for k=1:kmax_x3f

        x3_f = x3f(1,k);
        x4_f = 0;
        XF =[x1_f x2_f x3_f x4_f]';

        jmax=10;
        xf(:,1) = XF;

        x_bwd_prop = zeros(n,N);
        dist_bwd = zeros(N,1);

        for i=1:N+1

            j=1;
            err4_f = 1;

            while (err4_f>tol_err4_f || err_theta>tol_ang) && j<jmax

                if strcmp(it_num,'on')
                    fprintf('xf = [%.13f, %.13f, %.13f, %.13f]
(%d)\n',xf(1,j),xf(2,j),xf(3,j),xf(4,j),j-1)
                end
                % Vector field at current position
                V(1,1) = xf(2,j);
                V(2,1) = (1/m)*(-k1*xf(1,j) - k2*xf(1,j)^3 - c*xf(2,j) - xf(4,j)*(1/m));
                V(3,1) = xf(4,j)*(1/m)*(k1 + 3*k2*xf(1,j)^2);
                V(4,1) = -xf(3,j) + c*xf(4,j)*(1/m);

                T=T_bwd;
                [~,l1m] = func_FTLV(xf(:,j),T,NNN);

                l1m_1 = l1m(1,1);
                l1m_2 = l1m(2,1);
                l1m_3 = l1m(3,1);
                l1m_4 = l1m(4,1);

                err_theta = norm(asin(V'*l1m));

                num = (-l1m_1*xf(2,j) + l1m_2*(1/m)*(k1*xf(1,j)+k2*xf(1,j)^3+c*xf(2,j)) +
l1m_4*xf(3,j));
                den = (l1m_3*(1/m)*(k1+3*k2*xf(1,j)^2) + l1m_4*c*(1/m) - l1m_2*(1/m)^2);

                xf(4,j+1) = num/den;
                xf(3,j+1) = xf(3,j);
                xf(2,j+1) = xf(2,j);
                xf(1,j+1) = xf(1,j);

                err4_f = norm(xf(4,j+1)-xf(4,j))/norm(xf(4,j));
                j=j+1;
```

```
            end
            J=J+j-1;
            if strcmp(it_num,'on')
                cprintf([0 153/255 0],'Reinit.# =%d/%d ',i,N+1)
                cprintf([200/255 0 0],'Lyap. It# = %d\n',j-1)
                cprintf('black','X_BWD=[%.6f, %.6f, %.6f, %.6f] (%d)\n',xf(:,j),i)
            end

            x_bwd(:,i,k)=xf(:,j);

            if i>1
                dist_bwd(i-1) = norm(x_bwd(:,i,k)-x_bwd(:,i-1,k));
            end

            if i<N+1
                dt=-1/NN;
                flag = 'sims';

                [tt,xx] = ode45(func_name,[0 dt],x_bwd(:,i,k),options);

                x_bwd_prop(:,i) = xx(end,1:n)';
                xf(:,1) = x_bwd_prop(:,i);

                if strcmp(fig_traj,'on')
                    figure(1),hold on,grid off
                    subplot(2,2,1),hold on,grid off
                    plot3(xx(:,1),xx(:,2),xx(:,3),'linewidth',1.0,'color','r')

                    subplot(2,2,2),hold on,grid off
                    plot3(xx(:,1),xx(:,4),xx(:,2),'linewidth',1.0,'color','r')

                    subplot(2,2,3),hold on,grid off
                    plot3(xx(:,1),xx(:,3),xx(:,4),'linewidth',1.0,'color','r')

                    subplot(2,2,4),hold on,grid off
                    plot3(xx(:,2),xx(:,3),xx(:,4),'linewidth',1.0,'color','r')

                    figure(101),hold on
                    plot3(xx(:,1),xx(:,2),xx(:,3),'linewidth',1.0,'color','r')
                end
            end
            if i==1 && strcmp(fig_traj,'on')
                figure(1),hold on
                subplot(2,2,1),hold on,grid off

plot3(x_bwd(1,i,k),x_bwd(2,i,k),x_bwd(3,i,k),'linewidth',2.0,'color','k','marker','o',
'MarkerFaceColor','k')

                subplot(2,2,2),hold on,grid off

plot3(x_bwd(1,i,k),x_bwd(4,i,k),x_bwd(2,i,k),'linewidth',2.0,'color','k','marker','o',
'MarkerFaceColor','k')

                subplot(2,2,3),hold on,grid off

plot3(x_bwd(1,i,k),x_bwd(3,i,k),x_bwd(4,i,k),'linewidth',2.0,'color','k','marker','o',
'MarkerFaceColor','k')

                subplot(2,2,4),hold on,grid off

plot3(x_bwd(2,i,k),x_bwd(3,i,k),x_bwd(4,i,k),'linewidth',2.0,'color','k','marker','o',
'MarkerFaceColor','k')


                figure(101),hold on
```

```
1131
1132 plot3(x_bwd(1,i,k),x_bwd(2,i,k),x_bwd(3,i,k),'linewidth',2.0,'color','k','marker','o',
1133 'MarkerFaceColor','k')
1134             end
1135         end
1136         if strcmp(fig_traj,'on')
1137             set(gcf,'units','normalized','position',[0 0 0.8 0.8])
1138         end
1139         if strcmp(fig_traj,'on')
1140             figure(3),hold on,grid off
1141             set(gcf,'units','normalized','position',[0 0 0.8 0.8])
1142             plot(1:N,dist_bwd(:,1),'linewidth',1.0,'color','r')
1143             text(N,dist_bwd(N,1),['\lambda_1 = ', num2str(x3_f)])
1144         end
1145     end
1146 end
1147 cprintf('blue','Averaging Time ''T'' = %.2f\n',T_bwd)
1148 cprintf('blue','Total Reinitializations = %d\n',N+1)
1149 cprintf('blue','Total Lyap. Iterations (Avg.) = %d\n\n',J/(Nt_f+1))
1150
1151
1152 X_fwd = zeros(n,kmax_x30);
1153 X_bwd = zeros(n,kmax_x3f);
1154 distance = zeros(kmax_x30,kmax_x3f);
1155
1156 X_fwd(:,:) = x_fwd(:,end,:);
1157 X_bwd(:,:) = x_bwd(:,end,:);
1158
1159 for i=1:kmax_x30
1160    for j=1:kmax_x3f
1161        distance(i,j) = norm(X_fwd(:,i) - X_bwd(:,j));
1162    end
1163 end
1164
1165
1166 [~,K] = min(distance);
1167 [radius,k3f] = min(min(distance));
1168 k30 = K(k3f);
1169
1170 x30_approx = x30(1,k30);
1171 x3f_approx = x3f(1,k3f);
1172
1173 if kmax_x30>1 && kmax_x3f>1
1174     figure(16),hold on
1175     set(gcf,'units','normalized','position',[0 0 0.8 0.8])
1176     set(gcf,'PaperPositionMode', 'auto');
1177     xl=xlabel('$\lambda_1^0$');
1178     yl=ylabel('$\lambda_1^f$');
1179     set([xl,yl],'Interpreter', 'latex','FontSize', 18,'linewidth',1.0,'FontName', 'Times');
1180     set(gca,'FontSize', 18,'linewidth',1.0,'FontName', 'Times');
1181     [~,~]=contourf(x30, x3f, distance');
1182     d=colorbar;
1183     set(d,'FontSize', 18,'linewidth',1.0,'FontName', 'Times');
1184     colormap(jet)
1185
1186     set(gcf,'units','normalized','position',[0 0 0.8 0.9])
1187     fillPage(gcf, 'papersize', [11.5 8.5], 'margins', [0.1 0.1 0.1 0.1]);
1188
1189     if k30==1
1190         x30_new = [(3*x30(1,1)-x30(1,2))/2, x30(1,2)];
1191     else
1192         if k30==kmax_x30
1193             x30_new = [x30(1,kmax_x30-1), (3*x30(1,kmax_x30)-x30(1,kmax_x30-1))/2];
1194         else
1195             x30_new = x30(1,k30-1:k30+1);
```

```
        end
    end
    if k3f==1
        x3f_new = [(3*x3f(1,1)-x3f(1,2))/2, x3f(1,2)];
    else
        if k3f==kmax_x3f
            x3f_new = [x3f(1,kmax_x3f-1), (3*x3f(1,kmax_x3f)-x3f(1,kmax_x3f-1))/2];
        else
            x3f_new = x3f(1,k3f-1:k3f+1);
        end
    end


    dx30 = (x30_new(1,end)-x30_new(1,1))/Nt_0;
    dx3f = (x3f_new(1,end)-x3f_new(1,1))/Nt_f;

    x30 = x30_new(1,1):dx30:x30_new(1,end);
    x3f = x3f_new(1,1):dx3f:x3f_new(1,end);

    r_x30 = abs(x30(1,1)-x30(1,end))/abs(x30(1,1));
    r_x3f = abs(x3f(1,1)-x3f(1,end))/abs(x3f(1,1));
end
cprintf('comment','New Distance = %.5f\n',radius)
cprintf('black','x3_0 = [%.4e ; %.4e]\n',x30(1,1),x30(1,end))
cprintf('black','x3_f = [%.4e ; %.4e]\n\n',x3f(1,1),x3f(1,end))
cprintf('comment','~~~~~~~~~~~~~~~~~~~~~~~~~~~~~~~~~~~~~~~~~~~~~~~~~~~~~~~~~~~~~~~~~~~~\n')
cprintf('comment','~~~~~~~~~~~~~~~~~~~~~~~~~~~~~~~~~~~~~~~~~~~~~~~~~~~~~~~~~~~~~~~~~~~~\n')
end

x3_0 = x30_approx;
x3_f = x3f_approx;

cprintf('magenta','X0 =[%.4e,  %.4e,  %.4e]  \n',x1_0,x2_0,x3_0)
cprintf('magenta','XF =[%.4e,  %.4e,  %.4e]  \n',x1_f,x2_f,x3_f)
cprintf('comment' ,'Final Distance = %.4e\n\n',radius)
toc
```

B.2 Function: Computation of FTLEs and FTLVs

breaklines

```
function [ftle,ftlv] = func_FTLE_FTLV(x0,T,NNN)

global n flag
global options

% Final time
tf=T;
if T>0
    dt = 1/NNN;
else
    dt = -1/NNN;
end

N = abs(round(tf*NNN));

% Lyapunov Exponents/Vectors Integration (vector field + Jacobian)
flag = 'lyap';
```

```
states = zeros(n,N+1);

phi    = eye(n,n);
phidt = eye(n,n);
phi0   = zeros(n^2,1);

% Initializing the STM as a vector for the integration
for k=1:n;
      phi0((k-1)*n+1:k*n)=phi(:,k);
end

musvd = zeros(n,N);
Lvecs = zeros(n,n,N);

states(:,1) = x0;

% Integration of nonlinear and linearized dynamics
for i=1:N
      [~,xx] = ode45('func_MCK_integration',[(i-1)*dt i*dt],[states(:,i);phi0],options);

      % from 1 to n (ex 1-4)
      states(:,i+1) = xx(end,1:n);

      % from n+1 to n^2+n (ex 5-20)
      for k=1:n;
          phidt(:,k) = xx(end,(k)*n+1:(k+1)*n);
      end

      % STM update
      phi = phidt*phi;

      % SVD decomposition
      [~,SS,LL] = svd(phi);
      musvd(:,i) = log(diag(SS))/abs(i*dt);
      Lvecs(:,:,i) = LL;
end

% In forward integration Lyap Vect and LL columns order is reversed
% 14+ vector = 1st column of LL matrix
% In backward integration Lyap Vect and LL columns order is preserved
% 11- vector = 1st column of LL matrix
ftlv = Lvecs(:,1,N);
ftle = musvd;
```

B.3 Function: Integration of Dynamics

breaklines

```
function xdots = func_MCK_integration(t,y)

global n m k1 k2 c flag

x1 = y(1);
x2 = y(2);
x3 = y(3);
x4 = y(4);

xdots = zeros(n,1);
```

```
11  fx     = zeros(n,1);
12
13  fx(1,1) = x2;
14  fx(2,1) = (1/m)*(-k1*x1 - k2*x1^3 - c*x2 - x4*(1/m));
15  fx(3,1) = x4*(1/m)*(k1 + 3*k2*x1^2);
16  fx(4,1) = -x3 + c*x4*(1/m);
17
18  if strcmp(flag,'lyap')
19        xdots = zeros(n^2+n,1);
20        J=zeros(n,n);
21
22        J(1,2) = 1;
23        J(2,1) = (1/m)*(-k1-3*k2*x1^2);
24        J(2,2) = (1/m)*(-c);
25        J(2,4) = -(1/m)^2;
26        J(3,1) = x4*(1/m)*(6*k2*x1);
27        J(3,4) = (1/m)*(k1+3*k2*x1^2);
28        J(4,3) = -1;
29        J(4,4) = (1/m)*c;
30
31        phi = zeros(n,n);
32        for k=1:n;
33            phi(:,k) = y(k*n+1:(k+1)*n,1);
34        end
35
36        phidot = J*phi;
37
38        for k=1:n;
39            xdots(k*n+1:(k+1)*n,1)=phidot(:,k);
40        end
41  end
42
43  xdots(1:n,1) = fx;
```